Novel Gold and Molybdenum Catalysts

Dissertation zur Erlangung des Grades
„Doktor der Naturwissenschaften“
im Promotionsfach Chemie

am Fachbereich Chemie, Pharmazie, Geographie
und Geowissenschaften
der Johannes Gutenberg-Universität
Mainz

Maurice Philipp Schrick

geboren in Herdecke

Mainz, 2024

Die vorliegende Arbeit wurde unter der Betreuung von Prof. Dr. Katja Heinze in der Zeit von Dezember 2018 bis Februar 2024 am Institut für Anorganische Chemie und Analytische Chemie sowie dessen Nachfolger, dem Department Chemie der Johannes Gutenberg-Universität Mainz angefertigt.

[redacted]

1. Berichterstatter: [redacted]

2. Berichterstatter: [redacted]

Tag der mündlichen Prüfung: _____

Ich, Maurice Philipp Schrick, versichere, dass ich diese Promotionsarbeit selbstständig verfasst und keine anderen als die angegebenen schriftlichen und elektronischen Quellen genutzt habe. Alle Ausführungen, die anderen Schriften wörtlich oder sinngemäß entnommen wurden, habe ich kenntlich gemacht. Die Dissertation wurde nicht als Prüfungsarbeit für eine andere Prüfung eingereicht, sowie nicht als Dissertation bei einer anderen Fakultät oder einem anderen Fachbereich eingereicht.

_____ _____

(Datum) (Unterschrift)

Kurzzusammenfassung

Für viele Katalysatoren ist die katalysierte Reaktion gut erforscht, wohingegen der Aktivierungsmechanismus des Präkatalysators weniger gut erforscht und oft unbekannt ist.
In dieser Arbeit werden verschiedene synthetische und spektroskopische Methoden beschrieben, die in Kombination mit theoretischen Rechnungen einen Einblick in Aktivierungsmechanismen von bekannten Komplexen liefern.

Die Kohlenstoffmonoxiddehydrogenase (CODH) ist ein Enzym mit Molybdän im aktiven Zentrum, das zur Familie der Xanthin-Oxidasen gehört. Es wird in anaerobischen Bakterien gefunden, die ihren gesamten Energie- und Kohlenstoffbedarf durch Kohlenstoffmonoxid decken. Das aktive Zentrum der CODH enthält ein bimetallisches Molybdän- und Kupfer-Zentrum, wobei beide Metalle durch einen μ_2-Suflid Liganden verbrückt ist. Die Rolle des Kupferatoms ist nicht abschließend geklärt und die Synthese von biomimetischen CODH-Komplexen, die die exakte Koordinationsgeometrie des aktiven Zentrums nachbilden, war bisher nicht erfolgreich. Die Synthese und Charakterisierung des biomimetischen CODH-Vorläuferkomplexes der Form $Mo^{IV}(^{tBu}L)_2(SSiR_2R')_2$ mit 2-Iminopyrrolato Liganden bietet einen Startpunkt für die Synthese eines Komplexes, der das aktive Zentrum der CODH nachahmt. Die ölige, nicht feste Natur dieser Komplexe stellte eine Herausforderung für die Strukturaufklärung da. Diese Herausforderung wurde mittels 2D-Kernspinresonanz-(NMR)-Spektroskopie sowie Dichtefunktionaltheorie (DFT) Rechnungen überwunden. Cyclovoltammetrie (CV) zeigte, dass eine irreversible Oxidation stattfindet. Die versuchte Spaltung der S–Si Bindung mit Selectfluor und die darauffolgende Behandlung mit NaOMe führte zu einem Signal in der UV/vis Spektroskopie, das einer neuen Verbindung zugeordnet wurde. Obwohl keine Verbindung des Typs $Mo^{VI}(^{tBu}L)_2S_2$ nachgewiesen wurde, konnte diese theoretisch berechnet werden.

Acyclische (Aryl)(Amino)Carben Gold(I) Komplexe wurden von [redacted] aus der Gruppe von Prof. Dr. [redacted] an der Witwatersrand-Universität synthetisiert, charakterisiert und erfolgreich in der Katalyse eingesetzt. Darauf aufbauende von mir durchgeführte CV-Experimente halfen bei der Wahl eines passenden Oxidationsmittels für die Ein-Elektronenoxidation der ferrocenyl substituierten Gold(I) Komplexe. Die Oxidation erzeugte ein Elektronenspinresonanz (ESR) Signal, das einer Gold(II)-Spezies zugeordnet wurde. Stopped Flow UV/vis-Experimente bei tiefen Temperaturen bestätigten, dass eine schnelle initiale Oxidation der Gold(I) Komplexe am ferrocenyl Rückgrat stattfindet. Durch temperaturabhängige ESR-Spektroskopie wurde die Aktivierungsbarriere der darauffolgenden Valenzisomerisierung der oxidierten Gold(I)/Eisen(III) Komplexe hin zu

Gold(II)/Eisen(II) Spezies bestimmt. DFT-Rechnungen lieferten weitere Einblicke in die Molekülstruktur dieser katalytisch aktiven Spezies und in den Prozess der Valenzisomerisierung.

Theoretische Rechnungen der Di-substituierten ferrocenyl Fischer Gold(I) Komplexe lieferte Einblicke in die Struktur dieser Verbindungen. Die positive Ladung der ersten Oxidation ist über beide Gold-Atome verteilt, während die zweite Oxidation am Ferrocen-Rückgrat des Komplexes stattfindet.

Abstract

For many catalysts, including enzymes, the catalyzed reactions are well known, while often the activation mechanism is unexplored.
This work describes different synthetic and spectroscopic methods, as well as theoretical approaches to gain insight into activation mechanism of known complexes.

The carbon monoxide dehydrogenase (CODH) is a molybdenum containing enzyme of the xanthine oxidase family. It is found in aerobes, a class of bacteria who are supplying their whole energy and carbon need through carbon monoxide. The active center of the CODH consists of a bimetallic molybdenum and copper center, bridged by a μ_2-suflide ligand. The role of the copper atom is not entirely clear and the synthesis of CODH mimicking complexes resembling the exact coordination geometry of the active center has not been successful. The synthesis and characterization of biomimetic CODH precursor complexes of the form $Mo^{IV}(^{tBu}L)_2(SSiR_2R')_2$ with 2-iminopyrrolato ligands offers a staging point for the synthesis of a CODH mimicking complex. The non-solid but oily appearance of these complexes proofed challenging to characterization attempts. The challenge was overcome relying extensively on 2D-nuclear magnetic resonance (NMR) spectroscopy and density functional theory (DFT) calculations. Cyclic voltammetry (CV) experiments unraveled an irreversible oxidation taking place. Cleavage of the S–Si bond with Selectfluor and subsequently NaOMe yielded the appearance of a new species detected via UV/vis spectroscopy. Although no species of the type $Mo^{VI}(^{tBu}L)_2S_2$ was isolated so far, theoretical calculations gained insight into the geometry of it.

Acyclic (aryl)(amino)carbene gold(I) complexes were synthesized, characterized and applied in catalysis by [redacted] of the group of Prof. Dr. [redacted] at the university of the Witwatersrand, in Johannesburg, South Africa. CV experiments conducted by me aided in finding a suitable oxidant, which was used in the one electron chemical oxidation of the ferrocenyl substituted carbene gold(I) complexes. This yielded an electronic paramagnetic resonance (EPR) signal, which was assigned to a gold(II) species. Stopped flow UV/vis-experiments at low temperatures confirmed a fast initial oxidation, while temperature depending EPR spectroscopy gained insight into the activation barrier of the subsequent valence isomerization of the oxidized gold(I)/iron(III) species towards a gold(II)/iron(II) species. DFT calculations delivered further insight into the geometry of these catalytically active species and shed light onto the valence isomerization process.

Theoretical calculations of the di-substituted ferrocenyl Fischer gold(I) complex yielded insights into the structure. The positive charge after first oxidation accumulates at both gold atoms, while a second oxidation takes place at the ferrocenyl backbone of the complex.

Contents

Abbreviations

^{1}H-^{1}H-NOESY	proton-proton nuclear Overhauser effect
^{1}H-^{1}H-ROESY	proton-proton rotary nuclear Overhauser effect
^{31}P-NMR	Phosphorus-31 nuclear magnetic resonance
Ad	adamantyl
Ar	aromatic substituent
Asp	aspartate
BAr^{F}_{4}	tetrakis[3,5-bis(trifluoromethyl)phenyl]borate
BF_4	tetrafluoroborate
BINOL	[1,1'-binaphthalene]-2,2'-diol
Bn	benzyl
Bpy	bipyridine
Bu	butyl
CIP	Cahn-Ingold-Prelog
CODH	carbon monoxide dehydrogenase
COSY	correlation spectroscopy
Cp	cyclopentadienyl
Cp*	1,2,3,4,5-pentamethylcyclopentadienyl
CV	cyclic voltammetry
Cys	cysteine
d	doublet
dd	doublet of doublet
DFT	density functional theory
DMF	dimethylformamide
DMSO	dimethyl sulfoxide
DMSOR	DMSO reductase
dppn	1,8-bis(diphenylphosphano)naphthalene
EPR	electron paramagnetic resonance
Et	ethyl
FAD	flavine adenine dinucleotide
FcH	ferrocene
FcH^{+}	ferrocenium
Glu	glutamate
HMBC	heteronuclear multiple-bond correlation
HMDSO	hexamethyldisiloxane
HSQC	heteronuclear single-quantum correlation
$H^{tBu}L$	[1 *H*-pyrrole-2-yl)methylene]-4-(*tert*-butyl) aniline
i-Pr	*iso*-propyl
IR	infrared
Johnphos	(2-Biphenyl)di-*tert*-butylphosphane
LMCT	ligand to metal charge transfer
L_n	$ligand_{amount}$
m	multiplet
Magic Blue	tris(*p*-bromophenyl)ammoniumyl hexachloroantimonate
Magic Green	tris(2,4-dibromopheny)ammoniumyl hexachloroantimonate
Me	methyl
MLCT	metal to ligand charge transfer
NAD^{+}	nicotinamide adenine dinucleotide
^{n}Bu	*n*-butyl

NHC	*N*-heterocyclic carbene
NMR	nuclear magnetic resonance
NOE	nuclear Overhauser enhancement
Ns	nitrobenzene sulfonamide
NTf_2	bis(trifluormethanesulfonyl)imide
OTf	triflate
Pa	pascal
Ph	phenyl
R	organic substituent
s	singulet
Selectfluor	1-chloromethyl-4-fluoro-1,4-diazoniabicyclo[2.2.2]octane bis(tetrafluoroborate)
sept	septet
SIPr	1,3-bis-(2,6-diisopropylphenyl)imidazole-2-ylidene
SO	sulfide oxidase
Sub	substrate
t	triplet
^{t}Bu	*tert*-butyl
TDDFT	time depending density functional theory
TEP	*Tolman* electronic parameter
THF	tetrahydrofuran
tht	tetrahydrothiophene
TMEDA	tetramethyl ethylenediamine
TOCSY	total correlation spectroscopy
TOF	turn over frequency
TON	turn over number
TPP	tetraphenylporphyrinato
UV/Vis	ultraviolet/visible range
Xantphos	9,9-dimethyl-9*H*-xanthene-4,5-diyl)bis(diphenylphosphane)
XO	xanthine oxidase
XRD	X-ray diffraction

1 Introduction

1.1 Gold complexes as catalysts

For a long time, the noble metal gold was considered to be unreactive and thus not interesting for catalytic applications.[1],[2] Early examples of olefin gold(I) complexes with weakly coordinating anions are known since the late seventies which were unreactive in catalysis.[3] In 1986 *Ito* and coworkers presented a first example for the application of gold(I) in catalysis. The addition of isocyanides to an aldehyde was catalyzed by an *in situ* formed chiral gold(I) complex (scheme 1).[4],[5]

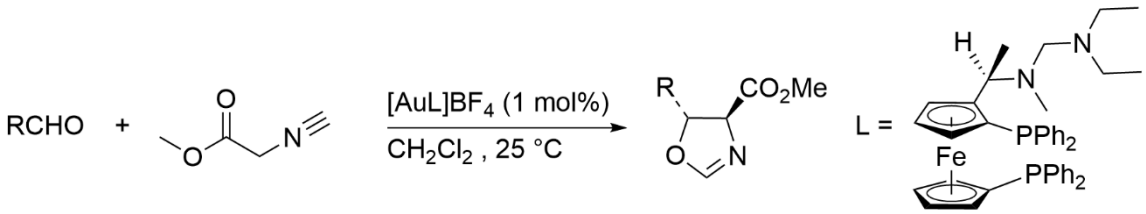

Scheme 1: Gold(I) catalyzed addition of isocyanides to an aldehyde presented by *Ito*.[4],[5]

Back then the work from *Ito* was considered as just an "exception that proved the rule" considering gold complexes as unreactive.[6] This paradigm shifted with a seminal publication from *Teles* and coworkers in 1998. They presented a cationic gold(I) complex, that catalyzed the addition of oxygen containing nucleophiles to acetylenes (scheme 2).[7] The catalyst is formed *in situ* through protonation of the pre-catalyst **1** with methyl sulfonic acid, which functions as co-catalyst. It already was known, that gold(III) halide catalysts such as $NaAuCl_4$ perform the same reaction, but suffered from deactivation through reduction.[8] Utilizing the less nucleophilic counter ion mesylate instead of chloride, alongside a cationic gold complex was the crucial advancement achieved by *Teles*.[6] The catalyst performed with exceptional turnover numbers (TON), several orders of magnitude higher compared to the previously used mercury(II) catalyzed process.[6] Internal alkenes are attacked at the sterically less hindered position under formation of a ketal **2**, with the formation of the corresponding enol ether **3** as side product. Propargyl alcohol dimerizes and forms a cyclic ketal **4**.[7]

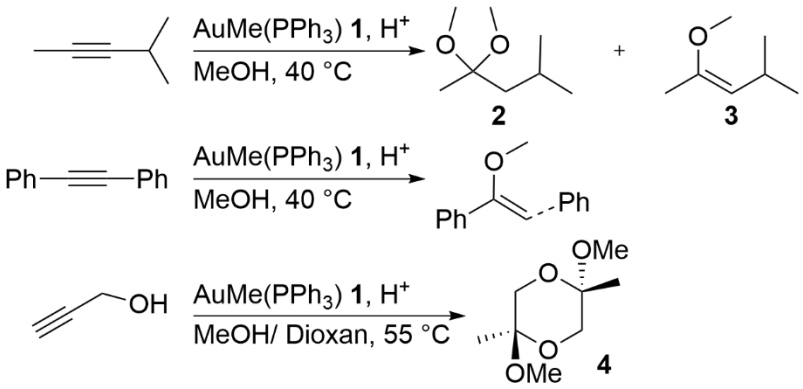

Scheme 2: Examples for the addition of methanol to alkynes, the catalyst is prepared from $AuMe(PPh_3)$ and methanesulfonic acid.[7]

The reaction introduced in this paper to generate catalytic active gold(I) species, was applied by numerous authors, was used in a plethora of examples and is still used today in gold(I) catalysis.[9]–[11] This general reaction starts with complexes of the form Au(L)X, which function as pre-catalysts. Important for the reaction are a good solubility of the pre-catalyst in common organic solvents and an adequate stability.[12] The catalytic active species $[AuL]^+$ is then generated *in situ*. Since the ligand (L) needs to stabilize the catalytic active complex cation, it is electron donating e.g. a phosphane or a *N*-heterocyclic carbene (NHC). X is either covalently bound, like in the *Teles* example, or an anion.[7] To generate the catalytic active $[AuL]^+$ cation the pre-catalyst needs to be activated. This is done by exchanging X with a weakly coordinating ion.[12] One way to remove covalently bound X is the use of strong acids.[7] When X is a halide, silver salts with poor coordinating anions like $AgBF_4$, $AgSbF_6$, AgOTf are used, since the silver halides are insoluble and easily separated through filtration.[9] This method to generate catalytic active $[AuL]^+$ cations has downsides, too. One problem concerning solutions with $[AuL]^+$ cations is their short-term stability which prevents storage.[12]

1.1.1 Exploring the scope of gold catalysts

Over the years the field of gold catalysis has expanded rapidly. Nowadays gold complexes have been reviewed heavily and are employed in numerous different types of catalytic reactions.[9],[10],[13]–[16] The most common substrates contain C−C-multiple bonds, however the activation of substrates with C=O-bonds is known as well.[9],[14]

Reactions between activated gold complexes and alkynes show a higher reactivity than with alkenes. Interestingly, activated gold complexes do not prefer coordination to C=C- over C≡C-bonds as shown in ^1H-^1H-NOESY experiments on enyne substrate **5** at 223 K (scheme 3).[17] For alkynes, the electro- and nucleophilic attacks are more favored, compared to alkenes, which ultimately determines the higher reactivity of gold complex towards alkyne containing substrates over alkene containing one.[17],[18]

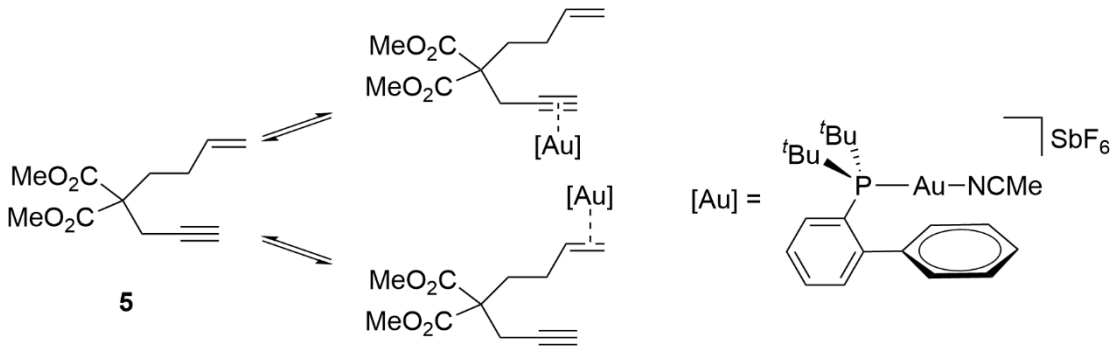

Scheme 3: An activated gold catalyst binds equally to alkyne and alkene functions of the enyne substrate **5**.[17]

The cyclisation of *N*-propargyl amides to oxazolines is commonly used to determine the reactivity of gold(I) complexes.[19]–[22] This reaction also gives information about the oxidation state of the gold center during catalysis: while gold(I) catalysts transform *N*-propargyl amides to oxazolines, oxazoles are the end product of gold(III) catalysts (scheme 4).[23],[24]

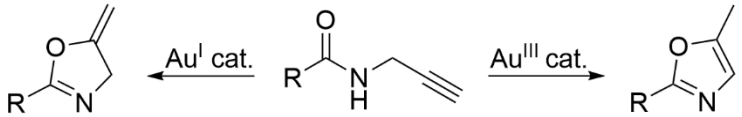

Scheme 4: The product of the *N*-propargyl amide cyclization is determined by the oxidation state of the gold catalyst.[23],[24]

The following mechanism leads to the cyclisation of *N*-propargyl amide (scheme 5). After activation of a pre-catalyst, the gold(I) complex binds to the alkyne in a π-type fashion (scheme 5, 1.).[25] Withdrawing electron density from the alkyne, leads to an elongated C–C triple bond, which is confirmed through infrared (IR) spectroscopy.[25] The intermolecular carbonyl group attacks the activated alkyne as a nucleophile (scheme 5, 2.). Tautomerization (3.), deprotonation (4.) and subsequent de-auration (5.) conclude the catalytic cycle and release the oxazole while regenerating the activated gold(I) complex.

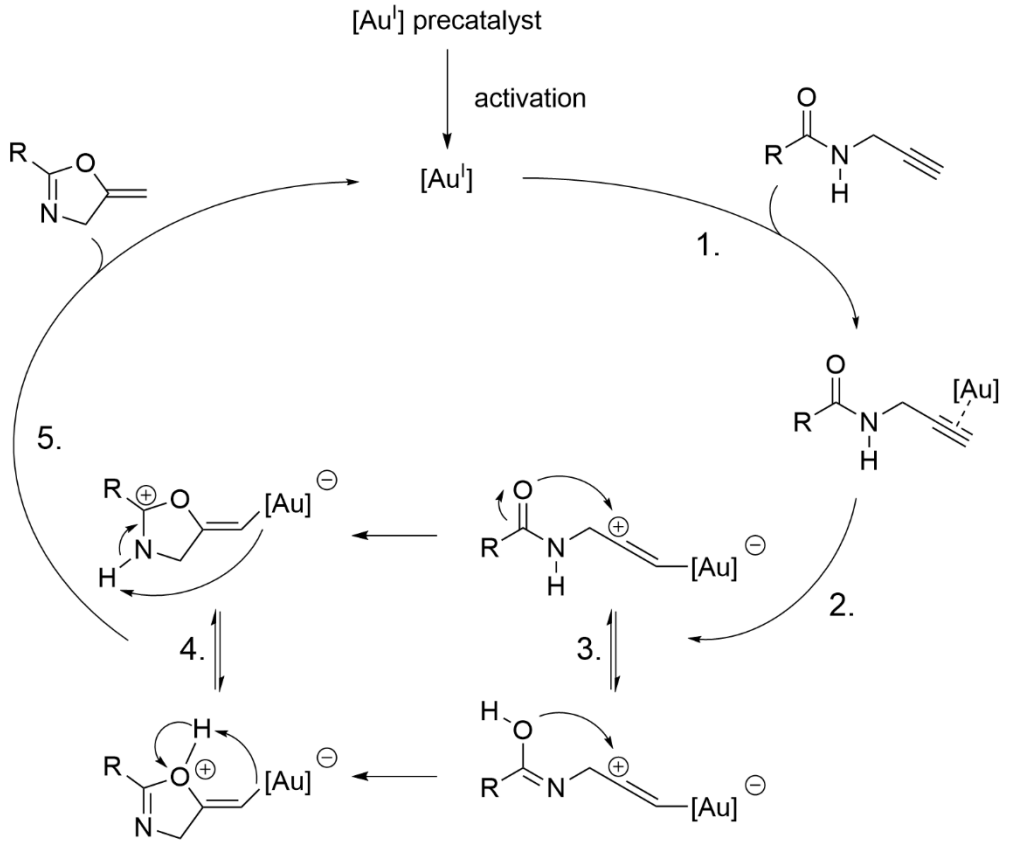

Scheme 5: The catalytic cycle of a gold(I) catalyzed cyclisation with *N*-propargyl amide as substrate.[26]

1.1.1.1 Hydrohalogenation

Hydrochlorination of acetylenes was first discovered 1976 by *Thomas* as a side product of the oxidation of the same substrate with chloroauric acid.[27] Chloroauric acid catalyzed the oxidation of phenyl acetylene in an aqueous methanol solution. The ketone **6** was obtained as major product (38 %) with ether **7** and vinyl chloride **8** as byproducts (each < 5 %) (scheme 6).[14]

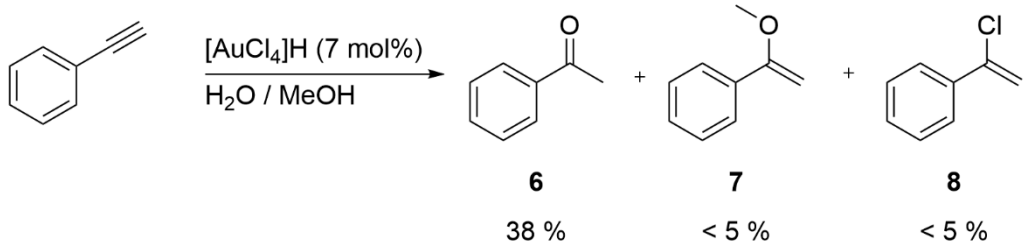

Scheme 6: Oxidation of phenyl acetylene in the presence of chloroauric acid, with hydrochlorination side product **8**.

The role of gold as catalyst was not discovered until 1985, when different metal chlorides supported on a carbon surface were tested as catalyst and gold(III) turned out to be the most active metal chloride tested in the vapor phase reaction to form vinyl chloride monomers through the hydrochlorination of

acetylene.[28] A detailed study of the reaction mechanism revealed the *anti*-addition of HCl, forming the *anti*-Markovnikov product **9** (scheme 7).[29]

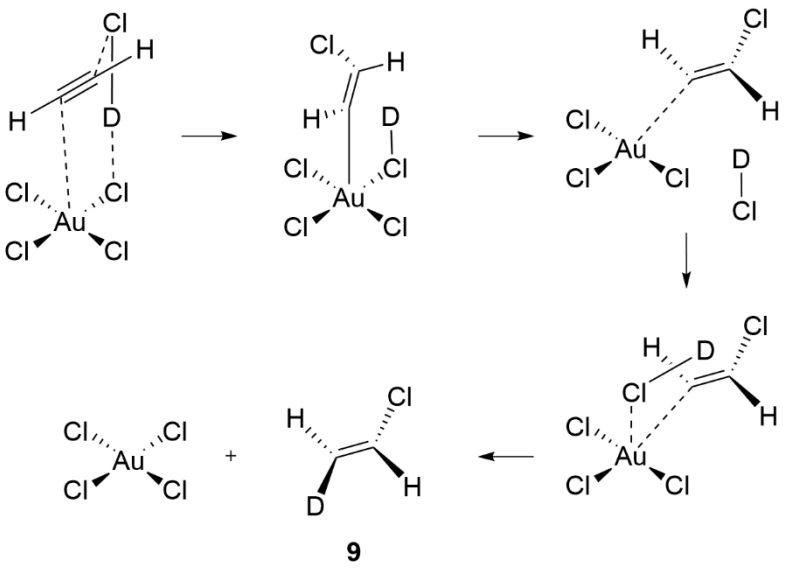

Scheme 7: Proposed reaction mechanism for the hydrochlorination of acetylene with DCl.[29]

The conversion rate correlates with the bulkiness of the alkyne, with internal alkynes e.g. hex-2-yne being least reactive (<2%). A mechanism involving a simultaneous coordination of both alkyne and HCl to the gold center was ruled out through DFT calculations.[29]

The hydrofluorination of acetylenes with a NHC gold(I) fluoride catalyst leads to the *trans* product. Interestingly, the intermediary fluorovinyl gold(I) complex **10** was isolated and stable enough for investigations through X-ray diffraction (XRD) (scheme 8).[30] The complex Au(O^{t}Bu)(SIPr) (SIPr = 1,3-Bis-(2,6-diisopropylphenyl)imidazole-2-ylidene) or the combination of the complex AuCl(SIPr) with $AgBF_4$ both lead to catalytic active species. Best results however were obtained with the bulkier and less electron-rich NHC-ligand 4,5-dichloro-1,3-bis(2,6-diisopropylphenyl)imidazol-2-ylidene with addition of a mild HF source. The scope of this reaction includes dialkyl-, diaryl-, and aryl/alkyl- or thienyl/alkyl-substituted alkynes (scheme 8).[30]

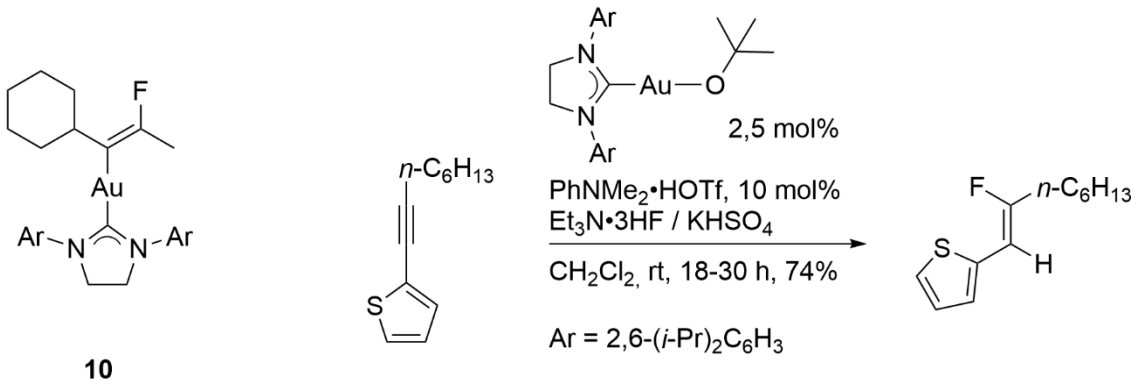

Scheme 8: Left: fluorovinyl gold(I) intermediate **10**, right: Au catalyzed hydrofluorination.[10],[30]

1.1.1.2 Hydroamination

The addition of aniline derivatives to aromatic and aliphatic alkynes is feasible with the gold(I) catalyst introduced by *Teles* after activation with an acid promoter under solvent free conditions.[31] The best results were achieved with heteropoly acids with nearly quantitative yields or with trifluoromethanesulfonic acid. A turn over number (TON) of up to 9000, with respect to the Au content, and near to 90% yield were achieved with $AuMe(PPh_3)$ as precatalyst (0.01 mol%) and $H_3PW_{12}O_{40}$ as acid promoter (0.05 mol%).[31] Anilines with electron-withdrawing substituents such as bromo-, cyano- and nitro-groups in *trans* position to the amino group were used in this case. Electron withdrawing substituents and steric hindrance in the aniline derivate did not hamper the activity, however aliphatic amines were unreactive. Internal alkynes are less reactive probably due to steric hindrance (scheme 9).[31]

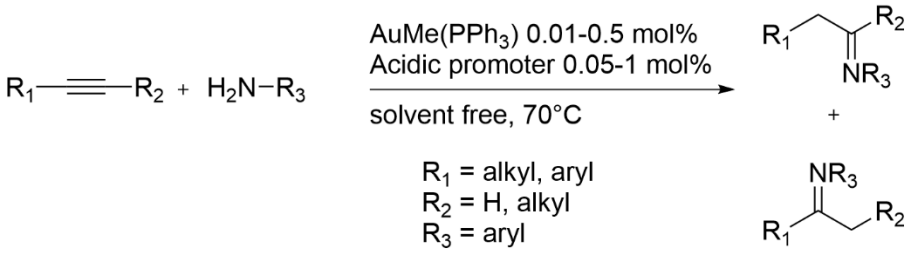

Scheme 9: Solvent free gold(I) catalyzed hydroamination of alkynes with anilines.[31]

1.1.1.3 Hydroalkoxylation

The most prominent example for hydroalkoxylation of alkynes is the above mentioned reaction between methanol and various alkynes, published by *Teles*.[7] Countless other examples are known, including intramolecular hydroalkoxylations and the use in natural product total synthesis (scheme 10).[32],[33]

Scheme 10: Gold(I) catalyzed hydroalkoxylation step in the total synthesis of andrachcinidine **11**.[33]

1.1.1.4 Hydrogenation

Since the middle of last century, it is known that gold surfaces are able to activate hydrogen. *Couper* and *Eley* converted *para*-hydrogen to *ortho*-hydrogen on a palladium/gold alloy surface.[34],[35] Another example of a reaction on a gold surface is the hydration of olefins at temperatures above 200°C on SiO_2, γ-Al_2O_3 or MgO surfaces impregnated with $HAuCl_4$.[36]–[38]

Ito and *Sawamura* demonstrated that gold not only actively catalyzed heterogenous hydrogenation reactions, when they reported an interesting example of a homogeneous gold catalyst. They used an $Au^{I}Cl$(Xantphos) complex **12** and $HSiEt_3$, to catalyze the dehydrogenative silylation of alcohols with high chemoselectivity and solvent tolerance.[39] They were able to selectively silylate the steroid derived substrate **13**, while a plethora of functional groups was tolerated. Later studies revealed a mechanism, that involves a gold(I) hydride species **14** as key intermediate (scheme 11).[18],[40]

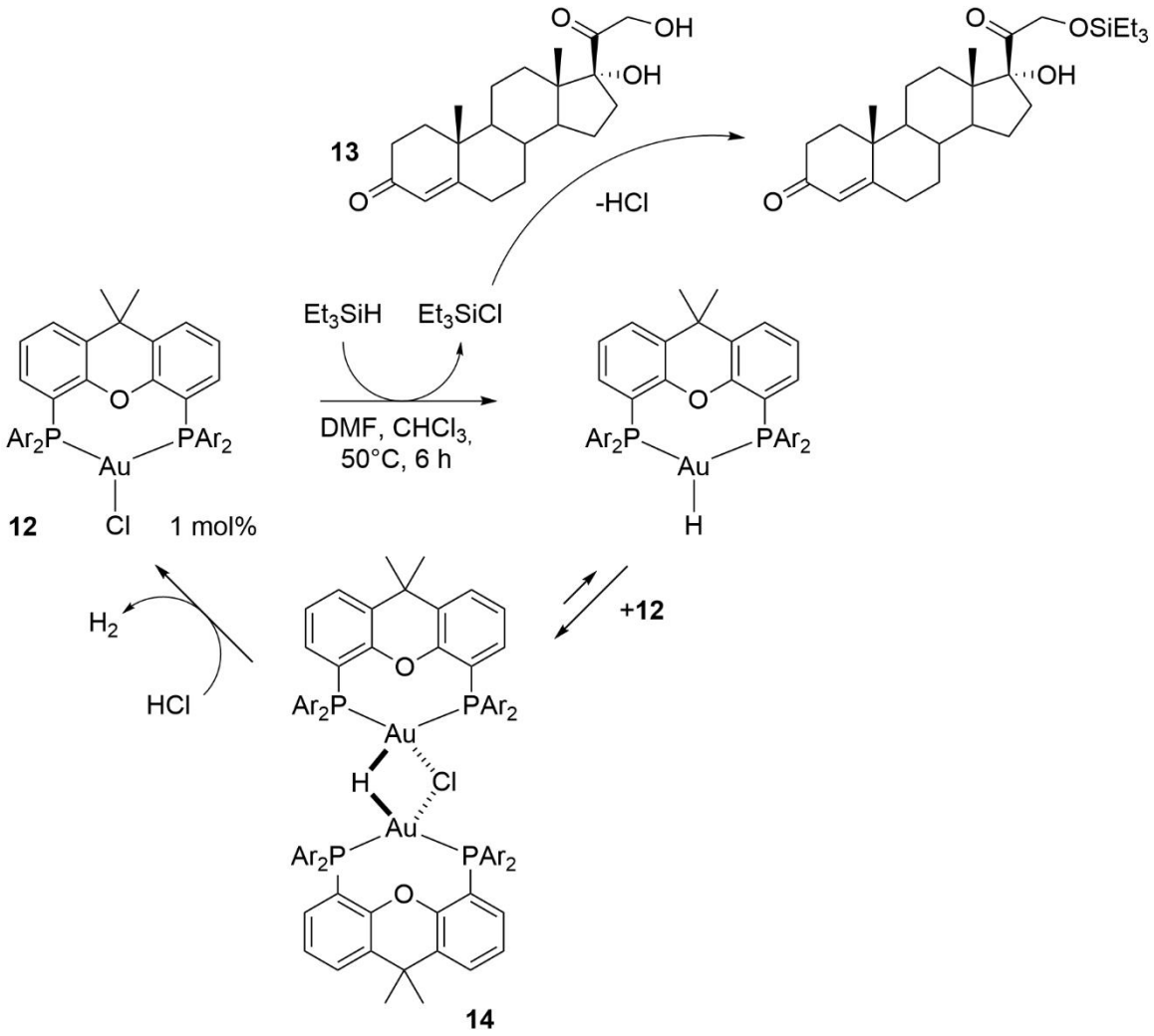

Scheme 11: Reaction mechanism of the gold(I) catalyzed dehydrogenative silylation of substrate **13**.[18],[40]

1.1.1.5 Oxidation

The majority of gold catalyzed oxidations are heterogeneous.[9],[10] Gold supported on different surfaces, such as silica,[41] carbon[42] or even CeO_2[43] was successfully used in the oxidation of sugar,[42] alcohols[41],[43] and various hydrocarbons.[44] Gold nanoparticles proved to be active in a variety of oxidation reactions, too.[45]–[47] Not only in heterogeneous reactions, but also in homogeneous reactions gold complexes were catalytically active.[48] The noble metal gold has a high oxidation state stability, which is an advantage when combined with mild oxidants.[48] Gold(I) and gold(III) complexes

have been used as catalysts to oxidize a variety of substrates, alongside different oxidants, such as sulfoxides,[49] *N*-oxides[50] and other oxygen based oxidants (scheme 12).[51]–[53] When gold(I) complexes are paired with strong oxidants however, they tend to be oxidized to gold(III) species, which subsequently undergo reductive elimination.[48] Selectfluor[54] or hypervalent iodine reagents[55] are examples for oxidants strong enough to oxidize gold(I) to gold(III).

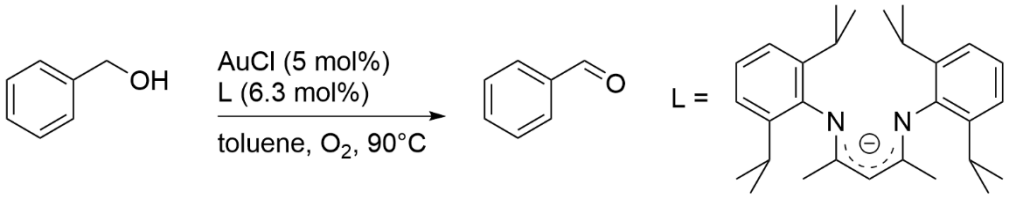

Scheme 12: Gold catalyzed oxidation of benzyl alcohol to benzaldehyde.[56]

1.1.1.6 Gold in cross coupling reactions

Oxidative addition, migratory insertion, transmetallation and reductive elimination are key reaction steps in cross-coupling reactions to generate C−C bonds with transition metal catalysts.[57] Nickel,[58] copper[59] and most prominently palladium[60] complexes are typically used in cross coupling reactions and the associated mechanisms are well understood.[13] For gold complexes especially the oxidative addition proved to be a problematic step, due to the high redox potential of the Au^{I}/Au^{III} pair, compared to the isoelectronic Pd^{0}/Pd^{II} couple.[61] However it is possible to use gold in cross coupling reactions, albeit with implementing auxiliary steps compared to palladium cross coupling reactions and several strategies have emerged to overcome these challenges.[48],[62] One strategy to oxidize Au^{I} to Au^{III} is the addition of a sacrificial oxidant e.g. Selectfluor[54] or hypervalent iodine species[55] (vide supra). Oxidant free methods rely on a photosensitizer, e.g. $[Ru(bpy)_3]^{2+}$ in order to facilitate the photochemical oxidation towards gold(III),[63] or on rational ligand design to lower the required energy for a direct oxidation.[64] Examples of direct oxidative addition without oxidant, light or special ligand design have emerged.[65],[66] *Patil* used aryldiazonium salts with various organostannanes in a gold catalyzed cross coupling reaction (scheme 13).[66]

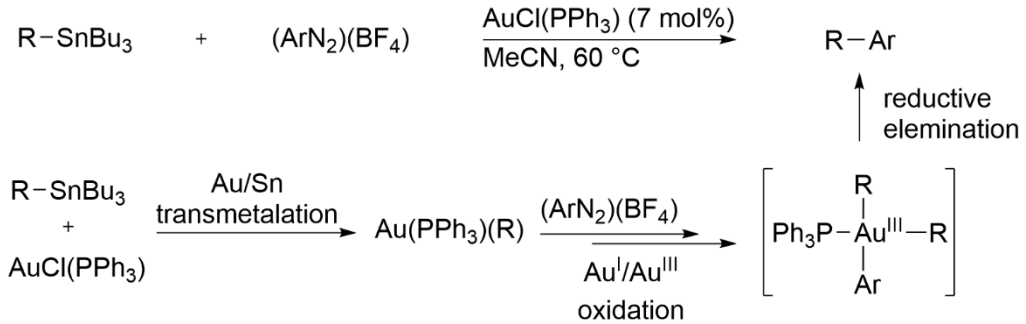

Scheme 13: Gold catalyzed cross coupling reaction, using aryldiazonium salts and organostannanes.[62]

1.1.2 Activating Gold(I) complexes

1.1.2.1 Problems related with silver salt activation

As above mentioned gold(I) complexes need to be activated in order to be catalytically active, which is often done with strong acids or silver salts.[7],[9],[12] Especially silver salts tend to have a range of problematic abilities. Silver salts are expensive, light-sensitive, have a poor solubility in several important organic solvents, high adsorptive properties and are easily reduced to metallic silver.[12],[67] The high metallophilic attraction of gold and silver in their low oxidation states towards each other opens a path to side reactions of the precatalyst with the dehalogenation agent and further hinders the complete silver removal.[68]–[72] Another problem is the non-innocence of silver(I) salts in catalytic reactions. Several reactions, that were thought to be genuine gold catalyzed, show different selectivity depending on the presence of silver salts, or have no turnover at all when silver salts are omitted (scheme 14, 1.).[73] It is even possible to combine both metals in cooperative silver/gold catalysis and in some cases both metals catalyze the same reaction (scheme 14, 2.).[74],[75] Examples of the inhibition of gold catalyzed reactions with silver salts have been reported, according to the authors this is due to the interaction with gold intermediates.[76]

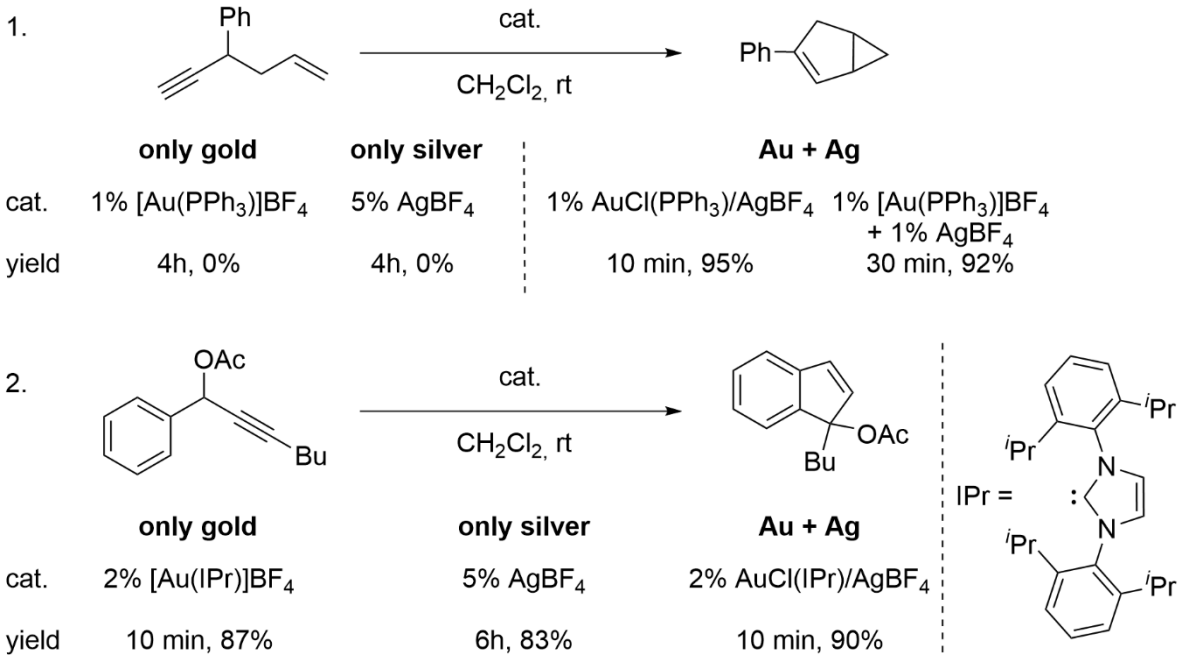

Scheme 14: 1. Example for a catalytic reaction, where only the combination of gold and silver yield a product,[73] 2. example for a catalytic reaction, where also the silver salt is catalytically active.[73],[77],[78]

Since solutions with activated $[AuL]^+$ cations and poor coordinating anions such as BF_4^-, SbF_6^- and OTf^- are not long term stable, other anions were investigated.[12] Reacting equimolar amounts of AuCl(L), (L = NHC or Ph_3P), and $AgNTf_2$ (NTf = Bis(trifluormethanesulfonyl)imide) in CH_2Cl_2 at room temperature yields complexes of the form $Au(L)(NTf_2)$ which are long term stable under air and moisture and are

easily purified by crystallization.[79],[80] Even though Ag is used in the activation process, this class of catalysts introduced by *Gagosz* ensures a silver free catalysis and has successfully been used in several examples.[12],[80]

1.1.3 Strategies for silver-free activation of gold complexes

Over the years many different approaches to omit silver salts as activating agent have emerged in gold chemistry.

1.1.3.1 Using polar solvents

Water as solvent gives the advantage of catalytic active complexes without the need of external activation. Neutral complexes of the form AuCl(L), L = NHC or phosphane, show moderate activity in aqueous solutions.[81] In order to get gold complexes water soluble, ligands with cationic moieties need to be used, such as alkyl sulfonates,[82] zwitterionic complexes[83] or ammonium groups.[84] Even simple gold complexes of the form AuCl(IPr) are catalytically active in a MeOH/water mixture and catalyze the hydration of terminal alkynes (scheme 15, 1.).[81] Next to gold complexes bearing NHC ligands also complexes bearing PMe_3 as ligand are catalytically active in water.[85] Complexes of the form AuCl(PMe_3) catalyze a tandem addition/cyclization of terminal alkynes with *o*-alkynylaryl aldehydes in a water/toluene mixture in the presence of *i*-Pr_2NEt (scheme 15).[85]

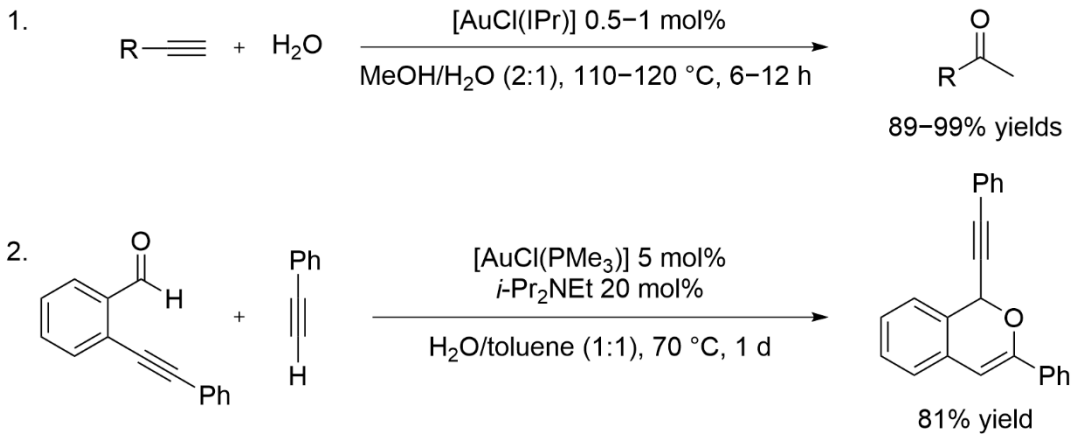

Scheme 15: 1. Gold catalyzed hydration of terminal alkynes in water without activation of the catalyst,[82] 2. gold catalyze tandem addition/cyclization of terminal alkynes with *o*-alkynylaryl aldehydes in water without activation of the catalyst.[81],[85]

In these reactions water not only is a solvent but also functions as educt, which is troublesome in other reactions if it is not desired.[81],[85] Other problems using polar solvents to activate gold(I) catalysts are solubility related, limiting the choice of catalysts and substrates.

1.1.3.2 Using alternative metal salts

Metal salts, other than silver salts, are also able to activate gold(I) complexes for catalysis.[67] A plethora of metal salts were successfully used in the activation of gold(I) catalysts such as the triflic salts of Ga^{II}, Y^{III},[86] Cu^{I}, Cu^{II}, In^{III}, Bi^{III}, Zn^{II} and $In(NTf_2)_3$.[87],[88] Next to heavy metal salts, alkali metal salts with non-coordinating anions such as $NaBAr^F_4$ or KPF_6 are also suitable activators for gold pre-catalysts.[89]–[91] The first example of activating gold(I) complexes with alternative metal salts was reported by *Shi*, who used $Yb(OTf)_3$ as activator in the cyclization of epoxy alkynes.[92] The metal salts not only activated the gold catalyst, but also functioned as co-catalyst. $Yb(OTf)_3$ as activating agent produced higher yield, compared to catalysts activated with AgOTf.[92] $Zn(ClO_4)_2$ was successfully used as activating agent in a gold(I) catalyzed tandem hydroamination-annulation reaction of 4-yne-nitriles and also delivered higher yields than parallel experiments with $AgSbF_6$ used for activation.[93]

The Cu^{I} and Cu^{II} salts are the most interesting alternative metal salt activators and are even used in gram-scale reactions, because they offer advantages at higher temperatures over silver(I) salts.[94],[95] At elevated temperatures the activated gold complexes tend to decompose to nano particles which are visible as a purple colored solution and subsequently decomposition to a gold(0) mirror which deactivates the catalyst. Silver salts convert gold complexes instantly and quantitatively to the active form $[AuL]^+$, which is exposed to the harsh conditions at elevated temperatures and rapidly decomposes into gold(0) and catalytically inactive $[AuL_2]^+$ species.[96] Cu^{II} salts however activate the gold pre-catalyst reversibly in a slow way, so that a low catalyst concentration is maintained while the temperature stable pre-catalyst functions as reservoir for the active species (scheme 16).[94],[96]

1. $[AuCl(PPh_3)] \underset{-\ Cu(OTf)_2}{\overset{Cu(OTf)_2}{\rightleftharpoons}} [Au(PPh_3)]OTf + CuCl(OTf)$

2. 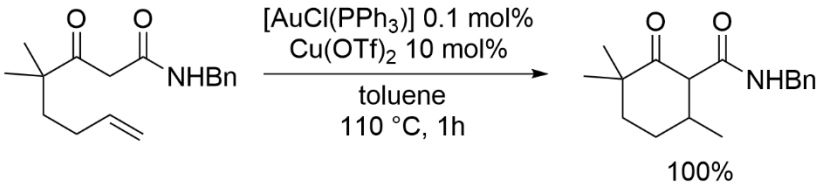

Scheme 16: 1. reversible activation with $Cu(OTf)_2$,[94] 2. copper(II) activated and gold catalyzed intramolecular hydroalkylation of alkenes.[94]

One disadvantage shared by all metal salts is the high molar amount needed for the activation, which is often up to 10 mol%.[67] On the contrary only an equimolar amount of silver salts is needed to activate gold complexes.[9]

1.1.3.3 Halogen-bond donors

Metal free activation is achieved by using halogen bond donors for the activation of gold pre-catalysts. A halogen bond donor, such as an iodonium salt, forms a halogen bond with the chloride atom of the gold pre-catalyst, withdrawing electron density from the chloride and subsequently the gold center, activating it for catalysis.[97] Hints towards the formation of an equilibrium of the pre-catalyst with, the proposed active species $[Au(PPh_3)_2]^+$ is found by ^{31}P-NMR-spectroscopy. Possible activation with $[BAr^F{}_4]^-$ and molecular iodine was ruled out through further experiments (scheme 17).[97]

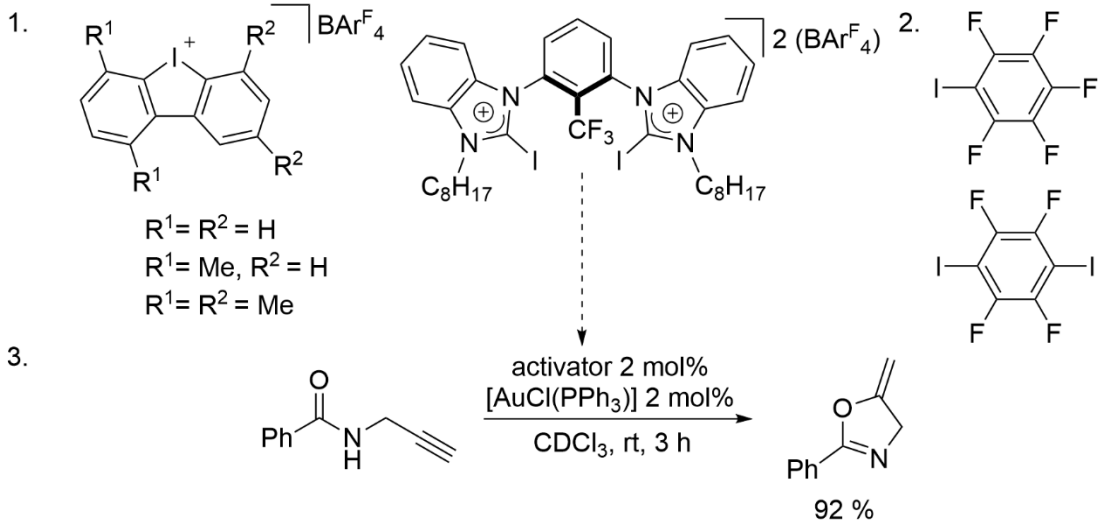

Scheme 17: Compounds as halogen bond donors. 1. iodonium salts,[97],[98] 2. iodofluorobenzenes,[99] 3. catalyzed reaction with iodonium salt as activator.[97]

1.1.4 Self-activating gold(I) chloride complexes

1.1.4.1 Activation by intramolecular chloride transfer

Similar to the above mentioned activation of gold(I) chloride complexes through an intermolecular halide bond, self-activation through an intramolecular hydrogen bond is feasible. In a prove of principle reaction *Gabbaï* used a phosphane ligand with a secondary amine in close proximity to the gold(I) chloride unit.[20] In the solid state two units of the complex **15** are held together through hydrogen bonding between the NH group and a chloride of a second complex (scheme 18). The interaction is accompanied by aurophilic interactions of the central atoms. In solution, pulse gradient spin-echo NMR spectroscopy pointed to an equilibrium between the monomer **15** and the dimer of the complex. The complex was only moderately active in catalyzing the cyclization of *N*-propargyl benzamides, with a conversion rate of up to 53% after 24h of reaction time, but proofed the method of activation through hydrogen bonding feasible.[20]

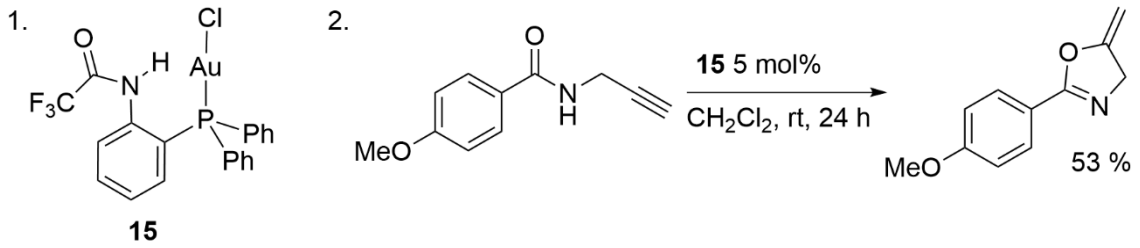

Scheme 18: 1. self-activating gold(I) complex by *Gabbaï* and 2. catalyzed reaction.[20]

Incorporating the same activation method into a carbene ligand let to a better catalytic activity of the activated gold(I) complex **16** as demonstrated by *Helaja*, reaching full conversion after 3 hours with a lower catalyst loading compared to the reaction presented by *Gabbaï*.[100] DFT calculations point towards a dual NH bridge formation between each the complex and the substrate with the chloride, which is not coordinating the central gold atom anymore, freeing up a coordination site on the later for substrate coordination (scheme 19).

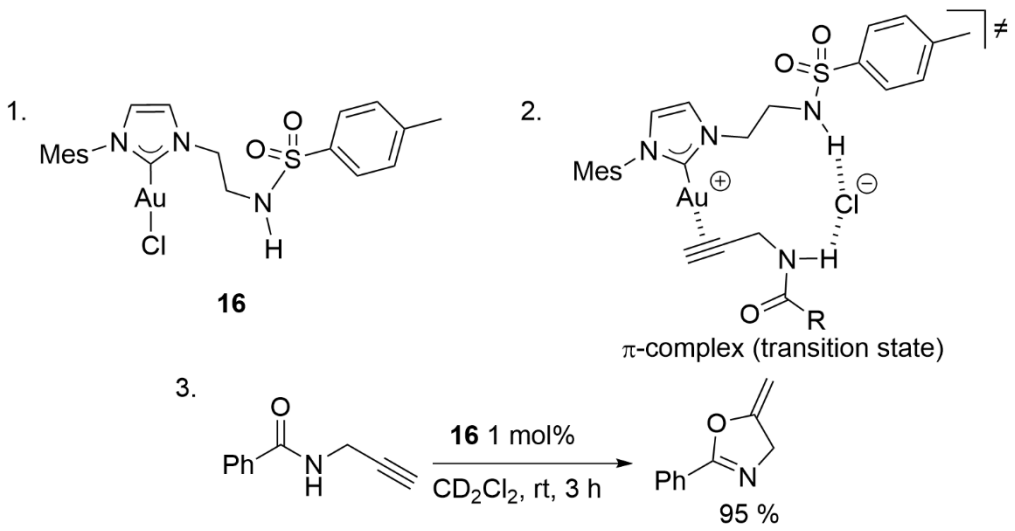

Scheme 19: 1. self-activating complex by *Helaja* and 2. DFT calculated π-complex state.[100]

Echavarren then incorporated bidentate H-bond donors into a ligand scaffold for the activation of gold(I) complex **17** and screened a variety of phosphane ligands for their activity in gold(I) catalyzed reactions.[101] They found a correlation between H-bonding ability of the ligand and catalytic activity of the complex **17**, which led to the conclusion that H-bonding indeed aids chloride abstraction from the gold(I)−Cl fragment (scheme 20, 2.). The proposed catalytic cycle, unraveled by kinetic and computational data, suggest the protodeauration to be the turnover-limiting step.[101] The H-bond donation not only self-activates the complex **17**, but also forms H-bridges with the carbonyl group of the substrate.

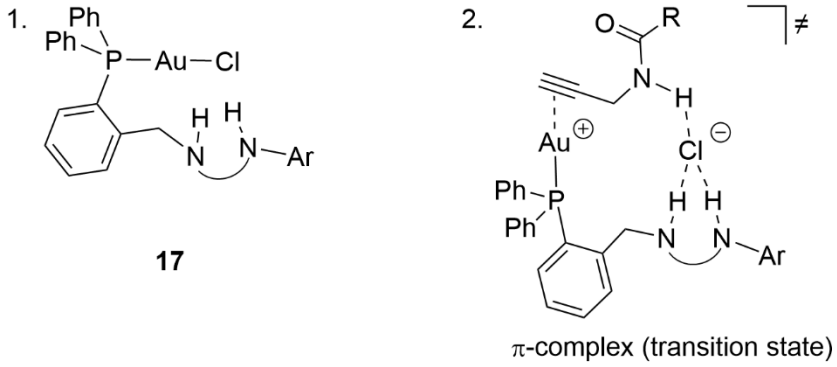

Scheme 20: 1. self-activating gold(I) complex by *Echavarren*, 2. coordination of a substrate with complex **17** forming a π-complex transition state.[101]

In a separate work the same group further explored the enantioselective catalysis with ligands bearing bidentate H-bond donors.[102] The afore mentioned activation of gold(I) complexes by dual H-bridge formation was adjusted in a way, that the H-bridges do not aid the self-activation of the complex, but stabilize an ion pair of the gold(I) complex with the chiral counter ion of a silver salt. This silver salt activates the gold complex via classical chloride abstraction. They combined an achiral Johnphos-derived phosphano urea gold(I) chloride complex **18** (Johnphos = (2-biphenyl)di-*tert*-butylphosphane), bearing the bidentate H-bond donor, with a chiral BINOL-derived phosphoramidate Ag^{I} salt **19** (BINOL = [1,1'-binaphthalene]-2,2'-diol), which resulted in complexes which performed enantioselective catalytic reactions with high yields and high enantiomeric ratios (scheme 21, 1.).[102] *Marinetti & Guinchard* used a similar approach on enantioselective gold(I) catalysis. They tethered a gold(I) complex via a chiral BINOL-derived phosphane ligand to a phosphate counter ion.[103] The self-activation then occurs through weakly basic nucleophiles, abstracting HCl from complex **20** (scheme 21, 2.). The phosphate subsequently coordinates the gold(I), resulting in the stabilization of the catalytically active species **21**. Gold(I) is no longer coordinated linearly, but in a slightly bend fashion (P−Au−O angle: 160 °), which results in an energetically higher laying species and facilitates substrate coordination.[67]

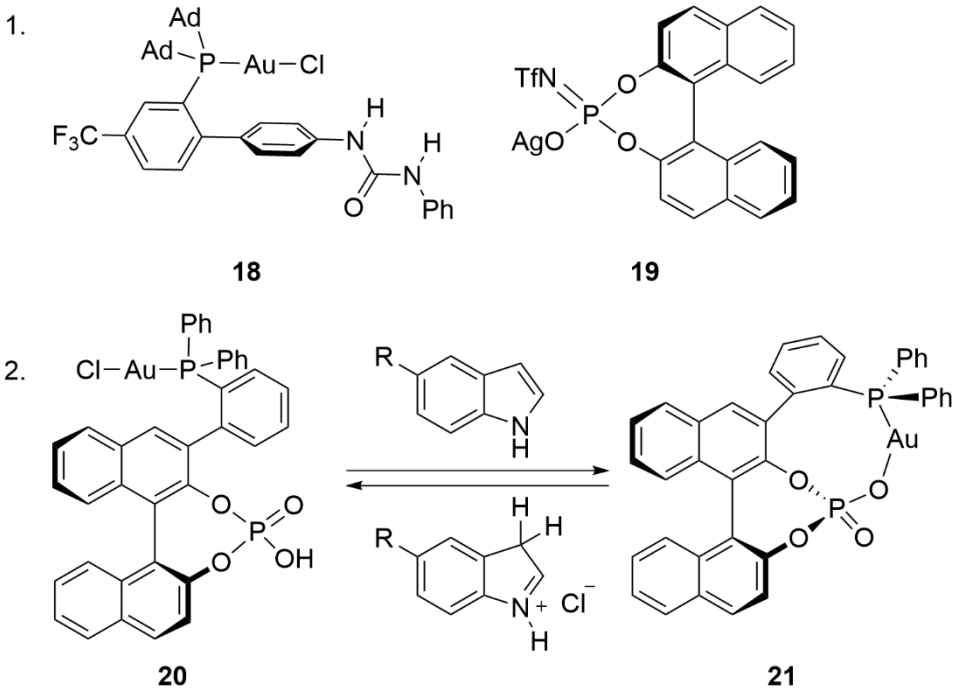

Scheme 21: 1. Example for a prochiral gold(I) complex **18** and a chiral silver salt **19**,[102] 2. self-activating gold(I) complex **20** and activation by basic HCl abstraction, forming the transition state **21**.[103]

1.1.4.2 Activation by positively charged ligands

A new way to activate gold(I) complexes is the incorporation of σ-acceptor ligands behaving as Lewis acids into gold(I) complexes. The ligand receives electron density from the metal center, which increases its electron withdrawing capability and tweaks the catalytic activity of the complex.[67],[104] The importance for a ligand design, which brings the Lewis acidic ligand site in close proximity of the gold(I) center **22**.[105] A complex synthesized by *Gabbaï* implements this by positioning a Lewis acidic Sb^{III} atom in close proximity to the gold(I) center (scheme 22, 1.). Natural bond orbital analysis as well as XRD analysis revealed only limited Au−Sb interactions. The interaction however was noticeable experimentally. The addition of PPh_3 let to the full abstraction of the gold bound chloride by the auxiliary antimony, while the new introduced PPh_3-ligand occupied the free coordination site at the gold(I) center. During catalysis a similar activation takes place, with the role of the PPh_3-ligand filled by the substrate (scheme 22, 2.). The functionality of the system was demonstrated, however it was inferior to the *Gagosz* complex (see above).[105]

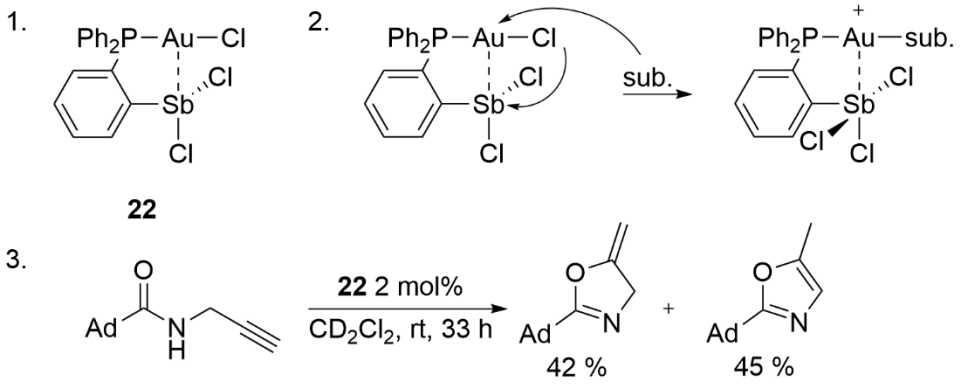

Scheme 22: 1. Gold(I) complex with an auxiliary antimony group for self-activation, 2. proposed π-complex with a substrate during catalysis, 3. catalyzed reaction.[105]

Tauchert pursued a similar approach by using a metalloligand with positively charged Lewis-acids to stabilize the Au−metal bond (M = Ag^+, Cu^+, Zn^{2+}). The Au/Zn complex was highly active in the cyclisation of *N*(2-propyn-1-yl)benzamids. For activating the complex, chloride scavengers (X = Cl) or weakly coordinating anions (X = OTf, NTf_2) were still necessary (scheme 23, 1.).[106]

In another example from the same group, they use xanthylium, acridinium or fluorenyl cations juxtaposed to the gold center for a similar activation of the gold(I) center.[107]–[109] The negatively charged carbenium center acts as strong σ-acceptor with a low lying empty p_x-orbital. The addition of chloride to the system let to the oxidation of the gold center to gold(III) and a subsequent coordination to the carbenium center. A likewise activation of the gold center during catalysis is estimated (scheme 23, 2.).

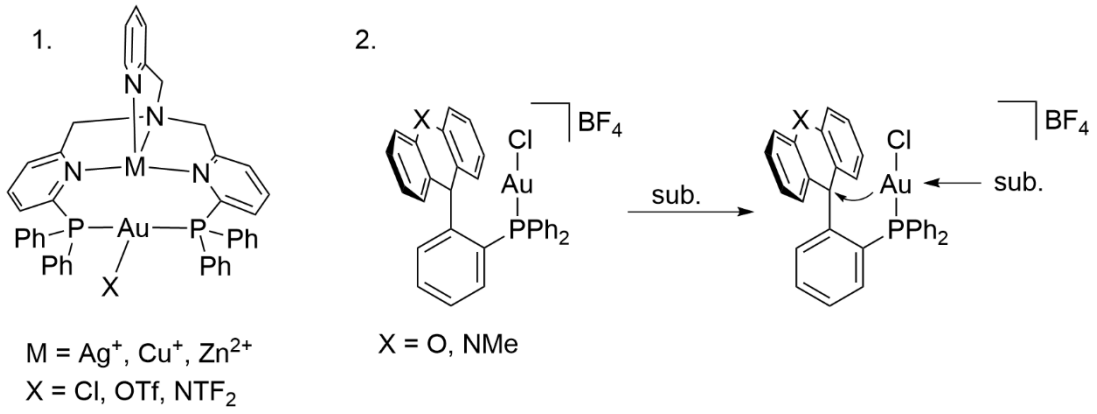

Scheme 23: 1. Complexes with incorporated Lewis acids by *Tauchert*,[106] 2. self-activating gold(I) complex with a carbenium incorporated into the ligand and proposed activation mode during catalysis.[67],[107]

1.1.4.3 Activation through oxidation and redox-switchable catalysis

In order to establish an activation through oxidation, a redox-active unite must be introduced into the ligand coordinating the gold(I) center, which oftentimes is a ferrocenyl group.[110] Oxidizing the redox

active ferrocenyl moiety with a suitable oxidant leads to a more electron-withdrawing ligand and subsequently increases the electrophilicity of the gold(I) center, enabling catalysis.

Sarkar synthesized heterobimetallic Au/Fe complexes with a pendant ferrocenyl backbone **23a,b** (scheme 24).[111] The oxidant acetylferrocenium tetrafluoroborate activated the complexes which were able to catalyze the cyclization of *N*-propargyl benzamide, whereas the neutral forms showed no conversion after 5h.[111] Through spectro-electrochemical measurements the reversibility of the oxidation was proven and calculations of the oxidized forms of **23a,b** revealed the spin density distributed on the ferroceniumyl moieties and not on the gold(I) center.

The same group also synthesized mesoionic gold carbene complexes with different ferrocenyl to gold ratios (2:1 **24** and 1:2 **25a,b**).[21] These complexes were reversibly oxidized similar to complexes **23a,b** at the ferrocenyl moieties, which was confirmed through CV experiments, UV-vis measurements and DFT calculations. By synthesizing the respective iridium-carbonyl complexes, the donor abilities of the ligands were determined. This was done by determining the Tolman electronic parameter (TEP) of the ligands by measuring the CO stretching frequencies via IR.[112] The ferrocenyl triazolylidene ligand of complex **24** changes from being better donating than imidazoline-2-ylidene NHCs in their neutral form, to being as electron poor as tricyclohexyl phosphane (**[24]**$^{+}$: TEP **=** 2056.9 cm^{-1}). A second oxidation of complex **24** pushed the donor properties of the corresponding ferrocenyl triazolylidene ligand in the range of the even electron poorer triphenyl phosphane (**[24]**$^{2+}$: TEP = 2068.3 cm^{-1}).[21] The complexes were almost inactive in catalytic reactions, with conversion rates of 5% after 5h for the cyclisation of *N*(2-propyn-1-yl)benzamide, but were active after oxidation. Complexes **25a,b** performed better than complex **24** which was attributed to different solubility in CH_2Cl_2.[21]

In contrast to complex **24**, *Bezuidenhout* substituted a ferrocene with two Fischer gold(I) carbenes **26**.[113] However no further measurements were performed and **26** was not tested as catalyst.

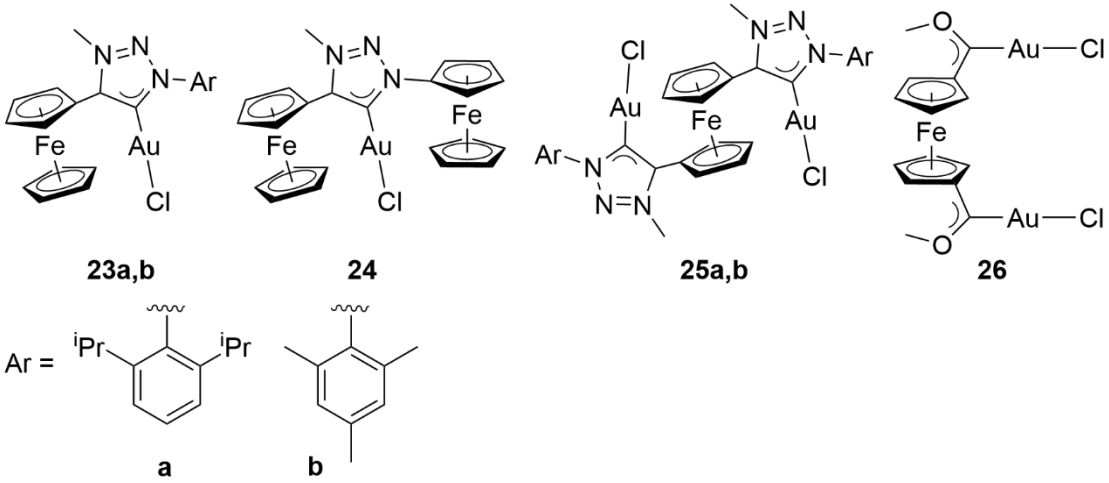

Scheme 24: Ferrocenyl gold(I) complexes by *Sarkar* and *Bezuidenhout*, with redox active ferrocenyl moieties.[21],[111],[113]

Changing the position of the ferrocenyl group in complex **27** bound to a nitrogen atom rather than a carbon atom as compared to complexes **23a,b** - **25a,b** increased the electron withdrawing capabilities and thus the catalytic activity.[114] For complex **[27]**$^+$ it was possible to re-reduce it after oxidation with decamethylferrocene as reduction agent, stopping the catalytic reaction (scheme 25).

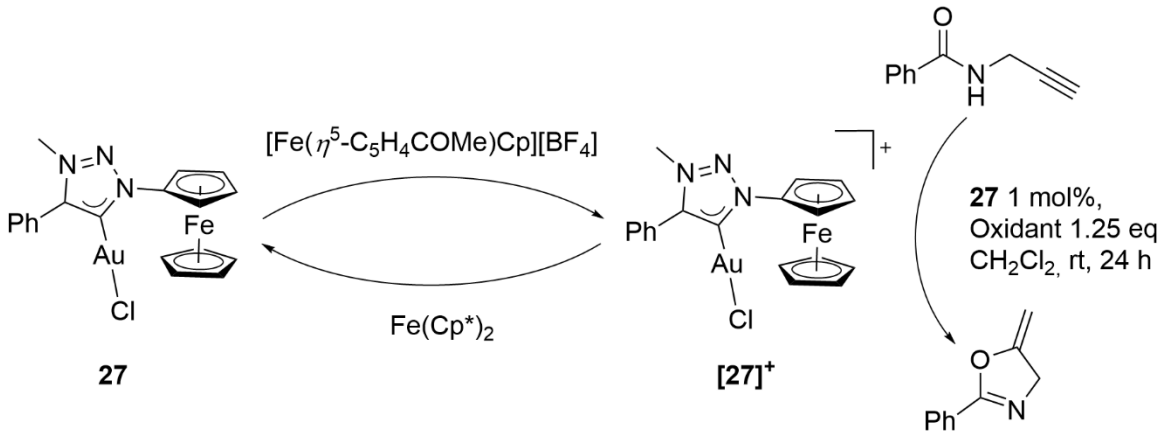

Scheme 25: Oxidation and reduction of redox-switchable complex **27** and cyclisation of *N*(2-propyn-1-yl)benzamide with oxidized **[27]**$^+$.[114]

Exchanging the ferrocenyl moieties with cobaltocene resulted in complex **[28]**, which readily catalyzed the reaction of *N*(2-propyn-1-yl)benzamide even without the addition of oxidants.[115] The TEP value of the cobaltoceniumyl triazolylidene ligand (2109 cm^{-1}) is in the range of the electron poorest phosphane PF_3. Reducing the complex with cobaltocene shut off the catalytic activity, but it was not possible to reactivate the complex, so **[28]** is not redox-switchable (scheme 26, 1.).[115]

Peris synthesized a ferrocenyl containing Gold(I) carbene complex **29** that, after oxidation with acectylferrocenium tetrafluoroborate, was active in the hydroamination of phenylacetylene with arylamines and in the cyclisation of 2,5-dimethylfuran.[116] In the hydroamination reaction, the complex **29** was performing only slightly better after oxidation, than in the neutral form. They explained it with a deprotonation of the protonated form of the complex by the basic aniline substrate, which regenerated the unoxidized catalyst **29**. In the cyclisation of 2,5-dimethylfuran however, **29** was only active after oxidation (scheme 25, 3.).

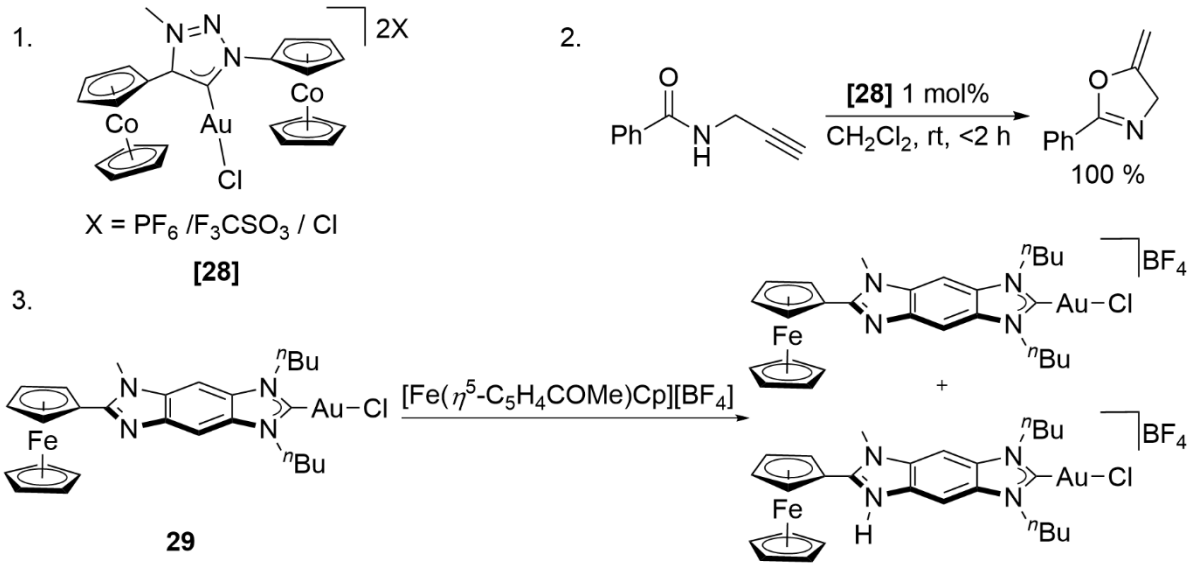

Scheme 26: 1. Catalytically active cobaltocene complex **[28]**,[115] 2. catalyzed reaction,[115] 3. ferrocenyl gold(I) complex **29** by *Peris* with redox active ferrocenyl moiety.[116]

Hey-Hawkins placed three ferrocenylphosphane moieties onto different arene centers **30a-c**.[117] During catalysis the neutral forms showed low activity in the cyclisation of *N*-propargyl benzamide (turn over frequency (TOF): **30a**: 1.97 h^{-1}, **30b**: 2.54 h^{-1}, **30c**: 0.017 h^{-1}), in contrast the monomeric complex **30** was completely inactive as catalyst.[22] Upon oxidation, complexes **30a-c** were active in catalysis. Adding one equivalent of oxidant resulted in a 5.5-fold (TOF: [**30a**]$^{+}$: 11.2 h^{-1}), two equivalents in a 10-fold (TOF: [**30a**]$^{2+}$: 19.1 h^{-1}) and three equivalents in a 13-fold increase (TOF: [**30a**]$^{3+}$: 24.7 h^{-1}) in the activity for **30a**.[22]

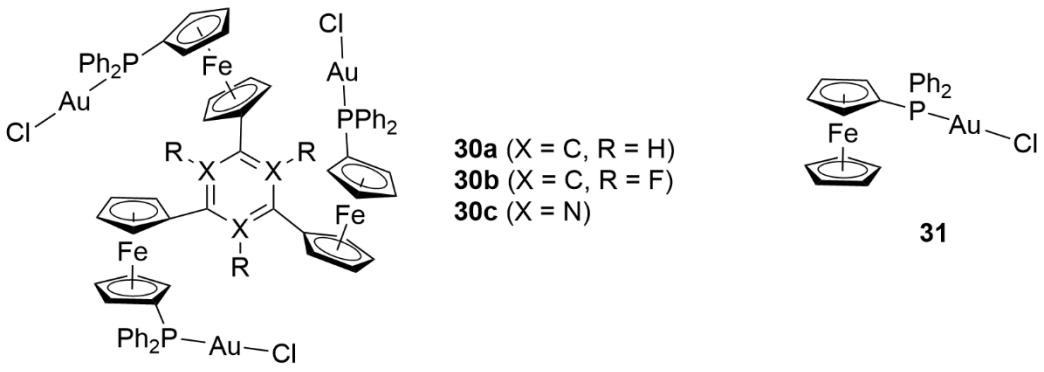

Scheme 27: 1. Ferrocenyl gold(I) complexes **30a-c** by *Hey-Hawkins* with redox active ferrocenyl moieties and complex **31** for comparison.[22],[117]

They ascribe the enhanced activity to cooperative effects. Using $NaBAr^{F}_{4}$ as chloride scavenger to activate the complexes **30a-c** however decreased the TOF compared to complex **31**, when used in the same concentration in respect to gold. This decrease in activity was explained due to side reactions forming *P,P'*-dicoordinated gold(I) complexes, which are more stable for complex **30a** compared to

complex **31**. Interestingly all Au−Cl bonds remain intact upon oxidation, as confirmed through XRD, pointing to an activation mode differing from the $[AuL]^+$ cations generated by halide abstraction (scheme 27). The Au−Cl bond stayed intact for all above mentioned redox-switchable catalysts. It remained unclear how a catalytic reaction is taking place without freeing a coordination site for the substrate.

A possible answer to the question of the active species of ferrocenyl gold(I) complexes after activation with an oxidant was given by *Heinze*. Activating a ferrocenyl gold(I) Fischer carbene complex **32** with the oxidant $[N(p\text{-}C_6H_4Br)_3][SbCl_6]$ (Magic Blue) resulted, after an induction period of two and a half hours, in an active complex which catalyzed the cyclisation of *N*(2-propyn-1-yl)benzamide (scheme 28).[19] It was possible to stop the catalysis with the reductant decamethylferrocene and turn it back on with another equivalent of Magic Blue. X-band EPR spectroscopy revealed a broad resonance around $g = 2$ after oxidizing **32** with different oxidants in different solvents.

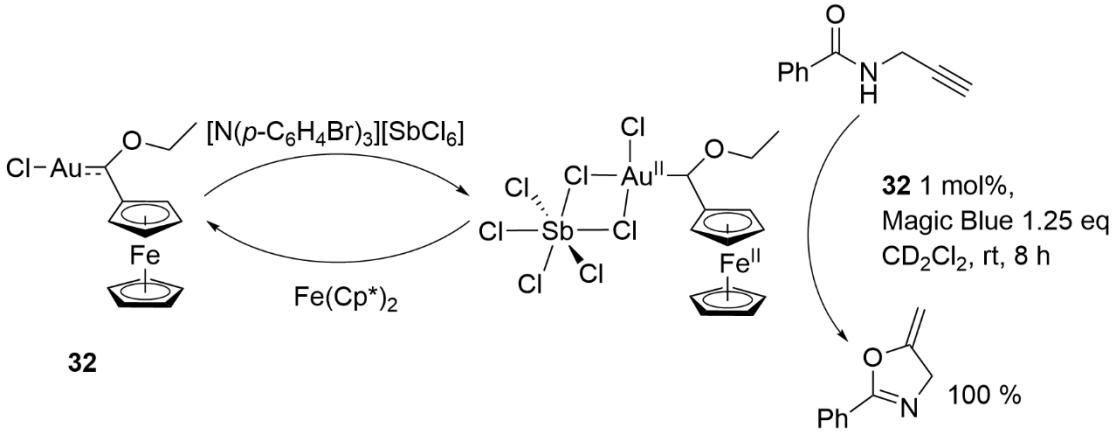

Scheme 28: Activation of ferrocenyl Fischer gold(I) complex **32** with presumed active species and cyclisation of *N*(2-propyn-1-yl)benzamide.[19]

This resonance, which was assigned to a gold(II) species, increased over time while the built up matched the observed induction period during catalysis (scheme 29, 1.). The induction period and the built up of the EPR resonance were explained through a reorganization taking place at the gold atom. First the oxidation takes place at the ferrocenyl moiety generating a Fe^{III}/Au^{I} species, then slowly a conversion towards a Fe^{II}/Au^{II} isomer occurs, with a concurrent geometrical reorganization taking place at the gold atom from a linear coordination towards a square-planar coordination. DFT calculations suggest the stabilization of the Fe^{II}/Au^{II} species through the chelating coordination of the $SbCl_6^-$ counterion of the oxidant Magic Blue. The coordination of oxygen nucleophiles, such as the substrate used in catalysis, tend to stabilize the Fe^{II}/Au^{II} species, too.[19] After oxidation, complex **[32]**$^+$ showed a higher TOF (**[31]**$^+$: 29.88 h^{-1}) during catalysis than the oxidized complexes **[23a,b]**$^+$ – **[25]**$^+$ and **[27]**$^+$.[21],[111],[114] The neutral form of the ligand of **32** already possesses a high TEP value (TEP = 2054 cm^{-1}), thus a low donicity and is even less donating after oxidation.[19]

Expanding the distance between the ferrocenyl moiety and the gold center by an additional nitrogen alters the characteristics of complexes **33a,b** significantly (scheme 29, 2.).[118] Determined through CV experiments the oxidation of complex **32** takes place at 580 mV vs. ferrocene, complexes **33a,b** are oxidized at a lower potential of 105mV/115 mV, under the same conditions.[19],[118] While the initial ferrocenyl to ferroceniumyl oxidation of complex **32** happens instantaneously, rapid freezing the solution of complexes **33a,b** with Magic Blue at 195 K revealed EPR signals derived from *N*-substituted ferrocenium ions as well as residue Magic Blue.[19],[118] The Magic Blue signal vanished over time while a new broad signal at around g = 2 appeared, which is characteristic for gold(I) species.[118]

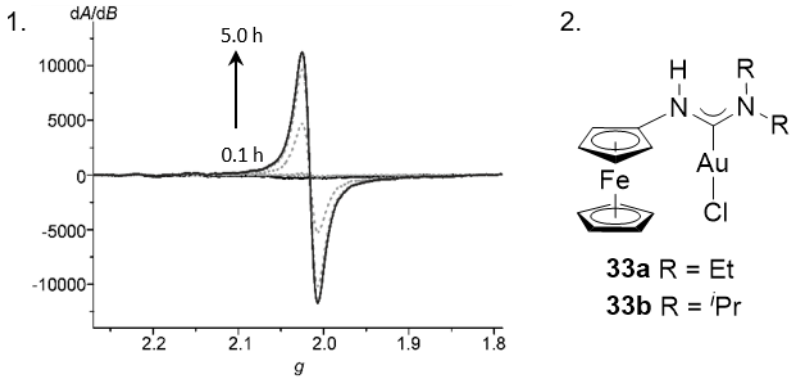

Scheme 29: 1. EPR resonance detected after oxidation of **32** with Magic Blue,[19] 2. ferrocenyl acyclic diamino carbene gold(I) complexes **33a,b**.[118]

Since *Teles'* work the noble metal gold has been used successfully as a catalyst in a plethora of reactions. Over time numerous new methods to activate gold(I) complexes have been published, each using slightly different approaches. Next to catalysis with gold(I) complexes and the well-known catalysis with gold(III) complexes,[119] also gold(II) complexes are catalytically active and are a topic of research.[120],[121]

1.1.5 Gold(II) complexes

The most stable gold complexes are in oxidation states +I or +III and way fewer gold compounds with the oxidation state +II are known. Especially mononuclear compounds with oxidation state +II are scarce, since gold(II) complexes either tend to dimerize or to form mixed-valent gold(I)/gold(III) compounds with only formal oxidation state +II.[122],[123] One explanation of the instability of the oxidation state +II in gold compounds lies in relativistic effects.[124] Gold(II) has a d^9 electron configuration and the unpaired electron is located in the $d_{x^2-y^2}$ or the d_{xz} orbital, which is energetically high lying and thus the atom is easily ionized.[122],[125] The unpaired electron in the $d_{x^2-y^2}$ orbital is the reason for the tendency of mononuclear gold(II) complexes to form gold(II)/gold(II) dimers or to mitigate this unfavoured electron configuration via disproportionation into gold(I) and gold(III).[126] This disproportionation is observed in the mixed-valent "$AuCl_2$" salt **34**, which is consisting of gold(I) and

gold(III) ions.[127] A comproportionation however was observed in perovskite-type mixed-valence compounds $Cs_2Au^{I}Au^{III}X_6$ (X = Cl, Br, I). Under high pressure of 52×10^8 Pa the gold atoms became spectroscopically indistinguishable, which means the presence of gold(II) ions.[128],[129] Recently a solid state mixed-valent gold(II)/gold(III) structure featuring a mononuclear gold(II) atom was synthesized.[130] In the perovskite $Cs_4Au^{II}Au^{III}{}_2Cl_{12}$ the gold(II) as well as the gold(III) center are coordinated in a square planar fashion.

Several examples for dimeric gold(II) complexes with a bridging ligand have been reported. *Wickleder* determined the crystal structure of $AuSO_4$ **35**, which turned out to not be a mixed-valent species but rather contains $[Au_2]^{4+}$ cations supported by two bridging sulfate anions with a gold(II)-gold(II) distance of 2.49 Å (scheme 30).[131] This close Au−Au contacts are a result of relativistic effects, as determined through DFT calculations.[132] Another true gold(II) salt is $Au(SbF_6)_2$.[133] Each gold atom is coordinated square planar by three oxygen and one gold atom (scheme 30). Other bridging ligands include $(CH_2PR_2CH_2)^-$ and $(S(CNR_2)S)^-$, supporting a plethora of complexes with a central $[Au_2]^{4+}$ cation, different counterions and gold(II)–gold(II) distances in the range of 2.5-2.7 Å.[122],[134]

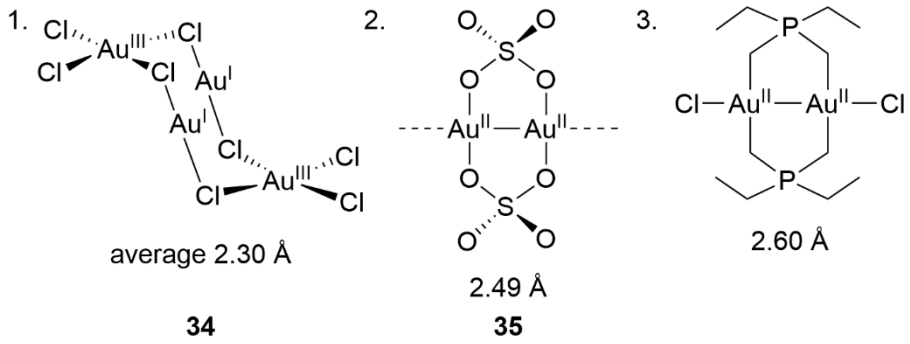

Scheme 30: 1. Mixed-valent $Au^{II}Cl_2$ salt **34**, [127] 2. coordination of the $[Au_2]^{4+}$ cation in the molecule structure of $AuSO_4$ **35**,[131] 3. example for a dimeric gold(II) complex with two bridging $(CH_2PR_2CH_2)^-$ ligands.[122] Au–Au distances shown.

There are also examples for dimeric gold(II) complexes with unsupported gold(II)-gold(II) bonds. *Yam* reacted $[Au_2(dppn)Cl_2]$, $[Ag(MeCN)_4]PF_6$ and dppn (dppn = 1,8-bis(diphenylphosphano)naphthalene) in MeCN and obtained the complex $[(Au^{II}(dppn)Cl)_2](PF_6)_2$ **[36]**, which featured a single unsupported gold(II)-gold(II) bond with a length of 2.61 Å (scheme 31).[135] A similar example of a complex with unsupported gold(II)-gold(II) bond was synthesized by *Bochmann* via reduction of two gold(III) complexes, featuring a gold(II)-gold(II) distance of 2.49 Å.[136] Under thermal conditions the complex **37** was stable, but disproportionated on irradiation in solution to give a mixed-valent gold(I)/gold(III) aggregate.[137] Through CV experiments the gold(II)-gold(II) dissociation energy was determined to be of 198±1 kJ/mol.[138]

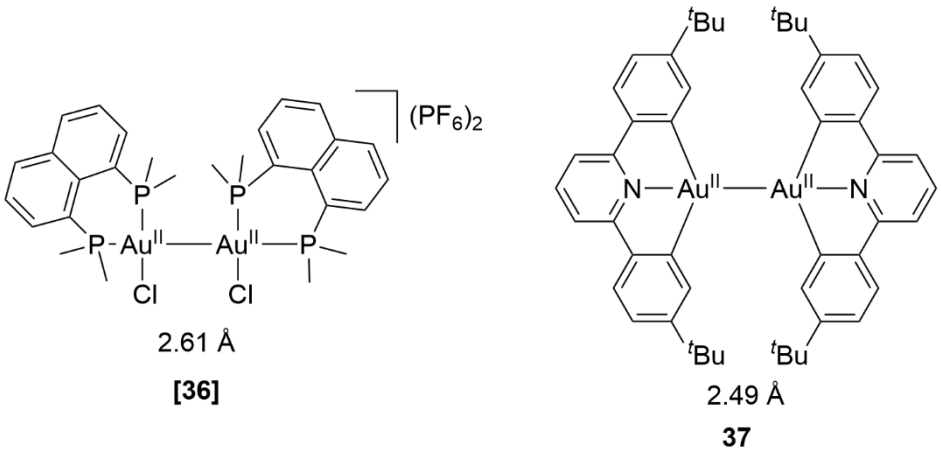

Scheme 31: Unbridged dimeric gold(II) complexes **[36]** by *Yam*[135] and **37** by *Bochmann*.[136]

There are only few mononuclear gold(II) complexes known.[126] One series of mononuclear gold(II) complexes prepared by *Seppelt* rely on hard donor ligands, stabilizing a planar $[AuXe_4]^{2+}$ cation with two $Sb_2F_{11}^-$ anions, which feature three weak contacts with the central cation.[139] The compound was only stable under 10 bar of Xe pressure and temperatures below −40 °C. Other examples of gold(II) compounds received from the AuF_3/Xe/HF/SbF_5 system under different conditions include $[Au^{II}Xe_4][Sb_2F_{11}]_2$, [*trans*-$Au^{II}Xe_2$][$SbF_6$]$_2$, [*cis*-$Au^{II}Xe_2$][$Sb_2F_{11}$]$_2$ and [(μ-F)-$Au^{II}{}_2Xe_2$][SbF_6]$_3$.[140],[141] These compounds only exist, because the solvent and counter ions are weaker bases than atomic xenon (scheme 32, 1.).[141] The nature of the Au−Xe bond was investigated thoroughly and is of the σ-donor type. A positive charge on the xenon is generated through donation of electron density from the filled 5d orbital into the vacant 5d orbital of the gold(II).[142]–[144] In HF acidified with SbF_5 and the absence of xenon, AuF_3 is reduced to $[Au^{II}(HF)_2(SbF_6)]_2$, which features a square planar $[AuF_4]$ coordination (scheme 32, 2.).[145]

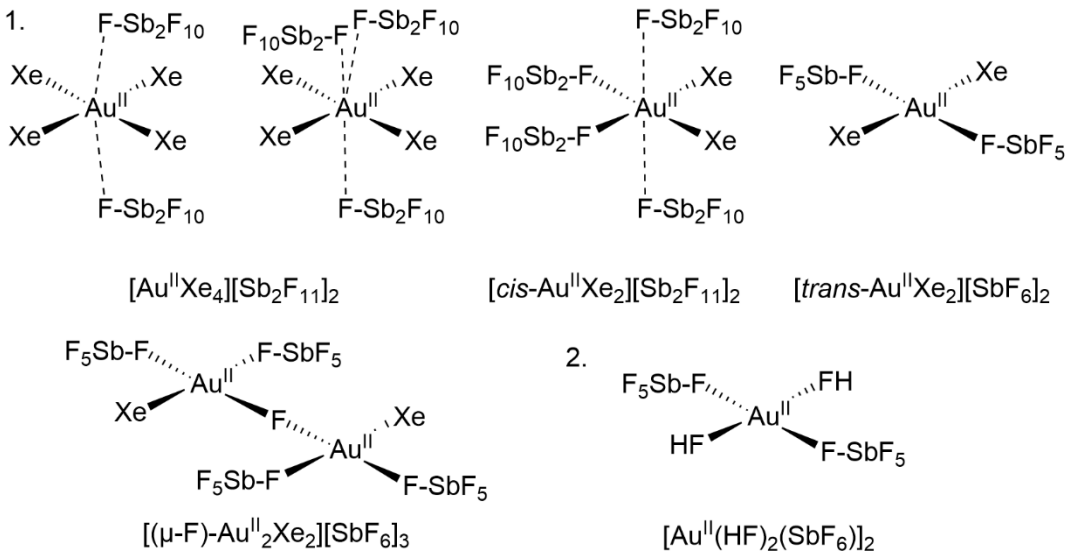

Scheme 32: 1. Mononuclear gold(II) compounds, with Xe−Au and F−Au bonds by *Seppelt*,[139]–[141] 2. without Xe present.[145]

Six-coordinating thioether ligands are also able to stabilize gold(II) complexes.[146] The gold(II) center is coordinated in a Jahn-Teller distorted octahedral $[Au^{II}S_6]^{2+}$ environment, similar to Cu^{II} complexes of the same $3d^9$ electron configuration.[147] The typical pathways to mitigate the oxidation state in gold(II) such as disproportionation or dimerization are not accessible through the shielding nature of the thioether ligand. Replacing the two sulfur atoms in the Jahn-Teller distorted axis with oxygen resulted in a similar complex with a $[Au^{II}S_4O_2]^{2+}$ core.[148] Experimental studies however revealed the non-innocent nature of the thioether ligands, with only about 25−30% spin density located in the Au $5d_{xy}$ orbital, with the rest distributed at the sulfur donor atoms of the thioether (scheme 33, 1.).[149],[150]
A mononuclear neutral gold(II) complex of the form Au^{II}(TPP) (TPP = tetraphenylporphyrinato) **38** was realized by reduction of the corresponding gold(III) complex with KC_8, cobaltocene or 1-benzyl-1,4-dihydronicotinamide (scheme 33, 2.).[151] DFT calculations place the spin density in the $5d_{x^2-y^2}$ orbital, suggesting a true gold(II) complex. This spin density distribution prevents possible dimerization pathways, since the TPP-ligand shields the AuN_4 plane. The nitrogen gold(II) bonds are not equal, but rather feature a two plus two coordination of two longer and two shorter N−Au bonds, due to a distortion of the TPP-ligand, similar to the gold(II) thioether complex. This second-order Jahn-Teller distortion is attributed to relativistic effects in the gold center, lowering the energy gap between the 6s orbital and the 5d orbitals.[152]
Next to the known gold(II) compounds a plethora of transient intermediary gold(II) species are suggested in catalytic cycles, especially in light-induced gold-catalyzed reactions involving radicals.[63],[153]–[160] These intermediates however never have been characterized and any spectroscopic evidence is missing.

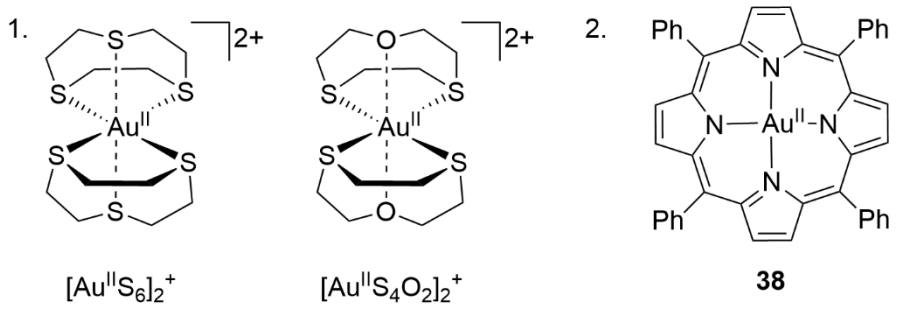

Scheme 33: 1. Mononuclear gold(II) compounds stabilized with thioether derivative ligands,[147],[148] and 2. stabilized by a TPP-ligand.[151]

1.2 Molybdenum complexes mimicking carbon monoxide dehydrogenase

Before discussing how Mo complexes can be designed to mimic enzymes, the first section is a short introduction to the sulfide ligand, followed by a section summarizing the structure and function of Mo containing enzymes.

1.2.1 The sulfide ligand

The strong nucleophile sulfide (S^{2-}) is not only found as ligand in Mo containing enzymes, but also in a number of other enzymes with different roles and coordination modes.[161],[162] It is found in complexes for metal storage, catalysis and in biological processes such as regulation, sensing and electron transfer.[161],[163]–[169] Iron sulfide salts are often insoluble compounds, in organisms the formation of this compounds is prevented by incorporating them into protein environments, facilitating cluster formation.[161] Of these metal sulfide clusters, iron-sulfur-clusters are among the most important classes of cofactors and are found in a multitude of enzymes and nearly all organisms, mostly to facilitate electron transfer.[170] In iron-sulfur-clusters the sulfide ligand is found in μ_2-S and μ_3-S binding modes depending on the cluster geometry.[170] Even μ_4-S binding modes are known, in the Cu/S cluster of the nitrous oxide reductase where a sulfide ligand bridges four Cu atoms.[171] In molybdenum containing enzymes, the sulfide ligand is found as terminal ligand in the xanthine oxidase family and in the carbon monoxide dehydrogenase as a bridging ligand between a Mo and a Cu atom.[163]

1.2.2 Mo in enzymes

Molybdenum is the highest concentrated transition metals in sea water, caused by the soluble molybdate $[MoO_4]^{2-}$ anion and the only known second row transition metal found in enzymes of all organisms (eukaryota, bacteria and archaea) including humans.[172],[173] Molybdenum shuttles between different oxidation states, ranging from –II to +VI and coordination numbers from four up to eight.[173] Molybdenum often is accompanied by sulfide ligands, due to the small energy gap between molybdenum 4d orbitals and the sulfur 3p orbital, which gives rise to a plethora of molybdenum sulfur complexes, clusters, solids and over 50 active enzyme sides.[163],[174],[175] Molybdenum enzymes mostly catalyze oxido-transfer reactions and play important roles in the carbon, nitrogen and sulfur metabolism of various organisms.[176]

Molybdenum enzymes are classified by *Hille* into three different groups, exemplified by the enzymes sulfite oxidase (SO), DMSO reductase (DMSOR) and xanthine oxidase (XO) (Scheme 34).[163],[172] The enzymes of these families in their oxidized form have a Mo^{IV} center in common and one or two pyranopterin cofactors as ligands, which covalently bind the Mo atom via the dithiolate moiety.[163],[172],[176],[177] The nitrogenase is the only molybdenum enzyme unsuitable for this classification, since the molybdenum is incorporated into a $[MoFe_7S_9]$ cluster rather than coordinated

by a pyranopterin cofactor.[163],[172] While all three enzyme classes have pyranopterine ligands in common, the co-ligands differ. In the XO family the pyramidal coordination geometry is complemented by a hydroxide and a sulfide ligand, in some cases the sulfite is replaced by either selenide or a sulfide bridged copper atom.[163],[172],[176],[177] In the similar coordination sphere of the enzymes of the SO family, the equatorial sulfide ligand is replaced by an oxide ligand and the hydroxide ligand by a cysteine. The DMSOR family is the structurally most diverse class of molybdenum enzymes.[163] The enzymes of this class all feature an equatorial coordination of two dithiolate moieties of the pyranopterin cofactor.[163],[172],[176],[177] Their trigonal prismatic coordination geometry is complemented by an oxido ligand, which is replaced by a sulfide or selenide ligand in some members of the family. The fourth ligand in the coordination geometry is an amino acid, such as serine, aspartate, cysteine or selenocysteine, while a hydroxide group coordinates to the molybdenum center in the arsenate oxidase (Scheme 34).[163],[172],[176],[177]

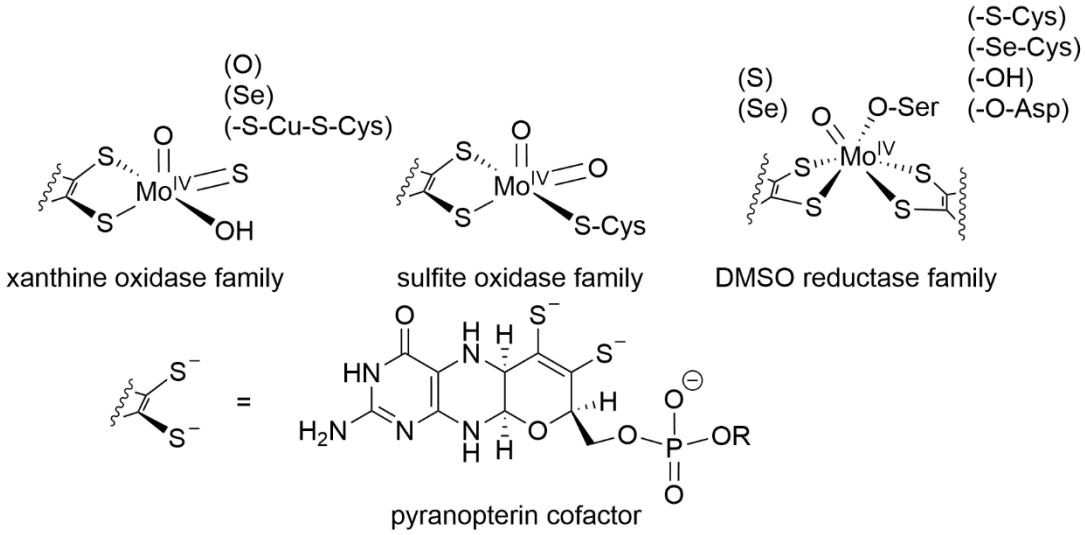

Scheme 34: Structures of Mo centers of the three mononuclear molybdenum enzymes, as well as the structure of the pyranopterin cofactor that is found by all three enzyme families.[163]

The pyranopterin cofactor coordinating the Mo atom (Moco) fulfills multiple roles within the enzyme. The Moco positions the catalytically active Mo atom in the active center of the enzyme through hydrogen bonding and is suggested to be involved in electron transfer steps from and towards the Mo atom, since it is oriented towards redox active cofactors found in the enzymes.[163],[172],[176],[177]

All three families of molybdenum enzymes catalyze oxygen atom transfer reactions. The general reaction mechanism for substrate oxidation starts with a substrate entering the binding pocket of the enzyme and the formation of an enzyme-substrate complex. The π*-orbitals of the oxido ligand of the active Mo center are attacked nucleophilic by the substrate, reducing the molybdenum to a Mo^{IV}-species (scheme 35, 1.).[178],[179] Theoretical studies show that the nucleophilicity of the substrate is increased through hydrogen bond formation in the binding pocket of the enzyme.[180]–[182] In

molybdenum centers coordinated by two oxido ligands, the bond of the equatorial oxido ligand weakens during the oxygen atom transfer. The bond of the axial oxido ligand however becomes more π-donating, resulting in one σ and two π bonds. The activation barrier of the oxygen atom transfer step is ultimately lowered through the increased bond strength of the axial oxido ligand, this effect is known as spectator oxo effect.[180],[183],[184] In the next step the oxidized substrate is liberated by hydrolysis (2.).[185] The oxidized Mo^{VI} species is then regenerated through intramolecular proton-coupled electron transfer steps (3., 4.).[178],[180] Electron transfer occurs along a chain of redox active cofactors, such as iron-sulfur clusters, flavines and or cytochromes, which differ for each family of enzymes.[163],[172],[180]

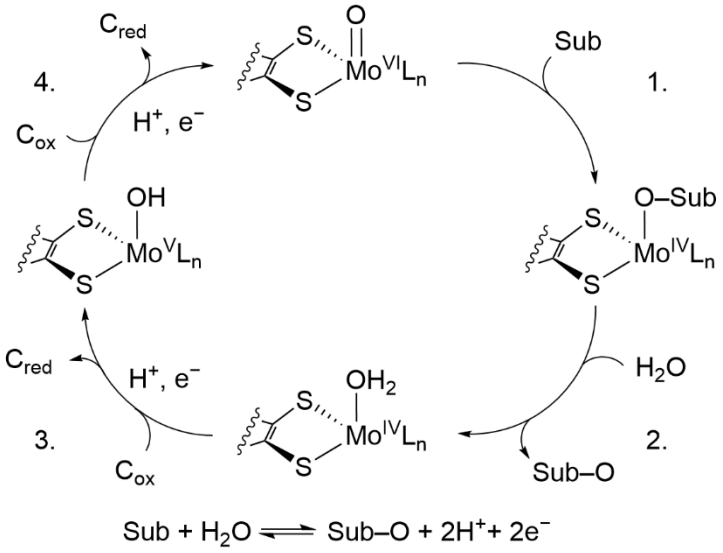

Scheme 35: Catalytic cycle for the general oxygen atom transfer reaction for substrate oxidation, catalyzed by mononuclear molybdenum enzymes. C_{red} and C_{ox} stands for electron carriers, such as iron sulfur clusters, flavines or cytochromes.[178],[186],[187]

Enzymes of the XO family commonly catalyze the oxidative hydroxylation of a substrate's carbon atom.[163] A common feature of members of the XO family are additional redox-active centers, such as [2Fe-2S] clusters and or flavine adenine dinucleotides (FAD) at which the oxidizing agents O_2 or nicotinamide adenine dinucleotide (NAD^+) react at.[163] Follow-up intramolecular electron transfer takes place from the FAD side of the enzyme via the iron-sulfur-clusters towards the molybdenum center.[163] Enzymes of the XO family found in eukaryotes consist of two identical subunits $(\alpha)_2$, whereas in bacterial enzymes of the XO family, organizations with more subunits such as $(\alpha\beta)_2$ or $(\alpha\beta\gamma)_2$ occur.[163],[172]

1.2.3 Carbon monoxide dehydrogenase

Carbon monoxide dehydrogenase (CODH) is a member of the xanthine oxidase family of molybdenum enzymes. It is found in aerobes, a class of bacteria which rely on carbon monoxide as their only energy

and carbon source.[163],[188],[189] CODH catalyzes the oxidation of carbon monoxide to carbon dioxide. Hence aerobes, such as *Oligotropha carboxidovorans* are responsible of fixing 2×10^8 tons of CO annually.[190],[191] The specific CODH variant of this organism will now be discussed in more detail.

The redox-active centers found in this CODH are two [2Fe-2S] clusters and one FAD. The enzyme consists of a dimer with three subunits $(\alpha\beta\gamma)_2$ (Scheme 36).[192],[193] The two [2Fe-2S] clusters, FAD and the Mo centers are organized in three separate subunits.[192],[193] The unique feature of CODH in comparison to other enzymes of the XO family is the exchange of the sulfide ligand with a μ-sulfide ligand that, bridging the Mo atom with a Cu atom.[192]–[194] The coordination sphere of the Cu atom is saturated with a cysteinato ligand and a water ligand with a longer bond of 2.40 Å.[188] In contrast to other members of enzymes of the XO family, the Mo atom in the CODH is not coordinated by a hydroxydo ligand, but rather a second terminal oxido ligand.[195]

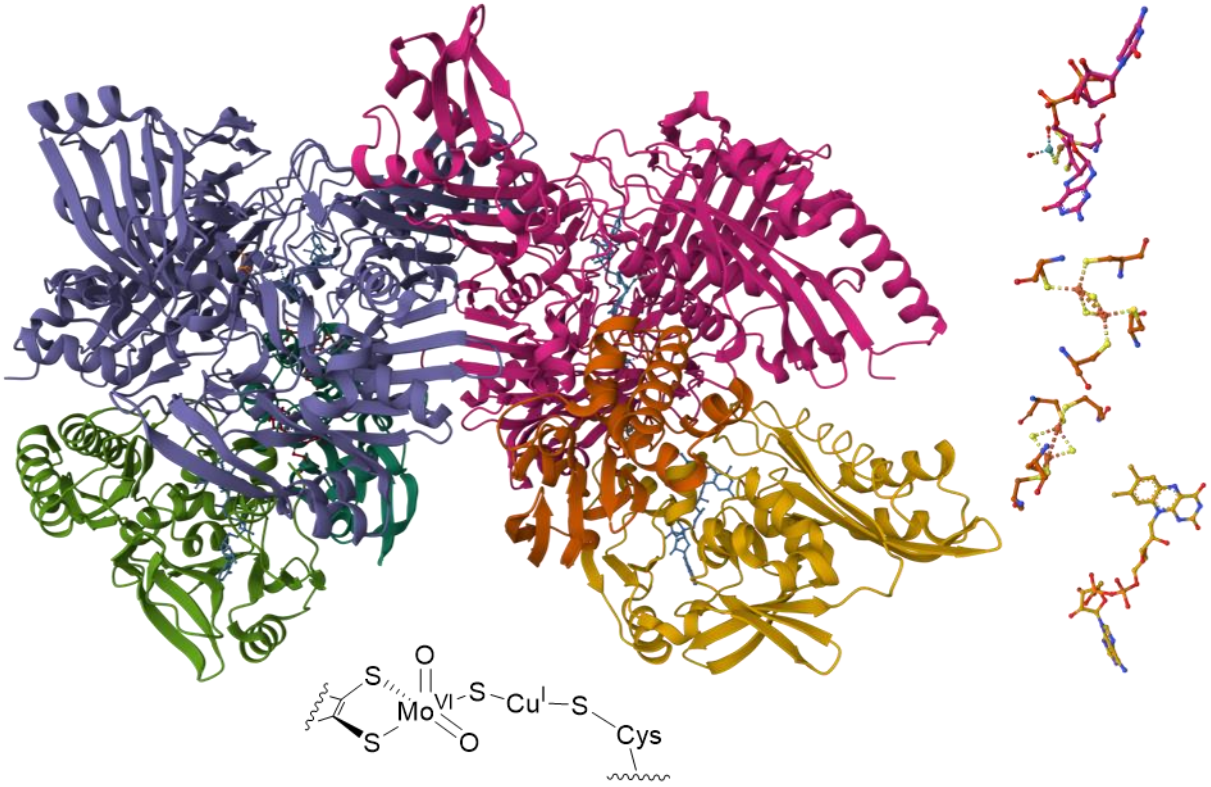

Scheme 36: Left: ribbon representation of the CODH with each subunit colored differently, right: cofactors of the CODH, from top to bottom: Molybdo-oxido group, [2Fe-2S] cluster, [2Fe-2S] cluster and FAD, bottom: structural motif of the active center of the CODH.[193]

The current knowledge about the mechanism of the oxidation of carbon monoxide catalyzed by the CODH of *Oligotropha carboxidovorans* is based on CV,[196] EPR and XRD measurements on the molecular structure of the enzyme with and without suicide inhibitors,[193] multiple approaches of computational modelling[197]–[200] as well as the synthesis of biomimetic complexes.[201]–[203] First, carbon monoxide coordinates to the Cu^I atom (Scheme 37, 1.). An oxido ligand of the Mo center attacks the carbon atom of the carbon monoxide as a nucleophile, leading to the oxidation of the substrate

(2.). The product carbon dioxide is released and the vacant coordination site on the Mo atom is occupied by a glutamate residue, located in close proximity (3.).[200] A water molecule exchanges the glutamate residue by coordinating to the central Mo atom (4.) and lastly two protons and two electrons are released, to re-oxidize the molybdenum and re-establish the coordination geometry (Scheme 37, 5.). The rate determining step is the carbon dioxide release, with an energy barrier of 11.4 kcal/mol (calculated: 12.6 kcal/mol).[195],[200]

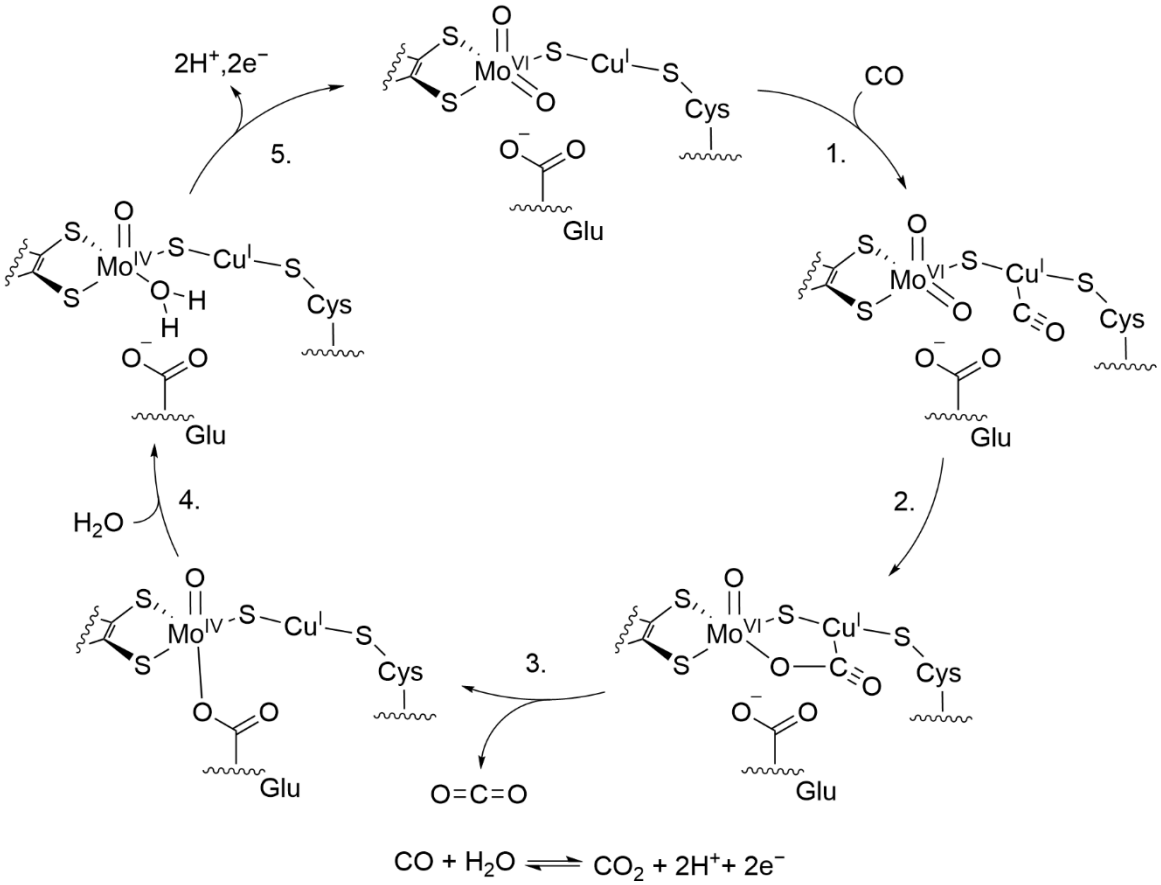

Scheme 37: One proposed catalytic cycle of the oxidation of carbon monoxide catalyzed by CODH, with net reaction equation (bottom).[200]

1.2.4 Biomimetic molybdenum model complexes for CODH

Enzymes are complex structures with the active center often buried inside the enzyme scaffold, which complicates direct examination. Biomimetic complexes are artificial inorganic complexes, modelling the active center of an enzyme to get insight into the mechanism on more accessible systems.

Mimicking the active center of the CODH has proven to be particularly challenging.[204] Some aspects to consider in a CODH mimicking complex are the square pyramidal coordination geometry of the Mo atom, the correct ligands in the coordination sphere of the Mo atom and the linear coordination of a Cu atom via a bridging sulfide ligand. Another problem arises from the combination of Mo^{VI} with anionic sulfur donors, which tend to reduce the Mo^{VI} center.[205] Exchanging the central atom with

tungsten avoids this reduction reaction, since W containing model complexes tend to be more stable than Mo complexes towards reduction (scheme 38).[204],[205] Molybdenum and tungsten model complexes for the CODH have some similarities, since their isoligated five and six-coordinated complexes are isoelectronic, isostructural and nearly isometric.[204],[206] However tungsten based model complexes for Mo containing biomimetic complexes may show different reactivity, which limits their scientific value in this regard.[202],[206]

Several model complexes mimicking the active center of CODH have been reported.[202],[204],[207] Often times the structural motif of one unsupported Mo–(μ_2-S)–Cu bridge is exchanged with two μ_2-S bridges between the metal centers, preventing a CO coordination on the Cu atom and thus an oxidation of CO.[208]–[210]

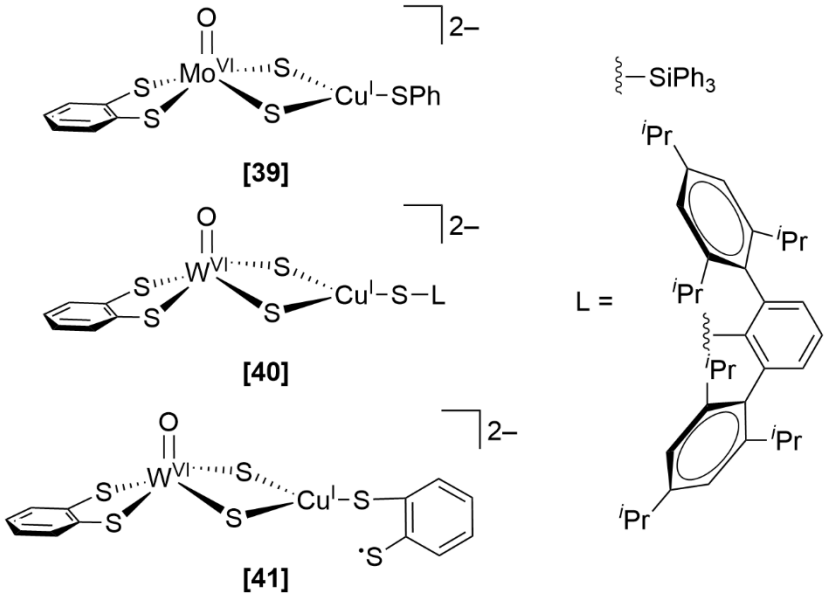

Scheme 38: Reported complexes mimicking the active center of CODH.[208]–[210]

Realizing a complex with a single unsupported Mo–(μ_2-S)–Cu bridge is feasible, albeit with compromises towards the coordination sphere at the Mo atom. Complex **42** has this structural motif, but features molybdenum in a +V oxidation state and coordination of both metal centers by nitrogen donors rather than sulfides (scheme 39).[211] The group of *Mankad* presented another model complex of the CODH active site with a W^{VI} instead of Mo^{VI} center and a NHC ligand coordinating the Cu^{I} instead of a second sulfide ligand **[43]**.[203] **42** shows a similar deactivation process with cyanides, as proposed for the CODH active site, but no activity in the oxidation of CO just as **[43]**.[203],[211],[212] *Lord* and *Groysman* used a design with a heterobimetallic ligand to bring Mo^{VI} and Cu^{I} in spatial proximity **[44]**, **[45]** but excluded any sulfide ligands.[213] Exchanging Cu^{I} with a metal carbonyl fragment simulated a CO coordination in close proximity to a Mo^{VI} center, but in both instances no CO_2 release was observed.[213],[214]

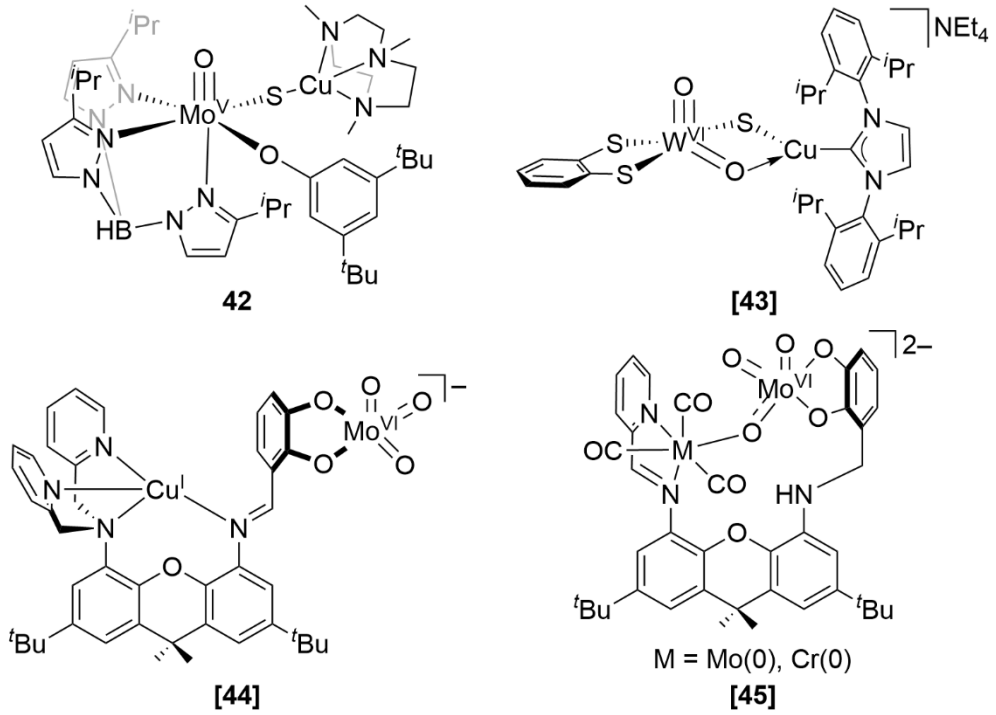

Scheme 39: Several takes on complexes mimicking the active center of the CODH.[203],[211],[213],[214]

The model complex **[46]** from *Mougel* relies on a Mo^{VI} center coordinated by a dithiolene ligand and two Mo–(μ_2-S)–Cu bridges and an additional cyanide coordinating the Cu^{I} center.[215] In contrast to the mechanism of CODH, **[46]** reacts with CO_2 in a two-electron reduction, transferring the oxido-ligand from Mo to CO_2, generating a carbonate anion and a Mo^{IV} center in an irreversible reaction.[215] The weak Lewis-acidic character of the Mo^{VI} center is lowered further by the two-electron reduction, which leads to it becoming basic enough to facilitate the oxido transfer towards CO_2.[215] Reducing the generated complex **[46]$_{red}$** further by a one electron reduction generates an active complex **[46]$_{2red}$**, catalyzing the reduction of CO_2 to formate and H_2 as side product (scheme 40).[215]

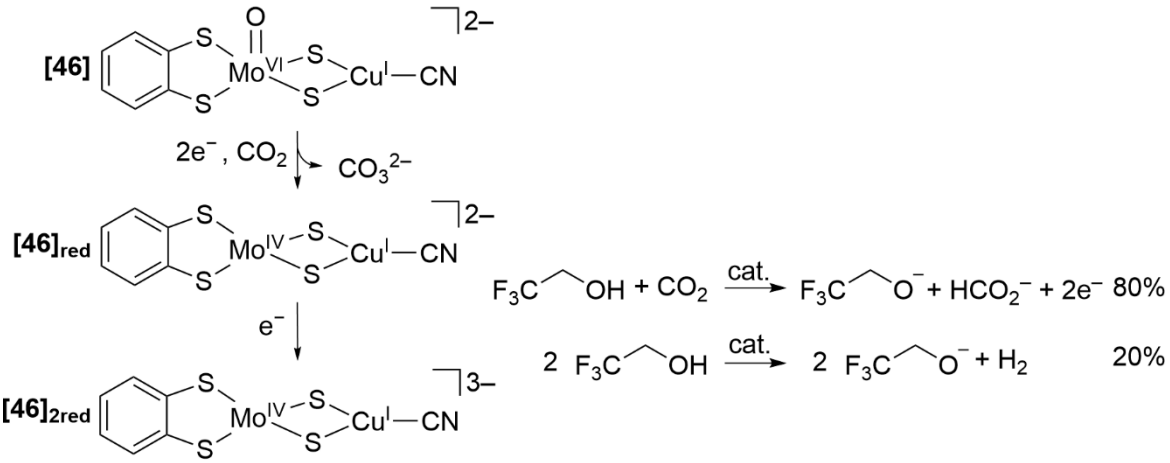

Scheme 40: Activation of the precatalyst **[46]** by two reduction steps (left) and catalyzed reactions (right).[215]

Molybdenum bis(dithiolene) complexes have been investigated mimicking the coordination of the pyranopterine-ligand, universal to all classes of Mo enzymes classified by *Hille*.[163],[172] *Holm* presented a series of Mo complexes $[Mo^{IV}O(S_2C_2R_2)_2]^{2-}$ with different substituents R, which are all oxidized reversibly at around ($E_{1/2}$ = –0.25 - +0.94 V vs. FcH/FcH^+). They were also able to apply a silyl protection group at the terminal oxido ligand with $^tBuPh_2SiCl$.[216]

Applying the combination of silyl protection groups at terminal sulfido ligands coordinated to a Mo^{IV} complex was done by *Back* (*AK Heinze*). He used trimethylsilyl protected monodentate thiolate ligands in six-coordinated Mo^{IV} complexes.[217] Reacting $K_2MoO_2S_2$ with $H^{tBu}L$ ($H^{tBu}L$ = [1 *H*-pyrrole-2-yl)methylene]-4-(*tert*-butyl) aniline) under presence of a silyl chloride resulted in the formation of the Mo^{IV} complexes of the form $Mo^{IV}(^{tBu}L)_2(SSiMe_3)_2$ **47** (scheme 41).[217] The highly water instable complex **47** was characterized via NMR, IR, EPR and UV/vis spectroscopy, as well as with CV and mass spectrometry.[217] It was however not possible to cleave the S–Si bonds, to generate free sulfide ligands at the molybdenum center.

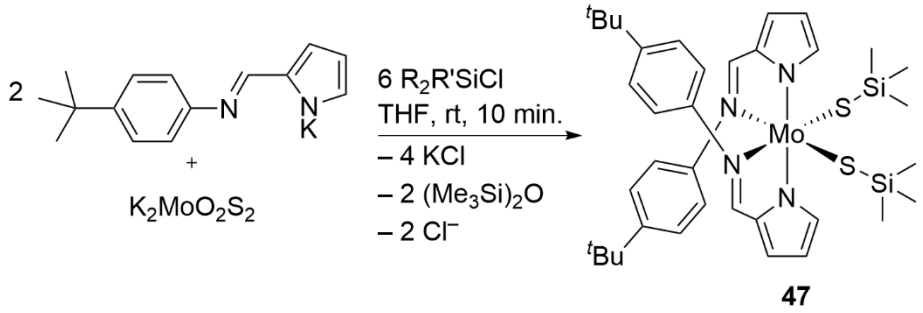

Scheme 41: Synthesis of the Mo^{IV} complex **47** with silyl protection groups at the terminal sulfido ligands.[217] Since it is not entirely clear what the reducing agent is in this reaction, it is not possible to balance the reaction equation.

A CODH mimicking complex with the same coordination sphere found in the enzyme, including an unsupported Mo–(μ_2-S)–Cu bridge, which is also active in the oxidation of carbon monoxide has not been found.

2 Aim of the work

For many catalytic systems, even with established reactions, the underlying reaction mechanism is not fully understood. This is not only the case for artificial systems, but also for biological systems, such as enzymes. Exploring the catalytic cycle in enzymes is even more challenging, since the catalytically active center is embedded into a protein scaffold, complicating measurements.

The enzyme carbon monoxide dehydrogenase (CODH) from the xanthine oxidase family is uniquely build, with a bimetallic molybdenum / copper active center, with the role of the copper atom not entirely clear. It has not been possible to remodel the active center synthetically. The synthesis of complexes with a *cis*-$[Mo^{VI}(L)_2(S)_2]$ unit have not yet been achieved, since terminal sulfido ligands are highly reactive and tend to form polysulfides.[207] The synthesis of a complex with a *cis*-$[Mo^{VI}(L)_2(SR)_2]$ unit with R = $SiMe_3$ has been successful, but the complex has a high instability against water and other proton sources.[217]

It is aimed to synthesize and characterize complexes with a *cis*-$[Mo^{VI}(L)_2(SR)_2]$ unit and bulkier substituents that are more stable. The deprotection of a complex with a *cis*-$[Mo^{VI}(L)_2(SR)_2]$ center to generate a complex with a *cis*-$[Mo^{VI}(L)_2(S)_2]$ center is another task to be carried out. The properties of the complexes will be studied with NMR and UV/vis spectroscopy as well as CV experiments. Furthermore, theoretical calculations of all suggested complexes will be calculated as well.

In a series of works, transient gold(II) species have been postulated as intermediates, especially in light-induced gold-catalyzed reactions involving radicals.[63],[153]–[160] These intermediates however never have been characterized and any spectroscopic evidence is missing. Redox-switchable catalysis is a way to activate gold(I) complexes for catalysis with an oxidant.[111] The complexes are catalytically active after oxidation, and a hypothesis for the active species included a gold(II) species coordinated by the counter ion of the oxidant. This postulated active state offers a free coordination site at the gold(I) atom. It is not known in detail, how this active species forms. One class of complexes successfully employed in redox-switchable catalysis are ferrocenyl substituted Fischer carbene gold(I) complexes.[19]

In this work, synthesizing derivatives of known ferrocenyl substituted Fischer carbene gold(I) complexes with different substituents is planned, to show if a redox active moiety is needed to generate an active complex for catalysis. Furthermore, it will be aimed to unravel the detailed process of the activation of redox switchable catalysis and how different oxidants perform in it. The different catalytic steps will be studied with UV/vis, EPR and NMR spectroscopy at different temperatures, as well as CV measurements. It is planned to support all measurements with DFT calculations and to

expand these calculations to the known system with a di-substituted ferrocenyl Fischer gold(I) center introduced by Bezuidenhout.[113]

3 Results and discussion

The synthesis and characterization of Mo($^{t\text{Bu}}$L)$_2$(SSi(^{i}Pr)$_3$)$_2$ and Mo($^{t\text{Bu}}$L)$_2$(SSi^{t}Bu(Ph)$_2$)$_2$ is described in the section 3.1 “Synthesis of biomimetic molybdenum model complexes for the CODH.” The structure of Mo($^{t\text{Bu}}$L)$_2$(SSi(^{i}Pr)$_3$)$_2$ is investigated by 2D-NMR experiments and DFT calculations. CV experiments unravel an irreversible oxidation and possibilities to cleave the S–Si bond are evaluated.

The findings of the chapter 3.2 were published as: “Maurice P. Schrick, G. Kabelo Ramollo, Cristina-Maria Hirschbiegel, Manuel Fernandes, Andreas Lemmerer, Christoph Förster, Daniela I. Bezuidenhout*, and Katja Heinze*, *Organometallics*, **2024**, *43*, 69–84. *Redox Activation of Acyclic (Aryl)(Amino)Carbene Gold(I) Complexes*” in *Organometallics*.

The manuscript “Redox Activation of Acyclic (Aryl)(Amino)Carbene Gold(I) Complexes” in section 3.2 describes the application of (aryl)(amino)carbene gold(I) complexes in a catalytic reaction and the uncovering of the activation mechanism. The synthesis, characterization and catalytic studies were performed by [redacted], the mechanistic investigation was performed by Maurice Schrick. Through a combination of EPR measurements, CV experiments, stopped flow UV/vis spectroscopy and DFT calculations, the mechanism for the activation of ferrocenyl substituted aryl amino carbene gold(I) complexes was unraveled. The initial fast oxidation takes place at the ferrocenyl moiety, followed by an intramolecular slow valence isomerization. The generated EPR-active gold(II) resting state is coordinated by the counterion of the oxidant. Dissociation of the counterion from this gold(II) species leads to a catalytically active complex and after reduction the pre-catalyst is fully recovered.

Theoretical investigations of a di-substituted Fischer gold(I) carbene complex are described in section 3.3. DFT calculations of the neutral and oxidized form of this complex elucidate which part of the molecule is oxidized and how this impacts the gold–gold interactions. Initial oxidation is taking place at the gold(I) atoms and only a second oxidation at the ferrocenyl backbone. A proposed covalent bond between the two gold center was not found experimentally.

3.1 Synthesis of biomimetic molybdenum model complexes for the CODH

Taking up the reaction introduced by *Back* (*AK Heinze*) to synthesize **1**, the complexes **2** and **3** of the form $Mo^{IV}(^{tBu}L)_2(SSiR_2R')_2$ were synthesized and characterized (scheme 1).

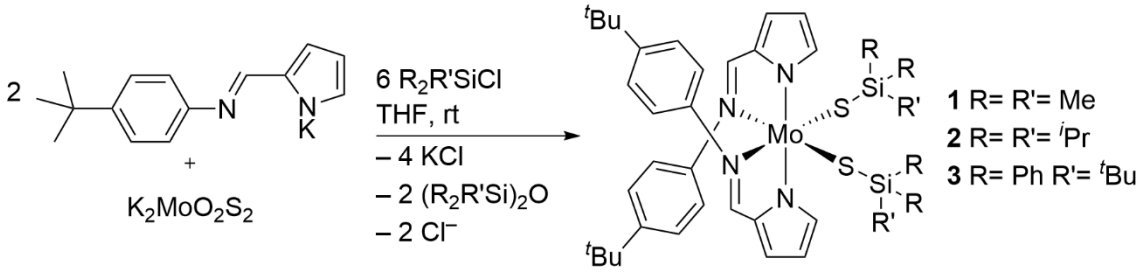

Scheme 1: Synthesis of complexes of the form $Mo^{IV}(^{tBu}L)_2(SSiR_2R')_2$ with different silyl chlorides. Since it is not entirely clear what the reducing agent is in this reaction, it is not possible to balance the reaction equation.

Since **1** is soluble in a plethora of organic solvents (Et_2O, THF, petroleum ether 40-60°, acetone, MeCN, benzene, toluene, DMSO, dichloromethane and HMDSO) even at low temperatures, all attempts to obtain the complex as a crystalline compound failed so far. Three possible isomers are conceivable for **1**, two C_2 and one C_s isomer, since only one set of ligand NMR resonances was observed.[217] DFT calculations suggest the C_2 isomer with the pyrrolato moieties oriented *trans* to each other (OC-6-4-4) to be favored by 44 kJ / mol^{-1} compared to the C_2 isomer with imine moieties oriented *trans* to each other (OC-6-3-3). The OC-6-4-4 isomer is again favored by 34 kJ / mol^{-1} compared to the C_s isomer (OC-6-1-2) with trimethylsilylthiolato ligands oriented *trans* to each other, probably owing to the *trans* influence of the trimethylsilylthiolato ligands (scheme 2).

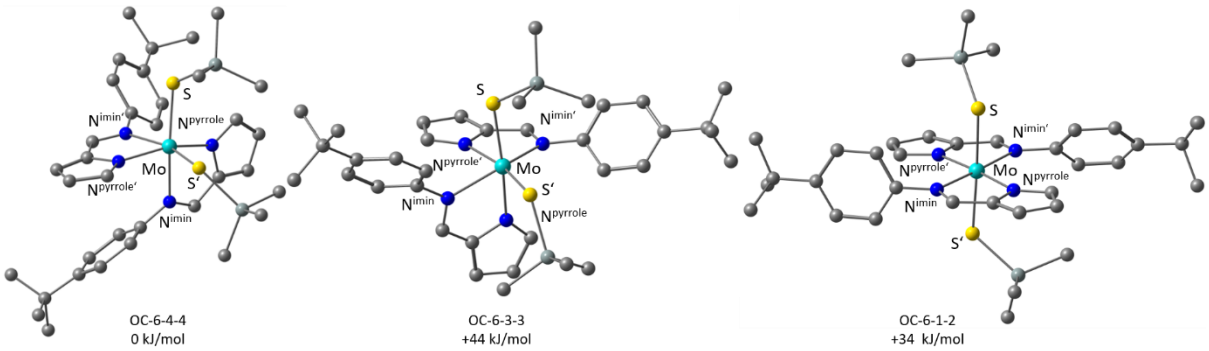

Scheme 2: Optimized geometries of isomers of **1** with respective energies. The underlined numbers indicate the Cahn-Ingold-Prelog (CIP) priority for the stereodescriptor, protons are omitted for clarity.[217]–[222] For an extensive explanation of the priority rules applied, see comment found in the references here:[223]

To generate a precursor complex of the CODH, **1** needs to be desilylated and the Mo^{IV} center oxidized to Mo^{VI}, to generate free sulfide ligands which are available for further functionalization. DMSO should fulfill both roles as oxidant, since it is facile reduced to dimethylsulfide, and as deprotecting agent (scheme 3).[224] Silicon and oxygen have a high affinity for each other and form bonds with high bond

energy, since the 3d orbitals of the Si participate in the formation of the p_π–d_π bond with partial π-character.[225]

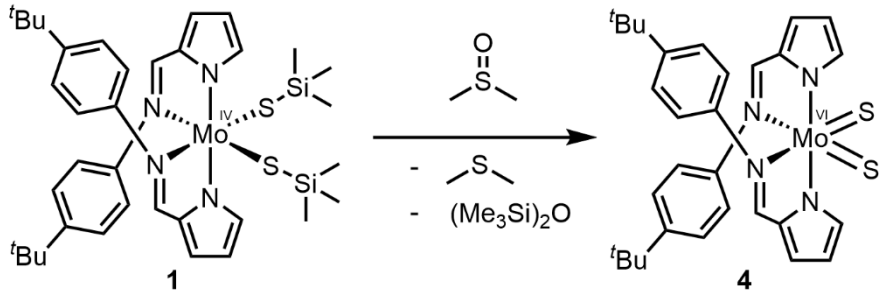

Scheme 3: Proposed reaction mechanism for the deprotection of **1** with DMSO.

A solution of **1** in C_6D_6 is mixed with an excess of DMSO-d^6 and heated for six hours at 40 °C and a ^{1}H-NMR spectrum measured. No change in the signal intensity is visible in comparison with the ^{1}H-NMR resonances of **1** without the addition of DMSO-d^6. Elevating the temperature to 60 °C for eight hours and subsequently to 75 °C over night does not impede any change on the ^{1}H-NMR resonances of **1**, nor on the DMSO-d^6 concentration (scheme 4).

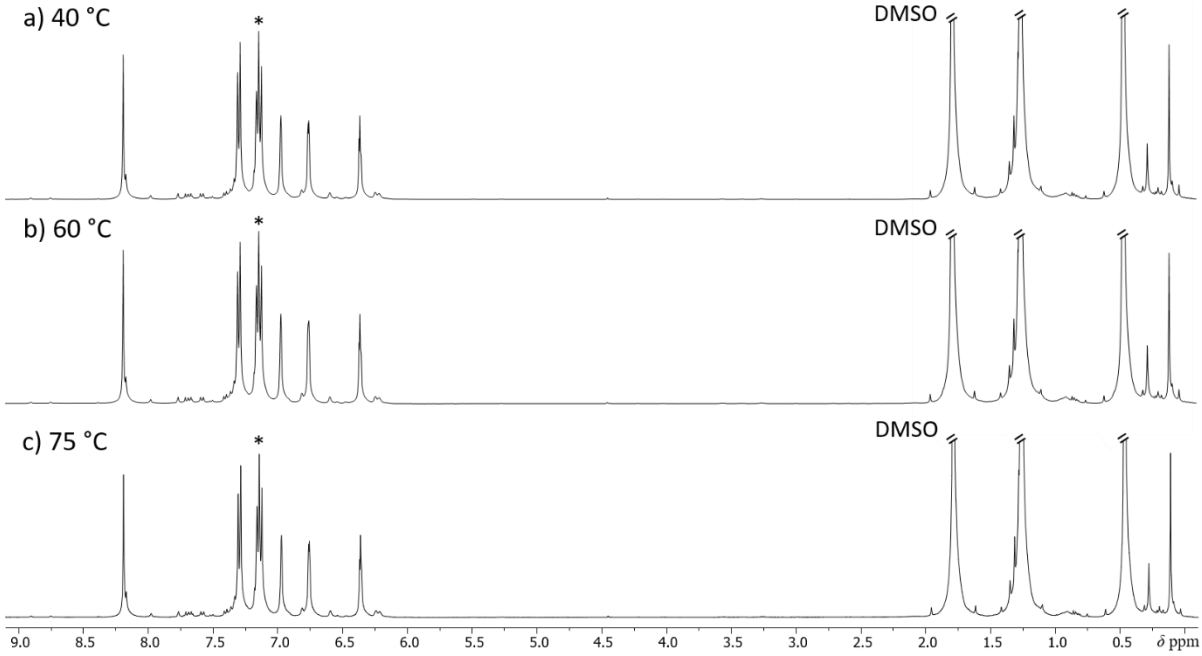

Scheme 4: ^{1}H-NMR spectra of **1** in C_6D_6 with an excess of DMSO-d^6. a) 40 °C for 6 h, b) 60 °C for 8 h, c) 75 °C over night. The asterisk denotes the solvent residue signal.

Hence, DMSO is not suitable to deprotect **1** and other substance classes are considered. *N*-oxides are strong oxidation agents and also bear oxygen atoms, to actively cleave the Si–S bond (scheme 5).[226]

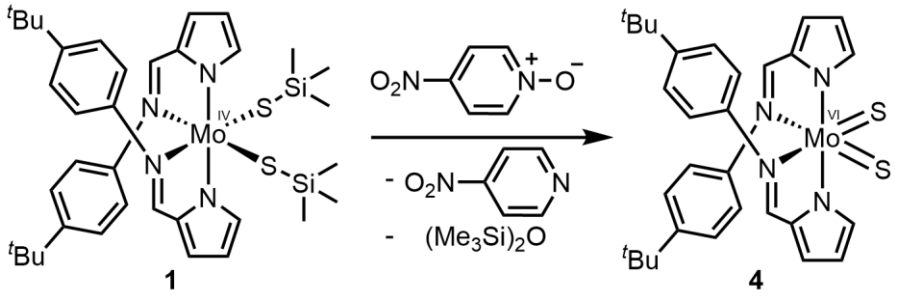

Scheme 5: Proposed reaction mechanism for the deprotection of **1** with *p*-nitropyridine-*N*-oxide.

A solution of **1** in CD_3CN is mixed with an excess of *p*-nitropyridine-*N*-oxide, heated to 40 °C over night and a ^{1}H-NMR spectrum measured. Since no change in the ^{1}H-NMR resonances occurs, it is further heated to 60 °C for another eight hours. Again the ^{1}H-NMR signals of neither complex **1** nor *p*-nitropyridine-*N*-oxide change in intensity, indicating *p*-nitropyridine-*N*-oxide to not be a suitable substance for the removal of the trimethylsilyl protection group (scheme 6).

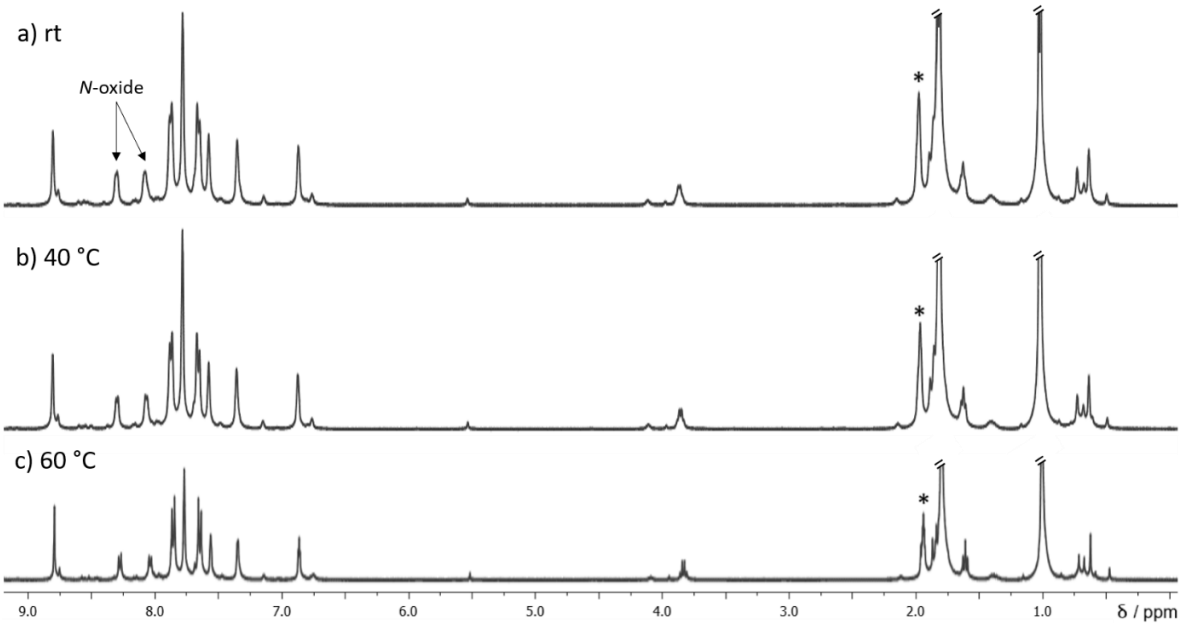

Scheme 6: ^{1}H-NMR spectra of **1** in CD_3CN with an excess of *p*-nitropyridine-*N*-oxide. a) room temperature, b) 40 °C over night, c) 60 °C 8 h. The asterisk denotes the solvent residue signal.

3.1.1 Synthesis of complex $Mo^{IV}(^{tBu}L)_2(SSi(^iPr)_3)_2$ **2**

The complex $Mo^{IV}(^{tBu}L)_2(SSi(^iPr)_3)_2$ **2** was synthesized following the same protocol as for the synthesis of **1**, but a longer reaction time of four hours was used (scheme 7). A higher reaction time is required since the $Si(^iPr)_3$ groups are sterically more demanding than the $SiMe_3$ groups but should lead to a more stable complex. Complexes **1** and **2** are both highly viscose red-brown liquids.

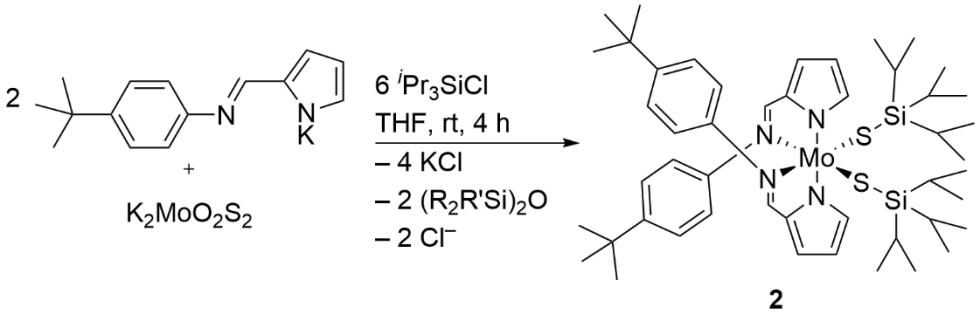

Scheme 7: Synthesis of the complex **2**. Since it is not entirely clear what the reducing agent is in this reaction, it is not possible to balance the reaction equation.

In the aromatic region of the ^{1}H-NMR spectrum of **2** the resonances of the protons of the ligands appear only slightly chemically shifted into the lower field, compared to the resonances of the protons of **1**.[217] The highest chemical shift is observed for proton H^{9} with a change of $\Delta\delta$ = 0.28 ppm, compared to proton H^{9} of **1**. Since only one set of resonances is detectable in the ^{1}H-NMR spectrum of **2**, each ligand $^{tBu}L^{-}$ and each silyl isopropyl group must be chemically equivalent (scheme 8). The septet resonance of the proton H^{14} of the silyl isopropyl group, as well as the doublet resonance of protons H^{15} both integrate to values expected for a 1:1 ratio between the isopropyl silyl group and the ligand ^{tBu}L. The assignment of the resonances to the corresponding protons was ensured through 2D-NMR experiments (see chapter 6.1).

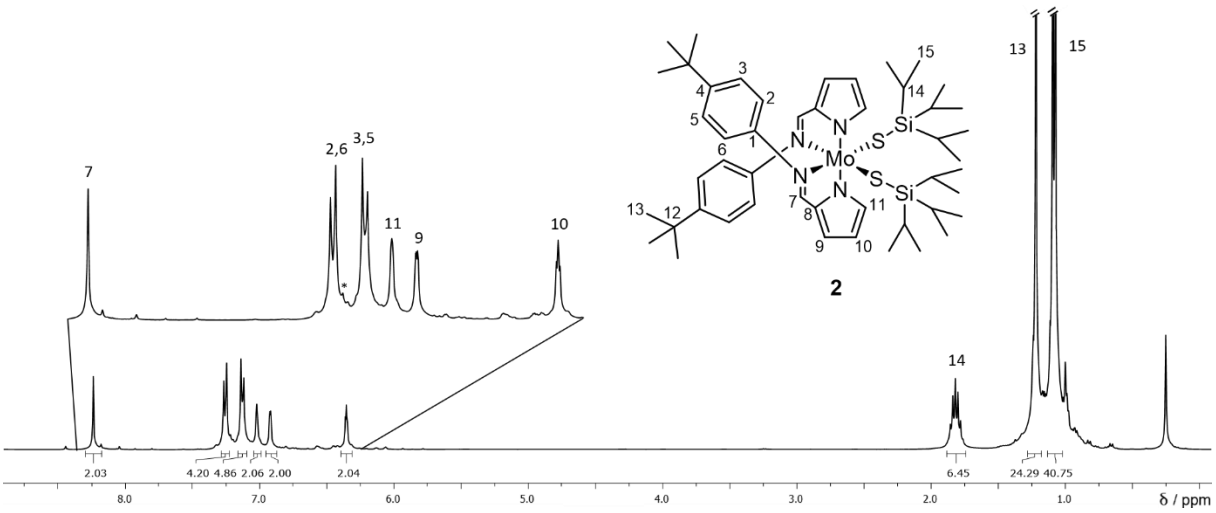

Scheme 8: ^{1}H-NMR spectrum of complex **2** in C_6D_6, with zoomed aromatic region of the spectrum. The asterisk denotes the solvent residue signal.

Also, for the ^{13}C-{^{1}H}-NMR spectrum of **2** all resonances were assigned through 2D-NMR experiments (scheme 9).

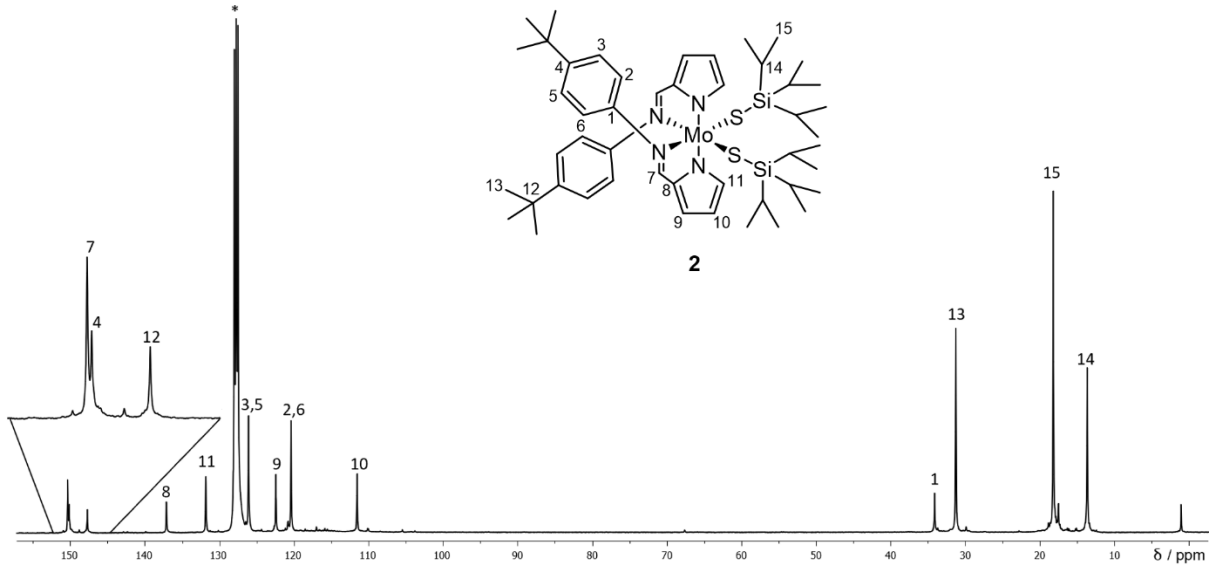

Scheme 9: ^{13}C-{^{1}H}-NMR spectrum of complex **2** in C_6D_6. The asterisk denotes the solvent resonance.

Complex **2** is a highly viscose liquid for which all crystallization attempts failed, so no XRD measurements and thus no information about the spatial arrangement is available. Through ^{1}H-^{1}H-ROESY-NMR experiments the dipolar coupling of two protons in spatial proximity is measured, which is giving information about the molecular structure of **2**. The distance between two protons should not be longer than 5 Å to generate nuclear Overhauser enhancement (NOE) cross signals in the ^{1}H-^{1}H-ROESY-NMR experiment.[227] In the ^{1}H-^{1}H-ROESY-NMR spectrum, cross signals between the protons H^{14} and H^{15} of the isopropyl group and the proton of the pyrrole ring H^{11} are visible (scheme 10). Some weaker NOE cross signals exist between proton H^{15} and the ligand protons H^{10}, H^{9}, H^{7}, $H^{2,6}$ and $H^{3,5}$. Another weak NOE cross signal exists between H^{14} and $H^{3,5}$.

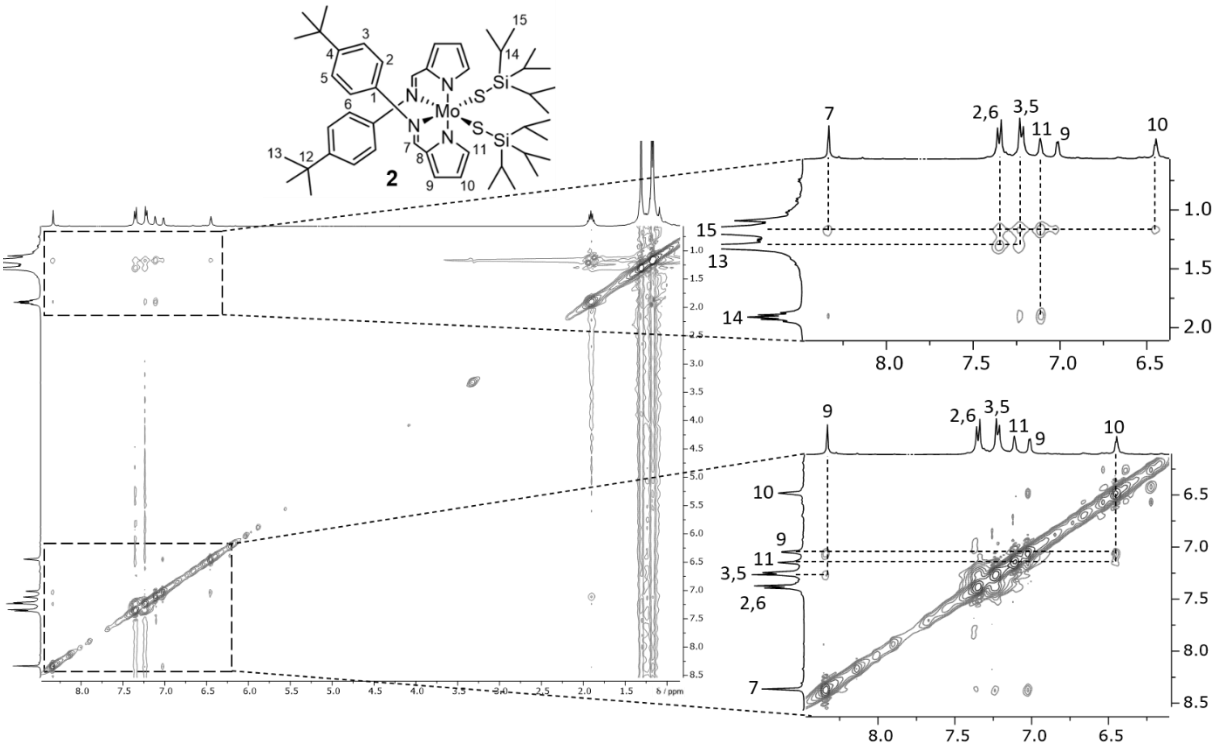

Scheme 10: ^{1}H-^{1}H-ROESY-NMR spectrum of complex **2** in C_6D_6, with zoomed details. Lines are added to guide the eye.

Additionally, all possible isomers of complex **2** are geometry optimized through DFT calculations (scheme 11). As in complex **1** the OC-6-4-4 isomer is determined to be the energetically favored isomer, the OC-6-3-3 isomer is energetically unfavoured by 43 kJ/mol and the isomer OC-6-1-2 is energetically unfavoured by 58 kJ/mol. In the energetically favored OC-6-4-4 isomer of complex **2**, the molybdenum atom is coordinated in a distorted octahedral fashion, with a dihedral angle of 92.6° between the two $^{t\mathrm{Bu}}\mathrm{L}^{-}$ ligands. The molybdenum $\mathrm{N}^{\mathrm{pyrrolato}}$ bond lengths with 2.093 Å and 2.150 Å are in the same range than the bond lengths found in the DFT calculated isomer OC-6-4-4 of **1** (2.098 Å, 2.126 Å), and in the same range as literature known mixed oxido/imido phosphane $\mathrm{Mo}^{\mathrm{IV}}$ complexes $\mathrm{MoO}(^{t\mathrm{Bu}}\mathrm{L})_2(\mathrm{PMe_3})$ 2.126(4) Å and $\mathrm{Mo}(^{t\mathrm{Bu}}\mathrm{L})_2(\mathrm{N}^{t}\mathrm{Bu})(\mathrm{PMe_3})$ 2.155(2) Å.[217],[218] The molybdenum $\mathrm{N}^{\mathrm{imine}}$ bond lengths (2.237 Å and 2.360 Å) are in the same range in comparison to the bond lengths found in the DFT calculated isomer OC-6-4-4 of **1** (2.278 Å, 2.310 Å), but elongated to the literature known complexes $\mathrm{Mo}(^{t\mathrm{Bu}}\mathrm{L})_2(\mathrm{N}^{t}\mathrm{Bu})(\mathrm{PMe_3})$ (2.182(4) Å, 2.213(4) Å) and $\mathrm{Mo}(^{t\mathrm{Bu}}\mathrm{L})_2(\mathrm{N}^{t}\mathrm{Bu})(\mathrm{PMe_3})$ (2.220(2) Å, 2.201(2) Å).[217],[218] The molybdenum sulfur bond lengths with 2.329 Å and 2.344 Å are the same as calculated for isomer OC-6-4-4 of **1** (2.330 Å, 2.338 Å). They are slightly longer than the bridging sulfide bond found in the CODH (2.27 Å).[193] The S–Mo–S' angle is calculated to be 93.5°, which differs slightly from the ideal octahedral angle, but differs significantly from the calculated angle in complex **1** (101.1°).[217] This is explained with the bulkier isopropyl substituents, requiring more space. The $\mathrm{N}^{\mathrm{pyrrolato}}$–Mo–$\mathrm{N}^{\mathrm{pyrrolato'}}$ angle 161.4° (**1**: 156.6°) the $\mathrm{N}^{\mathrm{imine}}$–Mo–S and $\mathrm{N}^{\mathrm{imine}}$–Mo–S' angles (158.9° and

163.5°), (**1**: 160.0° and 163.3°) and the N^{imine}–Mo– $N^{imine'}$ angle with 77.3° (**1**: 82.1°) are evidence of the strong distortion of **2**.[217] Compared to **1** the distortion of the $^{tBu}L^{-}$ ligands is similar, but the bulkier isopropyl groups require more space which causes a compression of the S–Mo–S' and N^{imine}–Mo– $N^{imine'}$ angles.

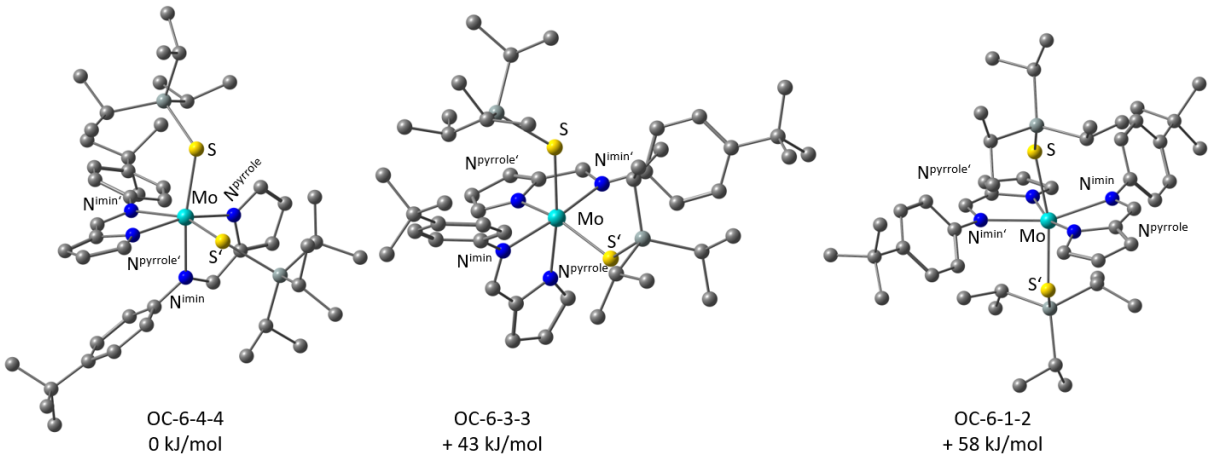

Scheme 11: Optimized geometries of the isomers of **2** with respective energies. Protons are omitted for clarity.

The distance between the protons H^{14} and H^{15} with the protons H^{2}-H^{11} of all isomers obtained through DFT calculations are summarized and compared to the result of the ^{1}H-^{1}H-ROESY-NMR experiment (table 1). Even though an upper threshold for the appearance of cross signals in the ^{1}H-^{1}H-ROESY-NMR experiment is determined to be 5 Å, a tighter upper threshold of shorter than 4 Å was chosen for complex **2**. In the ^{1}H-^{1}H-ROESY-NMR experiment cross signals for proton H^{15} with all listed ligand protons are found, but for H^{14} only cross signals appear for H^{11} and a weak one for $H^{3,5}$. In the calculated isomer OC-6-1-2 the distances found are short enough to explain the cross signals, for isomers OC-6-4-4 and OC-6-3-3, one of the ligand protons has a longer distance to proton H^{14}. Even though the spatial distances calculated for isomer OC-6-1-2 explains the appearance of cross signals, it is energetically the least favored isomer. Conclusively the ^{1}H-^{1}H-ROESY-NMR experiment did not rule out any possible isomers decisively. The calculated energies and the similar pattern of the chemical shifts in complexes **1** and **2** are pointing towards complex **2** taking the form of isomer OC-6-4-4, as assumed for **1**.[217]

Table 1: Measured smallest distance between the protons H^{14} and H^{15} and the protons of both ligands for each calculated isomer of **2** determined through DFT calculations. Distances < 4 Å in green, between 4 Å and 5 Å in orange and > 5 Å in red.

Isomer	Isomer OC-6-4-4		Isomer OC-6-3-3		Isomer OC-6-1-2	
Ligand proton	H^{14}	H^{15}	H^{14}	H^{15}	H^{14}	H^{15}
H^{11}	2.71 / 4.46	2.13 / 3.82	2.72 / 5.82	3.12 / 5.07	2.31 / 3.49	2.23 / 3.07
H^{10}	3.44 / 6.42	3.67 / 4.47	4.63 / 7.66	3.30 / 6.46	3.50 / 3.79	3.32 / 3.91
H^{9}	3.42 / 5.02	3.64 / 3.91	5.65 / 6.50	3.78 / 5.43	3.22 / 3.47	3.66 / 3.73
H^{8}	2.70 / 3.20	3.64 / 3.71	4.30 / 5.09	3.99 / 4.32	3.75 / 3.75	2.94 / 3.07
$H^{3,5}$	2.29 / 2.79	2.28 / 3.32	2.18 / 3.03	2.60 / 3.21	2.49 / 2.66	2.28 / 2.84
$H^{2,6}$	3.57 / 4.88	3.24 / 3.86	2.58 / 2.98	2.81 / 3.52	3.32 / 3.74	3.21 / 3.44

3.1.2 Synthesis of complex $Mo^{IV}(^{tBu}L)_2(SSi^tBu(Ph)_2)_2$ **3**

Complex $Mo^{IV}(^{tBu}L)_2(SSi^tBu(Ph)_2)_2$ **3** was synthesized and obtained as red-brown oil, using the same procedure to synthesize **2**, except the bulkier *tert*-butyldiphenylsilylchloride was used (scheme 12).

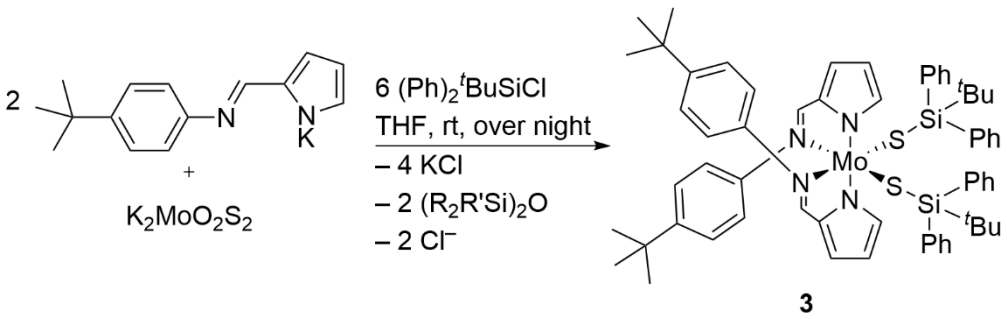

Scheme 12: Synthesis of the complex **3**. Since it is not entirely clear what the reducing agent is in this reaction, it is not possible to balance the reaction equation.

In the ^{1}H-NMR spectrum the imine proton H^7 is easily assigned to the resonance at 8.14 ppm, all other resonances were assigned through 2D-NMR experiments (scheme 13). The aromatic systems of the chelate ligand should produce characteristic ^{1}H coupling patterns, an ABC spin system with two doublets and one triplet for the pyrrole ring and a AA'BB' spin system for the *para* substituted phenyl ring, as found in the ^{1}H-NMR spectra of complexes **1** and **2**. The resonances of the pyrrole protons are found at 7.48 ppm (H^9), 7.45 ppm (H^{11}) and 6.56 ppm (H^{10}). The resonance of the *para* substituted phenyl ring is found at 6.59 ppm ($H^{2,6}$), while the other doublet ($H^{3,5}$) overlaps with the resonances of the aromatic protons, H^b and H^c between 7.22 ppm and 7.12 ppm.

The total correlation spectroscopy (TOCSY) ^{1}H-^{1}H-NMR experiment shows the isolated spin systems which helps to distinguish the protons of the silyl phenyl group from the *para* substituted phenyl ring (see chapter 6.1).[228] Correlations between proton H^a with $H^{2,6}$ are detected in the TOCSY-NMR

spectrum, which are explained with a common chemical shift of both phenyl groups in **3**. The phenyl silyl group has an ABC-spin system with one doublet and two triplets. The doublet resonance at 7.67 ppm is assigned to proton H^a, while both triplets share a chemical shift with proton $H^{3,5}$ as a multiplet and are not distinguishable.

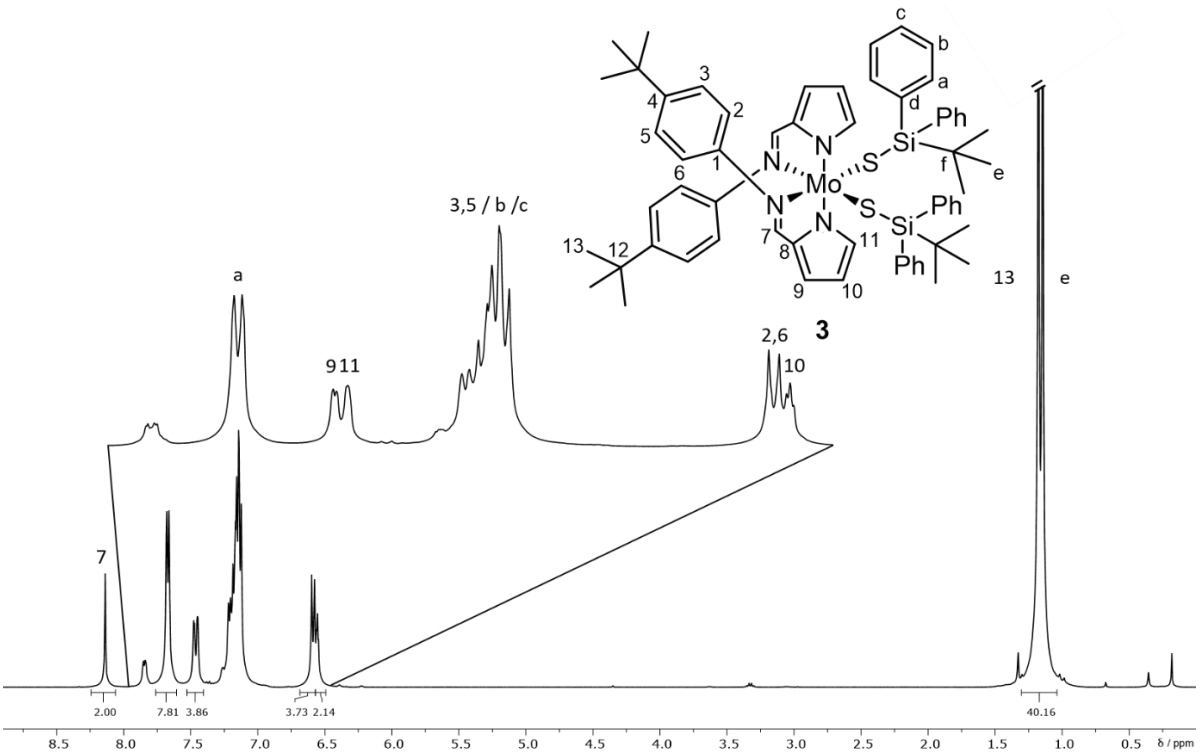

Scheme 13: ^{1}H-NMR spectrum of complex **3** in C_6D_6, with zoomed aromatic region of the spectrum.

The ^{13}C-NMR resonances were assigned through heteronuclear single-quantum correlation (HSQC) spectroscopy ^{1}H-^{13}C-NMR experiments to determine the direct proton carbon correlations and all other resonances of quaternary carbon atoms were assigned through heteronuclear multiple-bond correlation (HMBC) spectroscopy ^{1}H-^{13}C-NMR experiments.[229] The ^{13}C-NMR resonances for carbons C^b, C^c and C^d could not be assigned, since two of these signals are overlaid by the solvent signal (scheme 14).

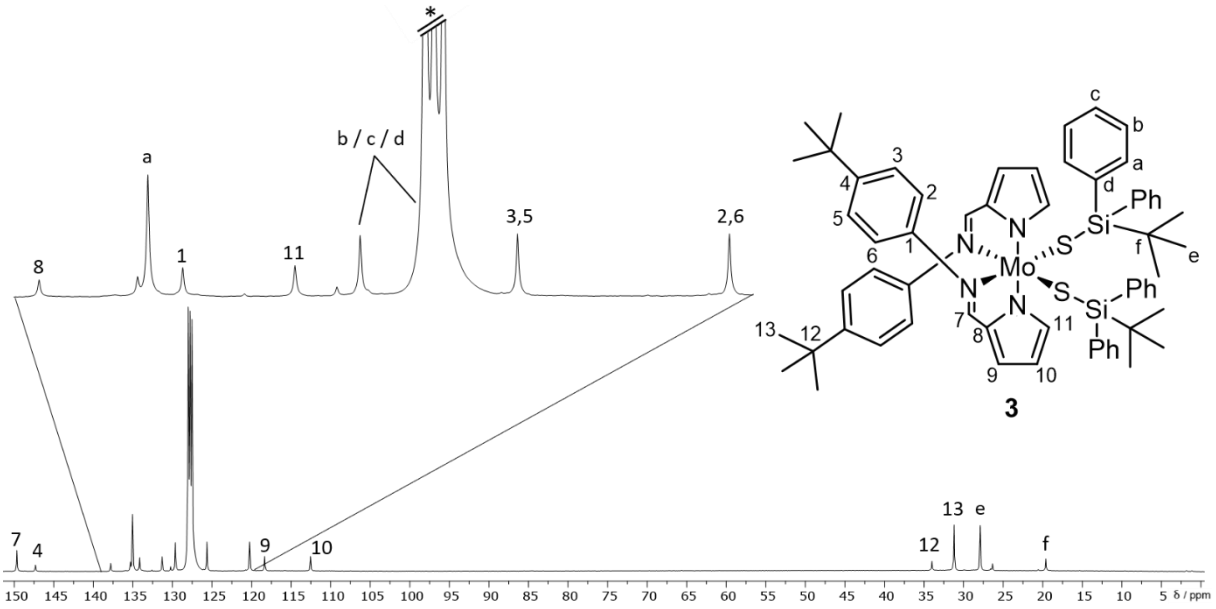

Scheme 14: ^{13}C-{^{1}H}-NMR spectrum of complex **3** in C_6D_6. The asterisk denotes the solvent resonance.

The ^{1}H-^{15}N-HMBC-NMR spectrum reveals only two nitrogen resonances, which points towards a complex with a C_s or C_2 symmetry with a ligand to silyl ratio of 1:1, determined through the integration of ^{1}H-NMR signals (see chapter 6.1.). The N^{imine} is coupling with only two proton resonances (H^7 and $H^{2,6}$) while $N^{pyrrolato}$ is coupling with four proton resonances (H^7, H^9, H^{11} and H^{10}).

Comparing all proton resonances of the common ligand $^{t\mathrm{Bu}}L^-$ in the complexes **1**, **2** and **3** measured in C_6D_6 delivers no clear trend for the resonances of the protons $H^{3,5}$ and $H^{2,6}$ (table 2). For the resonances of the pyrrolato protons a low field shift becomes apparent. The resonance of the protons H^9 shifts from δ = 6.74 ppm in complex **1** to δ = 7.48 ppm in complex **3**, a change of $\Delta\delta$ = 0.54 ppm. A possible explanation is the higher shielding of the silylthiolato ligands, preventing the C_6D_6 solvent molecules interacting with the ligand through π-π-interactions. The low field shift of the pyrrolato protons between complexes **2** and **3** is even stronger than between complexes **1** and **2**, in accordance to the even higher shielding of the silylthiolato ligands in complex **3**.

Table 2: Chemical shifts of all protons of the ligand $^{t\text{Bu}}L^-$ in the complexes **1**, **2** and **3** measured in C_6D_6 in ppm.[217]

	1	**2**	**3**
H^{13}	s, 1.27	s, 1.31	s, 1.18
$H^{3,5}$	d, 7.29, *J* = 8.5 Hz	d, 7.35, *J* = 8.5 Hz	d, 6.59, *J* = 8.5 Hz
*$H^{2,6}$	d, 7.12, *J* = 8.5 Hz	d, 7.22, *J* = 8.5 Hz	m, 7.22–7.12
H^7	s, 8.17	s, 8.33	s, 8.14
*H^9	dd, 6.74, *J* = 3.5 Hz, *J* = 1.5 Hz	dd, 7.01, *J* = 3.5 Hz, *J* = 1.4 Hz	s, 7.48
H^{10}	t, 6.35, *J* = 3.1 Hz	t, 6.45, *J* = 3.1 Hz	t, 6.56, *J* = 3.2 Hz
*H^{11}	s, 6.97	s, 7.11	s, 7.45

* The resonance of the protons $H^{2,6}$ in **3** are overlaid by further proton resonances, forming a multiplet. For proton H^9 in **3** no coupling constants were found due to low resolution; for H^{11} a doublet is expected for all complexes but not resolved due to low resolution.

The UV/vis spectrum of **2** has a broad low energy shoulder tailing to around λ = 500 nm and a maximum at λ = 330 nm (scheme 15). The low energy shoulder is very similar to the UV/vis-spectrum of **1** and both complexes share a maximum at the same wavelength.[217] Through TDDFT calculations the maximum of **1** was attributed to LMCT transitions from the ligand $^{t\text{Bu}}L^-$ to the $[Mo^{IV}(SSiMe_3)_2]^{2+}$ moiety and MLCT transitions to the ligand $^{t\text{Bu}}L^-$.[217] This is also assumed for **2**, since the maxima are at the same wavelength and the coordination geometry at the central Mo-atom is the same. During the synthesis of **2**, traces of $H^{t\text{Bu}}L$ are generated which are not separable from **2**, since both have the same solubility, thus no extinction coefficient was determined.

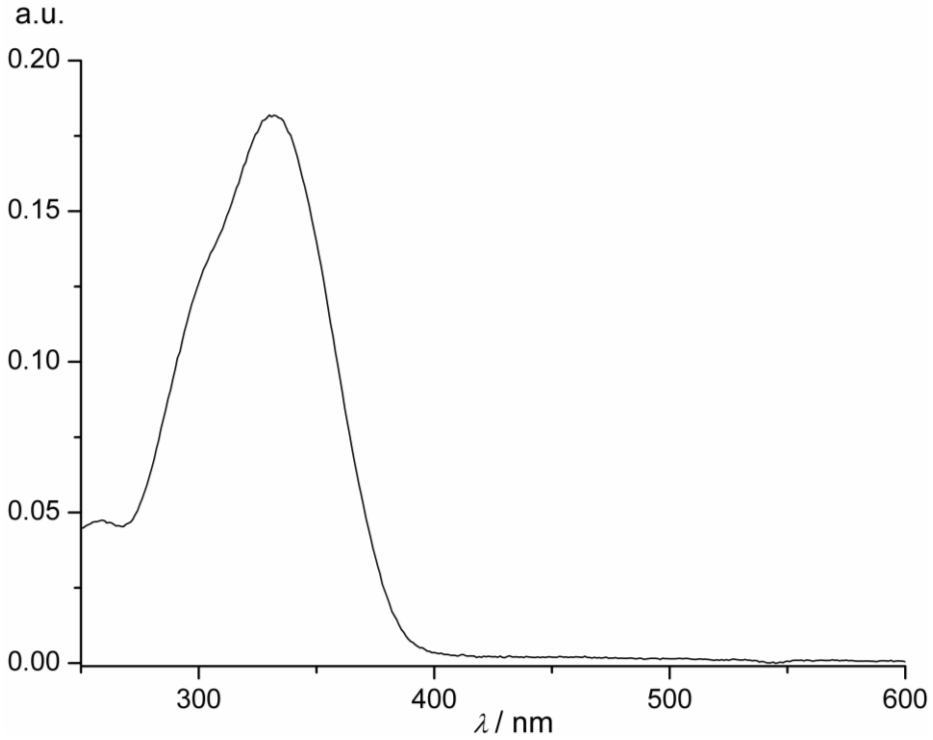

Scheme 15: UV/vis spectrum of **2** in THF at 22°C with traces of $H^{t\text{Bu}}L$.

Traces of H_2O or another unknown proton source led to decomposition of **2** and the formation of colorless crystals. XRD measurements of these crystals reveal a monoclinic unit cell and the molecular structure of a decomposition product **5**. The ligand $^{tBu}L^-$ is covalently bound to the isopropyl silyl protection group through the $N^{pyrrole}$ atom and accompanied by a protonated ligand (scheme 16). Between the protonated ligand $H^{tBu}L$ and an adjacent protonated ligand in the same unit cell, hydrogen bonds exist.

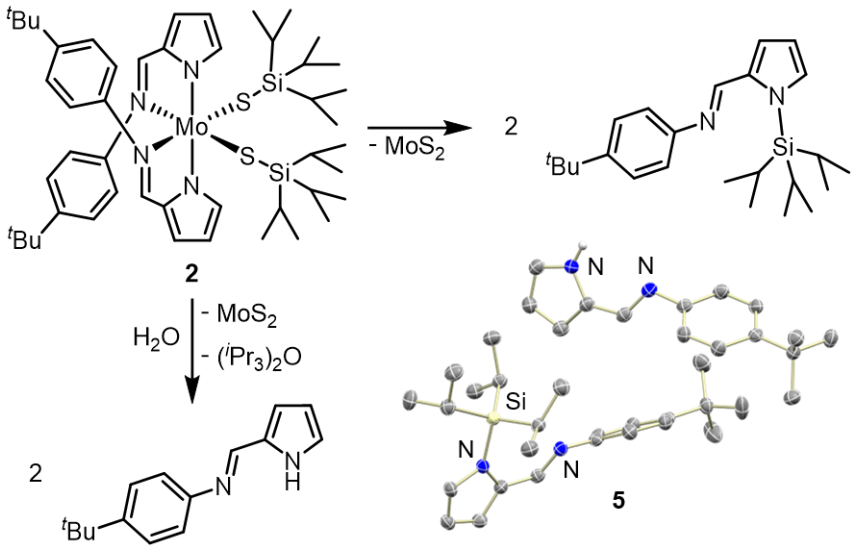

Scheme 16: Possible reactions leading to the formation of **5**: silyl migration and hydrolysis. Partially labeled ellipsoid plot (50% probability) of the decomposition product **5**. CH hydrogen atoms omitted for clarity.

To convert **2** to a CODH precursor complex, the isopropyl protection groups need to be removed and the molybdenum center oxidized. In order to find a suitable oxidant, complex **2** is investigated by CV experiments in THF with $[^nBu_4N][B(C_6F_5)_4]$ as supporting electrolyte. The cyclic voltammogram of **2** in THF shows an irreversible oxidation wave at E_p = +0.82 V against the FcH/FcH^+ redox couple (scheme 17). The wave is assigned to an irreversible oxidation from Mo^{IV} to Mo^{V} and lies in a range of reported Mo^{IV} complexes.[216],[217] Compared to the peak potential of complex **1** the irreversible oxidation wave of **2** is ΔU = 0.08 V higher.[217]

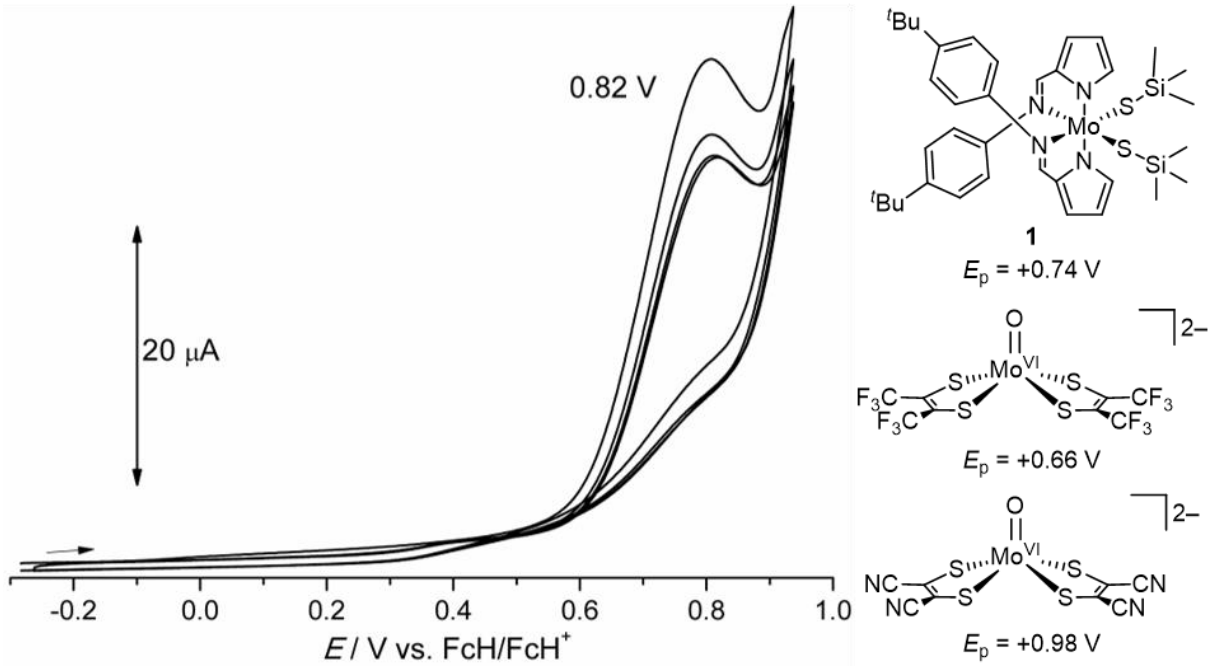

Scheme 17: Left: cyclic voltammogram of **2** in THF with [^{n}Bu$_4$N][B(C$_6$F$_5$)$_4$] as supporting electrolyte. Right: reported Mo^{IV} complexes with similar irreversible peak potentials.[216],[217]

Since **2** is oxidized at E_p = +0.82 V, the choice of an oxidant is limited and [N(C$_6$H$_3$Br$_2$-2,4)$_3$][SbCl$_6$], Magic Green, with an sufficiently high enough oxidation potential of $E_{½}$ = +1.14 V vs. FcH/FcH$^+$ in MeCN is chosen.[230] Just as **1**, the neutral form of complex **2** is EPR silent as expected for diamagnetic Mo^{IV} complexes with d^2 electron configuration.[217] The chemical oxidation of **2** did not led to a single oxidized species, as expected for the irreversible nature of the oxidation, but rather to a complex mix of resonances in the EPR spectrum (scheme 18). The *g*-values observed in the EPR spectrum of complex **[2]**$^+$ six hours after addition of Magic Green in THF are below *g* = 2.0, with *g* = 1.9847, *g* = 1.9656 and *g* = 1.9516. Next to the three most intensive resonances a total of seven resonances is found. This accounts for the $^{95/97}$Mo hyperfine coupling observed.[231],[232] In contrast, for complex **[1]**$^+$ one distinguished signal with g_{iso} = 1.9607 and a $^{95/97}$Mo hyperfine coupling was found after oxidation with Magic Green, which is typical for single mononuclear Mo^V species.[217]

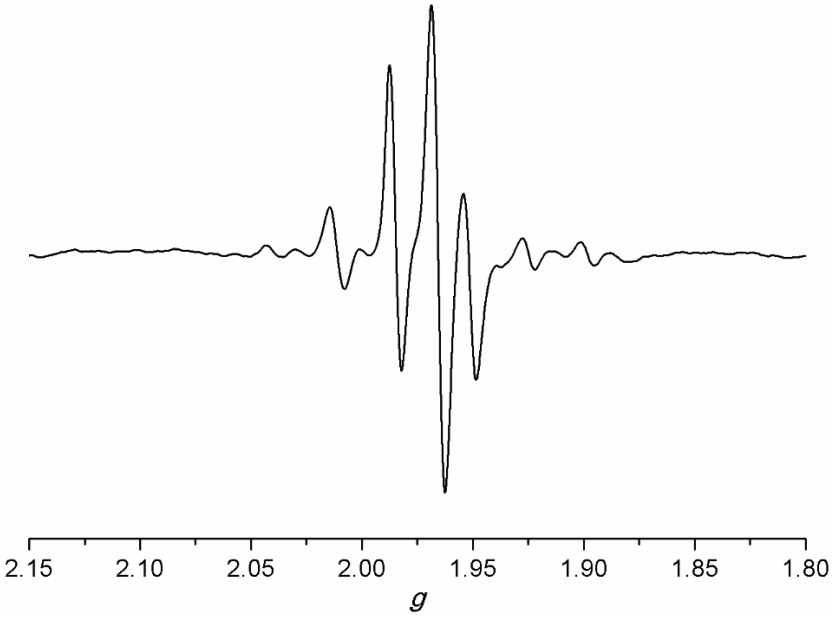

Scheme 18: EPR spectrum of **2** in THF at room temperature, six hours after addition of 0.9 equivalents of $[N(C_6H_3Br_2\text{-}2,4)_3][SbCl_6]$, Magic Green.

Since removal of the protection group on complex **1** did not succeed with neither DMSO nor *N*-oxides, fluorine containing compounds are tested as deprotecting agents. Combining an electrophilic F^+-source like Selectfluor with a fluoride source circumvents the toxicity of directly using elemental fluorine gas.[233] Selectfluor not only functions as a F^+-source, but also as oxidant, oxidizing the Mo^{IV} center to a Mo^{V} center.[234] Combining Selectfluor with a fluoride source and using it to de-protect **2** would result in formation of complex **4** (scheme 19).

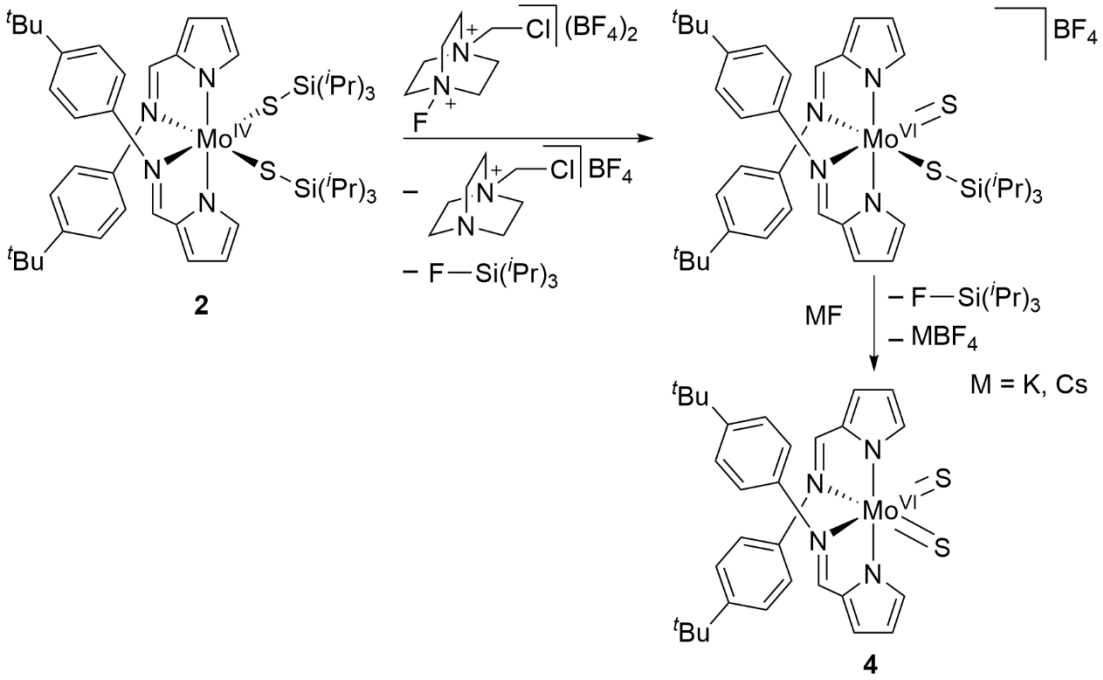

Scheme 19: Proposed synthesis of complex **4** through deprotection of **2** with Selectfluor and a fluoride ion source.

A solution of Selectfluor in MeCN is added to a solution of complex **2** in MeCN and the reaction progress was followed spectroscopically. In the UV-vis spectra of **2** after Selectfluor addition, isosbestic points at λ = 276 nm and λ = 347 nm are detected, indicating that a reaction between Selectfluor and **2** takes place and no intermediates are present (scheme 20).

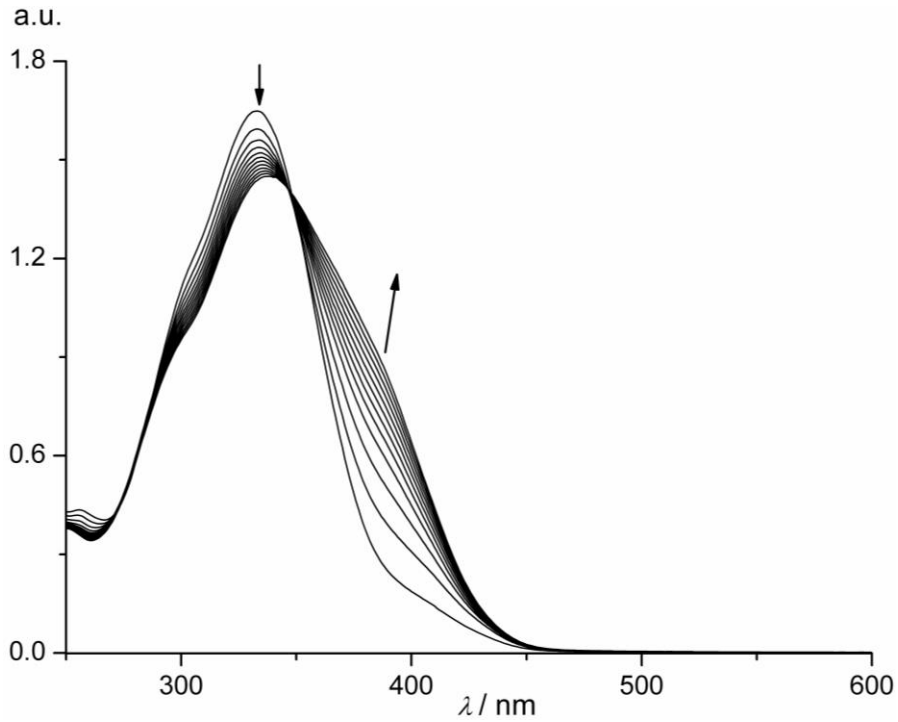

Scheme 20: UV/vis spectra of **2** in MeCN after Selectfluor addition, recorded every 5 minutes for a total time of one hour. Arrows indicate change of the spectra intensity over time.

The Selectfluor addition is followed by addition of a fluoride source, to conclude the deprotection of **2**. Adding a solution of $[Cs(18\text{-crown-}6)_2^+]F^-$ or $[K(18\text{-crown-}6)^+]F^-$ to a solution of Selectfluor and **2** did not result in a change of the UV/vis spectrum and thus no further reaction took place. Using the small, non protic oxygen source $NaOMe_{(s)}$ instead, let to a follow up reaction visible by UV/vis spectroscopy (scheme 21). After adding $NaOMe_{(s)}$ and continuously stirring the solution let to the appearance of an isosbestic point at 338 nm and a gradual shift of the maximum from λ = 327 nm towards λ = 361 nm over time. Since NaOMe is added as a solid, a slower heterogeneous reaction takes place while this change in the reaction rate is visible in the UV/vis spectra. The first spectrum recorded after $NaOMe_{(s)}$ addition appears to be similar to the spectra depicted in scheme 20, but a gradual change towards spectra derived from a new species are apparent.

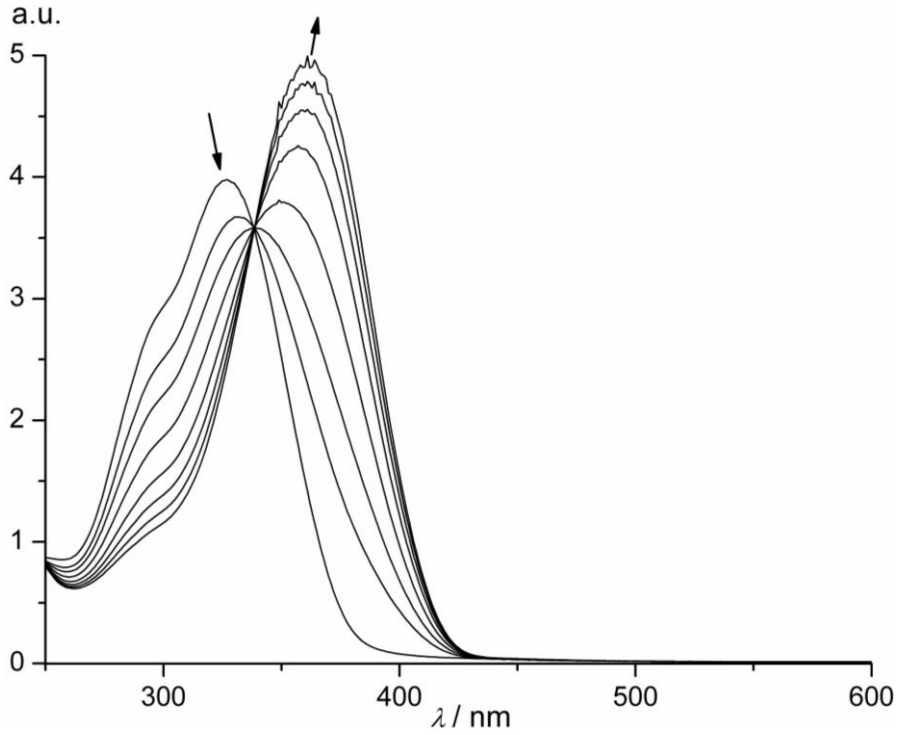

Scheme 21: UV/vis spectra of **2** and Selectfluor in MeCN after $NaOMe_{(s)}$ addition, recorded every 15 minutes for a total of two hours. Arrows indicate change of the spectra intensity over time.

Viewing the reaction of **2** with Selectfluor and $NaOMe_{(s)}$ with ^{1}H-NMR spectroscopy shows one resonance which is assigned to the protons of the methyl group of methanol (scheme 22). After removing all volatiles in vacuum, this resonance disappears, alongside another resonance which was not assigned, but resembles the doublet of an isopropyl group. It is however not possible to assign the resonance to an isopropyl group, since in the ^{1}H-NMR spectrum of an isopropyl group a doublet coupling with a septet is expected, which is absent in the spectrum. Three resonances belong to the *N*-chloromethyl-triethylenediammonium (tetrafluoroborate) cation formed after F^{+} transfer from Selectfluor and all remaining resonances are similar to the resonances of the ligand $^{t\mathrm{Bu}}$L, albeit have other chemical shifts and no resonance from the $N^{pyrrole}$–H proton is detected in the ^{1}H-NMR spectrum, suggesting a coordination of the ligand $^{t\mathrm{Bu}}L^{-}$ to the Mo atom.

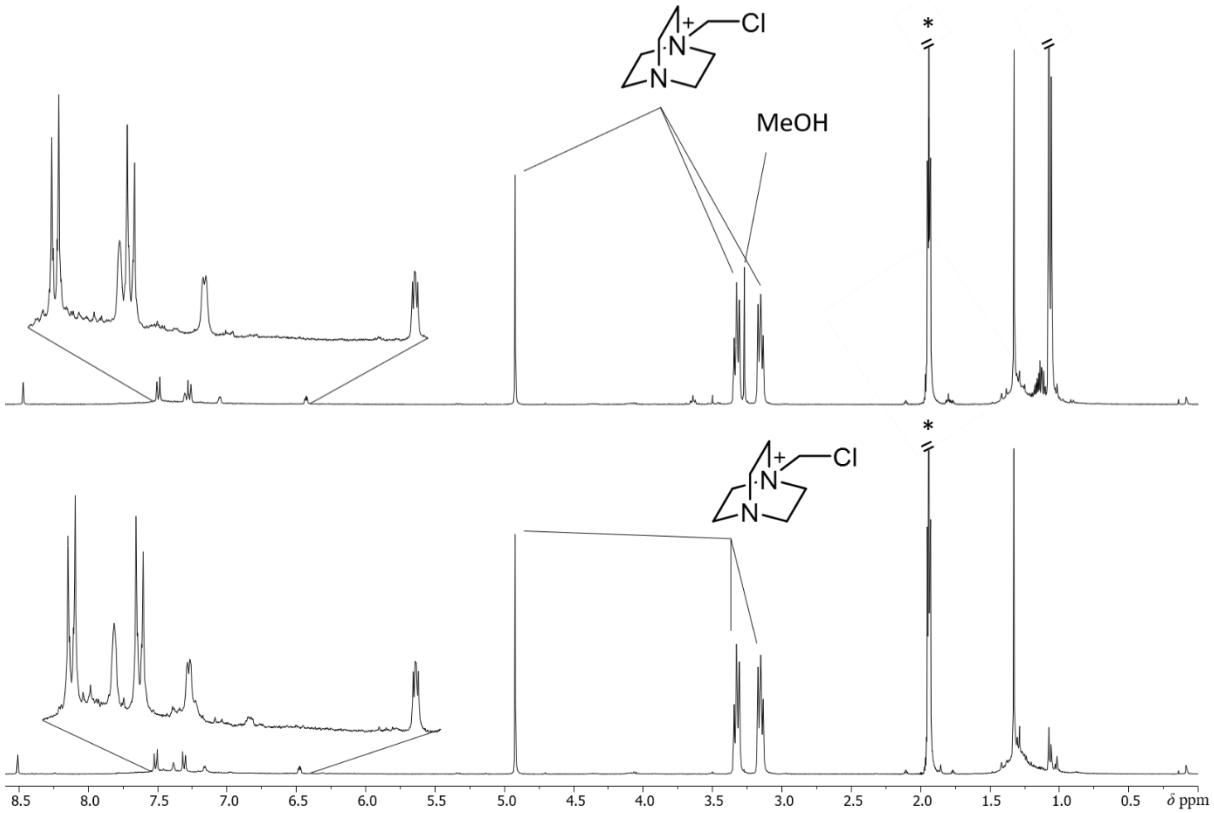

Scheme 22: ^{1}H-NMR spectrum of the reaction of **2** with Selectfluor and $NaOMe_{(s)}$ in MeCN-d^3. Top: after completion of the reaction, bottom: after removing all volatiles in vacuum and re-dissolving in MeCN-d^3. The asterisks denotes the solvent residue signals.

Although these results seem promising, no hints to the formation of complex **4** were found through mass spectrometry and all crystallization attempts were unsuccessful. One problem using Selectfluor is the removal of the remaining *N*-chloromethyl-triethylenediammonium (tetrafluoroborate) cation after F^+ transfer, since the solubility of the cation and the possible complex **4** might be similar. Literature procedures to remove the cation rely on column chromatography, a method not suitable for a complex coordinated by the anionic ligand $^{t\text{Bu}}$L, since it would lead to cleavage of the N–Mo bond and protonation of the ligand to H$^{t\text{Bu}}$L.[235],[236]

3.1.3 Geometry optimizations of complex **4** via DFT calculations

Since complex **4** has not yet been isolated and characterized, DFT calculations are used to predict the geometry and possible isomers. In contrast to the possible isomers of complexes **1** and **2** no OC-6-1-2 isomer was found for complex **4** (scheme 23). Since sulfide ligands are π-donor ligands, they exert a strong *trans* influence and avoid this coordination. Out of the two possible isomers, OC-6-4-4 is energetically favored by 39 kJ/mol compared to isomer OC-6-3-3.

In the OC-6-4-4 isomer of complex **4** the calculation reveals a distorted octahedral geometry, as found in the molecular structure (XRD) of the know dioxido substituted complex **6**.[218] The molybdenum

$N^{pyrrolato}$ bond lengths with 2.092 Å are the same range as measured in complex **6** (between 2.081(2) Å and 2.066(2) Å). The molybdenum N^{imine} bond lengths of **4** (2.335 Å) lay in the same range as measured for complex **6** (between 2.353(2) Å and 2.320(2) Å).[218]

The molybdenum sulfur bond length calculated in the OC-6-4-4 isomer of **4** with 2.157 Å is in accordance to the molybdenum sulfide bond length (2.15 Å) found in the active center of the oxidized form of the aldehyde oxidoreductase found in *D. gigas* but slightly shorter than the bond lengths found in complexes $[Mo^{VI}(Me_4(phen))O(OSiPh_3)_2S]$ (2.203(2) Å) and $[Mo^{VI}O(OC_6H_4{}^tBu\text{-}2)S(Tp^{iPr})]$, with Tp^{iPr} = hydrotris(3-isopropylpyrazol-1-yl)borate) (2.193(3) Å).[172],[237]–[241] The S–Mo–S' angle is with 107.6° close to the measured O–Mo–O' angles found in **6** (106.0° and 105.5°).[218] With 153.2° the $N^{pyrrolato}$–Mo–$N^{pyrrolato'}$ angle is less distorted than the one measured in **6** (151.6° and 149.0°).[218] The N^{imine}–Mo–S and $N^{imine'}$–Mo–S' angles (159.7° and 158.9°) are again close to the measured N^{imine}–Mo–O/O' ones found in complex **5** (163.5° and 159.5°).[218] The N^{imine}–Mo– $N^{imine'}$ angle is with 72.3° (**5**: 77.9° and 74.5°) tighter compared to the one found in **5**.[218]

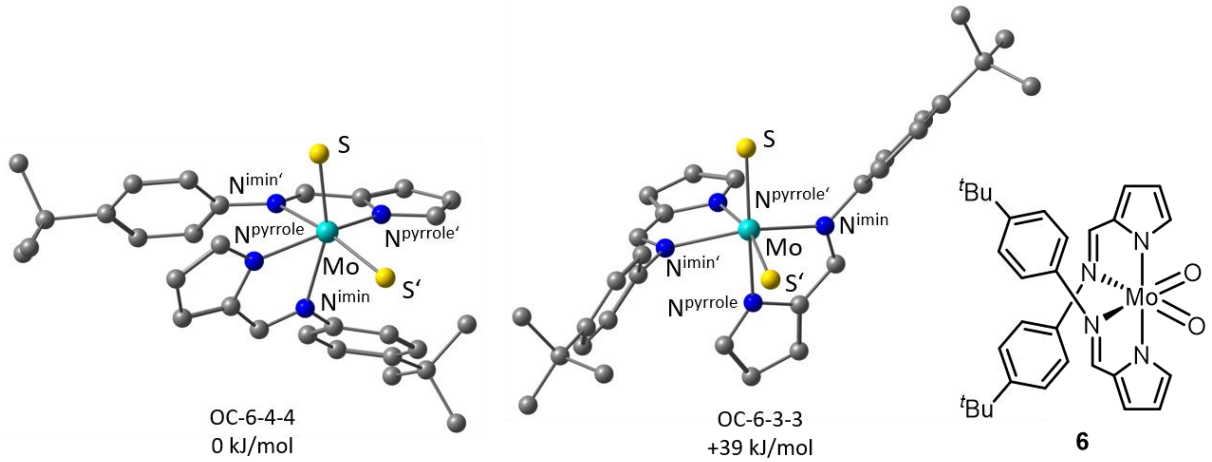

Scheme 23: Optimized geometries of isomers of **4** with respective energies. Protons omitted for clarity. Right: reference complex **6**.[218]

3.2 Redox Activation of Acyclic (Aryl)(Amino)Carbene Gold(I) Complexes

Maurice P. Schrick, G. Kabelo Ramollo, Cristina-Maria Hirschbiegel, Manuel Fernandes, Andreas Lemmerer, Christoph Förster, Daniela I. Bezuidenhout*, and Katja Heinze*

Organometallics, **2024**, *43*, 69–84.

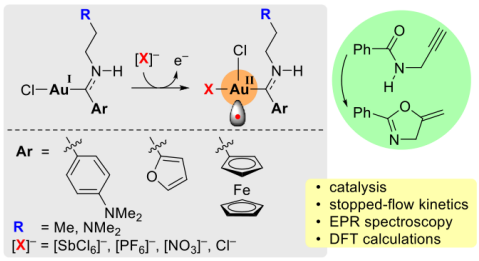

Fischer-type carbene gold(I) pre-catalysts featuring redox-active substituents were synthesized and characterized. Single electron oxidation of the ferrocenyl substituted gold(I) pre-catalysts leads to a fast reversible oxidation at the ferrocenyl moiety. This is followed by slow valence isomerization from an Au^{I}/Fe^{III} species to an Au^{II}/Fe^{II} species. The generated Au^{II} species is EPR-active and coordinated by the counterion of the oxidant. After dissociation of the counterion, the complex becomes catalytically active in the cyclisation of *N*-propargyl amide. It is possible to turn the catalytic reaction off with a suitable reductive agent. The activation process is unraveled and analyzed thoroughly by CV experiments, temperature depending EPR and stopped-flow UV/vis spectroscopy as well as by computational methods.

Author contributions

Maurice P. Schrick carried out the EPR, CV and UV/vis stopped flow measurements, as well as the oxidation/re-reduction NMR measurements. Maurice P. Schrick as well performed all DFT calculations. [redacted] performed the synthesis and catalytic studies of the complexes. Together with [redacted] characterized the complexes. [redacted] synthesized the phenyl-substituted gold(I) complex and performed CV measurements on it during her bachelor thesis under supervision of Maurice P. Schrick. [redacted] wrote the first draft of the chapter about synthesis and catalysis, Maurice P. Schrick wrote the first draft of the manuscript while [redacted] wrote the final version of the manuscript. [redacted] and [redacted] guided the overall direction of the project.

Supporting Information

for this article found in chapter 6.2.

Cartesian coordinates of calculated DFT-structures are found online at:

https://pubs.acs.org/doi/10.1021/acs.organomet.3c00395

ORGANOMETALLICS

pubs.acs.org/Organometallics Article

Redox Activation of Acyclic (Aryl)(amino)carbene Gold(I) Complexes

Maurice P. Schrick,[‖] G. Kabelo Ramollo,[‖] Cristina-Maria Susanne Hirschbiegel, Manuel Fernandes, Andreas Lemmerer, Christoph Förster, Daniela I. Bezuidenhout,* and Katja Heinze*

Cite This: *Organometallics* 2024, 43, 69−84 Read Online

ACCESS | Metrics & More | Article Recommendations | Supporting Information

ABSTRACT: Activation of halido gold(I) precatalysts Au(L)X to a cationic species $[Au(L)]^+$ with a vacant coordination site for substrate binding typically requires abstraction of the halide X^-. The Fischer-type carbene gold(I) precatalysts **2**−**4** feature redox-active dimethylanilinyl, 2-furyl, and ferrocenyl substituents without (**2a**−**4a**) and with (**2b**−**4b**), a dangling dimethylamino substituent. After single-electron oxidation, **2**−**4** catalyze the cyclization of *N*(2-propyn-1-yl)benzamide to 2-phenyl-5-vinylidene-2-oxazoline without the presence of a halide scavenger. While all dimethylanilinyl and 2-furyl substituted precatalysts likely form catalytically active nanoparticles after oxidation, the ferrocenyl substituted gold(I) complexes **4a** and **4b** operate in a homogeneous fashion. The dimethylamino substituted ferrocenyl precatalyst **4b** is the most active one. The formation of the catalytically active molecular species after oxidation was probed by stopped-flow experiments, quantitative EPR spectroscopy, and quantum chemical calculations to arrive at a consistent mechanistic picture that involves one-electron oxidation of the ferrocene, valence isomerization to a gold(II) species and anion coordination to the gold(II) center. This oxidation/isomerization/coordination activation mechanism is fundamentally different from the typical activation of gold(I) precatalysts by halide abstraction and opens new avenues in gold catalysis beyond gold(I) and gold(III) catalyses.

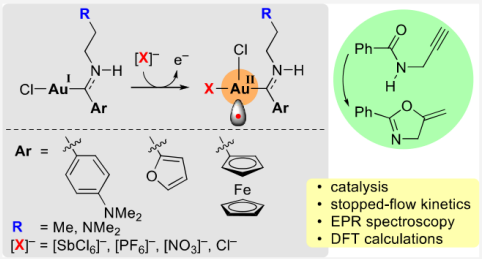

■ INTRODUCTION

Chlorido gold(I) complexes with phosphane or carbene ligands are highly useful precatalysts for a variety of organic transformations, in particular with substrates containing carbon−carbon multiple bonds with a considerable number of reviews documenting the huge progress of the research field.[1−18] Activation of the precatalyst to a cationic species with a vacant coordination site for substrate binding is required. This is most often realized by halide abstraction using silver(I), copper(I), or alkali metal salts with weakly coordinating counterions or halogen-bond donors, either isolated in a separate step before the catalysis or prepared in situ.[19−27] Silver- or additive-free methods, using so-called self-activating precatalysts, operate by intramolecular hydrogen bonding to activate the halido−gold bond.[28−32] Potentially self-activating (and counterion-binding) precatalysts **A**−**E** (Chart 1a) with N−H groups in ligand side arms reported by Gabbaï, Helaja, Marinetti & Guinchard, and Echavarren have been suggested to abstract the chlorido ligand from the gold(I) center providing the cationic gold(I) species with a vacant coordination site.[28−32]

An alternative method to inter- or intramolecular halide abstraction employs positively charged ligands (Chart 1b).[33−39] The charge seems to form highly electrophilic gold centers, while the halide remains coordinated to the gold(I) ion. Sarkar et al. developed chlorido gold(I) precatalysts with ferrocenyl-substituted mesoionic carbene ligands ($\mathbf{F^{Ar}}$; Chart 1b).[33−35] Oxidation of $\mathbf{F^{Ar}}$ with acetylferrocenium tetrafluoroborate to the ferrocenium complex $[\mathbf{F^{Ar}}]^{\bullet+}$ yields the catalytically active species for the cyclization of *N*(2-propyn-1-yl)benzamide to 2-phenyl-5-vinylidene-2-oxazoline. The high activity of $[\mathbf{F^{Ar}}]^{\bullet+}$ was rationalized by the strongly electron-withdrawing character of the cationic mesoionic carbene ligand; however, a vacant coordination site at the two-coordinate gold(I) center is not easily conceivable. Similarly, Gabbaï placed a cationic fluorenylium, xanthylium, or acridinium substituent close to the gold(I) center achieving highly active catalysts by dative bonds ($[\mathbf{G}]^+$; Chart 1b) or noncovalent interactions ($[\mathbf{H}]^+$, $[\mathbf{I}]^+$; Chart 1b), apparently without chloride dissociation (Chart 1b).[36,37] With two positively charged cobaltoceniumyl substituents close to the gold center, Sarkar et al. developed a highly active catalyst $[\mathbf{J}]^{2+}$ (Chart 1b) without the need for addition of halide scavengers,

Received: September 12, 2023
Revised: December 19, 2023
Accepted: December 22, 2023
Published: January 8, 2024

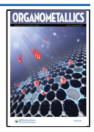

https://doi.org/10.1021/acs.organomet.3c00395
Organometallics 2024, 43, 69−84

Chart 1. Gold(I) Complexes Pertinent to the Current Study; (a) Self-Activating/Anion-Binding Pre-Catalysts A–E with N–H Hydrogen Bond Donors for Chloride Abstraction; (b) Catalysts with Positively Charged Ligands $[F^{Ar}]^{\bullet+}$–$[M^{R}]^{+}$, and (c) Cationic Gold(I) Catalysts $[2]^{\bullet+}$–$[4]^{\bullet+}$ with Redox-Active Aryl Units, N–H Hydrogen-Bond Donors and NMe_2 Functionalized Side Chains Investigated in the Present Study; Red Arrows Indicate Possible Flow of Electron Density; Black Arrows Indicate Possible Chloride Abstraction

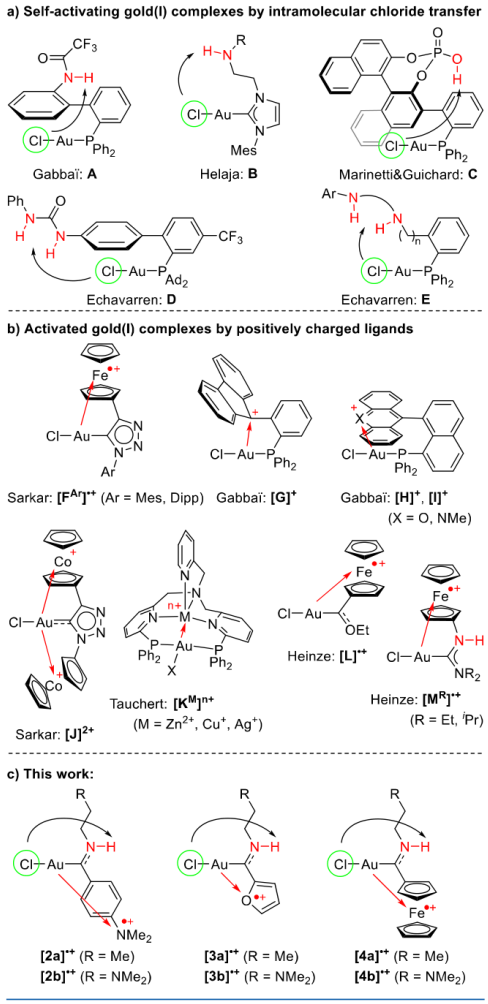

yet a vacant coordination site is not easily envisioned as well.[38] Furthermore, an induction period is observed pointing to some as-yet undiscovered self-activation mechanism.[38] Placing positively charged Lewis acids (M = Zn^{2+}, Cu^{+}, or Ag^{+}) close to a di(phosphane) gold(I) fragment $[K^{M}]^{n+}$ (Chart 1b), Tauchert observed high activity in the cycloisomerization of *N*(2-propyn-1-yl)benzamide. Yet weakly coordinating anions (X = OTf, NTf_2) or chloride scavengers are required (X = Cl).[39] The ligand scaffold suggests an electron-deficient T-shaped tricoordinate gold(I) center as the catalytically active site.

Peris et al. reported a ferrocenyl imidazolylidene gold(I) complex, which becomes active in the hydroamination of phenylacetylene with arylamines and in the cyclization of 2,5-dimethylfuran after oxidation with acetylferrocenium tetrafluoroborate.[40] However, protonated species, probably arising from traces of water, were detected after oxidation. These might be the active species in the catalytic reactions after chloride abstraction from gold(I) via hydrogen-bonding to the newly formed NH group (cf. self-activating gold(I) complexes, Chart 1a). The combination of ferrocenyl ligand oxidation by $[FcOAc][Al\{OC(CF_3)_3\}_4]$ and chloride abstraction by $Na[B\{C_6H_3(CF_3)_2\}_4]$ forms highly active cationic complexes for the hydroamination of alkynes as reported by Breher et al.[41] Clearly, activation of gold(I) precatalysts by ligand oxidation or cationic ligand side arms shows many facets and not all atomistic aspects are fully understood. Notably, gold(III) chloride $AuCl_3$ also transforms *N*(2-propyn-1-yl)benzamide to 2-phenyl-5-vinylidene-2-oxazoline, which further isomerizes to the 2,5-disubstituted oxazole under these conditions.[42] Consequently, both gold(I) and gold(III) derived precatalysts can be active for this transformation.

We reported the Fischer-type ferrocenyl ethoxycarbene gold(I) complex **L** (Chart 1b) as being active in the cyclization of *N*(2-propyn-1-yl)benzamide to 2-phenyl-5-vinylidene-2-oxazoline after oxidation to $[L]^{\bullet+}$ with the oxidant $[N(4\text{-}C_6H_4Br)_3][SbCl_6]$ (Magic Blue)[43,44] without requiring chloride scavengers.[45] No protonation to cationic complexes was observed. Instead an EPR-active species with a broad resonance around $g = 2.017$ forms quantitatively over time.[45] The increasing amount of EPR-active species correlates with the catalytic activity. As the EPR resonance is even observed at room temperature, the evolving EPR-active species is not a ferrocenium ion, which would be EPR-silent at room temperature.[46−51]

Magic Blue oxidizes the acyclic ferrocenyl diaminocarbene gold(I) complexes $\mathbf{M^R}$ to the respective ferrocenium ions $[M^R]^{\bullet+}$ (Chart 1b). These could be trapped by rapid freezing and EPR spectroscopically detected at low temperature.[52] At room temperature, these ferrocenium ions slowly convert to the species with the characteristic broad EPR resonance at $g \approx 2.014$.[52] This EPR-active species had been assigned to a persistent gold(II) radical with the unpaired electron occupying an orbital of mainly $5d_{x^2-y^2}$ character.[45,52] These proposed active gold(II) species are hence placed in between gold(I) and gold(III) catalysts.

Genuine mononuclear gold(II) complexes are, however, very rare[53−60] due to their propensity to dimerize via gold–gold σ bonds or to disproportionate into gold(III) and gold(I)/gold(0).[53,61−63] Radical addition to linearly coordinated gold(I) complexes can yield T-shaped gold(II) complexes,[64−82] which have been proposed as intermediates in thermal radical addition reactions and in photoredox catalytic cycles.[13,68−77] Gold(II) species $[Au(tpy)(OH_2)]^{2+}$ has been proposed to arise from hydrogen-atom transfer to the hydroxido gold(III) complex $[Au(tpy)(OH)]^{2+}$ (tpy = 2,2′:6′,2-terpyridine).[78] Gold(II) radicals $[Au^{II}X_3]^{-}$ were generated in the gas phase by Au–C bond homolysis from $[Au^{III}(CF_3)X_3]^{-}$ (X = F, Cl, Br) and a T-shaped geometry was

https://doi.org/10.1021/acs.organomet.3c00395
Organometallics 2024, 43, 69−84

assigned on the basis of quantum chemical calculations.[79] Computationally, neutral unsaturated AuX_2 species coordinate an additional X^- ligand to give $[Au^{III}X_3]^-$.[79] Yet, preparative isolation of three-coordinate gold(II) complexes had not been reported, and these are likely highly reactive, electrophilic and Lewis-acidic species.[64−82]

To elucidate the role of oxidizable units in the ligand for the activation of gold(I) precatalysts by their electron withdrawing or even electron accepting nature (Chart 1b) and the potential role of N−H groups for self-activation (Chart 1a), we report novel Fischer-type carbene gold(I)[83−85] precatalysts **2**−**4** (Chart 1c) for the cyclization of *N*(2-propyn-1-yl)benzamide to 2-phenyl-5-vinylidene-2-oxazoline. Importantly, these precatalysts can potentially be activated by oxidation of the oxidizable substituents dimethylanilinyl (4-DMA), 2-furyl, or ferrocenyl (Fc) to $[\mathbf{2}]^{\bullet+}$, $[\mathbf{3}]^{\bullet+}$, and $[\mathbf{4}]^{\bullet+}$, respectively. Additionally, the $[\mathbf{2b}]^{\bullet+}$, $[\mathbf{3b}]^{\bullet+}$, and $[\mathbf{4b}]^{\bullet+}$ derivatives possess basic and potentially coordinating dimethylamine side chains for stabilization of unsaturated gold intermediates, substrate coordination by hydrogen bonding or assistance in the protodeauration step.[86,87] The nature and reactivity of the resulting radical cations $[\mathbf{2}]^{\bullet+}$, $[\mathbf{3}]^{\bullet+}$, and $[\mathbf{4}]^{\bullet+}$ will be probed by cyclic voltammetry, EPR spectroscopy, kinetic studies, stopped-flow experiments, quantum chemical calculations, and catalytic experiments in comparison to a carbene gold(I) precatalyst **1** lacking oxidizable side chains, N−H, and NMe_2 groups. These mechanistic studies serve to arrive at a consistent mechanistic picture for the oxidative activation of Fischer-type carbene gold(I) precatalysts.

RESULTS AND DISCUSSION

Synthesis and Characterization. The targeted (aryl)(amino)carbene chlorido gold(I) complexes **2a**−**4b** were prepared starting from corresponding aryl ethoxycarbene pentacarbonyl tungsten complexes with aryl being 4-dimethylanilinyl (4-DMA), 2-furyl, or ferrocenyl (Fc) substituents.[83−85] Transmetalation to gold(I) with AuCl(tht) gives the gold(I) complexes **P2**−**P4** (Scheme 1, Figures S1−S4, Supporting Information; tht = tetrahydrothiophene). Subsequent aminolysis with *n*-propyl amine or *N*,*N*-dimethylethylenediamine yields **2a**−**4a** (R = Me) and **2b**−**4b** (R = NMe_2), respectively, in nearly quantitative yields (Scheme 1). The phenyl ethoxycarbene gold(I) complex **1**[88] lacking a redox active unit Ar, N−H moieties, and basic NMe_2 sites serves as a reference complex (Scheme 1; Figures S5 and S6, Supporting Information).

Scheme 1. General Scheme for the Synthesis of (Aryl)(amino)carbene Gold(I) Complexes 2a−4b from Aryl Ethoxycarbene Gold(I) Precursor Complexes P2−P3 and Reference Complex 1[88]

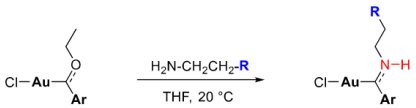

Ar	Ph	4-DMA	2-furyl	Fc
	1	**P2**	**P3**	**P4**

R \ Ar	4-DMA	2-furyl	Fc
Me	**2a**	**3a**	**4a**
NMe_2	**2b**	**3b**	**4b**

Gold(I) complexes **2**−**4** were characterized by NMR and IR spectroscopy, HR-ESI mass spectrometry, and elemental analyses (Figures S7−S21, Supporting Information). The chemical shifts of the carbene ^{13}C resonance of $\delta(^{13}C_{carbene})$ = 196.0/195.9 (**3a**/**3b**), 214.0/213.0 (**2a**/**2b**) and 216.7/215.8 ppm (**4a**/**4b**) correlate with the Tolman electronic parameter[89] (TEP) of the carbene ligands with Fc < 4-DMA < 2-furyl.[90,91] The 2-furyl substituent stabilizes the carbene p_π orbital best, while the ferrocenyl substituent is less involved in inductive or π-resonance stabilization of the p_π orbital. The pendant NMe_2 group has only a minor influence on $\delta(^{13}C_{carbene})$. Yet, the NMe_2 group exerts a moderate to strong effect on the NH proton resonance with $\delta(^1H_{NH})$ = 8.86/9.37 (**2a**/**2b**), 9.21/9.43 (**3a**/**3b**), and 8.29/9.11 ppm (**4a**/**4b**) in $CDCl_3$ (Figures S7, S9, S11, S13, S15 and S17, Supporting Information). The shift of $\delta(^1H_{NH})$ to lower field observed for the NMe_2 substituted complexes indicates hydrogen bonding of the NH group. In full agreement, the comparably sharp IR absorption bands of the N−H stretching vibrations of **2a**/**3a**/**4a** at $\tilde{\nu}_{NH}$ = 3333, 3318, and 3329 cm^{-1} in CH_2Cl_2 broaden to absorption bands of **2b**/**3b**/**4b** at $\tilde{\nu}_{NH}$ = 3266, 3273, and 3266 cm^{-1}, respectively, with the original N−H stretching bands diminished to weak shoulders (Figures S19−S21, Supporting Information). This further supports the formation of NH···NMe_2 hydrogen bonds of **2b**−**4b** in noncoordinating solvents.

Single crystals suitable for X-ray diffraction (Tables S1 and S2, Figures S22 and S23, Supporting Information) were obtained for ethoxy carbene gold(I) complexes **P2**−**P4** and the amino carbene gold(I) complexes **2a**, **2b**, **3a**, **4a**, and **4b** (Figure 1). The Au−$C_{carbene}$ bond lengths (1.982(4)−2.011(12) Å) fall within the range for gold(I) complexes with an sp^2-hybridized carbon trans to a chlorido ligand.[84,92−94] The $C_{carbene}$−N bond lengths [1.294(6)−1.338(15) Å] are indicative of a bond order larger than one. The amino carbene complexes exhibit the expected linear coordination of gold(I) with $C_{carbene}$−Au−Cl of 177.4(11)−179.8(14)° and a trigonal coordination of the carbene C atom with C_{ipso}−$C_{carbene}$−N bond angles between 116.0(3)−120.8(10)°. The more acute C_{ipso}−$C_{carbene}$−O bond angles of **P2**−**P4** ranging between 112.2(4)−114.6(13)° (Figure S22, Supporting Information) suggest a stronger π-donation of the amino substituent as compared to the ethoxy substituent. The (hetero)aryl rings lie approximately in the plane of the carbene ligand, except for **4a** and **2a** with C_α−C_{ipso}−$C_{carbene}$−N torsion angles of 28.2(6) and 18.6(6)°, respectively.

All amino carbene gold(I) complexes except **4b** lack Au···Au contacts with Au···Au distances being well above 4 Å. Instead these complexes display short intermolecular contacts between the amino group and the chlorido ligand of a neighboring complex with N···Cl distances of 3.294(4), 3.29(1), 3.298(4), and 3.265(4) Å for **2a**, **2b**, **3a**, and **4a**, respectively, indicative of NH···Cl hydrogen bonding (Chart 2a). These values are even shorter than the distance found for the diamino carbene complex $\mathbf{M}^{Et}$ in the solid state (3.402(4) Å, Chart 1).[52] The NMe_2 substituted complex **2b** possesses a short intramolecular N···N distance of 2.86(1) Å indicative of an intramolecular NH···N hydrogen bonding interaction in addition (Chart 2a).

Complex **4b** crystallized together with its hydrochloric acid adduct **[H-4b]Cl** in a 1:1 ratio with the NMe_2 substituent protonated to the ammonium group $NHMe_2^+$. **4b** and $[\mathbf{H\text{-}4b}]^+$ form gold(I)−gold(I) dimers with an Au1−Au2 distance of 3.0783(5) Å (Figure S23, Supporting Information). These dimers are connected to chains via intermolecular NH···N

https://doi.org/10.1021/acs.organomet.3c00395
Organometallics 2024, 43, 69−84

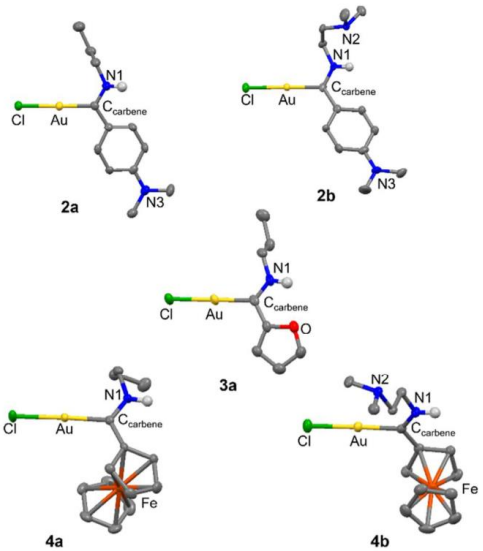

Figure 1. Partially labeled ellipsoid plots (50% probability) of complexes **2a**, **2b**, **3a**, **4a**, and **4b**. Solvent molecules and CH hydrogen atoms were omitted for clarity. Selected bond lengths (Å), bond angles (deg), and torsion angles (deg) for **2a** Au–$C_{carbene}$ 1.992(5), $C_{carbene}$–N 1.306(6), $C_{carbene}$–C_{ipso} 1.468(6), Au–Cl 2.308(11), $C_{carbene}$–Au–Cl 177.5(12), N–$C_{carbene}$–C_{ipso} 117.4(4), C_{α}–C_{ipso}–$C_{carbene}$–N 18.6(6); **2b** Au–$C_{carbene}$ 2.011(12), $C_{carbene}$–N 1.338(15), $C_{carbene}$–C_{ipso} 1.457(16), Au–Cl 2.299(3), $C_{carbene}$–Au–Cl 179.2(4), N–$C_{carbene}$–C_{ipso} 120.8(10), C_{α}–C_{ipso}–$C_{carbene}$–N 10.0(18); **3a** Au–$C_{carbene}$ 1.991(5), $C_{carbene}$–N 1.294(6), $C_{carbene}$–C_{ipso} 1.450(7), Au–Cl 2.294(12), $C_{carbene}$–Au–Cl 179.8(14), N–$C_{carbene}$–C_{ipso}) 116.6(4), C_{α}–C_{ipso}–$C_{carbene}$–N 4.3(6); **4a** Au–$C_{carbene}$ 1.982(4), $C_{carbene}$–N 1.310(5), $C_{carbene}$–C_{ipso} 1.447(5), Au–Cl 2.292(11), $C_{carbene}$–Au–Cl 177.4(11), N–$C_{carbene}$–C_{ipso} 116.0(3), C_{α}–C_{ipso}–$C_{carbene}$–N 28.2(6); **4b** Au–$C_{carbene}$ 2.000(3), $C_{carbene}$–N 1.300(4), $C_{carbene}$–C_{ipso} 1.454(5), Au–Cl 2.311(9), $C_{carbene}$–Au–Cl 178.6(9), N–$C_{carbene}$–C_{ipso} 117.0(3), C_{α}–C_{ipso}–$C_{carbene}$–N 3.7(5).

Chart 2. (a) Hydrogen Bonding Motifs Observed in the Solid State and in Solution and (b) Conceivable Hydrogen Bonding Interactions with the Substrate *N*(2-Propyn-1-yl)benzamide (Green) and Oxidative Activation of the Gold(I) Pre-Catalyst

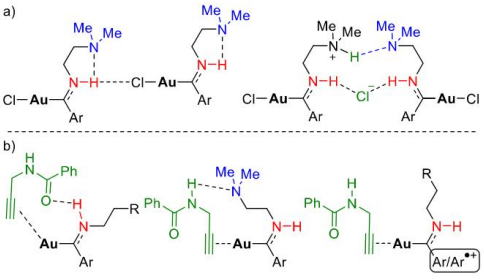

hydrogen bonds between $NHMe^{+}$ and NMe_2 groups with an N···N distance of 2.750(4) Å and via the additional chloride ion coordinated by two NH groups of the amino carbene ligands with N···Cl distances of 3.101(3) and 3.102(3) Å (Chart 2a).

These intra- and intermolecular interactions in the solid state confirm the possibility for NH substituents acting as intermolecular hydrogen bond donors to free and coordinated chloride ions and for NMe_2 substituents acting as hydrogen bond acceptors as already inferred from ^{1}H NMR and IR spectroscopy. NMe_2 substituents in these substituted amino carbene gold(I) complexes are even competent as Brønsted bases thanks to their high basicity [cf. $pK_b(NMe_3)$ = 4.2].[95] Consequently, it appears feasible that the substrate for cyclization to the oxazoline *N*(2-propyn-1-yl)benzamide can also interact with the gold(I) precatalyst via hydrogen bonding involving the NH_{amide} or the CO_{amide} moiety of the substrate (Chart 2b).

To probe the oxidative activation (Chart 2b), all gold(I) complexes **1**, **2a**–**4b** were investigated by cyclic voltammetry in CH_3CN with [^{n}Bu$_4$N][PF_6] as the supporting electrolyte (Figures S24–S30, Supporting Information). Only **4a** and **4b** show reversible oxidative waves at 0.31 and 0.34 V vs ferrocene, respectively (Figure 2). These are assigned to the

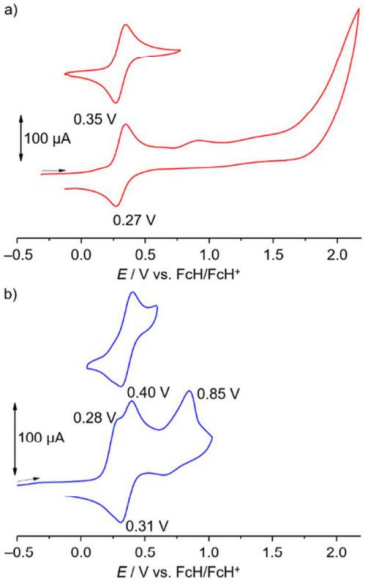

Figure 2. Cyclic voltammograms of (a) **4a** (red) and (b) **4b** (blue) in CH_3CN/[^{n}Bu$_4$N][PF_6]. The shoulder at 0.28 V possibly arises from partially protonated **4b** (vide supra) which disappears after consecutive scans (Figure S30, Supporting Information).

ferrocenium/ferrocene couple, with the potentials in between those of the ferrocenyl carbene complexes **L** (0.60 V) and $\mathbf{M}^{Et}$/$\mathbf{M}^{iPr}$ (0.105/0.115 V).[45,52] All other complexes are irreversibly oxidized with peak potentials E_p = ~1.0, 0.71, 0.44, 0.98, and 0.66 V for **1**, **2a**, **2b**, **3a**, and **3b**, respectively. Oxidation of gold(I) complexes is mostly irreversible, often leading to gold(III) species.[96−104] The significantly lower potentials of **2b** and **3b** as compared to **2a** and **3a** arise from the irreversible

https://doi.org/10.1021/acs.organomet.3c00395
Organometallics 2024, 43, 69−84

$NMe_2^{0/\bullet+}$ oxidation followed by deprotonation.[105] For comparison, NEt_3 is irreversibly oxidized in CH_3CN at 0.47 V.[44] Oxidation of the Ph, 4-DMA, and 2-furyl substituents seems to be irreversible as well and occurs at comparably high potentials. Nevertheless, activation for catalysis by oxidation with a strong oxidant[44,106,107] was attempted for all potential precatalysts **1**, **2a**–**4b**.

Oxidatively Induced Catalysis. The precatalysts **2a**–**4b**, the ethoxy carbene complex **1** without a side chain and *N*,*N*-dimethylethylenediamine (DMEN) mimicking the side arm of **2b**, **3b**, and **4b** (1 mol % loading) were employed in catalytic experiments with and without the oxidant $[N(4\text{-}C_6H_4Br)_3][SbCl_6]$ (Magic Blue, $E_{1/2}$ = 0.67 V, 1.25 mol %) as a cocatalyst in CH_2Cl_2. The cyclization of *N*(2-propyn-1-yl)benzamide to 2-phenyl-5-vinylidene-2-oxazoline served as the catalytic test reaction (Scheme 2, Table 1).

Scheme 2. Intramolecular Cyclization of *N*(2-Propyn-1-yl)benzamide to 2-Phenyl-5-vinylidene-2-oxazoline Catalyzed by Carbene Gold Pre-Catalysts and Magic Blue as Oxidant. No Chloride Scavenger Was Added

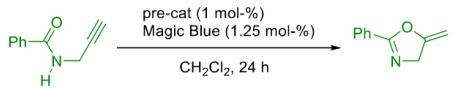

Table 1. Screening of Reaction Conditions[a]

entry	precatalyst	addition of Magic Blue	yield (%) after 24 h[a]
1	DMEN	–	0
2	DMEN	+	0
3[b]	**1**	+	2(2)
4[b]	**2a**	+	40(6)
5[b]	**2b**	+	71(0)
6[b]	**2b**	–	0
7[b]	**3a**	+	42(2)
8[b]	**3b**	+	71(1)
9[b]	**3b**	–	1(1)
10	**4a**	+	59(9)
11	**4a**	–	2(1)
12	**4b**	+	88(6)
13	**4b**	–	0
14	**4b** + Hg[c]	+	83

[a]Catalytic experiments were performed in duplicates, and standard deviations are indicated in parentheses. [b]Formation of a gold mirror on the reaction vessel surface was observed. [c]Excess Hg(l) was added to the reaction tube.

While DMEN and ethoxy derivative **1** gave essentially no conversion under these conditions (Table 1, entries 1–3), all amino carbene gold(I) precatalysts **2**–**4** catalyzed the reaction in the presence of the oxidant (Table 1, entries 4, 5, 7, 8, 10, 12). Notably the NMe_2-substituted precatalysts **2b**, **3b**, and **4b** were more active than the unsubstituted counterparts **2a**, **3a**, and **4a**, with yields increased from 40 to 71%, from 42 to 71% and from 59 to 88%, respectively (Table 1). No product formation is observed in the absence of oxidant (Table 1, 6, 9, 11, 13) suggesting that **2b**, **3b**, **4a**, and **4b** are not self-activating precatalysts (cf. examples shown in Chart 1a). This suggests that the N–H group of the amino carbenes is incompetent for chloride abstraction, possibly caused by the inappropriate position of the NH group (cf. Chart 1a and Figure 1).

Importantly, ethoxy carbene **1** and the 4-DMA and 2-furyl amino carbene derivatives **2** and **3** produced a gold mirror on the tube wall during the reaction. This suggests that gold nanoparticles[108−112] decorated with amino carbene ligands instead of a homogeneous catalytic active species might be the catalytically active species. On the other hand, no gold mirror or gold precipitate is observed with the ferrocenyl substituted precatalysts **4a** and **4b** substantiating the formation of a molecular catalytically active species. Addition of mercury (mercury poisoning test)[113] does not significantly reduce the yields of the **4b**/oxidant catalyzed reaction confirming the homogeneous nature of the catalytically active species (Table 1, entries 12/14).

Attempts to regenerate the reduced precatalysts **2b** and **3b** employing the reductant decamethylferrocene $FeCp_2^*$ (1.05 equiv; $E_{1/2}$ = −0.48 V[44]) in the absence or presence of the substrate yielded only complex mixtures including the amides $ArC(O)NHCH_2CH_2NMe_2$ (Ar = 4-DMA, 2-furyl). This liberation and oxidation of the carbene ligand is consistent with the irreversible oxidation of **2b** and **3b** observed in the cyclic voltammograms (Figures S26 and S28, Supporting Information) and the formation of a gold mirror during catalysis. On the other hand, the ferrocenyl complex **4a** was successfully regenerated after the catalytic reaction by reduction with decamethylferrocene $FeCp_2^*$ (1.05 equiv) according to ^{1}H NMR spectroscopy in 92 ± 5 spectroscopic yield (Figure S31, Supporting Information) in agreement with the reversible oxidation and the mercury poisoning test.

Consequently, the ferrocenyl precatalysts **4a** and **4b** essentially retain their structural integrity during the catalysis. However, as no chloride scavenger has been added, the gold(I) center remains coordinated by the chlorido ligand and binding of the alkinyl substrate to the linearly coordinated gold(I) center appears difficult. This contradicts the observed high activity of **4a** and **4b** in the presence of the oxidant (Table 1). To investigate this discrepancy, we spectroscopically investigated the outcome of the oxidation of **4a** and **4b** with various oxidants.

Mechanistic Investigations. Stopped-flow kinetics of the reaction of **4a**/**4b** with Magic Blue were recorded to probe the initial oxidation event and potential follow-up reactions in CH_2Cl_2 at 22 °C and −90 °C, respectively (Figure 3 for **4b** and Figure S32 for **4a**, Supporting Information).

In all cases, the characteristic absorption band of Magic Blue at 728 nm (Figure S33, Supporting Information) has completely vanished already after the mixing time. This suggests that the electron transfer from **4a**/**4b** to $[N(4\text{-}C_6H_4Br)_3]^{\bullet+}$ is faster than the dead time of the stopped-flow spectrometer (0.7 ms). The electron transfer gives rise to the cations $[\mathbf{4a}]^{\bullet+}$ and $[\mathbf{4b}]^{\bullet+}$, respectively, with a characteristic absorption band at 480 nm (Figure 3). According to time-dependent DFT calculations on $[\mathbf{4a}]^{\bullet+}$, this band possesses gold(I) to iron(III) charge transfer character (Figure S32c, Supporting Information). The band persists up to 40 ms at −90 °C (Figure 3b), while at 22 °C, this band loses intensity and a new band at 353 nm appears (Figure 3a). Consequently, a slower, thermally activated follow-up reaction takes place after the fast initial electron transfer at room temperature.

Oxidation of ferrocenyl carbene complexes **4a** and **4b** with the oxidant $[N(4\text{-}C_6H_4Br)_3]^{\bullet+}$ in THF bleached the sharp EPR resonance of $[N(4\text{-}C_6H_4Br)_3]^{\bullet+}$ at g = 2.016.[52] Initially, no other EPR-active species is detected, yet over minutes, broad EPR resonances appear at g = 2.021 and 2.028, respectively

https://doi.org/10.1021/acs.organomet.3c00395
Organometallics 2024, 43, 69−84

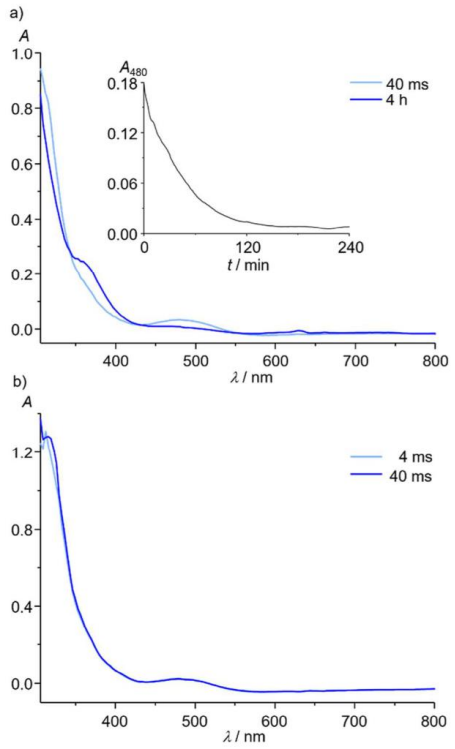

Figure 3. (a) UV−vis spectra of **4b** in CH_2Cl_2 recorded (a) at 22 °C 40 ms (light blue) and 4 h (blue) after mixing with Magic Blue including a time trace observed at λ = 480 nm (inset) and (b) at −90 °C 4 ms (light blue; essentially identical to the 40 ms trace) and 40 ms (blue) after mixing with Magic Blue.

(Figures 4a,b and S34 and S35, Supporting Information). These resonances are very similar to those obtained for the cationic complexes $[\mathbf{K}]^{\bullet+}$ and $[\mathbf{L}^{R}]^{\bullet+}$ with g = 2.017 and 2.014, respectively (Chart 1b).[45,52] In CH_2Cl_2 solution, the EPR resonances of the radical cations derived from **4a** and **4b** are much broader suggesting some aggregation phenomena and solubility issues associated with this solvent (Figures S36 and S37, Supporting Information).

As ferrocenium ions are generally EPR-silent at room temperature,[46−51] the broad resonances are assigned to different paramagnetic species generated from the initially formed ferrocenium cations $[\mathbf{L}]^{\bullet+}$, $[\mathbf{M}^{R}]^{\bullet+}$, $[\mathbf{4a}]^{\bullet+}$, and $[\mathbf{4b}]^{\bullet+}$.[45,52] A slow intramolecular electron transfer (valence isomerization) from gold(I) to iron(III) had been suggested resulting in a gold(II)/iron(II) character of the paramagnetic EPR-active species.[45,52] As ferrocene possesses a diamagnetic low-spin iron(II) ion, the unpaired electron is essentially localized at the gold center. We note that complexes **1**−**3** do not furnish any detectable X-band EPR resonances after oxidation with Magic Blue initially to the reactive and unstable radical cations $[\mathbf{1}]^{\bullet+}$−$[\mathbf{3}]^{\bullet+}$ suggesting that the gold nanoparticles formed after oxidation of **1**−**3** are EPR-silent.[114,115]

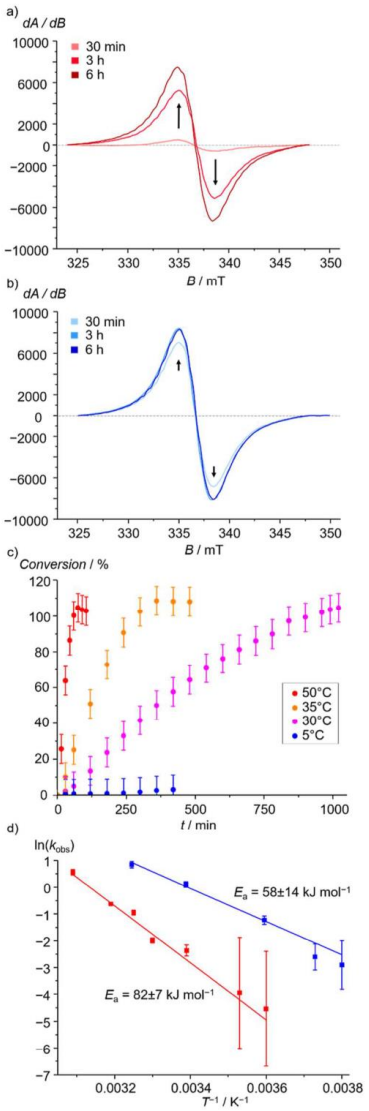

Figure 4. EPR spectra of (a) **4a** and (b) **4b** with Magic Blue added in THF at 22 °C and time delays 0.5, 3, and 6 h. (c) Plot of the doubly integrated intensity of the EPR resonance versus time at selected temperatures for **4a**. (d) Arrhenius plots of the observed zeroth-order rate constant k_{obs}, for the reaction of **4a** and **4b** with Magic Blue in THF.

Using different oxidants (aminiumyl radical cations in $[N(4\text{-}C_6H_4Br)_3][SbCl_6]$, thianthrenium radical cations in $[C_{12}H_8S_2][SbCl_6]$ or $[C_{12}H_8S_2][PF_6]$ and cerium(IV) ions in ceric ammonium nitrate $[NH_4]_2[Ce(NO_3)_6]$)[44,106,107] deliver essentially identical EPR signatures, confirming that the

https://doi.org/10.1021/acs.organomet.3c00395
Organometallics 2024, 43, 69−84

resonances arise from the oxidized gold complexes and not from oxidant-derived species (Figures S34–S37, Supporting Information). Similar to the oxidation with $[N(4\text{-}C_6H_4Br)_3]^{\bullet+}$, the sharp EPR resonance of the thianthrenium radical cation $[C_{12}H_8S_2]^{\bullet+}$ of $[C_{12}H_8S_2][PF_6]$ at g = 2.016 has completely vanished confirming the successful and quantitative oxidation also with these oxidants (Figure S38, Supporting Information).

Addition of potentially coordinating chloride anions (1 equiv) as $[^nBu_4N]Cl$ to the oxidation experiment of **4a** with $[C_{12}H_8S_2][PF_6]$ did not inhibit the formation of the EPR-active species (Figure S36, Supporting Information). This suggests that chloride dissociation from $[\mathbf{4a}]^{\bullet+}$ is an unlikely pathway in this case. In contrast, Nataro et al. observed Cl^- loss instead of oxidation for $(Au^ICl)_2(P \cap P)$ after treatment with $[N(4\text{-}C_6H_4Br)_3][B(C_6F_5)_4]$ to yield $[Au^I_2(\mu\text{-}Cl)(P \cap P)][B(C_6F_5)_4]$ (P ∩ P = various 1,1′-bis(phosphano)ferrocene ligands).[116] On the other hand, treatment of **4a** with $[N(4\text{-}C_6H_4Br)_3][Al\{OC(CF_3)_3\}_4]$ yielded no significant amounts of EPR-active species.

This series of various oxidant salts suggests that at least a weakly coordinating anion X^- = $[SbCl_6]^-$, $[PF_6]^-$, $[NO_3]^-$ or Cl^- is required for the development of the EPR-active species from the initially formed ferrocenium cation $[\mathbf{4a}]^{\bullet+}$. In the following, we denote this EPR-active, anion-dependent species **4a-X**. For $[\mathbf{4b}]^{\bullet+}$, coordination of a counterion (**4b-X**) or the NMe_2 group $[\mathbf{4b'}][X]$ is conceivable.

At this point, we summarize that electron transfer from **4a** or **4b** to various oxidants is fast, initially yielding EPR-silent ferrocenium ions $[\mathbf{4a}]^{\bullet+}$ and $[\mathbf{4b}]^{\bullet+}$. EPR-active molecular species **4a-X** and **4b-X**/$[\mathbf{4b'}][X]$ form over time in a follow-up reaction. **4a-X** and **4b-X**/$[\mathbf{4b'}][X]$ form independently from the type of oxidant. This reaction is rather slow and hence an appreciable activation barrier is associated with it.

To study this activation barrier, we measured the rates of the total reaction of **4a**/**4b** with Magic Blue to the EPR-active species **4a-X** and **4b-X**/$[\mathbf{4b'}][X]$ in THF at various temperatures (−10 to +50 °C) using quantitative EPR spectroscopy (double integration calibrated with $Cu^{II}(TPP)$, TPP^{2-} = *meso*-tetraphenylporphyrinato(2−); Figure 4c; Figures S39 and S40, Supporting Information).[117] The NMe_2-substituted complex **4b** reacts faster than **4a** (Figures 4, S41 and S42, Supporting Information) confirming an accelerating effect of the NMe_2 substituent.

Within the experimental uncertainty of the EPR double integration technique, complexes **4a** and **4b** reach quantitative conversion within 1000 min at 30 °C and within 400 min at 5 °C, respectively (Figures 4, S41 and S42, Supporting Information). Formation of the EPR-active species is linear with time almost up to consumption of all material. This behavior corresponds to a reaction of (pseudo)zeroth order ($d[\mathbf{4\text{-}X}]/dt = k_{obs}$).[118] Arrhenius plots of the temperature dependence of the observed rate constant $\ln(k_{obs}) = \ln A - E_a/RT$ of the reaction of **4a**/**4b** with Magic Blue are linear over the observed temperature ranges giving activation barriers E_a = 82 ± 7 and 58 ± 14 kJ mol^{-1}, respectively (Figure 4d). The smaller barrier for **4b** confirms the positive influence of the pendant NMe_2 group for the formation of the EPR-active species **4b-X**/$[\mathbf{4b'}][X]$ in agreement with its higher catalytic activity (Table 1). The experimental (pseudo)zeroth order rate law indicates that a pre-equilibrium is rate-determining followed by a faster follow-up reaction. The barriers obtained are thus associated with the rate-determining step of this pre-equilibrium. Such a mechanistic scenario has been found, for example, for the iodination of acetone, where the tautomerization to the enol of acetone is rate-determining and the overall rate is independent of iodine and acetone concentrations.[119,120]

As the initial oxidation of **4a** and **4b** to the ferrocenium ions $[\mathbf{4a}]^{\bullet+}$ and $[\mathbf{4b}]^{\bullet+}$ is very fast (vide supra), these ferrocenium cations $[\mathbf{4a}]^{\bullet+}$ and $[\mathbf{4b}]^{\bullet+}$ are likely involved in the pre-equilibrium. Furthermore, we suggest that the counterions X^- of the oxidant plays a role for $[\mathbf{4a}]^{\bullet+}$ as the very weakly coordinating anion $[Al\{OC(CF_3)_3\}_4]^-$ does not support the formation of the EPR-active species **4a-X**, while $[SbCl_6]^-$, $[PF_6]^-$, or $[NO_3]^-$ do. Coordinating Cl^- ions do not inhibit the formation of the EPR-active species **4a-X** and **4b-X**/$[\mathbf{4b'}][X]$.

A minimal model (Scheme 3) accounting for the experimental data consists of a slow, reversible valence-isomerization of the initially formed ferrocenium ions $[\mathbf{4a}]^{\bullet+}$/$[\mathbf{4b}]^{\bullet+}$ to $Au^{II}Fe^{II}$ valence isomers **4a-X** and $[\mathbf{4b'}][X]$ initiated by counteranion or NMe_2 coordination to the gold center. In agreement with the lower activation barrier, $[\mathbf{4b'}][X]$ forms faster than **4a-X** thanks to the chelate assistance of the NMe_2 substituent (Scheme 3). These species

Scheme 3. Proposed Mechanism for the Oxidative Activation of Ferrocenyl Substituted Amino Carbene Gold(I) Pre-Catalysts 4a and 4b to Ferrocenium Cations $[\mathbf{4a}]^{\bullet+}$/$[\mathbf{4b}]^{\bullet+}$ Followed by a Slow Au^IFe^{III}/$Au^{II}Fe^{II}$ Valence Isomerization by Coordination of X^- or the NMe_2 Group Giving the EPR-Active and Catalytically Competent Gold(II) Species 4a-X and $[\mathbf{4b'}][X]$; One-Electron Reduction and Dissociation of X^- Regenerates 4a and 4b, Respectively

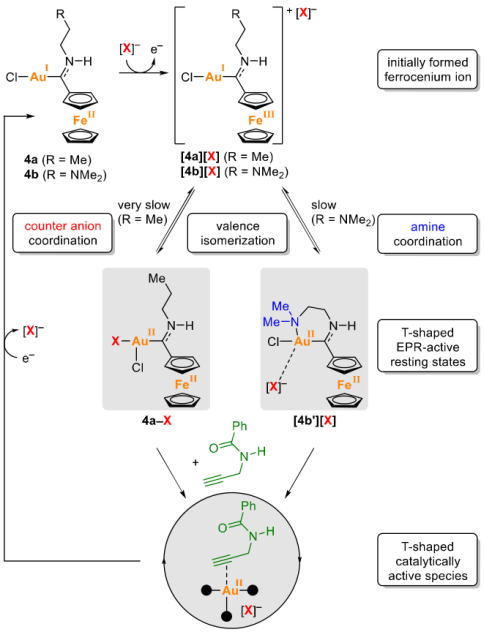

https://doi.org/10.1021/acs.organomet.3c00395
Organometallics 2024, 43, 69−84

are proposed to act as catalytically active molecular species. Rereduction likely dissociates the anion X^- and the NMe_2 donor reforming **4a** and **4b**, respectively, with two-coordinate gold(I) centers (Scheme 3) as observed experimentally for **4a** (Figure S31, Supporting Information).

Consistent with our mechanistic model involving $Au^{II}Fe^{II}$ valence isomers, a related (ferrocenyl oxazoline) palladium(II) complex is oxidized by silver(I) salts to EPR-active d^7 palladium(III) species instead of the initially assumed oxidation of the ferrocenyl moiety.[121] A chlorido (ferrocenyl oxazoline) gold(I) complex is also oxidized by $AuCl(SMe_2)$ at the gold ion instead of the ferrocenyl substituents, yet a diamagnetic gold(II) dimer with a gold−gold σ-bond forms.[122,123] Such a dimerization to diamagnetic species does not seem to play a major role in the present case as spin quantification suggests essentially quantitative formation of EPR-active species (Figure 4c). In order to identify the nature of potential EPR-active $Au^{II}Fe^{II}$ valence isomers of $[\mathbf{4a}]^{\bullet+}$ and $[\mathbf{4b}]^{\bullet+}$ in the absence and presence of coordination anions X^-, we turned to quantum chemical calculations.

Density Functional Theory Calculations. All open-shell species were optimized on the UB3LYP/def2-TZVP level of theory including relativistically adjusted basis sets, dispersion correction, and a solvent model. Mulliken spin population analyses were used to identify the localization of the electron hole in the radical cations $[\mathbf{1}]^{\bullet+}$−$[\mathbf{4}]^{\bullet+}$. In $[\mathbf{1}]^{\bullet+}$, the spin density is distributed over Au, Cl, and the phenyl carbene unit, while in $[\mathbf{2a}]^{\bullet+}$ and $[\mathbf{3a}]^{\bullet+}$, the spin density is more localized on the DMA and furyl substituents (Figure S43, Supporting Information). A larger spin density at the gold center is accompanied by a larger deviation from a linear Cl−Au−C coordination.

The NMe_2 substituted complexes $[\mathbf{2b}]^{\bullet+}$ and $[\mathbf{3b}]^{\bullet+}$ localize most spin density on the NMe_2 moiety (Figure 5). This is consistent with the assignment of the oxidative redox waves of **2b** and **3b** in the cyclic voltammograms to the irreversible $NMe_2^{\bullet+/0}$ oxidations (vide supra). Coordinating the NMe_2 group of $[\mathbf{2b}]^{\bullet+}$ and $[\mathbf{3b}]^{\bullet+}$ to the gold center forming a six-membered chelate ring and a T-shaped coordination geometry at the gold is favored by a few kJ mol^{-1} leading to sharing of the spin density between gold and NMe_2 ($[\mathbf{2b'}]^{\bullet+}$ and $[\mathbf{3b'}]^{\bullet+}$; Figure 5). Yet this thermodynamically only slightly favored coordination $[\mathbf{2b'}]^{\bullet+}$ and $[\mathbf{3b'}]^{\bullet+}$ apparently cannot compete with the irreversible deprotonation and decomposition of the unstable $NMe_2^{\bullet+}$ radical cation substituent of $[\mathbf{2b}]^{\bullet+}$ and $[\mathbf{3b}]^{\bullet+}$.[105]

The radical cations $[\mathbf{4a}]^{\bullet+}$ and $[\mathbf{4b}]^{\bullet+}$ are genuine and stable ferrocenium ions according to the spin density distribution (Figure 6) as expected and in agreement with the EPR-silent character at room temperature. Coordination of the NMe_2 group of $[\mathbf{4b}]^{\bullet+}$ to the gold center forms a six-membered chelate ring and a T-shaped coordination geometry at the gold center ($[\mathbf{4b'}]^{\bullet+}$). Importantly, the amine coordination shifts the spin density to gold forming the $Au^{II}Fe^{II}$ valence isomer (Figure 6). However, this valence isomer $[\mathbf{4b'}]^{\bullet+}$ is destabilized by 36 kJ mol^{-1} relative to the $Au^{I}Fe^{III}$ valence isomer $[\mathbf{4b}]^{\bullet+}$ (Figure 6) and hence should not be present in high yields.

Adding the counterions hexachloroantimonate, hexafluorophosphate, and nitrate (experimentally introduced with the cationic oxidants $[N(4\text{-}C_6H_4Br)_3][SbCl_6]$, $[C_{12}H_8S_2][SbCl_6]$, $[C_{12}H_8S_2][PF_6]$, and $[NH_4]_2[Ce(NO_3)_6]$) to $[\mathbf{4a}]^{\bullet+}$ and $[\mathbf{4b'}]^{\bullet+}$ yields the gold(II) complexes **4a-X**/**4b-X** and

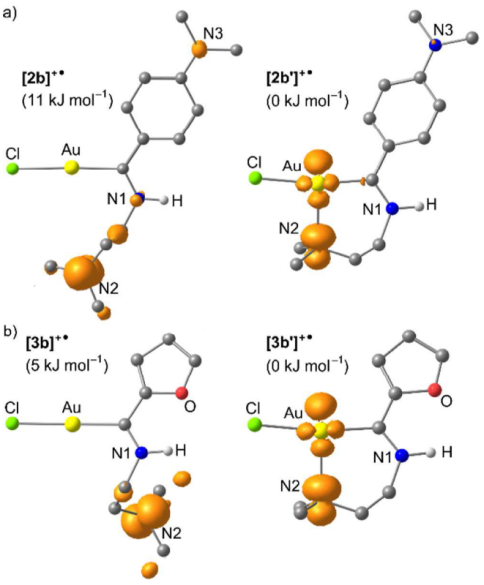

Figure 5. DFT-optimized geometries and spin densities of (a) $[\mathbf{2b}]^{\bullet+}$/$[\mathbf{2b'}]^{\bullet+}$ and (b) $[\mathbf{3b}]^{\bullet+}$/$[\mathbf{3b'}]^{\bullet+}$. Spin densities are displayed in orange at a contour value of 0.01 a.u.; CH hydrogen atoms omitted.

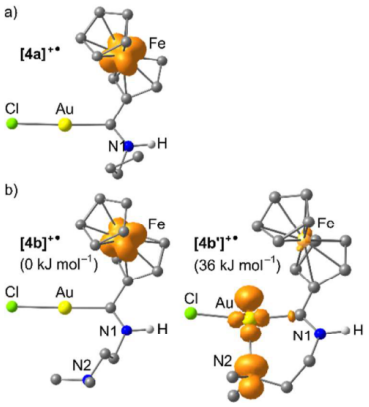

Figure 6. DFT-optimized geometries and spin densities of $[\mathbf{4a}]^{\bullet+}$, $[\mathbf{4b}]^{\bullet+}$, and $[\mathbf{4b'}]^{\bullet+}$. Spin densities are displayed in orange at a contour value of 0.01 a.u.; CH hydrogen atoms omitted.

$[\mathbf{4b'}][\mathbf{X}]$ with X^- = $[SbCl_6]^-$, $[PF_6]^-$, and $[NO_3]^-$ (Figure 7). For **4a-X**/**4b-X**, the Au−Cl, Au−F, and Au−O distances amount to 2.468/2.452, 2.251/2.259, and 2.133/2.140 Å, respectively, suggesting a true bonding interaction (Figure 7a,b). Notably, the X^- anions coordinate trans to the carbene, while attempts to coordinate the anion in cis position lead to dissociation of X^-. Again, the resulting spin density of the $Au^{II}Fe^{II}$ valence isomers **4a-X**/**4b-X** is not exclusively located at the gold(II) center (Mulliken spin densities of 0.40−0.43)

https://doi.org/10.1021/acs.organomet.3c00395
Organometallics 2024, 43, 69−84

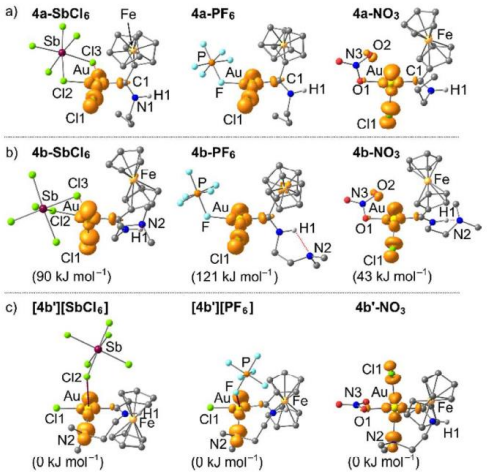

Figure 7. (a) DFT-optimized geometries of (a) **4a-X**, (b) **4b-X**, and (c) [**4b′**][**X**]/**4b′-NO$_3$** with X$^-$ = [SbCl$_6$]$^-$, [PF$_6$]$^-$, and [NO$_3$]$^-$. Spin densities are displayed in orange at a contour value of 0.01 a.u.; CH hydrogen atoms omitted.

but also partially delocalized over the chlorido ligand (Mulliken spin densities of 0.34−0.36) and the $C_{carbene}$ atom (Mulliken spin densities of 0.11−0.17) (Figure 7a,b).

Coordinating the NMe_2 group in [**4b′**][**SbCl$_6$**] and [**4b′**][**PF$_6$**] substitutes the anion forming ion pairs of T-shaped gold cations with the anions located at Au···Cl and Au···F distances of 3.21 and 3.30 Å, respectively (Scheme 3, Figure 7c). These chelate structures are strongly stabilized relative to **4b-X** by 90 and 121 kJ mol^{-1} for X$^-$ = [SbCl$_6$]$^-$ and [PF$_6$]$^-$, respectively. The spin density is shared between the gold and nitrogen atom of the coordinated NMe_2 group with Mulliken spin densities of 0.39−0.41 and 0.38−0.40, respectively), similar to [**2b′**]$^{\bullet+}$, [**3b′**]$^{\bullet+}$, and [**4b′**]$^{\bullet+}$ (Figures 5 and 6). In contrast to the weakly coordinating [SbCl$_6$]$^-$ and [PF$_6$]$^-$ anions, the nitrate remains coordinated *trans* to the carbene in **4b′-NO$_3$** with an Au−O distance of 2.167 Å giving an approximately square-planar four-coordinate gold(II) ion. The NMe_2 chelation in **4b′-NO$_3$** is favored by 43 kJ mol^{-1} as compared to **4b-NO$_3$**. The spin density is shared between the gold center and the coordinated chlorine, nitrogen, carbon, and oxygen atoms with Mulliken spin densities of 0.40, 0.22, 0.20, 0.11, and 0.03 respectively.

In order to follow the anion coordination and gold → iron electron transfer computationally, we chose a chloride ion Cl$^-$(*cis*) approaching the gold center of [**4a**]$^{\bullet+}$ as a well-defined reaction coordinate (Au···Cl$^-$(*cis*) distance; Figure 8). The monatomic chloride anion eliminates complications through further degrees of freedom, which would arise from multiatomic anions such as [SbCl$_6$]$^-$, [PF$_6$]$^-$, and [NO$_3$]$^-$. As the calculated energies along this pathway merely reflect the intramolecular modes and neglect the solvent motion, in particular, the entropic changes, when polar solvent molecules are released from the solvent shell around anion and cation, we refrain from discussing the calculated energy values and merely focus on the intramolecular structural changes along the Cl$^-$(*cis*) coordination/dissociation pathway and the electron

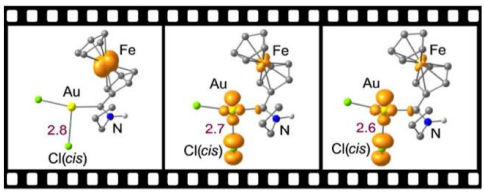

Figure 8. Schematic of the electron transfer coordinate of [**4a**]$^{\bullet+}$ + Cl$^-$(cis) → **4a-Cl** illustrated by the spin density plots calculated at defined Au···Cl$^-$(cis) distances. Spin densities are displayed in orange at a contour value of 0.01 a.u.; CH hydrogen atoms omitted.

hole position derived from a spin population analysis (Figure 8).[124]

In the absence of X$^-$ (Figure 6a, [**4a**]$^{\bullet+}$) and at Au···Cl$^-$(*cis*) distances above 2.8 Å (Figure 8), the Fe−$Cp_{centroid}$ distances of 1.73/1.72 Å correspond to typical calculated distances of ferrocenium ions.[49−51] The Au−Cl and Au−C distances in [**4a**]$^{\bullet+}$ amount to 2.32 and 1.99 Å, respectively, typical for gold(I) complexes. Upon approaching the additional Cl$^-$(cis) to the gold center from 2.8 to 2.6 Å, the Au−Cl and Au−C distances slightly increase to 2.344 and 2.017 Å, respectively. Importantly, the shortened Fe−$Cp_{centroid}$ distances of 1.678/1.668 Å correspond to typical values calculated for ferrocenes.[49−51] In agreement with the characteristic structural changes at the iron center, the Mulliken spin density of 1.27 in the ferrocenium ion [**4a**]$^{\bullet+}$ is reduced to 0.05 in the ferrocene valence isomer **4a-Cl** at 2.6 Å distance (Figure 8). Concomitantly, the spin density at gold has increased from zero to 0.39 in **4a-Cl** at 2.6 Å distance (Figure 8). The spin density is further distributed over the coordinated Cl$^-$(cis) and carbon atoms (0.04, 0.11). This spin evolution substantiates the reaction coordinate with an approaching X$^-$ ion as suitable electron transfer coordinate (within the limits of neglecting the explicit solvent reorganization).

The possible dimerization of the T-shaped radical **4a-ONO$_2$** (Figure 7a) via formation of a gold(II)−gold(II) σ-bond in the three possible isomeric configurations of (**4a-ONO$_2$**)$_2$ has been probed computationally. Figure 9 displays the most stable

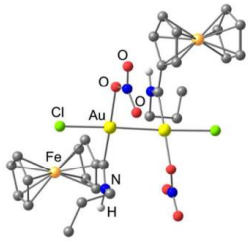

Figure 9. DFT-optimized geometry of the most stable diamagnetic dimer **SP-4-2-(4a-ONO$_2$)$_2$** with a gold−gold σ-bond.

isomer **SP-4-2-(4a-ONO$_2$)$_2$**; the two other dimers derived from SP-4-3 and SP-4-4 isomers which are 11 and 119 kJ mol^{-1} higher in energy are shown in Figure S44 (Supporting Information). In the **SP-4-2-(4a-ONO$_2$)$_2$** dimer, the Au−Au distance amounts to 2.624 Å (Figure 9). For comparison, the reported chlorido (ferrocenyl oxazoline) gold(II) *syn*/*anti*

https://doi.org/10.1021/acs.organomet.3c00395
Organometallics 2024, 43, 69−84

dimers possess shorter Au−Au distances of 2.565/2.533 Å.[122] The bond dissociation energy of the most stable **SP-4-2-(4a-ONO$_2$)$_2$** isomer to give two **4a-ONO$_2$** is calculated as 103 kJ mol^{-1} (neglecting entropic contributions). The reported bond dissociation energy of a [Au^{II}C^N^C()]$_2$ complex neglecting entropic contributions is with 198 kJ mol^{-1} almost twice as large.[62]

In spite of the sizable calculated bond dissociation energy of **SP-4-2-(4a-ONO$_2$)$_2$** (neglecting entropic contributions), dimerization seems to be only a minor pathway for **4a-X** and **4b-X** as the EPR yield of the paramagnetic species is quantitative within uncertainty and hence the formation of diamagnetic dimers appears negligible. Possibly, a coordinated solvent molecule, the coordinated NMe$_2$ group in **4b′-X**, or a semichelating [SbCl$_6$]$^-$ anion in **4a-SbCl$_6$** and **4b-SbCl$_6$** with a longer Au···Cl distance around 3.0 Å (Figure 7) gives a square-planar gold(II) coordination environment that prevents dimerization of the gold(II) radicals. This situation resembles the geometric and electronic structure of Au^{II}(TPP) with the $5d_{x^2-y^2}$ orbital of the gold(II) ion carrying the major spin density and the porphyrin's N atoms carrying minor fractions, thereby efficiently inhibiting dimerization.[54]

Discussion of the Proposed Mechanism. With the proposed mechanistic picture for the ferrocenyl precatalysts **4a** and **4b** depicted in Scheme 3, the role of the reversible ferrocenium ferrocenyl redox couple is to provide a stable hole reservoir, which slowly oxidizes the gold(I) center to T-shaped gold(II) with the aid of coordinating anions X$^-$ and chelating NMe$_2$ groups (for **4b**) giving **4a-X** and [**4b′**][**X**]. Consequently, the proposed active species **4a-X** and [**4b′**][**X**] form in the presence of coordinating anions X$^-$. This contrasts the conventional gold(I) catalysis requiring the scavenging of coordinating chloride anions to form the catalytically active species [Au^I(L)]$^+$.[19−27] The ferrocenium hole reservoir prevents irreversible nanoparticle formation as found for organic 4-DMA and 2-furyl substituents in **2a**, **2b**, **3a**, and **3b** and allows regeneration of the precatalyst by reduction as also observed for the **L**/[**L**]$^{\bullet+}$ redox couple (Chart 1b) showing redox-switchable catalysis.[45]

The role of the NMe$_2$ group in **4b** might primarily be assisting the gold(II) formation by chelation lowering the barrier for valence isomerization (Scheme 3). Furthermore, the proposed catalytically active T-shaped gold(II) species are cationic for [**4b′**]$^{\bullet+}$ but neutral for **4a-X**, which might increase their electrophilicity. Additionally, hydrogen bonding and eventually deprotonation of the substrate's amide group as well as assistance with the protodeauration step[86,87] might occur during catalysis after dissociation from gold(II) (Chart 2b). The observation of protonated **4b** in single crystals corroborates this possibility. All these features of the NMe$_2$ group in **4b** might serve to explain the better catalytic performance of **4b** as compared to **4a**.

On the other hand, the N−H group of the amino substituted carbenes **2**−**4** does not seem to be actively involved in the formation of catalytically active species as the ethoxy carbene complex **L** is also active after oxidation and as **2**−**4** are not self-activating in contrast to catalysts **A**−**E** (Chart 1a).

CONCLUSIONS

(Aryl)(amino)carbene chlorido gold(I) complexes **2**−**4** with 4-dimethylanilinyl (4-DMA), 2-furyl, or ferrocenyl (Fc) substituents and amino side arms with (**2b**, **3b**, and **4b**) and without a pendant NMe$_2$ group (**2a**, **3a**, and **4a**) catalyze the ring closure reaction of *N*(2-propyn-1-yl)benzamide to 2-phenyl-5-vinylidene-2-oxazoline after oxidation without requiring chloride scavengers. Precatalysts with 4-DMA and 2-furyl substituents (**2a**, **2b**, **3a**, and **3b**) are only irreversibly oxidized and form gold mirrors during catalysis suggesting ligand dissociation, gold nanoparticle formation, and hence a heterogeneous catalytic reaction. The ferrocenyl substituted precatalysts **4a** and **4b** are reversibly oxidized to the ferrocenium cations [**4a**]$^{\bullet+}$ and [**4b**]$^{\bullet+}$, respectively. Initiated by anion X$^-$ or NMe$_2$ coordination, a slow valence isomerization of the initially formed Au^{I}Fe^{III} isomers to the EPR-active and catalytically active Au^{II}Fe^{II} isomers **4a-X** and [**4b′**][**X**] follows with barriers of E_a = 82 ± 7 and 58 ± 14 kJ mol^{-1}, respectively. These species retain their structural integrity and molecular nature. Coordination of the NMe$_2$ substituent to the gold center lowers the barrier for the valence isomerization compared to anion-assisted valence isomerization and provides cationic active T-shaped species. The hemilabile and basic NMe$_2$ group of **4b**/**4b-X** might additionally serve to bind the substrate by hydrogen bonding and to assist in the protodeauration step explaining the higher activity of precatalyst **4b** as compared to **4a**.

In summary, one-electron oxidative activation of chlorido (ferrocenyl)(amino)carbene gold(I) precatalysts to homogeneous molecular active species circumvents the need for chloride scavengers to form the classical active species [Au^I(L)]$^+$. Instead, T-shaped gold(II) σ-radicals form in the presence of X$^-$ or chelating NMe$_2$ side arms as a novel type of active species for the cyclization reaction complementing the known cationic gold(I) and gold(III) catalysts. Oxidation and addition of a Lewis base X$^-$ is a net radical X$^\bullet$ addition to Au^{I}Cl(L), conceptually similar to the often proposed addition of radicals R$^\bullet$ to Au^{I}Cl(L).[68−82] Future studies aim at transferring this redox/coordination activation to reactive gold(II) species toward other types of catalytic reactions.

EXPERIMENTAL SECTION

General Considerations. The preparation, purification, and reactions of the complexes described were carried out under an atmosphere of dry, oxygen-free N$_2$ or Ar using standard Schlenk or glovebox techniques. The precursors W(CO)$_5$[C(OEt)(Ar)] (Ar = 2-furyl, 4-DMA, Fc),[83−85] AuCl(tht)[125] and **1**[88] as well as the oxidants [C$_{12}$H$_8$S$_2$][SbCl$_6$], [C$_{12}$H$_8$S$_2$][PF$_6$] and [N(4-C$_6$H$_4$Br)$_3$][Al{OC(CF$_3$)$_3$}$_4$] were prepared according to literature procedures.[106,107] New complexes of gold(I) reported were synthesized following literature reports of similar carbene complexes.[92,93] Synthesis, characterization, and structures of the gold(I) ethoxycarbene precursors AuCl[C(OEt)(Ar)] (Ar = 4-DMA, **P2**; Ar = 2-furyl, **P3**) are reported in the Supporting Information. **P4** (Ar = Fc) was prepared according to a literature procedure.[84] Anhydrous diethyl ether and *n*-hexane were distilled from sodium, tetrahydrofuran (THF) was distilled from potassium, and dichloromethane and acetonitrile were distilled from CaH$_2$. All other reagents were commercially available and used as received.

Elemental analyses were carried out using an Elementar varioELcube CHNS-O analyzer. Melting points were measured with a Stuart SMP10 melting point apparatus.

NMR spectra were recorded on Bruker Avance-III-400 and Bruker Avance-III-500 spectrometers using CDCl$_3$, THF-d_8, and CD$_2$Cl$_2$ as solvents at 25 °C. The NMR spectra were recorded for ^{1}H at 400.13 and 500.13 MHz and for ^{13}C at 100.63 and 125.78 MHz.[126]

Infrared spectroscopy was performed on a PerkinElmer Spectrum FT-IR spectrophotometer over the range 4000−1400 cm^{-1}. Solution IR spectra were recorded in CH$_2$Cl$_2$ using a NaCl cell with a path length of ca. 1.0 mm.

https://doi.org/10.1021/acs.organomet.3c00395
Organometallics 2024, 43, 69−84

Mass spectrometric analyses were performed on a Bruker Compact Q-TOF mass spectrometer (Bruker Daltonics, Bremen, Germany) with a positive electron spray as the ionization technique by direct infusion at 0.3 mL min^{-1} in the range of m/z = 50−1000 in acetonitrile. Prior to analysis, the instrument was calibrated with sodium formate (5 mM) in resolution mode.

Cyclic voltammetry experiments were carried out on a BioLogic SP-200 voltammetric analyzer using platinum wires as counter and working electrodes and a 0.01 M $Ag/AgNO_3$ electrode as reference electrode using 0.1 M [^{n}Bu$_4$N][PF$_6$] as the supporting electrolyte in CH_3CN at scan rates of 0.050−0.100 V s^{-1}. Potentials are referenced to the ferrocene/ferrocenium couple (between $E_{1/2}$ = 0.085 and 0.140 V under the experimental conditions).

Stopped-flow spectroscopy experiments were performed using a stopped-flow mixing system SFM-4000/S-stopped-flow-mixer from BioLogic Science Instruments with a Cryo-stopped flow accessory and a MMS-VIS-SPEN high-speed-diode array spectrometer in CH_2Cl_2 at 22 and −90 °C with concentrations of 6.15 × 10^{-5} M^{-1} (**4a**/**4b**, [N(4-$C_6H_4Br)_3$][$SbCl_6$]) and a path length of 1 cm. The mixing time given by BioLogic is 0.7 ms.

X-band CW EPR spectra were recorded on a Miniscope MS 300 with a TC H02 temperature controller (Magnettech GmbH, Berlin, Germany). g factors are referenced to external Mn^{2+} in ZnS (g = 2.118, 2.066, 2.027, 1.986, 1.946, and 1.906). Quantification of EPR resonances was performed via an adapted literature procedure.[45,49,117] EPR tubes with an internal diameter of 2.0 mm were used. The calibration curve was recorded using commercially available *meso*-tetraphenylporphyrinato copper(II) Cu(TPP) in THF. All samples were prepared in a glovebox under argon. The EPR tubes were filled with 400 μL of the solution and sealed with Critoseal. They were inserted into the EPR spectrometer at a position 10.4 cm measured from the top of the Teflon holder. Four concentrations (c = 1.67, 0.84, 0.42, and 0.21 mM) in THF were used for the calibration. Settings for calibration and sample EPR spectra were as follows: temperature = 298 K, field = 2999 G, sweep = 2498 G, sweep time = 60 s, modulation = 2000 mG, MW attenuation = 10 dB, and number of passes = 3. The double integral of the experimental, baseline corrected spectra was plotted against the concentration. The resulting calibration by linear regression $y = (1.45 \pm 0.07) \times 10^5 \times c\ (\mathrm{mM}) - (0.19 \pm 0.05) \times 10^5 \times c\ (\mathrm{mM})$ (R^2 = 0.9939) was used to quantify the experimental EPR spectra of **4a**/**4b** after oxidation with Magic Blue.

Crystals for single-crystal X-ray diffraction were grown by slow diffusion of *n*-hexane into a concentrated CH_2Cl_2 solution of the carbene complex at 4 °C. Single crystal X-ray diffraction data for complexes **P2**, **P4**, **2a**/**2b**, **3a**, and **4a**/**4b** were collected at 173 K on a Bruker Apex II CCD diffractometer, while data for complex **P3** were collected at 173 K using a Bruker Venture D8 Photon CMOS diffractometer, with a graphite-monochromated Mo−K_α (λ = 0.71073 Å) radiation using an Oxford Cryostream 600 cooler. All data reductions were carried out using the program SAINT+, version 6.02,[127] and empirical absorption corrections were made using SADABS.[127] Space group assignments were made using XPREP.[127] The structures were solved in the WinGX[128] Suite of programs, using intrinsic phasing through SHELXT[129] and refined using full-matrix least-squares/difference Fourier techniques on F^2 using SHELXL-2017.[129] All carbon bound hydrogen atoms were placed at idealized positions and refined as riding atoms with isotropic parameters 1.2 times those of their parent atoms. The N−H hydrogen atom positions in **2**−**4** were located and refined. All diagrams and publication material were generated using OLEX2, ORTEP-3,[128] and PLATON.[130]

Density functional theory calculations were carried out using the ORCA program package (version 4.1.2).[131] All calculations were performed using the B3LYP functional[132−134] and the RIJCOSX approximation was employed.[135,136] Relativistic effects were calculated at the zeroth order regular approximation (ZORA) level.[137] The ZORA keyword automatically invokes relativistically adjusted basis sets. To account for solvent effects, a conductor-like screening model (CPCM) modeling CH_2Cl_2 was used in all calculations.[138,139] Geometry optimizations were performed using Ahlrichs' split-valence triple-ξ basis set ZORA-def2-TZVP[140] An auxiliary basis set for General-purpose Coulomb fitting SARC/J decontracted def2/J up to Kr was used.[141−144] The segmented all-electron relativistically contracted (SARC) auxiliary basis set beyond Kr, SARC-ZORA-TZVP, was used for gold and a special grid of 7 (default 4). Atom-pairwise dispersion correction was performed with the Becke-Johnson damping scheme (D3BJ).[145,146] The presence of energy minima was checked by numerical frequency calculations. To assign the absorption band of the initially formed oxidation product [**4a**]$^{\bullet+}$, 50 vertical spin-allowed transitions were calculated by TD-DFT. A transition at 553 nm (f = 0.002999) possesses gold(I) to iron(III) charge transfer character according to the difference electron density.

AuCl[C(NH^{n}Pr)(2-Furyl)] (***3a***). ^{n}PrNH$_2$ was slowly added to a brown-orange solution of **P3** (0.100 g, 0.28 mmol) in THF at room temperature. The mixture was stirred for 1 h, and the THF subsequently removed under reduced pressure. The resulting gray-black paste was washed with *n*-hexane (4 × 10 mL) and cannula-extracted with CH_2Cl_2 to give a pale gray powder after drying. Yield = 0.093 g, 90%. mp (dec) 135−137 °C. ^{1}H NMR (400 MHz, $CDCl_3$): δ 9.21 (s, br, 1H, NHCH$_2$CH$_2$CH$_3$), 7.70 (d, br, ^3J(HH) = 1.7 Hz, 1H, Fu-H$_\gamma$), 7.51 (d, ^3J(HH) = 3.9 Hz, 1H, Fu-H$_\alpha$), 6.60 (dd, ^3J(HH) = 3.7 Hz, ^3J(HH) = 1.8 Hz, 1H, Fu-H$_\beta$), 3.94 (q, ^3J(HH) = 6.8 Hz, 2H, NHCH$_2$CH$_2$CH$_3$), 1.86 (h, ^3J(HH) = 7.4 Hz, 2H, NHCH$_2$CH$_2$CH$_3$), 1.01 (t, ^3J(HH) = 7.4 Hz, 3H, NHCH$_2$CH$_2$CH$_3$). ^{13}C{^{1}H} NMR (101 MHz, $CDCl_3$): δ 196.0 ($C_{carbene}$), 154.4 (Fu-C_{ipso}), 148.4 (Fu-C_γ), 129.6 (Fu-C_α), 114.2 (Fu-C_β), 56.7 (NHCH$_2$CH$_2$CH$_3$), 23.0 (NHCH$_2$CH$_2$CH$_3$), 11.2 (NHCH$_2$CH$_2$CH$_3$). IR (CH_2Cl_2): $\tilde{\nu}$(NH) = 3318 cm^{-1}. Anal. Calcd for $C_8H_{11}NOClAu$: C, 26.00; H, 3.00; N, 3.79. Found: C, 26.48; H, 3.06; N, 3.84. ESI-HRMS (15 V, positive mode, m/z): calcd for [$C_8H_{11}NOAu$]$^+$, 334.0506; found, 334.0467.

The analogues AuCl[C(NH^{n}Pr)(Ar)] [Ar = 4-DMA (**2a**), Fc (**4a**)] and AuCl[C(NH(CH$_2$CH$_2$)NMe$_2$)(Ar)] [Ar = 4-DMA (**2b**), 2-furyl (**3b**), Fc (**4b**)] were prepared in analogous procedures as lime-green powders (**2a**, **2b**), red powders (**4a**, **4b**), and a gray powder (**3b**).

AuCl[C(NH^{n}Pr)(4-DMA)] (***2a***). Yield = 0.196 g, 93%. mp 96−98 °C. ^{1}H NMR (500 MHz, $CDCl_3$): δ 8.86 (s, br, 1H, NHCH$_2$CH$_2$CH$_3$), 7.88 (d, ^3J(HH) = 9.1 Hz, 2H, DMA-H$_{\alpha\alpha'}$), 6.75 (d, ^3J(HH) = 8.5 Hz, 2H, DMA-H$_{\beta\beta'}$), 4.04 (dt, ^3J(HH) = 7.6 Hz, ^3J(HH) = 6.2 Hz, 2H, NHCH$_2$CH$_2$CH$_3$), 3.09 (s, 6H, DMA-N(CH$_3$)$_2$), 1.88 (h, ^3J(HH) = 7.3 Hz, 2H, NHCH$_2$CH$_2$CH$_3$), 1.04 (t, ^3J(HH) = 7.4 Hz, 3H, NHCH$_2$CH$_2$CH$_3$). ^{13}C{^{1}H} NMR (126 MHz, $CDCl_3$): δ 214.0 ($C_{carbene}$), 153.1 (DMA-C_q), 133.0 (DMA-C_{ipso}), n.o. (DMA-C$_{\alpha\alpha'}$), 112.6 (DMA-C$_{\beta\beta'}$), 56.4 (NHCH$_2$CH$_2$CH$_3$), 41.1 (DMA-N(CH$_3$)$_2$), 23.2 (NHCH$_2$CH$_2$CH$_3$), 11.3 (NHCH$_2$CH$_2$CH$_3$). IR (CH_2Cl_2): $\tilde{\nu}$(NH) = 3333 cm^{-1}. Anal. Calcd for $C_{12}H_{18}N_2ClAu$: C, 34.10; H, 4.29; N, 6.63. Found: C, 34.12; H, 4.22; N, 6.39. ESI-HRMS (15 V, positive mode, m/z): calcd for [$C_{12}H_{18}N_2Au$]$^+$, 387.1136; found, 387.1103.

AuCl[C(NH(CH$_2$CH$_2$)NMe$_2$)(4-DMA)] (***2b***). Yield = 0.259 g, 96%. mp 91−93 °C. ^{1}H NMR (500 MHz, $CDCl_3$): δ 9.37 (s, br, 1H, NHCH$_2$CH$_2$N(CH$_3$)$_2$), 7.87 (d, ^3J(HH) = 8.4 Hz, 2H, DMA-H$_{\alpha\alpha'}$), 6.64 (d, ^3J(HH) = 8.3 Hz, 2H, DMA-H$_{\beta\beta'}$), 4.08 (t, ^3J(HH) = 5.4 Hz, 2H, NHCH$_2$CH$_2$N(CH$_3$)$_2$), 3.07 (s, 6H, DMA-N(CH$_3$)$_2$), 2.73 (t, ^3J(HH) = 5.4 Hz, 2H, NHCH$_2$CH$_2$N(CH$_3$)$_2$), 2.36 (s, 6H, NHCH$_2$CH$_2$N(CH$_3$)$_2$). ^{13}C{^{1}H} NMR (126 MHz, $CDCl_3$): δ 213.0 ($C_{carbene}$), 154.2 (DMA-C_q), 133.5 (DMA-C_{ipso}), 127.3 (DMA-C$_{\alpha\alpha'}$), 111.3 (DMA-C$_{\beta\beta'}$), 57.5 (NHCH$_2$CH$_2$N(CH$_3$)$_2$), 50.8 (NHCH$_2$CH$_2$N(CH$_3$)$_2$), 45.3 (NHCH$_2$CH$_2$N(CH$_3$)$_2$), 40.2 (DMA-N(CH$_3$)$_2$). IR (CH_2Cl_2): $\tilde{\nu}$(NH) = 3266 (br), 3333 (sh) cm^{-1}. Anal. Calcd for $C_{13}H_{21}N_3ClAu$: C, 34.56; H, 4.69; N, 9.30. Found: C, 35.19; H, 4.75; N, 9.28. ESI-HRMS (15 V, positive mode, m/z): calcd for [$C_{13}H_{21}N_3Au$]$^+$, 416.1401; found, 416.1386.

AuCl[C(NH(CH$_2$CH$_2$)NMe$_2$)(2-Furyl)] (***3b***). Yield = 0.300 g, 95%. mp 119−121 °C. ^{1}H NMR (400 MHz, $CDCl_3$): δ 9.43 (s, br, 1H, NHCH$_2$CH$_2$N(CH$_3$)$_2$), 7.71 (d, ^3J(HH) = 1.8 Hz, 1H, Fu-H$_\gamma$), 7.58 (d, ^3J(HH) = 3.6 Hz, 1H, Fu-H$_\alpha$), 6.62 (dd, ^3J(HH) = 3.6 Hz, ^3J(HH) = 1.8 Hz, 1H, Fu-H$_\beta$), 4.02 (t, ^3J(HH) = 5.8 Hz, 2H, NHCH$_2$CH$_2$N(CH$_3$)$_2$), 2.67 (t, ^3J(HH) = 5.8 Hz, 2H, NHCH$_2$CH$_2$N(CH$_3$)$_2$), 2.33 (s, 6H, NHCH$_2$CH$_2$N(CH$_3$)$_2$).

https://doi.org/10.1021/acs.organomet.3c00395
Organometallics 2024, 43, 69−84

$^{13}C\{^1H\}$ NMR (101 MHz, $CDCl_3$): δ 196.0 ($C_{carbene}$), 154.6 (Fu-C_{ipso}), 148.3 (Fu-C_{γ}), 130.0 (Fu-C_{α}), 114.2 (Fu-C_{β}), 57.0 ($NHCH_2CH_2N(CH_3)_2$), 51.5 ($NHCH_2CH_2N(CH_3)_2$), 45.3 ($NHCH_2CH_2N(CH_3)_2$). IR (CH_2Cl_2): $\tilde{\nu}$(NH) = 3273 (br), 3311 (sh) cm^{-1}. Anal. Calcd for $C_9H_{14}N_2OClAu$: C, 27.12; H, 3.54; N, 7.03. Found: C, 27.23; H, 3.37; N, 7.80. ESI-HRMS (15 V, positive mode, m/z): calcd for $[C_9H_{14}N_2OAu]^+$, 363.0772; found, 363.0756.

*AuCl[C(NH^{n}Pr)Fc] (**4a**).* Yield = 0.286 g, 93%. mp 119−120 °C. ^1H NMR (400 MHz, $CDCl_3$): δ 8.29 (s, br, 1H, $NHCH_2CH_2CH_3$), 4.87 (dd, ^3J(HH) = 1.7 Hz, ^3J(HH) = 1.9 Hz, 2H, FeCp′-$H_{\alpha\alpha'}$), 4.74 (dd, ^3J(HH) = 1.5 Hz, ^3J(HH) = 1.8 Hz, 2H, FeCp′-$H_{\beta\beta'}$), 4.35 (s, 5H, FeCp), 3.89 (q, ^3J(HH) = 6.8 Hz, 2H, $NHCH_2CH_2CH_3$), 1.85 (h, ^3J(HH) = 7.3 Hz, 2H, $NHCH_2CH_2CH_3$), 1.06 (t, ^3J(HH) = 7.4 Hz, 3H, $NHCH_2CH_2CH_3$). $^{13}C\{^1H\}$ NMR (101 MHz, $CDCl_3$): δ 216.7 ($C_{carbene}$), 84.2 (FeCp′-C_{ipso}), 74.4 (FeCp′-$C_{\alpha\alpha'}$), 71.2 (FeCp′-$C_{\beta\beta'}$), 70.7 (FeCp), 56.5 ($NHCH_2CH_2CH_3$), 23.1 ($NHCH_2CH_2CH_3$), 11.2 ($NHCH_2CH_2CH_3$). IR (CH_2Cl_2): $\tilde{\nu}$(NH) = 3329 cm^{-1}. Anal. Calcd for $C_{14}H_{17}NClFeAu$: C, 34.49; H, 3.51; N, 2.87. Found: C, 34.59; H, 3.56; N, 2.15. ESI-HRMS (15 V, positive mode, m/z): calcd for $[C_{14}H_{17}NFeAu]^+$, 452.0376; found, 452.0149.

*AuCl[C(NH(CH$_2$CH$_2$)NMe$_2$)Fc] (**4b**).* Yield = 0.098 g, 90%. mp 117−119 °C. ^1H NMR (500 MHz, $CDCl_3$): δ 9.11 (s, br, 1H, $NHCH_2CH_2N(CH_3)_2$), 4.91 (s, 2H, FeCp′-$H_{\alpha\alpha'}$), 4.73 (s, 2H, FeCp′-$H_{\beta\beta'}$), 4.34 (s, 5H, FeCp), 3.97 (t, ^3J(HH) = 5.6 Hz, 2H, $NHCH_2CH_2N(CH_3)_2$), 2.73 (t, ^3J(HH) = 5.7 Hz, 2H, $NHCH_2CH_2N(CH_3)_2$), 2.39 (s, 6H, $NHCH_2CH_2N(CH_3)_2$). $^{13}C\{^1H\}$ NMR (126 MHz, $CDCl_3$): δ 215.8 ($C_{carbene}$), 84.0 (FeCp′-C_{ipso}), 74.3 (FeCp′-$C_{\alpha\alpha'}$), 71.4 (FeCp′-$C_{\beta\beta'}$), 70.6 (FeCp), 57.6 ($NHCH_2CH_2N(CH_3)_2$), 51.6 ($NHCH_2CH_2N(CH_3)_2$), 45.4 ($NHCH_2CH_2N(CH_3)_2$). IR (CH_2Cl_2): $\tilde{\nu}$(NH) = 3266 (br), 3329 (sh) cm^{-1}. Anal. Calcd for $C_{15}H_{20}N_2ClFeAu$: C, 34.88; H, 3.90; N, 5.42. Found: C, 35.19; H, 3.90; N, 5.38. ESI-HRMS (15 V, positive mode, m/z): calcd for $[C_{15}H_{20}N_2FeAu]^+$, 481.0641; found, 481.0628.

Gold-Catalyzed *N*(2-Propyn-1-yl)benzamide Cyclization. *N*(2-Propyn-1-yl)benzamide (0.016 g, 0.10 mmol) was dissolved in CD_2Cl_2 (1 mL) in an inert-gas NMR tube. The precatalyst (1.0×10^{-3} mmol, 1 mol %), tris(4-bromophenyl)ammoniumyl hexachloroantimonate (Magic Blue; 1.00 mg, 1.25×10^{-3} mmol, 1.25 mol %), and 1,4-di-*tert*-butylbenzene (0.019 g, 0.10 mmol) as internal standard were added. The reactions were monitored by ^1H NMR spectroscopy wherein conversion of the substrate to the cyclic product was calculated by integration of the resonance of the NCH_2 group of the product with respect to the internal standard.

EPR Experiments. All samples were prepared in an Ar filled glovebox.

In the absence of chloride: complex **4a** or **4b** (1.67 mmol) was dissolved in THF or CH_2Cl_2 (0.5 mL). The respective oxidant (1.67 mmol) was dissolved in THF or CH_2Cl_2 (0.5 mL) and added to the complex solution. The final mixture (0.4 mL) was filled in an EPR tube, which was sealed with Critoseal. The temperature was controlled with a water bath.

In the presence of chloride: complex **4a** or **4b** (1.67 mmol) was dissolved in THF or CH_2Cl_2 (0.3 mL). The respective oxidant (1.67 mmol) was dissolved in THF or CH_2Cl_2 (0.3 mL) and added to the complex solution. A solution of [^{n}Bu$_4$N]Cl (1.67 mmol) in THF (0.3 mL) was added. The final mixture (0.4 mL) was filled in an EPR tube, which was sealed with Critoseal.

Regeneration Experiments with 2b. **2b** (8.6 mg, 0.019 mmol) was dissolved in CD_2Cl_2 (0.5 mL) at room temperature. After ^1H and ^{13}C NMR analyses, tris(4-bromophenyl)ammoniumyl hexachloroantimonate (Magic Blue; 16 mg, 0.019 mmol) was added to the NMR tube. ^1H and ^{13}C NMR spectra were thereafter recorded, indicating a new NH resonance and disappearance of the original $C_{carbene}$ resonance. Decamethylferrocene (0.019 mmol) was added to the NMR tube in an attempt to reduce the oxidized species back to **2b** and NMR spectra were recorded. The spectra indicated no recovery of **2b**.

Regeneration Experiments with 3b. **3b** (7.6 mg, 0.019 mmol) and tris(4-bromophenyl)ammoniumyl hexachloroantimonate (Magic Blue, 16 mg, 0.019 mmol) were dissolved in CD_2Cl_2 (0.5 mL) at room temperature. NMR spectra immediately after oxidation and after 24 h showed complex mixtures. After purification attempts, the NMR spectra indicated the presence of the amide protonated at the NMe_2 group [(4-DMA)C(O)$NHCH_2CH_2NMe_2H$]$^+$.

Regeneration experiments with **3b** in the presence of substrate: in this case, the substrate was also added to the NMR tube in an attempt to stabilize the oxidized species upon addition of Magic Blue. **3b** (0.019 mmol), Magic Blue (16 mg, 0.019 mmol), and *N*(2-propyn-1-yl)benzamide (0.019 mmol) were dissolved in CD_2Cl_2 (0.5 mL) in an NMR tube. Immediate formation of the catalytic product 2-phenyl-5-vinylidene-2-oxazoline was observed in both the ^1H and ^{13}C NMR spectra, as well as the presence of broad signals attributed to the oxidized gold complex. After 24 h, no clear presence of a carbene gold complex was observed.

Regeneration Experiments with 4a. *N*(2-Propyn-1-yl)-benzamide (15.92 mg, 0.1 mmol) was dissolved in CD_2Cl_2 (1 mL) in an inert-gas NMR tube. The precatalyst **4a** (4.88 mg, 0.01 mmol, 10 mol %), tris(4-bromophenyl)ammoniumyl hexachloroantimonate (Magic Blue; 8.16 mg, 0.01 mmol), and 1,4-di-*tert*-butylbenzene (1.90 mg, 0.01 mmol) as internal standard were added. A ^1H NMR spectrum was recorded immediately. The catalysis was stopped after ca. 20 min (79% conversion) by pouring the solution onto solid decamethylferrocene (3.43 mg, 0.0105 mmol). A ^1H NMR spectrum was recorded. Recovery was calculated based on the CH_3 resonance of the precatalyst and the CH_3 resonance of the internal standard.

■ ASSOCIATED CONTENT

Supporting Information

The Supporting Information is available free of charge at https://pubs.acs.org/doi/10.1021/acs.organomet.3c00395.

Experimental details, including synthesis and characterization of precursors, NMR and FT-IR spectra, SC-XRD, EPR, CV, and computational details (PDF)

Cartesian coordinates (XYZ)

Accession Codes

CCDC 2008751−2008755 and 2009078−2009080 contain the supplementary crystallographic data for this paper. These data can be obtained free of charge via www.ccdc.cam.ac.uk/data_request/cif, or by emailing data_request@ccdc.cam.ac.uk, or by contacting The Cambridge Crystallographic Data Centre, 12 Union Road, Cambridge CB2 1EZ, UK; fax: +44 1223 336033.

■ AUTHOR INFORMATION

Corresponding Authors

Daniela I. Bezuidenhout − *Laboratory of Inorganic Chemistry, Environmental and Chemical Engineering, University of Oulu, Oulu 90014, Finland*; orcid.org/0000-0001-7776-8227; Email: daniela.bezuidenhout@oulu.fi

Katja Heinze − *Department of Chemistry, Johannes Gutenberg University, Mainz 55128, Germany*; orcid.org/0000-0003-1483-4156; Email: katja.heinze@uni-mainz.de

Authors

Maurice P. Schrick − *Department of Chemistry, Johannes Gutenberg University, Mainz 55128, Germany*

G. Kabelo Ramollo − *Molecular Sciences Institute, School of Chemistry, University of the Witwatersrand, Johannesburg 2050, South Africa*

Cristina-Maria Susanne Hirschbiegel − *Department of Chemistry, Johannes Gutenberg University, Mainz 55128, Germany*

Manuel Fernandes − *Molecular Sciences Institute, School of Chemistry, University of the Witwatersrand, Johannesburg 2050, South Africa;* orcid.org/0000-0002-4849-5335
Andreas Lemmerer − *Molecular Sciences Institute, School of Chemistry, University of the Witwatersrand, Johannesburg 2050, South Africa;* orcid.org/0000-0003-1569-2831
Christoph Förster − *Department of Chemistry, Johannes Gutenberg University, Mainz 55128, Germany;* orcid.org/0000-0003-4971-5368

Complete contact information is available at: https://pubs.acs.org/10.1021/acs.organomet.3c00395

Author Contributions

[‖]M.P.S. and G.K.R. contributed equally.

Notes

The authors declare no competing financial interest.

■ ACKNOWLEDGMENTS

G.K.R. and D.I.B. gratefully acknowledge the National Research Foundation, South Africa (NRF 105529; NRF 105740; and NRF 116494), and Sasol Technology R&D Pty. Ltd. (South Africa) for financial support. K.H. and M.P.S. thank the Deutsche Forschungsgemeinschaft DFG for funding via grant HE2778/16-1. Parts of this research were conducted using the supercomputers Mogon and Elwetritsch and advisory services offered by the Johannes Gutenberg University Mainz (https://hpc.uni-mainz.de) and University of Kaiserslautern-Landau (https://hpc.rz.rptu.de), which are members of the AHRP and Gauss Alliance eV.

■ REFERENCES

(1) Fürstner, A. Gold and platinum catalysis-a convenient tool for generating molecular complexity. *Chem. Soc. Rev.* **2009**, *38*, 3208−3221.
(2) Hashmi, A. S. K. Homogeneous Gold Catalysis Beyond Assumptions and Proposals - Characterized Intermediates. *Angew. Chem., Int. Ed.* **2010**, *49*, 5232−5241.
(3) Liu, L.-P.; Hammond, G. B. Recent advances in the isolation and reactivity of organogold complexes. *Chem. Soc. Rev.* **2012**, *41*, 3129−3139.
(4) Hashmi, A. S. K. Dual Gold Catalysis. *Acc. Chem. Res.* **2014**, *47*, 864−876.
(5) Obradors, C.; Echavarren, A. M. Intriguing mechanistic labyrinths in gold(I) catalysis. *Chem. Commun.* **2014**, *50*, 16−28.
(6) Dorel, R.; Echavarren, A. M. Gold(I)-Catalyzed Activation of Alkynes for the Construction of Molecular Complexity. *Chem. Rev.* **2015**, *115*, 9028−9072.
(7) Joost, M.; Amgoune, A.; Bourissou, D. Reactivity of Gold Complexes towards Elementary Organometallic Reactions. *Angew. Chem., Int. Ed.* **2015**, *54*, 15022−15045.
(8) Zi, W.; Dean Toste, F. Recent advances in enantioselective gold catalysis. *Chem. Soc. Rev.* **2016**, *45*, 4567−4589.
(9) Nijamudheen, A.; Datta, A. Gold-Catalyzed Cross-Coupling Reactions: An Overview of Design Strategies, Mechanistic Studies, and Applications. *Chem.—Eur. J.* **2020**, *26*, 1442−1487.
(10) Praveen, C.; Dupeux, A.; Michelet, V. Catalytic Gold Chemistry - From Simple Salts to Complexes for Regioselective C-H Bond Functionalization. *Chem.—Eur. J.* **2021**, *27*, 10495−10532.
(11) Jazzar, R.; Soleilhavoup, M.; Bertrand, G. Cyclic (Alkyl)- and (Aryl)-(amino)carbene Coinage Metal Complexes and Their Applications. *Chem. Rev.* **2020**, *120*, 4141−4168.
(12) Rocchigiani, L.; Bochmann, M. Recent Advances in Gold(III) Chemistry: Structure, Bonding, Reactivity, and Role in Homogeneous Catalysis. *Chem. Rev.* **2021**, *121*, 8364−8451.
(13) Witzel, S.; Hashmi, A. S. K.; Xie, J. Light in Gold Catalysis. *Chem. Rev.* **2021**, *121*, 8868−8925.
(14) Herrera, R. P.; Gimeno, M. C. Main Avenues in Gold Coordination Chemistry. *Chem. Rev.* **2021**, *121*, 8311−8363.
(15) Lu, Z.; Li, T.; Mudshinge, S. R.; Xu, B.; Hammond, G. B. Optimization of Catalysts and Conditions in Gold(I) Catalysis - Counterion and Additive Effects. *Chem. Rev.* **2021**, *121*, 8452−8477.
(16) Praveen, C.; Dupeux, A.; Michelet, V. Catalytic Gold Chemistry: From Simple Salts to Complexes for Regioselective C-H Bond Functionalization. *Chem.—Eur. J.* **2021**, *27*, 10495−10532.
(17) Font, P.; Ribas, X. Fundamental Basis for Implementing Oxidant-Free Au(I)/Au(III) Catalysis. *Eur. J. Inorg. Chem.* **2021**, *2021*, 2556−2569.
(18) Pérez-Sánchez, J. C.; Herrera, R. P.; Gimeno, M. C. Ferrocenyl gold complexes as efficient catalysts. *Eur. J. Inorg. Chem.* **2022**, *2022*, No. e202101067.
(19) Wang, D.; Cai, R.; Sharma, S.; Jirak, J.; Thummanapelli, S. K.; Akhmedov, N. G.; Zhang, H.; Liu, X.; Petersen, J. L.; Shi, X. Silver Effect in Gold(I) Catalysis: An Overlooked Important Factor. *J. Am. Chem. Soc.* **2012**, *134*, 9012−9019.
(20) Canseco-Gonzalez, D.; Petronilho, A.; Mueller-Bunz, H.; Ohmatsu, K.; Ooi, T.; Albrecht, M. Carbene Transfer from Triazolylidene Gold Complexes as a Potent Strategy for Inducing High Catalytic Activity. *J. Am. Chem. Soc.* **2013**, *135*, 13193−13203.
(21) Guérinot, A.; Fang, W.; Sircoglou, M.; Bour, C.; Bezzenine-Lafollée, S.; Gandon, V. Copper Salts as Additives in Gold(I)-Catalyzed Reactions. *Angew. Chem., Int. Ed.* **2013**, *52*, 5848−5852.
(22) Hettmanczyk, L.; Schulze, D.; Suntrup, L.; Sarkar, B. Mono- and Digold(I) Complexes with Mesoionic Carbenes: Structural Characterization and Use in Catalytic Silver-Free Oxazoline Formation. *Organometallics* **2016**, *35*, 3828−3836.
(23) Fang, W.; Presset, M.; Guérinot, A.; Bour, C.; Bezzenine-Lafollée, S.; Gandon, V. Silver-Free Two-Component Approach in Gold Catalysis:Activation of [LAuCl] Complexes with Derivatives of Copper, Zinc, Indium, Bismuth, and Other Lewis Acids. *Chem.—Eur. J.* **2014**, *20*, 5439−5446.
(24) Pretorius, R.; Fructos, M. R.; Müller-Bunz, H.; Gossage, R. A.; Pérez, P. J.; Albrecht, M. Synthesis and catalytic applications of 1,2,3-triazolylidene gold(I) complexes in silver-free oxazoline syntheses and C-H bond activation. *Dalton Trans.* **2016**, *45*, 14591−14602.
(25) Wolf, J.; Huber, F.; Erochok, N.; Heinen, F.; Guérin, V.; Legault, C. Y.; Kirsch, S. F.; Huber, S. M. Activation of a Metal-Halogen Bond by Halogen Bonding. *Angew. Chem., Int. Ed.* **2020**, *59*, 16496−16500.
(26) Mikherdov, A. S.; Jin, M.; Ito, H. Exploring Au(I) involving halogen bonding with N-heterocyclic carbene Au(I) aryl complexes in crystalline media. *Chem. Sci.* **2023**, *14*, 4485−4494.
(27) Franchino, A.; Montesinos-Magraner, M.; Echavarren, A. M. Silver-Free Catalysis with Gold(I) Chloride Complexes. *Bull. Chem. Soc. Jpn.* **2021**, *94*, 1099−1117.
(28) Sen, S.; Gabbaï, F. P. An ambiphilic phosphine/H-bond donor ligand and its application to the gold mediated cyclization of propargylamides. *Chem. Commun.* **2017**, *53*, 13356−13358.
(29) Seppänen, O.; Aikonen, S.; Muuronen, M.; Alamillo-Ferrer, C.; Burés, J.; Helaja, J. Dual H-bond activation of NHC-Au(I)-Cl complexes with amide functionalized side-arms assisted by H-bond donor substrates or acid additives. *Chem. Commun.* **2020**, *56*, 14697−14700.
(30) Zhang, Z.; Smal, V.; Retailleau, P.; Voituriez, A.; Frison, G.; Marinetti, A.; Guinchard, X. Tethered Counterion-Directed Catalysis: Merging the Chiral Ion-Pairing and Bifunctional Ligand Strategies in Enantioselective Gold(I) Catalysis. *J. Am. Chem. Soc.* **2020**, *142*, 3797−3805.
(31) Franchino, A.; Martí, À.; Nejrotti, S.; Echavarren, A. M. Silver-Free Au(I) Catalysis Enabled by Bifunctional Urea and Squaramide-Phosphine Ligands via H-Bonding. *Chem.—Eur. J.* **2021**, *27*, 11989−11996.

(32) Franchino, A.; Martí, À.; Echavarren, A. M. H-Bonded Counterion-Directed Enantioselective Au(I) Catalysis. *J. Am. Chem. Soc.* **2022**, *144*, 3497−3509.
(33) Hettmanczyk, L.; Manck, S.; Hoyer, C.; Hohloch, S.; Sarkar, B. Heterobimetallic complexes with redox-active mesoionic carbenes as metalloligands: electrochemical properties, electronic structures and catalysis. *Chem. Commun.* **2015**, *51*, 10949−10952.
(34) Hettmanczyk, L.; Suntrup, L.; Klenk, S.; Hoyer, C.; Sarkar, B. Heteromultimetallic Complexes with Redox-Active Mesoionic Carbenes: Control of Donor Properties and Redox-Induced Catalysis. *Chem.—Eur. J.* **2017**, *23*, 576−585.
(35) Klenk, S.; Rupf, S.; Suntrup, L.; van der Meer, M.; Sarkar, B. The Power of Ferrocene, Mesoionic Carbenes, and Gold: Redox-Switchable Catalysis. *Organometallics* **2017**, *36*, 2026−2035.
(36) Litle, E. D.; Gabbaï, F. P. A cationic gold-fluorenyl complex with a dative Au → C^+ bond: synthesis, structure, and carbophilic reactivity. *Chem. Commun.* **2023**, *59*, 603−606.
(37) Liu, W.; Gabbaï, F. P. Placing gold on a π^+-surface: ligand design and impact on reactivity. *Chem. Sci.* **2023**, *14*, 277−283.
(38) Vanicek, S.; Podewitz, M.; Stubbe, J.; Schulze, D.; Kopacka, H.; Wurst, K.; Müller, T.; Lippmann, P.; Haslinger, S.; Schottenberger, H.; Liedl, K. R.; Ott, I.; Sarkar, B.; Bildstein, B. Highly Electrophilic, Catalytically Active and Redox-Responsive Cobaltoceniumyl and Ferrocenyl Triazolylidene Coinage Metal Complexes. *Chem.—Eur. J.* **2018**, *24*, 3742−3753.
(39) Eltester, M. A.; Gildenast, H.; Rabatinová, K.; Pütz, C.; Cremer, C.; Lanzerath, P.; Schroers, J. P.; Tauchert, M. E. Au → M bonds promote catalytic alkyne hydrofunctionalisation. *Chem. Commun.* **2023**, *59*, 5459−5462.
(40) Ibáñez, S.; Poyatos, M.; Dawe, L. N.; Gusev, D.; Peris, E. Ferrocenyl-Imidazolylidene Ligand for Redox-Switchable Gold-Based Catalysis. A Detailed Study on the Redox-Switching Abilities of the Ligand. *Organometallics* **2016**, *35*, 2747−2758.
(41) Deck, E.; Wagner, H. E.; Paradies, J.; Breher, F. Redox-responsive phosphonite gold complexes in hydroamination catalysis. *Chem. Commun.* **2019**, *55*, 5323−5326.
(42) Hashmi, A. S. K.; Weyrauch, J. P.; Frey, W.; Bats, J. W. Gold Catalysis: Mild Conditions for the Synthesis of Oxazoles from N-Propargylcarboxamides and Mechanistic Aspects. *Org. Lett.* **2004**, *6*, 4391−4394.
(43) Quiroz-Guzman, M.; Brown, S. N. Tris(4-bromophenyl)-aminium hexachloridoantimonate (Magic Blue): a strong oxidant with low inner-sphere reorganization. *Acta Crystallogr., Sect. C: Struct. Chem.* **2010**, *66*, m171−m173.
(44) Connelly, N. G.; Geiger, W. E. Chemical Redox Agents for Organometallic Chemistry. *Chem. Rev.* **1996**, *96*, 877−910.
(45) Veit, P.; Volkert, C.; Förster, C.; Ksenofontov, V.; Schlicher, S.; Bauer, M.; Heinze, K. Gold(II) in Redox-Switchable Gold(I) Catalysis. *Chem. Commun.* **2019**, *55*, 4615−4618.
(46) Dong, T.-Y.; Hendrickson, D. N.; Pierpont, C. G.; Moore, M. F. Mixed-Valence 1′,6′-Dihalobiferrocenium Salts: The Effect of the Solid-state Environment on Electron-Transfer Rates. *J. Am. Chem. Soc.* **1986**, *108*, 963−971.
(47) Solodovnikov, S. P. Investigation of Paramagnetic Metallocenes and Diarene Complexes of Transition Metals by Magnetic Resonance Methods. *Russ. Chem. Rev.* **1982**, *51*, 961−974.
(48) Cowan, D. O.; Candela, G. A.; Kaufman, F. Organic solid state. V. Symmetry distortions in ferrocenium compounds. *J. Am. Chem. Soc.* **1971**, *93*, 3889−3893.
(49) Neidlinger, A.; Kienz, T.; Heinze, K. Spin Trapping of Carbon-Centered Ferrocenyl Radicals with Nitrosobenzene. *Organometallics* **2015**, *34*, 5310−5320.
(50) Neidlinger, A.; Ksenofontov, V.; Heinze, K. Proton coupled electron transfer in ferrocenium-phenolate radicals. *Organometallics* **2013**, *32*, 5955−5965.
(51) Siebler, D.; Förster, C.; Gasi, T.; Heinze, K. Biferrocene amino acid - A ferrocenylogoue of ferrocene amino acid: Synthesis, Crosslinking, and Redox Chemistry. *Organometallics* **2011**, *30*, 313−327.
(52) Waniek, S. D.; Förster, C.; Heinze, K. Protic ferrocenyl acyclic diamino carbene gold(I) complexes. *Eur. J. Inorg. Chem.* **2022**, *2022*, No. e202100905.
(53) Heinze, K. The Quest for Mononuclear Gold(II) and its Potential Role in Photocatalysis and Drug Action. *Angew. Chem., Int. Ed.* **2017**, *56*, 16126−16134.
(54) Preiß, S.; Förster, C.; Otto, S.; Bauer, M.; Müller, P.; Hinderberger, D.; Hashemi Haeri, H.; Carella, L.; Heinze, K. Structure and Reactivity of a mononuclear gold(II) complex. *Nat. Chem.* **2017**, *9*, 1249−1255.
(55) Blake, A. J.; Greig, J. A.; Holder, A. J.; Hyde, T. I.; Taylor, A.; Schröder, M. Bis(1,4,7-trithiacyclononane)gold Dication: A Paramagnetic, Mononuclear Au^{II} Complex. *Angew. Chem., Int. Ed.* **1990**, *29*, 197−198.
(56) Kampf, M.; Olk, R.-M.; Kirmse, R. $[Au^{II}([12]anS_4)]^{2+}$ - X- and Q-Band EPR Evidence of a New Monomeric Gold(II) Compound. *Z. Anorg. Allg. Chem.* **2002**, *628*, 34−36.
(57) Ihlo, L.; Kampf, M.; Böttcher, R.; Kirmse, R. S-, X-, Q- und W-Band-Pulver-EPR-Untersuchungen am mononuklearen Au^{II}-Komplex $[Au^{II}([9]anS_3)_2](BF_4)_2$. *Z. Naturforsch. B* **2002**, *57*, 171−176.
(58) Kampf, M.; Griebel, J.; Kirmse, R. EPR Spectroscopic Characterization (X-Q-Band) of Monomeric Ag^{II} and Au^{II}-Complexes of the Thiacrownethers $[12]aneS_4$, $[16]aneS_6$ and $[27]aneS_9$. *Z. Anorg. Allg. Chem.* **2004**, *630*, 2669−2676.
(59) Seidel, S.; Seppelt, K. Xenon as a Complex Ligand: The Tetra Xenono Gold(II) Cation in $AuXe_4^{2+}(Sb_2F_{11}^-)_2$. *Science* **2000**, *290*, 117−118.
(60) Seppelt, K. Metal Xenon Complexes. *Z. Anorg. Allg. Chem.* **2003**, *629*, 2427−2430.
(61) Laguna, A.; Laguna, M. Coordination chemistry of gold(II) complexes. *Coord. Chem. Rev.* **1999**, *193*−*195*, 837−856.
(62) Dann, T.; Roşca, D. A.; Wright, J. A.; Wildgoose, G. G.; Bochmann, M. Electrochemistry of Au^{II} and Au^{III} pincer complexes: determination of the Au^{II}-Au^{II} bond energy. *Chem. Commun.* **2013**, *49*, 10169−10171.
(63) Roşca, D. A.; Bochmann, M. A. Photochemical Disproportionation of an Au^{II} Pincer Complex: Synthesis and Structure of an $Au^{I}_4Au^{III}_4$ Macrocycle. *Organometallics* **2016**, *35*, 27−31.
(64) Barakat, K.; Cundari, T. R. Chemical and photophysical properties of Au^{I}, Au^{II}, Au^{III}, and Au^{I}-dimer complexes. *Chem. Phys.* **2005**, *311*, 3−11.
(65) Zhang, Q.; Zhang, Z.-Q.; Fu, Y.; Yu, H.-Z. Mechanism of the Visible Light-Mediated Gold-Catalyzed Oxyarylation Reaction of Alkenes. *ACS Catal.* **2016**, *6*, 798−808.
(66) Sherborne, G. J.; Gevondian, A. G.; Funes-Ardoiz, I.; Dahiya, A.; Fricke, C.; Schoenebeck, F. Modular and Selective Arylation of Aryl Germanes (C-$GeEt_3$) over C-Bpin, C-SiR_3 and Halogens Enabled by Light-Activated Gold Catalysis. *Angew. Chem., Int. Ed.* **2020**, *59*, 15543−15548.
(67) Mehara, J.; Koovakattil Surendran, A.; van Wieringen, T.; Setia, D.; Foroutan-Nejad, C.; Straka, M.; Rulíšek, L.; Roithová, J. Cationic Gold(II) Complexes: Experimental and Theoretical Study. *Chem.—Eur. J.* **2022**, *28*, No. e202201794.
(68) Sahoo, B.; Hopkinson, M. N.; Glorius, F. Combining Gold and Photoredox Catalysis: Visible Light-Mediated Oxy- and Amino-arylation of Alkenes. *J. Am. Chem. Soc.* **2013**, *135*, 5505−5508.
(69) Winston, M. S.; Wolf, W. J.; Toste, F. D. Photoinitiated Oxidative Addition of CF_3I to Gold(I) and Facile Aryl-CF_3 Reductive Elimination. *J. Am. Chem. Soc.* **2014**, *136*, 7777−7782.
(70) Shu, X.-z.; Zhang, M.; He, Y.; Frei, H.; Toste, F. D. Dual Visible Light Photoredox and Gold-Catalyzed Arylative Ring Expansion. *J. Am. Chem. Soc.* **2014**, *136*, 5844−5847.
(71) Tlahuext-Aca, A.; Hopkinson, M. N.; Sahoo, B.; Glorius, F. Dual gold/photoredox-catalyzed C(sp)-H arylation of terminal alkynes with diazonium salts. *Chem. Sci.* **2016**, *7*, 89−93.
(72) Hopkinson, M. N.; Tlahuext-Aca, A.; Glorius, F. Merging Visible Light Photoredox and Gold Catalysis. *Acc. Chem. Res.* **2016**, *49*, 2261−2272.

https://doi.org/10.1021/acs.organomet.3c00395
Organometallics 2024, 43, 69−84

(73) Huang, L.; Rudolph, M.; Rominger, F.; Hashmi, A. S. K. Photosensitizer-Free Visible-Light-Mediated Gold-Catalyzed 1,2-Difunctionalization of Alkynes. *Angew. Chem., Int. Ed.* **2016**, *55*, 4808−4813.
(74) Tlahuext-Aca, A.; Hopkinson, M. N.; Daniliuc, C. G.; Glorius, F. Oxidative Addition to Gold(I) by Photoredox Catalysis: Straightforward Access to Diverse (C,N)-Cyclometalated Gold(III) Complexes. *Chem.—Eur. J.* **2016**, *22*, 11587−11592.
(75) Li, H.; Cheng, Z.; Tung, C.-H.; Xu, Z. Atom Transfer Radical Addition to Alkynes and Enynes: A Versatile Gold/Photoredox Approach to Thio-Functionalized Vinylsulfones. *ACS Catal.* **2018**, *8*, 8237−8243.
(76) Kim, S.; Toste, F. D. Mechanism of Photoredox-Initiated C-C and C-N Bond Formation by Arylation of IPrAu(I)-CF_3 and IPrAu(I)-Succinimide. *J. Am. Chem. Soc.* **2019**, *141*, 4308−4315.
(77) Xia, Z.; Corcé, V.; Zhao, F.; Przybylski, C.; Espagne, A.; Jullien, L.; Le Saux, T.; Gimbert, Y.; Dossmann, H.; Mouriès-Mansuy, V.; Ollivier, C.; Fensterbank, L. Photosensitized oxidative addition to gold(I) enables alkynylative cyclization of o-alkylnylphenols with iodoalkynes. *Nat. Chem.* **2019**, *11*, 797−805.
(78) Lovisari, M.; McDonald, A. R. Hydrogen Atom Transfer Oxidation by a Gold-Hydroxide Complex. *Inorg. Chem.* **2020**, *59*, 3659−3665.
(79) Baya, M.; Pérez-Bitrián, A.; Martínez-Salvador, S.; Martín, A.; Casas, J. M.; Menjón, B.; Orduna, J. Gold(II) Trihalide Complexes from Organogold(III) Precursors. *Chem.—Eur. J.* **2018**, *24*, 1514−1517.
(80) Johnson, A.; Puddephatt, R. J. Mechanistic Studies of Reactions of Benzenethiol with Methyl Derivatives of Platinum(II) and Gold-(I) and -(III). *J. Chem. Soc., Dalton Trans.* **1975**, 115−120.
(81) Johnson, A.; Puddephatt, R. J. Reactions of Trifluoromethyl Iodide with Methylgold(I) Complexes. Preparation of Trifluoromethyl-gold(I) and -gold(III) Complexes. *J. Chem. Soc., Dalton Trans.* **1976**, 1360−1363.
(82) Medina-Mercado, I.; Asomoza-Solís, E. O.; Martínez-González, E.; Ugalde-Saldívar, V. M.; Ledesma-Olvera, L. G.; Barquera-Lozada, J. E.; Gómez-Vidales, V.; Barroso-Flores, J.; Frontana-Uribe, B. A.; Porcel, S. Ascorbic Acid as an Aryl Radical Inducer in the Gold-Mediated Arylation of Indoles with Aryldiazonium Chlorides. *Chem.—Eur. J.* **2020**, *26*, 634−642.
(83) van der Westhuizen, B.; Swarts, P. J.; van Jaarsveld, L. M.; Liles, D. C.; Siegert, U.; Swarts, J. C.; Fernández, I.; Bezuidenhout, D. I. Metal-Metal Interaction in Fischer Carbene Complexes: A Study of Ferrocenyl and Biferrocenyl Tungsten Alkylidene Complexes. *Inorg. Chem.* **2013**, *52*, 6674−6684.
(84) Bezuidenhout, D. I.; van der Westhuizen, B.; Rosenthal, A. J.; Wörle, M.; Liles, D. C.; Fernández, I. Fischer-type gold(I) carbene complexes stabilized by aurophilic interactions. *Dalton Trans.* **2014**, *43*, 398−401.
(85) Veit, P.; Förster, C.; Heinze, K. On the Mechanism of Imine Elimination from Fischer Tungsten Carbene Complexes. *Beilstein J. Org. Chem.* **2016**, *12*, 1322−1333.
(86) BabaAhmadi, R.; Ghanbari, P.; Rajabi, N. A.; Hashmi, A. S. K.; Yates, B. F.; Ariafard, A. A Theoretical Study on the Protodeauration Step of the Gold(I)-Catalyzed Organic Reactions. *Organometallics* **2015**, *34*, 3186−3195.
(87) Stylianakis, I.; Nieto Faza, O.; López, C. S.; Kolocouris, A. The key role of protodeauration in the gold-catalyzed reaction of 1,3-diynes with pyrrole and indole to form complex heterocycles. *Org. Chem. Front.* **2020**, *7*, 997−1005.
(88) Aumann, R.; Fischer, E. O. Neue Gold-Carben-Komplexe durch Carbenübertragung. *Chem. Ber.* **1981**, *114*, 1853−1857.
(89) Tolman, C. A. Steric Effects of Phosphorus Ligands in Organometallic Chemistry and Homogeneous Catalysis. *Chem. Rev.* **1977**, *77*, 313−348.
(90) Mashabane, T. L.; Ramollo, G. K.; Kleinhans, G.; de Doncker, S.; Siangwata, S.; Fernandes, M. A.; Lemmerer, A.; Smith, G. S.; Bezuidenhout, D. I. Tunable Rh(I) Fischer carbene complexes for application in the hydroformylation of 1-octene. *J. Organomet. Chem.* **2020**, *920*, 121341.
(91) Ramollo, G. K.; Strydom, I.; Fernandes, M. A.; Lemmerer, A.; Ojwach, S. O.; van Wyk, J. L.; Bezuidenhout, D. I. Fischer Carbene Complexes of Iridium(I) for Application in Catalytic Transfer Hydrogenation. *Inorg. Chem.* **2020**, *59*, 4810−4815.
(92) Strasser, C. E.; Cronje, S.; Raubenheimer, H. G. Fischer-type tungsten acyl (carbeniate), carbene and carbyne complexes bearing C5-attached thiazolyl substituents: interaction with gold(I) fragments. *New J. Chem.* **2010**, *34*, 458.
(93) Strasser, C. E.; Stander-Grobler, E.; Schuster, O.; Cronje, S.; Raubenheimer, H. G. Preparation of Remote NHC Complexes of Rhodium(I) and Gold(I) by Ligand Transfer. *Eur. J. Inorg. Chem.* **2009**, *2009*, 1905−1912.
(94) Schaper, L.-A.; Öfele, K.; Kadyrov, R.; Bechlars, B.; Drees, M.; Cokoja, M.; Herrmann, W. A.; Kühn, F. E. N-Heterocyclic carbenes via abstraction of ammonia: normal carbenes with abnormal character. *Chem. Commun.* **2012**, *48*, 3857−3859.
(95) Hall, H. K. Correlation of the Base Strengths of Amines. *J. Am. Chem. Soc.* **1957**, *79*, 5441−5444.
(96) Kühlkamp, P.; Raubenheimer, H. G.; Field, J. S.; Desmet, M. Cyclic voltammetry of heterocyclic Au(I) and Au(III) carbene complexes. *J. Organomet. Chem.* **1998**, *552*, 69−74.
(97) Koelle, U.; Laguna, A. Electrochemistry of Au-complexes. *Inorg. Chim. Acta* **1999**, *290*, 44−50.
(98) de Frémont, P.; Singh, R.; Stevens, E. D.; Petersen, J. L.; Nolan, S. P. Synthesis, Characterization and Reactivity of N-Heterocyclic Carbene Gold(III) Complexes. *Organometallics* **2007**, *26*, 1376−1385.
(99) Pažický, M.; Loos, A.; Ferreira, M. J.; Serra, D.; Vinokurov, N.; Rominger, F.; Jäkel, C.; Hashmi, A. S. K.; Limbach, M. Synthesis, Reactivity, and Electrochemical Studies of Gold(I) and Gold(III) Complexes Supported by N-Heterocyclic Carbenes and Their Application in Catalysis. *Organometallics* **2010**, *29*, 4448−4458.
(100) Goetzfried, S. K.; Gallati, C. M.; Cziferszky, M.; Talmazan, R. A.; Wurst, K.; Liedl, K. R.; Podewitz, M.; Gust, R. N-Heterocyclic Carbene Gold(I) Complexes: Mechanism of the Ligand Scrambling Reaction and Their Oxidation to Gold(III) in Aqueous Solutions. *Inorg. Chem.* **2020**, *59*, 15312−15323.
(101) Xie, J.; Sekine, K.; Witzel, S.; Krämer, P.; Rudolph, M.; Rominger, F.; Hashmi, A. S. K. Light-Induced Gold-Catalyzed Hiyama Arylation: A Coupling Access to Biarylboronates. *Angew. Chem., Int. Ed.* **2018**, *57*, 16648−16653.
(102) Asomoza-Solís, E. O.; Rojas-Ocampo, J.; Toscano, R. A.; Porcel, S. Arenediazonium salts as electrophiles for the oxidative addition of gold(I). *Chem. Commun.* **2016**, *52*, 7295−7298.
(103) Zeineddine, A.; Estévez, L.; Mallet-Ladeira, S.; Miqueu, K.; Amgoune, A.; Bourissou, D. Rational development of catalytic Au(I)/Au(III) arylation involving mild oxidative addition of aryl halides. *Nat. Commun.* **2017**, *8*, 565.
(104) Vanicek, S.; Beerhues, J.; Bens, T.; Levchenko, V.; Wurst, K.; Bildstein, B.; Tilset, M.; Sarkar, B. Oxidative Access via Aqua Regia to an Electrophilic, Mesoionic Dicobaltoceniumyltriazolylidene Gold-(III) Catalyst. *Organometallics* **2019**, *38*, 4383−4386.
(105) Masui, M.; Sayo, H.; Tsuda, Y. Anodic oxidation of amines. Part I. Cyclic voltammetry of aliphatic amines at a stationary glassy-carbon electrode. *J. Chem. Soc. B* **1968**, 973−976.
(106) Balch, A. L.; Cornman, C. R.; Latos-Grazynski, L.; Olmstead, M. M. Characterization of Five- and Six-Coordinate Iron(III) Complexes of *N*-Methylporphyrins. *J. Am. Chem. Soc.* **1990**, *112*, 7552−7558.
(107) Schorpp, M.; Heizmann, T.; Schmucker, M.; Rein, S.; Weber, S.; Krossing, I. Synthesis and Application of a Perfluorinated Ammoniumyl Radical Cation as a Very Strong Deelectronator. *Angew. Chem., Int. Ed.* **2020**, *59*, 9453−9459.
(108) Wang, C.; Brudo, A.; Ducrot, L.; Fu, F.; Ruiz, J.; Escobar, A.; Martinez-Villacorta, A.; Moya, S.; Astruc, D. Generation of Catalytically Active Gold Nanocrystals in Water Induced with Ferrocene Carboxylate. *Eur. J. Inorg. Chem.* **2021**, *2021*, 2471−2479.

https://doi.org/10.1021/acs.organomet.3c00395
Organometallics 2024, 43, 69−84

(109) Aprile, C.; Boronat, M.; Ferrer, B.; Corma, A.; García, H. Radical Trapping by Gold Chlorides Forming Organogold Intermediates. *J. Am. Chem. Soc.* **2006**, *128*, 8388−8389.
(110) Man, R. W. Y.; Yi, H.; Malola, S.; Takano, S.; Tsukuda, T.; Häkkinen, H.; Nambo, M.; Crudden, C. M. Synthesis and Characterization of Enantiopure Chiral Bis NHC-Stabilized Edge-Shared Au_{10} Nanocluster with Unique Prolate Shape. *J. Am. Chem. Soc.* **2022**, *144*, 2056−2061.
(111) Walter, M.; Akola, J.; Lopez-Acevedo, O.; Jadzinsky, P. D.; Calero, G.; Ackerson, C. J.; Whetten, R. L.; Gronbeck, H.; Hakkinen, H. A unified view of ligand-protected gold clusters as superatom complexes. *Proc. Natl. Acad. Sci. U.S.A.* **2008**, *105*, 9157−9162.
(112) Narouz, M. R.; Osten, K. M.; Unsworth, P. J.; Man, R. W. Y.; Salorinne, K.; Takano, S.; Tomihara, R.; Kaappa, S.; Malola, S.; Dinh, C. T.; Padmos, J. D.; Ayoo, K.; Garrett, P. J.; Nambo, M.; Horton, J. H.; Sargent, E. H.; Häkkinen, H.; Tsukuda, T.; Crudden, C. M. N-heterocyclic carbene-functionalized magic-number gold nanoclusters. *Nat. Chem.* **2019**, *11*, 419−425.
(113) Crabtree, R. H. Resolving Heterogeneity Problems and Impurity Artifacts in Operationally Homogeneous Transition Metal Catalysts. *Chem. Rev.* **2012**, *112*, 1536−1554.
(114) Kislyuk, V. V.; Melnyk, A. K.; Buryak, N. I.; Trachevskij, V. V. Quantum Confinement Features in EPR and UV-vis Spectra of Al/Au Nanosystems. *J. Nano- Electron. Phys.* **2019**, *11*, 04036.
(115) Kislyuk, V.; Melnyk, A.; Buryak, N.; Trachevskij, V. NMR study of Au/Al nanosytems in solution. *J. Electr. Eng.* **2019**, *70*, 95−100.
(116) Hartlaub, S. F.; Lauricella, N. K.; Ryczek, C. N.; Furneaux, A. G.; Melton, J. D.; Piro, N. A.; Kassel, W. S.; Nataro, C. Late Transition Metal Compounds with 1,1'-Bis(phosphino)ferrocene Ligands. *Eur. J. Inorg. Chem.* **2017**, *2017*, 424−432.
(117) Eaton, G. R.; Eaton, S. S.; Barr, D. P.; Weber, R. T. Quantitative EPR. *A Practitioners Guide*, 1st ed.; Springer Verlag Wien: New York, 2010.
(118) Meek, S. J.; Pitman, C. L.; Miller, A. J. M. Deducing Reaction Mechanism: A Guide for Students, Researchers, and Instructors. *J. Chem. Educ.* **2016**, *93*, 275−286.
(119) Hu, B.; Baird, J. K. Reaction Kinetics and Critical Phenomena: Iodination of Acetone in Isobutyric Acid + Water near the Consolute Point. *J. Phys. Chem. A* **2010**, *114*, 355−359.
(120) Lo Nostro, P.; Mazzini, V.; Ninham, B. W.; Ambrosi, M.; Dei, L.; Baglioni, P. Specific Anion Effects on the Kinetics of Iodination of Acetone. *ChemPhysChem* **2016**, *17*, 2567−2571.
(121) Eitel, S. H.; Bauer, M.; Schweinfurth, D.; Deibel, N.; Sarkar, B.; Kelm, H.; Krüger, H. J.; Frey, W.; Peters, R. Paramagnetic Palladacycles with Pd^{III} Centers Are Highly Active Catalysts for Asymmetric Aza-Claisen Rearrangements. *J. Am. Chem. Soc.* **2012**, *134*, 4683−4693.
(122) Ayerbe Garcia, M.; Frey, W.; Ringenberg, M. R.; Schwilk, M.; Peters, R. Dinuclear planar chiral ferrocenyl gold(I) & gold(II) complexes. *Chem. Commun.* **2015**, *51*, 16806−16809.
(123) Holz, J.; Ayerbe García, M.; Frey, W.; Krupp, F.; Peters, R. Diastereoselective synthesis, structure and reactivity studies of ferrocenyloxazoline gold(I) and gold(II) complexes. *Dalton Trans.* **2018**, *47*, 3880−3905.
(124) Šrut, A.; Lear, B. J.; Krewald, V. Identifying the Marcus dimension of electron transfer from ab initio calculations. *Chem. Sci.* **2023**, *14*, 9213−9225.
(125) Uson, R.; Laguna, A.; Laguna, M.; Briggs, D. A.; Murray, H. H.; Fackler, J. P., Jr. (Tetrahydrothiophene)Gold(I) or Gold(III) Complexes. *Inorg. Synth.* **1989**, *26*, 85−91.
(126) Fulmer, G. R.; Miller, A. J. M.; Sherden, N. H.; Gottlieb, H. E.; Nudelman, A.; Stoltz, B. M.; Bercaw, J. E.; Goldberg, K. I. NMR Chemical Shifts of Trace Impurities: Common Laboratory Solvents, Organics, and Gases in Deuterated Solvents Relevant to the Organometallic Chemist. *Organometallics* **2010**, *29*, 2176−2179.
(127) Bruker. *APEX-3, SAINT+*, version 6.02 (Includes XPREP and SADABS); Bruker AXS Inc.: Madison, Wisconsin, USA, 2016.
(128) Farrugia, L. J. WinGX and ORTEP for Windows: an update. *J. Appl. Crystallogr.* **2012**, *45*, 849−854.
(129) Sheldrick, G. M. SHELXT - Integrated space-group and crystal-structure determination. *Acta Crystallogr., Sect. C: Struct. Chem.* **2015**, *71*, 3−8.
(130) Spek, A. L. Structure validation in chemical crystallography. *Acta Crystallogr., Sect. D: Struct. Biol.* **2009**, *65*, 148−155.
(131) Neese, F. Software update: the ORCAprogram system, version 4.0. *Wiley Interdiscip. Rev.: Comput. Mol. Sci.* **2012**, *2*, 73−78.
(132) Becke, A. D. Density-functional thermochemistry. III. The role of exact exchange. *J. Chem. Phys.* **1993**, *98*, 5648−5652.
(133) Lee, C.; Yang, W.; Parr, R. G. Development of the Colle-Salvetti correlation-energy formula into a functional of the electron density. *Phys. Rev. B* **1988**, *37*, 785−789.
(134) Miehlich, B.; Savin, A.; Stoll, H.; Preuss, H. Results obtained with the correlation energy density functionals of becke and Lee, Yang and Parr. *Chem. Phys. Lett.* **1989**, *157*, 200−206.
(135) Neese, F.; Wennmohs, F.; Hansen, A.; Becker, U. Efficient, approximate and parallel Hartree-Fock and hybrid DFT calculations. A chain-of-spheres algorithm for the Hartree-Fock exchange. *Chem. Phys.* **2009**, *356*, 98−109.
(136) Izsák, R.; Neese, F. An overlap fitted chain of spheres exchange method. *J. Chem. Phys.* **2011**, *135*, 144105.
(137) Pantazis, D. A.; Chen, X.-Y.; Landis, C. R.; Neese, F. All-Electron Scalar Relativistic Basis Sets for Third-Row Transition Metal Atoms. *J. Chem. Theory Comput.* **2008**, *4*, 908−919.
(138) Barone, V.; Cossi, M. Quantum Calculation of Molecular Energies and Energy Gradients in Solution by a Conductor Solvent Model. *J. Phys. Chem. A* **1998**, *102*, 1995−2001.
(139) Miertuš, S.; Scrocco, E.; Tomasi, J. Electrostatic interaction of a solute with a continuum. A direct utilizaion of AB initio molecular potentials for the prevision of solvent effects. *J. Chem. Phys.* **1981**, *55*, 117−129.
(140) Weigend, F.; Ahlrichs, R. Balanced basis sets of split valence, triple zeta valence and quadruple zeta valence quality for H to Rn: Design and assessment of accuracy. *Phys. Chem. Chem. Phys.* **2005**, *7*, 3297−3305.
(141) Weigend, F. Accurate Coulomb-fitting basis sets for H to Rn. *Phys. Chem. Chem. Phys.* **2006**, *8*, 1057−1065.
(142) Pantazis, D. A.; Neese, F. All-Electron Scalar Relativistic Basis Sets for the Lanthanides. *J. Chem. Theory Comput.* **2009**, *5*, 2229−2238.
(143) Pantazis, D. A.; Neese, F. All-electron scalar relativistic basis sets for the 6p elements. *Theor. Chem. Acc.* **2012**, *131*, 1292.
(144) Pantazis, D. A.; Neese, F. All-Electron Scalar Relativistic Basis Sets for the Actinides. *J. Chem. Theory Comput.* **2011**, *7*, 677−684.
(145) Grimme, S.; Antony, J.; Ehrlich, S.; Krieg, H. A consistent and accurate ab initio parametrization of density functional dispersion correction (DFT-D) for the 94 elements H-Pu. *J. Chem. Phys.* **2010**, *132*, 154104.
(146) Grimme, S.; Ehrlich, S.; Goerigk, L. Effect of the damping function in dispersion corrected density functional theory. *J. Comput. Chem.* **2011**, *32*, 1456−1465.

https://doi.org/10.1021/acs.organomet.3c00395
Organometallics 2024, 43, 69−84

3.3 Di-substituted Fischer gold(I) carbene complexes

In 2014 the *Bezuidenhout* group published a complex with a ferrocene substituted at each Cp ring with a Fischer carbene gold(I) chloride, **7**.[113] Starting from the corresponding tungsten complex, they synthesized the Fischer carbene complex **7** through transmetallation onto a gold(I) precursor (scheme 1).[113] Interesting about **7** is a relative short Au–Au distance in the solid state of 3.035 Å, determined through XRD measurements. This distance is well below the sum of two van der Waals radii (3.80 Å) and is attributed to aurophilic interactions.[113],[242]

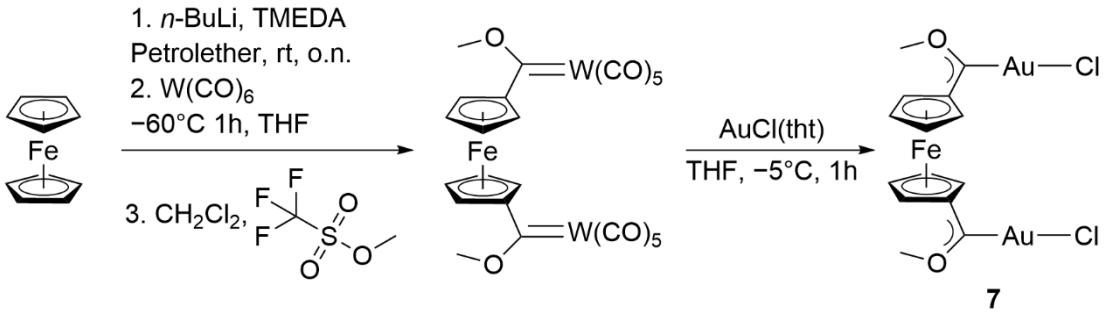

Scheme 1: Synthesis route towards complex **7** used by Bezuidenhout.[113]

Even though the complex **7** was fully characterized by them, no further investigations on its oxidized form **[7]**$^+$ were performed and no UV/vis or CV measurements were carried out. Since the mono substituted ferrocenyl Fischer carbene gold(I) complex is catalytically active after oxidation and an induction period of two and a half hours, it was of interest how two gold center in one molecule would affect the activation process and possibly the catalytic performance.[19] As shown in chapter 3.2 for similar complexes, the initial oxidation takes place at the ferrocenyl backbone and through coordination of the counter ion of the oxidant and a subsequent valence tautomerization a catalytically active gold(II) species is generated.

Having a second gold(I) center adjacent could stabilize the first gold center through aurophilic interactions or by forming a bond with bond order 0.5 upon oxidation. For each gold center a T-shaped crystal field is assumed, since each gold(I) center is linearly coordinated by a chlorido ligand, a carbene ligand and interacting with a second gold(I) in a 90° angle. Through the d-orbital splitting of the T-shaped crystal field the $d_{x^2-y^2}$ orbital is the energetically highest laying orbital. Oxidation of the complex **7** with charge distributed at the gold(I) atoms and linear combination of the $d_{x^2-y^2}$ orbitals would lead to molecule orbitals. The occupation of the bonding orbital would be two electrons and the antibonding orbital would be occupied with one electron, thus a bond order of 0.5. This bond formation could mitigate the use of external cations to stabilize the catalytically active gold(II) species.

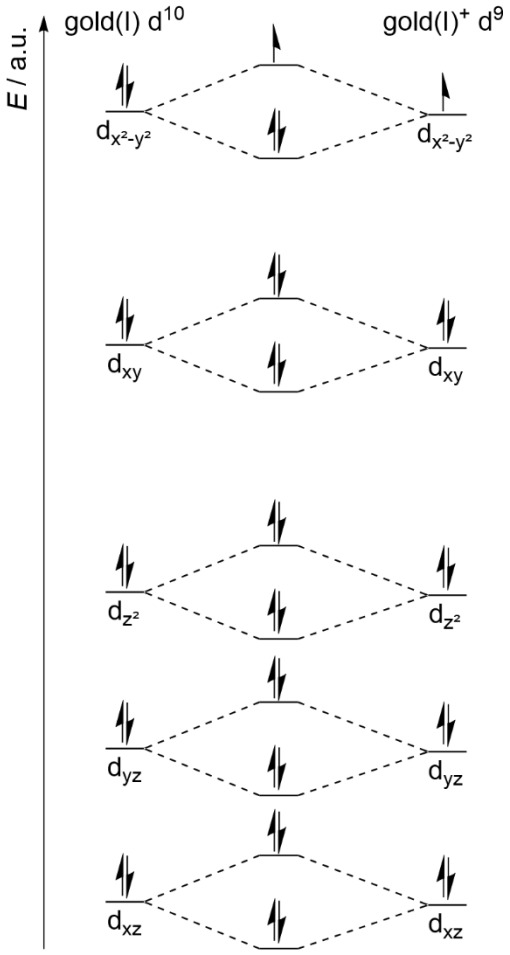

Scheme 2: d-Orbitals in a T-shaped ligand field with linear combination of the atom orbitals of each a gold(I) and a gold(I)$^+$ atom. The linear combination of both $d_{x^2-y^2}$ orbitals could lead to the formation of bond orbitals and a bond order 0.5.

The molecular geometries in the neutral and in the oxidized state were calculated, to investigate the nature of the Au–Au interactions upon oxidation. The calculations were performed on the B3LYP/ZORA-def2-TZVP level of theory, with relativistically adjusted basis sets, dispersion correction and a CPCM solvent model (CH_2Cl_2).

The DFT optimized structure of **7** differs slightly from the structure obtained via XRD measurements (scheme 3). The calculated Au–Au distance (3.141 Å) is slightly longer than the one obtained from the XRD measurement (exp. 3.035(1) Å), for the Fe–$Cp_{centroid}$ distance (calcd. 1.675 Å, exp. 1.657(4) Å) and the $Cp_{centroid}$–Fe–$Cp_{centroid}$ angle (calcd. 174°, exp. 173°) the calculation reflects the measured values.

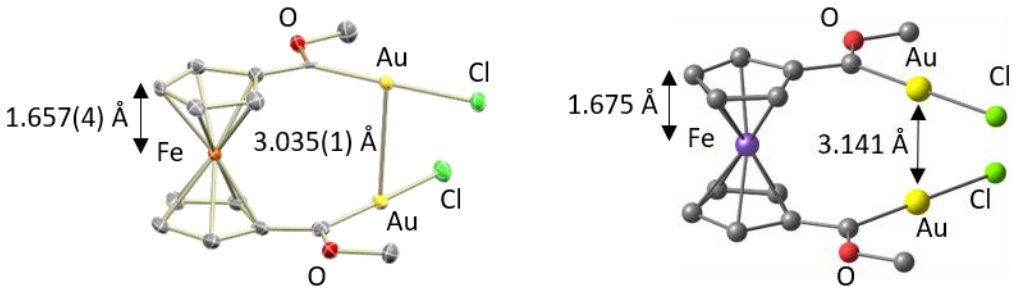

Scheme 3: Left: molecular structure of **7** with partially labeled ellipsoid plots (50% probability). Hydrogen atoms omitted for clarity.[113] Right: DFT optimized geometry of **7**. $Cp_{centroid}$–Fe and Au–Au distances shown for both.

Chart 1: Selected bond length and angles for the molecular structure and the DFT calculation of complex **7**.[113]

	7 (molecular structure)	**7** (DFT)
Au–Au [Å]	3.035(1)	3.141
Au–Cl [Å]	2.294(1), 2.283(2)	2.328, 2.330
$Cp_{centroid}$–Fe [Å]	1.657(4)	1.675
$C_{carbene}$–Au [Å]	1.969(7), 1.960(5)	1.985, 1987
$Cp_{centroid}$–Fe–$Cp_{centroid}$ [°]	173	174
Cl–Au–Au–Cl [°]	-74	-78
O–$C_{carbene}$–C_{ipso} [°]	112	113

In the calculated structure of the oxidized species **[7]**$^{+}$ the spin density is localized at the two gold(I) centers (Scheme 4). **[7]**$^{+}$ contains a shorter Au–Au distance (2.714 Å) than in the calculated neutral form of **7** (3.141 Å). The positive charge located at the gold atoms also lead to shorter Au–Cl bonds of 2.309 Å and 2.310 Å (**7**: 2.328 Å and 2.330 Å). The majority of the spin (Mulliken spin population of 0.364 and 0.358) is localized at the gold(I) centers, presumably in the $d_{x^2-y^2}$ orbitals and small shares are at the chlorides. The spin density localization shared at both gold centers implies a stronger interaction and a bond order of 0.5 for both gold atoms, but does not impede any structural changes on the ferrocenyl part of the molecule when compared to the calculated neutral complex **7**.

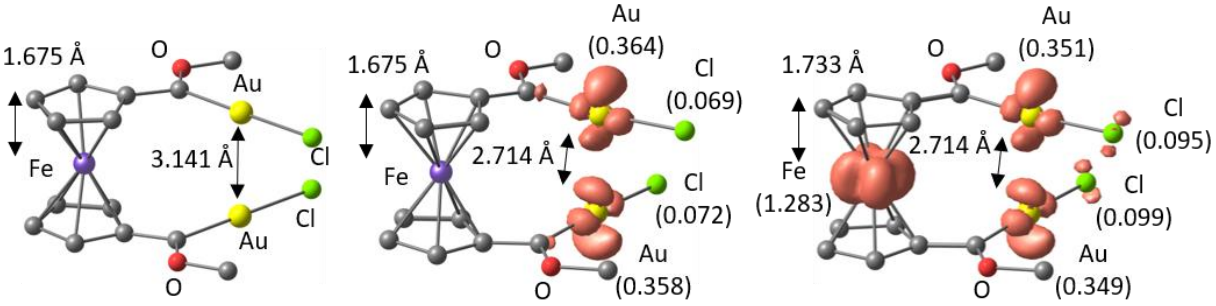

Scheme 4: Optimized geometries and spin density plots of **7**, **[7]**$^{+}$ and **[7]**$^{2+}$ with $Cp_{centroid}$–Fe and Au–Au distances shown, Mulliken spin population in parentheses. The contour value is at 0.01.

A second oxidation of complex **[7]**$^{+}$ could lead to a bond order of 1 for both gold atoms, which implies a covalent bond between the gold centers. Calculating the double oxidation **[7]**$^{2+}$ leads to a spin density

distribution located at both gold atoms (Mulliken spin population of 0.351 and 0.349), numbers slightly lower than for **[7]**$^{+}$. The majority of the spin however is located at the ferroceniumyl moiety (Mulliken spin population of 1.283). Smaller contributions are again found at the chlorides. Since the second oxidation takes place at the ferrocenyl backbone, the bond order of the gold atoms does not change and the possibility of a covalent bond with bond order one between the gold centers is discarded.

With the oxidation to a ferroceniumyl in **[7]**$^{2+}$ the geometry changes in comparison with **[7]**$^{+}$ in this part of the molecule. The Fe–$Cp_{centroid}$ distance enlarges upon double oxidation (**[7]**$^{+}$ 1.675 Å, **[7]**$^{2+}$ 1.733 Å and 1.734 Å) and the $Cp_{centroid}$–Fe–$Cp_{centroid}$ angle enlarges as well (**[7]**$^{+}$ 173°, **[7]**$^{2+}$ 177°). As expected, the calculated Au–Au distance stays the same (**[7]**$^{+}$ 2.714 Å, **[7]**$^{2+}$ 2.714 Å), since there are no changes in the spin density distribution for the gold atoms of **[7]**$^{2+}$. The Au–Cl bonds are shorter in **[7]**$^{2+}$ with bond lengths of 2.292 Å and 2.293 Å, compared to **[7]**$^{+}$ (2.309 Å and 2.310 Å), continuing the trend of shorter Au–Cl bonds with higher oxidation states. The more electron withdrawing ferroceniumyl leads to a positive polarization of the Au atoms and a shorter ionic bond (chart 2).[113]

Chart 2: Selected bond length and angles of **7**, **[7]**$^{+}$ and **[7]**$^{2+}$.

	7	**[7]**$^{+}$	**[7]**$^{2+}$
Au–Au [Å]	3.141	2.714	2.714
Au–Cl [Å]	2.328, 2.330	2.309, 2.310	2.292, 2.293
$Cp_{centroid}$–Fe [Å]	1.675	1.675	1.733, 1.734
$C_{carbene}$–Au [Å]	1.985, 1987	2.010, 2.0121	2.004, 2.006
$Cp_{centroid}$–Fe–$Cp_{centroid}$ [°]	174	173	177
Cl–Au–Au–Cl [°]	-78	-77	-80
O–$C_{carbene}$–C_{ipso} [°]	113	115	114

4 Summary and outlook

In this work synthetic, spectroscopic and theoretical approaches were taken to gain insight into known classes of complexes and their behavior during oxidation and catalysis.

The search for precursor complexes mimicking the active center of the CODH with a mixed *cis*-$[MoO(\mu_{2}\text{-}S)Cu]^{2+}$ unit let to the synthesis and characterization of 2-iminopyrrolato bis(silylthiolato) molybdenum(IV) complexes $Mo(^{t\text{Bu}}L)_2(SSi(^{i}Pr)_3)_2$ and $Mo(^{t\text{Bu}}L)_2(SSi^{t}Bu(Ph)_2)_2$ as complexes with protected sulfide ligands (section 3.1). The synthesis proceeds through the deoxygenation of the precursor $K_2MoO_2S_2$ with $K(^{t\text{Bu}}L)$, the addition of a silylchloride and delivers the complexes in good yields as red-brown oils. The spatial arrangement of complex $Mo(^{t\text{Bu}}L)_2(SSi(^{i}Pr)_3)_2$ was characterized through 2D-NMR experiments and DFT calculations. Investigation of the redox properties unraveled an irreversible Mo^{IV}/Mo^{V} oxidation at 0.82 V versus FcH/FcH^{+}. UV/vis spectroscopy revealed a maximum at λ = 330 nm and a broad low energy shoulder tailing to around λ = 500 nm. Chemical oxidation with Magic Green delivered a complex EPR signal, while the neutral complex is EPR silent. In analogy to the know $Mo(^{t\text{Bu}}L)_2(SSiMe_3)_2$ complex, this is hinting towards a Mo^{IV} oxidation state of the $Mo(^{t\text{Bu}}L)_2(SSi(^{i}Pr)_3)_2$ complex. The molecular structure of a decomposition product of $Mo(^{t\text{Bu}}L)_2(SSi(^{i}Pr)_3)_2$ with likely H_2O reveals that the migration of the isopropyl-silyl group to the N^{imine} nitrogen of the $^{t\text{Bu}}L^{-}$ ligand took place, while also $^{t\text{Bu}}L^{-}$ becomes protonated. Cleavage of the S–Si bond of $Mo(^{t\text{Bu}}L)_2(SSiMe_3)_2$ with DMSO and *p*-nitropyridine-*N*-oxide, as possible ways to synthesize a molybdenum(VI) complex $Mo(^{t\text{Bu}}L)_2S_2$ with free sulfide groups, was ruled out. Using Selectfluor in combination with $NaOMe_{(s)}$ on $Mo(^{t\text{Bu}}L)_2(SSi(^{i}Pr)_3)_2$ however let to a visible change in the UV/vis spectrum. The appearance of isosbestic points is hinting towards a successful cleavage of the S–Si bond, albeit no complex was isolated. The structure of the molybdenum(VI) complex $Mo(^{t\text{Bu}}L)_2S_2$, which would form after successful cleavage of the S–Si bonds was determined via DFT calculations. In contrast to complexes of the form $Mo(^{t\text{Bu}}L)_2(SSi(R)_3)_2$ with three possible isomers, only two possible isomers are found, since the *trans* influence of the sulfide ligands prevents them from this coordination geometry.

Another idea, which has not yet been tested to cleave the S–Si bonds and to isolate the resulting complex, is the use of *N*-fluoropyridinium triflate. The pyridine remaining after fluorination is simply removable in vacuum, in contrast to the cation remaining after using Selectfluor and could lead to successful crystal growth for structure determination.

After removal of the silyl protection groups and the generation of $Mo(^{t\text{Bu}}L)_2S_2$, a reaction with a suitable $[Cu^{II}L']^{2+}$ complex could yield a complex $Mo(^{t\text{Bu}}L)_2S(SCu^{I}L')$ mimicking the active center of the CODH.

Chlorido (ferrocenyl)(amino)carbene gold(I) pre-catalysts with redox-active substituents are able, after oxidation, to catalyze the cyclisation of N(2-propyn-1-yl)benzamide to 2-phenyl-5-vinylidene-2-oxazoline, without additional chloride scavengers needed for activation (section 3.2). The catalytic reaction did not proceed, if the complex is missing an oxidize-able moiety. Investigation of the redox properties of the complexes showed reversible oxidation between 0.27 V and 0.40 V for ferrocenyl substituted gold(I) precatalysts. For complexes with dimethylanilinyl and 2-furyl substituted gold(I) precatalysts only irreversible oxidations were found. Using Magic Blue as a single electron oxidant on the ferrocenyl substituted gold(I) precatalysts let to the detection of signals derived from gold(II) species in the EPR spectra. Through EPR measurements at different temperatures a zeroth order reaction rate for the generation of the EPR active species was determined and the activation barrier calculated. Stopped-flow UV/vis spectroscopy demonstrated the initial oxidation to be faster than 0.7 ms at –90°C in dichloromethane. Oxidation and re-reduction experiments confirm the switchable nature of these complexes. DFT calculations of the active species aided in uncovering the activation process. The initial fast oxidation takes place at the ferrocenyl moiety, followed by a slow valence isomerization towards a gold(II) species. In the generated EPR-active resting state, the counterion of the oxidant coordinates the gold(II) center and after dissociation, the complex becomes catalytically active. Of interest is the implementation of this redox/coordination activation to perform other catalytic reactions.

Incorporating two Fischer gold(I) carbenes on each cyclopentadienyl ring of a ferrocene was demonstrated by the *Bezuidenhout* group. DFT calculations yielded more insight into the electron structure of the mono and double oxidized products (section 3.3). After initial oxidation the positive charge is distributed between both gold atoms, the second oxidation takes place at the ferrocenyl moiety. Comparing the calculations with experimental data and applying this knowledge in catalytic reactions are topics of interest in the future.

5 References

[1] B. Hammer, J. K. Norskov, *Nature* **1995**, *376*, 238–240.
[2] H. Schmidbaur, *Naturwiss. Rundsch.* **1995**, *48*, 443–451.
[3] S. Komiya, J. K. Kochi, *J. Organomet. Chem.* **1977**, *135*, 65–72.
[4] Y. Ito, M. Sawamura, T. Hayashi, *J. Am. Chem. Soc.* **1986**, *108*, 6405–6406.
[5] Y. Fukuda, K. Utimoto, *Bull. Chem. Soc. Jpn.* **1991**, *64*, 2013–2015.
[6] W. A. Nugent, *Angew. Chem.* **2012**, *124*, 9066–9080; *Angew. Chem. Int. Ed.* **2012**, *51*, 8936–8949.
[7] J. H. Teles, S. Brode, M., Chabanas, *Angew. Chem.* **1998**, *110*, 1475–1478; *Angew. Chem. Int. Ed.* **1998**, *37*, 1415–1418.
[8] Y. Fukuda, K. Utimoto, *J. Org. Chem.* **1991**, *56*, 3729–3731.
[9] A. S. K. Hashmi, *Chem. Rev.* **2007**, *107*, 3180–3211.
[10] A. Arcadi, *Chem. Rev.* **2008**, *108*, 3266–3325.
[11] J.-J. Jiang, M.-K. Wong, *Chem. Asian J.* **2021**, *16*, 364–377.
[12] H. Schmidbaur, A. Schier, *Z. Naturforsch. B* **2011**, *66*, 329–350.
[13] M. Joost, A. Amgoune, D. Bourissou, *Angew. Chem.* **2015**, *127*, 15234–15258; *Angew. Chem. Int. Ed.* **2015**, *54*, 15022–15045.
[14] A. S. K. Hashmi, F. D. Toste, *Modern Gold Catalyzed Synthesis*, Wiley-VCH, Chichester, Weinheim, **2012**.
[15] C. Obradors, A. M. Echavarren, *Chem. Commun.* **2014**, *50*, 16–28.
[16] C. C. Chintawar, N. T. Patil, *Gold Bull.* **2022**, *55*, 161–168.
[17] M. García-Mota, N. Cabello, F. Maseras, A. M. Echavarren, J. Pérez-Ramírez, N. Lopez, *ChemPhysChem.* **2008**, *9*, 1624–1629.
[18] A. S. K. Hashmi, *Angew. Chem.* **2010**, *122*, 5360–5369; *Angew. Chem. Int. Ed.* **2010**, *49*, 5232–5241.
[19] P. Veit, C. Volkert, C. Förster, V. Ksenofontov, S. Schlicher, M. Bauer, K. Heinze, *Chem. Commun.* **2019**, *55*, 4615–4618.
[20] S. Sen, F. P. Gabbaï, *Chem. Commun.* **2017**, *53*, 13356–13358.
[21] L. Hettmanczyk, L. Suntrup, S. Klenk, C. Hoyer, B. Sarkar, *Chem. Eur. J.* **2017**, *23*, 576–585.
[22] A. Straube, P. Coburger, L. Dütsch, E. Hey-Hawkins, *Chem. Sci.* **2020**, *11*, 10657–10668.
[23] A. S. K. Hashmi, M. Rudolph, S. Schymura, J. Visus, W. Frey, *Eur. J. Org. Chem.* **2006**, *2006*, 4905–4909.
[24] C. Ferrer, C. H. M. Amijs, A. M. Echavarren, *Chem. Eur. J.* **2007**, *13*, 1358–1373.
[25] H. Schmidbaur, A. Schier, *Organometallics* **2010**, *29*, 2–23.
[26] A. S. K. Hashmi, M. Rudolph, *Chem. Soc. Rev.* **2008**, *37*, 1766–1775.
[27] R. O. C. Norman, W. J. E. Parr, C. B. Thomas, *Perkin Trans. 1* **1976**, 1983.
[28] G. HUTCHINGS, *J. Catal.* **1985**, *96*, 292–295.
[29] M. Conte, A. F. Carley, C. Heirene, D. J. Willock, P. Johnston, A. A. Herzing, C. J. Kiely, G. J. Hutchings, *J. Catal.* **2007**, *250*, 231–239.
[30] J. A. Akana, K. X. Bhattacharyya, P. Müller, J. P. Sadighi, *J. Am. Chem. Soc.* **2007**, *129*, 7736–7737.
[31] E. Mizushima, T. Hayashi, M. Tanaka, *Org. Lett.* **2003**, *5*, 3349–3352.
[32] J. Barluenga, A. Diéguez, A. Fernández, F. Rodríguez, F. J. Fañanás, *Angew. Chem.* **2006**, *118*, 2145–2147; *Angew. Chem. Int. Ed.* **2006**, *45*, 2091–2093.
[33] H. H. Jung, P. E. Floreancig, *J. Org. Chem.* **2007**, *72*, 7359–7366.
[34] A. Couper, D. D. Eley, *Faraday Discuss.* **1950**, *8*, 172.

[35] A. Couper, D. D. Eley, M. J. Hulatt, D. R. Rossington, *Bull. Soc. Chim. Belg.* **1958**, *67*, 343–357.
[36] G. C. Bond, P. A. Sermon, *Gold Bull.* **1973**, *6*, 102–105.
[37] P. A. Sermon, G. C. Bond, P. B. Wells, *J. Chem. Soc. Faraday Trans. 1* **1979**, *75*, 385.
[38] S. Naito, M. Tanimoto, *J. Chem. Soc., Chem. Commun.* **1988**, 832.
[39] H. Ito, K. Takagi, T. Miyahara, M. Sawamura, *Org. Lett.* **2005**, *7*, 3001–3004.
[40] H. Ito, T. Saito, T. Miyahara, C. Zhong, M. Sawamura, *Organometallics* **2009**, *28*, 4829–4840.
[41] S. Biella, M. Rossi, *Chem. Commun.* **2003**, 378–379.
[42] N. Dimitratos, F. Porta, L. Prati, A. Villa, *Catal. Lett.* **2005**, *99*, 181–185.
[43] A. Abad, P. Concepción, A. Corma, H. García, *Angew. Chem.* ***2005****, 117*, 4134–4137; *Angew. Chem. Int. Ed.* **2005**, *44*, 4066–4069.
[44] M. D. Hughes, Y.-J. Xu, P. Jenkins, P. McMorn, P. Landon, D. I. Enache, A. F. Carley, G. A. Attard, G. J. Hutchings, F. King, E. H. Stitt, P. Johnston, K. Griffin, C. J. Kiely, *Nature* **2005**, *437*, 1132–1135.
[45] S. Kanaoka, N. Yagi, Y. Fukuyama, S. Aoshima, H. Tsunoyama, T. Tsukuda, H. Sakurai, *J. Am. Chem. Soc.* **2007**, *129*, 12060–12061.
[46] M. Comotti, C. Della Pina, R. Matarrese, M. Rossi, *Angew. Chem.* **2004**, *116*, 5936–5939; *Angew. Chem. Int. Ed.* **2004**, *43*, 5812–5815.
[47] P. Beltrame, M. Comotti, C. Della Pina, M. Rossi, *Appl. Catal.* **2006**, *297*, 1–7.
[48] Z. Zheng, X. Ma, X. Cheng, K. Zhao, K. Gutman, T. Li, L. Zhang, *Chem. Rev.* **2021**, *121*, 8979–9038.
[49] M. J. Barrett, P. W. Davies, R. S. Grainger, *Org. Biomol. Chem.* **2015**, *13*, 8676–8686.
[50] A. Homs, M. E. Muratore, A. M. Echavarren, *Org. Lett.* **2015**, *17*, 461–463.
[51] C.-H. Chen, Y.-C. Tsai, R.-S. Liu, *Angew. Chem.* **2013**, *125*, 4697–4701; *Angew. Chem. Int. Ed.* **2013**, *52*, 4599–4603.
[52] B. P. Taduri, S. M. A. Sohel, H.-M. Cheng, G.-Y. Lin, R.-S. Liu, *Chem. Commun.* **2007**, 2530–2532.
[53] H. Zhan, L. Zhao, J. Liao, N. Li, Q. Chen, S. Qiu, H. Cao, *Adv. Synth. Catal.* **2015**, *357*, 46–50.
[54] G. Zhang, Y. Peng, L. Cui, L. Zhang, *Angew. Chem.* **2009**, *121*, 3158–3161; *Angew. Chem. Int. Ed.* **2009**, *48*, 3112–3115.
[55] P. Feige, T. de Haro, G. Rusconi, E. Merino, C. Nevado, *Monatsh. Chem.* **2018**, *149*, 749–754.
[56] B. Guan, D. Xing, G. Cai, X. Wan, N. Yu, Z. Fang, L. Yang, Z. Shi, *J. Am. Chem. Soc.* **2005**, *127*, 18004–18005.
[57] J. F. Hartwig, *Organotransition metal chemistry*. *From bonding to catalysis*, University Science Books, Mill Valley, **2010**.
[58] B. M. Rosen, K. W. Quasdorf, D. A. Wilson, N. Zhang, A.-M. Resmerita, N. K. Garg, V. Percec, *Chem. Rev.* **2011**, *111*, 1346–1416.
[59] G. Evano, N. Blanchard, M. Toumi, *Chem. Rev.* **2008**, *108*, 3054–3131.
[60] C. C. C. Johansson Seechurn, M. O. Kitching, T. J. Colacot, V. Snieckus, *Angew. Chem.* **2012**, *124*, 5150–5174; *Angew. Chem. Int. Ed.* **2012**, *51*, 5062–5085.
[61] S. G. Bratsch, *J. Phys. Chem. Ref. Data* **1989**, *18*, 1–21.
[62] A. Nijamudheen, A. Datta, *Chem. Eur. J.* **2020**, *26*, 1442–1487.
[63] B. Sahoo, M. N. Hopkinson, F. Glorius, *J. Am. Chem. Soc.* **2013**, *135*, 5505–5508.
[64] C.-Y. Wu, T. Horibe, C. B. Jacobsen, F. D. Toste, *Nature* **2015**, *517*, 449–454.
[65] Eric Omar Asomoza-Solís, Jonathan Rojas-Ocampo, Rubén Alfredo Toscano, Susana Porcel, *Chem. Commun.* **2016**, *52*, 7295–7298.
[66] Manjur O. Akram, Popat S. Shinde, Chetan C. Chintawar, Nitin T. Patil, *Org. Biomol. Chem.* **2018**, *16*, 2865–2869.
[67] A. Franchino, M. Montesinos-Magraner, A. M. Echavarren, *Bull. Chem. Soc. Jpn.* **2021**, *94*, 1099–1117.

[68] V. J. Catalano, M. A. Malwitz, A. O. Etogo, *Inorg. Chem.* **2004**, *43*, 5714–5724.
[69] E. J. Fernández, A. Laguna, J. M. López-de-Luzuriaga, M. E. Olmos, R. C. Puelles, *Z. Naturforsch. B* **2009**, *64*, 1500–1512.
[70] Hubert Schmidbaur, *Z. Naturforsch. B* **225**, 301–304.
[71] A. Laguna, T. Lasanta, J. M. López-de-Luzuriaga, M. Monge, P. Naumov, M. E. Olmos, *J. Am. Chem. Soc.* **2010**, *132*, 456–457.
[72] T. Osuga, T. Murase, K. Ono, Y. Yamauchi, M. Fujita, *J. Am. Chem. Soc.* **2010**, *132*, 15553–15555.
[73] D. Wang, R. Cai, S. Sharma, J. Jirak, S. K. Thummanapelli, N. G. Akhmedov, H. Zhang, X. Liu, J. L. Petersen, X. Shi, *J. Am. Chem. Soc.* **2012**, *134*, 9012–9019.
[74] Y. Yang, P. Antoni, M. Zimmer, K. Sekine, F. F. Mulks, L. Hu, L. Zhang, M. Rudolph, F. Rominger, A. S. K. Hashmi, *Angew. Chem.* **2019**, *131*, 5183–5187; *Angew. Chem. Int. Ed.* **2019**, *58*, 5129–5133.
[75] M. Jalali, C. J. T. Hyland, A. C. Bissember, B. F. Yates, A. Ariafard, *ACS Catal.* **2021**, *11*, 5795–5807.
[76] Z. Lu, J. Han, G. B. Hammond, B. Xu, *Org. Lett.* **2015**, *17*, 4534–4537.
[77] M. R. Luzung, J. P. Markham, F. D. Toste, *J. Am. Chem. Soc.* **2004**, *126*, 10858–10859.
[78] N. Marion, S. Díez-González, P. de Frémont, A. R. Noble, S. P. Nolan, *Angew. Chem.* **2006**, *118*, 3729–3732. *Angew. Chem. Int. Ed.* **2006**, *45*, 3647–3650.
[79] N. Mézailles, L. Ricard, F. Gagosz, *Org. Lett.* **2005**, *7*, 4133–4136.
[80] L. Ricard, F. Gagosz, *Organometallics* **2007**, *26*, 4704–4707.
[81] F. Li, N. Wang, L. Lu, G. Zhu, *J. Org. Chem.* **2015**, *80*, 3538–3546.
[82] A. Almássy, C. E. Nagy, A. C. Bényei, F. Joó, *Organometallics* **2010**, *29*, 2484–2490.
[83] E. Tomás-Mendivil, P. Y. Toullec, J. Borge, S. Conejero, V. Michelet, V. Cadierno, *ACS Catal.* **2013**, *3*, 3086–3098.
[84] K. Belger, N. Krause, *Eur. J. Org. Chem.* **2015**, *2015*, 220–225.
[85] X. Yao, C.-J. Li, *Org. Lett.* **2006**, *8*, 1953–1955.
[86] X. Wang, Z. Yao, S. Dong, F. Wei, H. Wang, Z. Xu, *Org. Lett.* **2013**, *15*, 2234–2237.
[87] W. Fang, M. Presset, A. Guérinot, C. Bour, S. Bezzenine-Lafollée, V. Gandon, *Chem. Eur. J.* **2014**, *20*, 5439–5446.
[88] Weizhen Fang, Marc Presset, Amandine Guérinot, Christophe Bour, Sophie Bezzenine-Lafollée, Vincent Gandon, *Org. Chem. Front.* **2014**, *1*, 608–613.
[89] F. Kleinbeck, F. D. Toste, *J. Am. Chem. Soc.* **2009**, *131*, 9178–9179.
[90] C. García-Morales, B. Ranieri, I. Escofet, L. López-Suarez, C. Obradors, A. I. Konovalov, A. M. Echavarren, *J. Am. Chem. Soc.* **2017**, *139*, 13628–13631.
[91] René Pretorius, Manuel R. Fructos, Helge Müller-Bunz, Robert A. Gossage, Pedro J. Pérez, Martin Albrecht, *Dalton Trans.* **2016**, *45*, 14591–14602.
[92] L.-Z. Dai, M. Shi, *Chem. Eur. J.* **2010**, *16*, 2496–2502.
[93] Ayhan S. Demir, Mustafa Emrullahoğlu, Kerem Buran, *Chem. Commun.* **2010**, *46*, 8032–8034.
[94] A. Guérinot, W. Fang, M. Sircoglou, C. Bour, S. Bezzenine-Lafollée, V. Gandon, *Angew. Chem.* **2013**, *125*, 5960–5964; *Angew. Chem. Int. Ed.* **2013**, *52*, 5848–5852.
[95] W. Fang, *Org. Synth.* **2015**, *92*, 117–130.
[96] C. Bour, V. Gandon, *Synlett* **2015**, *26*, 1427–1436.
[97] J. Wolf, F. Huber, N. Erochok, F. Heinen, V. Guérin, C. Y. Legault, S. F. Kirsch, S. M. Huber, *Angew. Chem.* **2020**, *132*, 16638–16643; *Angew. Chem. Int. Ed.* **2020**, *59*, 16496–16500.
[98] S. H. Jungbauer, S. M. Huber, *J. Am. Chem. Soc.* **2015**, *137*, 12110–12120.
[99] A. S. Mikherdov, M. Jin, H. Ito, *Chem. Sci.* **2023**, *14*, 4485–4494.

[100] O. Seppänen, S. Aikonen, M. Muuronen, C. Alamillo-Ferrer, J. Burés, J. Helaja, *Chem. Commun.* **2020**, *56*, 14697–14700.
[101] A. Franchino, À. Martí, S. Nejrotti, A. M. Echavarren, *Chem. Eur. J.* **2021**, *27*, 11989–11996.
[102] A. Franchino, À. Martí, A. M. Echavarren, *J. Am. Chem. Soc.* **2022**, *144*, 3497–3509.
[103] Z. Zhang, V. Smal, P. Retailleau, A. Voituriez, G. Frison, A. Marinetti, X. Guinchard, *J. Am. Chem. Soc.* **2020**, *142*, 3797–3805.
[104] A. Amgoune, D. Bourissou, *Chem. Commun*. **2011**, *47*, 859–871.
[105] J. S. Jones, F. P. Gabbai, *Chem. Eur. J.* **2017**, *23*, 1136–1144.
[106] M. A. Eltester, H. Gildenast, K. Rabatinová, C. Pütz, C. Cremer, P. Lanzerath, J. P. Schroers, M. E. Tauchert, *Chem. Commun.* **2023**, *59*, 5459–5462.
[107] L. C. Wilkins, Y. Kim, E. D. Litle, F. P. Gabbaï, *Angew. Chem.* **2019**, *131*, 18434–18438; *Angew. Chem. Int. Ed.* **2019**, *58*, 18266–18270.
[108] E. D. Litle, F. P. Gabbaï, *Chem. Commun.* **2023**, *59*, 603–606.
[109] W.-C. Liu, F. P. Gabbaï, *Chem. Sci.* **2023**, *14*, 277–283.
[110] J. C. Pérez-Sánchez, R. P. Herrera, M. C. Gimeno, *Eur J. Inorg. Chem.* **2022**, *2022*.
[111] L. Hettmanczyk, S. Manck, C. Hoyer, S. Hohloch, B. Sarkar, *Chem. Commun.* **2015**, *51*, 10949–10952.
[112] C. A. Tolman, *Chem. Rev.* **1977**, *77*, 313–348.
[113] Daniela I. Bezuidenhout, Belinda van der Westhuizen, Amos J. Rosenthal, Michael Wörle, David C. Liles, Israel Fernández, *Dalton Trans.* **2013**, *43*, 398–401.
[114] S. Klenk, S. Rupf, L. Suntrup, M. van der Meer, B. Sarkar, *Organometallics* **2017**, *36*, 2026–2035.
[115] S. Vanicek, M. Podewitz, J. Stubbe, D. Schulze, H. Kopacka, K. Wurst, T. Müller, P. Lippmann, S. Haslinger, H. Schottenberger, K. R. Liedl, I. Ott, B. Sarkar, B. Bildstein, *Chem. Eur. J.* **2018**, *24*, 3742–3753.
[116] S. Ibáñez, M. Poyatos, L. N. Dawe, D. Gusev, E. Peris, *Organometallics* **2016**, *35*, 2747–2758.
[117] A. Straube, P. Coburger, M. Michak, M. R. Ringenberg, E. Hey-Hawkins, *Dalton Trans.* **2020**, *49*, 16667–16682.
[118] S. D. Waniek, C. Förster, K. Heinze, *Eur. J. Inorg. Chem.* **2022**, *2022*.
[119] L. Rocchigiani, M. Bochmann, *Chem. Rev.* **2021**, *121*, 8364–8451.
[120] J. C. Pérez-Sánchez, R. P. Herrera, M. Concepción Gimeno, *Dalton Trans.* **2024**, *53*, 382–393.
[121] S. Preiß, A. Päpcke, L. Burkhardt, L. Großmann, S. Lochbrunner, M. Bauer, T. Opatz, K. Heinze, *Chem. Eur. J.* **2019**, *25*, 5940–5949.
[122] A. Laguna, M. Laguna, *Coord. Chem. Rev.* **1999**, *193-195*, 837–856.
[123] A. A. Mohamed, H. E. Abdou, J. P. Fackler, *Coord. Chem. Rev.* **2010**, *254*, 1253–1259.
[124] V. W.-W. Yam, E. C.-C. Cheng, *Chem. Soc. Rev.* **2008**, *37*, 1806–1813.
[125] N. Bartlett, *Gold Bull.* **1998**, *31*, 22–25.
[126] K. Heinze, *Angew. Chem.* **2017**, *129*, 16342–16350; *Angew. Chem. Int. Ed.* **2017**, *56*, 16126–16134.
[127] D. B. Dell'Amico, F. Calderazzo, F. Marchetti, S. Merlino, *J. Chem. Soc., Dalton Trans.* **1982**, 2257.
[128] W. Denner, H. Schulz, H. d'Amour, *Acta Crystallogr. A* **1979**, *35*, 360–365.
[129] N. Kojima, M. Hasegawa, H. Kitagawa, T. Kikegawa, O. Shimomura, *J. Am. Chem. Soc.* **1994**, *116*, 11368–11374.
[130] K. P. Lindquist, A. Eghdami, C. R. Deschene, A. J. Heyer, J. Wen, A. G. Smith, E. I. Solomon, Y. S. Lee, J. B. Neaton, D. H. Ryan, H. I. Karunadasa, *Nat. Chem.* **2023**, 1–7.
[131] M. S. Wickleder, *Z. Anorg. Allg. Chem.* **2001**, *627*, 2112.
[132] P. Jerabek, A. Santhosh, P. Schwerdtfeger, *Inorg. Chem.* **2022**, *61*, 13077–13084.
[133] S. H. Elder, G. M. Lucier, F. J. Hollander, N. Bartlett, *J. Am. Chem. Soc.* **1997**, *119*, 1020–1026.

[134] J. D. Basil, H. H. Murray, J. P. Fackler, J. Tocher, A. M. Mazany, B. Trzcinska-Bancroft, H. Knachel, D. Dudis, T. J. Delord, D. Marler, *J. Am. Chem. Soc.* **1985**, *107*, 6908–6915.
[135] Vivian Wing-Wah Yam, Sam Wing-Kin Choi, Kung-Kai Cheung, *Chem. Commun.* **1996**, 1173–1174.
[136] D.-A. Roşca, D. A. Smith, D. L. Hughes, M. Bochmann, *Angew. Chem.* **2012**, *124*, 10795–10798; *Angew. Chem. Int. Ed.* **2012**, *51*, 10643–10646.
[137] D.-A. Roşca, M. Bochmann, *Organometallics* **2016**, *35*, 27–31.
[138] T. Dann, D.-A. Roşca, J. A. Wright, G. G. Wildgoose, M. Bochmann, *Chem. Commun.* **2013**, *49*, 10169–10171.
[139] S. Seidel, K. Seppelt, *Science* **2000**, *290*, 117–118.
[140] T. Drews, S. Seidel, K. Seppelt, *Angew. Chem.* **2002**, *114*, 470–473; *Angew. Chem. Int. Ed.* **2002**, *41*, 454–456.
[141] K. Seppelt, *Z. Anorg. Allg. Chem.* **2003**, *629*, 2427–2430.
[142] W. P. Hu, C. H. Huang, *J. Am. Chem. Soc.* **2001**, *123*, 2340–2343.
[143] S. Berski, Z. Latajka, J. Andrés, *Chem. Phys. Lett.* **2002**, *356*, 483–489.
[144] L. Xinying, *J. Chem. Phys.* **2012**, *137*, 124301.
[145] I.-C. Hwang, K. Seppelt, *Z. Anorg. Allg. Chem.* **2002**, *628*, 765.
[146] A. J. Blake, J. A. Greig, A. J. Holder, T. I. Hyde, A. Taylor, M. Schröder, *Angew. Chem.* **1990**, *102*, 203–204; *Angew. Chem. Int. Ed.* **1990**, *29*, 197–198.
[147] M. A. Halcrow, *Chem. Soc. Rev.* **2013**, *42*, 1784–1795.
[148] D. Huang, X. Zhang, E. J. L. McInnes, J. McMaster, A. J. Blake, E. S. Davies, J. Wolowska, C. Wilson, M. Schröder, *Inorg. Chem.* **2008**, *47*, 9919–9929.
[149] M. Kampf, J. Griebel, R. Kirmse, *Z. anorg. allg. Chem.* **2004**, *630*, 2669–2676.
[150] J. L. Shaw, J. Wolowska, D. Collison, J. A. K. Howard, E. J. L. McInnes, J. McMaster, A. J. Blake, C. Wilson, M. Schröder, *J. Am. Chem. Soc.* **2006**, *128*, 13827–13839.
[151] S. Preiß, C. Förster, S. Otto, M. Bauer, P. Müller, D. Hinderberger, H. Hashemi Haeri, L. Carella, K. Heinze, *Nat. Chem.* **2017**, *9*, 1249–1255.
[152] R. G. Pearson, *Proc. Natl. Acad. Sci. U.S.A.* **1975**, *72*, 2104–2106.
[153] A. Johnson, R. J. Puddephatt, *J. Chem. Soc., Dalton Trans.* **1975**, 115.
[154] A. Johnson, R. J. Puddephatt, *J. Chem. Soc., Dalton Trans.* **1976**, 1360.
[155] S. Kim, J. Rojas-Martin, F. D. Toste, *Chem. Sci.* **2016**, *7*, 85–88.
[156] L. Huang, M. Rudolph, F. Rominger, A. S. K. Hashmi, *Angew. Chem.* **2016**, *128*, 4888–4893; *Angew. Chem. Int. Ed.* **2016**, *55*, 4808–4813.
[157] M. N. Hopkinson, A. Tlahuext-Aca, F. Glorius, *Acc. Chem. Res.* **2016**, *49*, 2261–2272.
[158] X. Shu, M. Zhang, Y. He, H. Frei, F. D. Toste, *J. Am. Chem. Soc.* **2014**, *136*, 5844–5847.
[159] A. Tlahuext-Aca, M. N. Hopkinson, B. Sahoo, F. Glorius, *Chem. Sci.* **2016**, *7*, 89–93.
[160] M. S. Winston, W. J. Wolf, F. D. Toste, *J. Am. Chem. Soc.* **2014**, *136*, 7777–7782.
[161] B. K. Maiti, L. B. Maia, J. J. Moura, *J. Inorg. Biochem.* **2022**, *227*, 111687.
[162] M. R. Filipovic, J. Zivanovic, B. Alvarez, R. Banerjee, *Chem. Rev.* **2018**, *118*, 1253–1337.
[163] R. Hille, J. Hall, P. Basu, *Chem. Rev.* **2014**, *114*, 3963–4038.
[164] H. Beinert, *Eur. J. Biochem.* **2000**, *267*, 5657–5664.
[165] E. I. Stiefel, *ACS Symp. Ser. Am. Chem. Soc.* **1996**, *653*, 2–38.
[166] M. K. Johnson, *Curr. Opin. Chem. Biol.* **1998**, *2*, 173–181.
[167] D. Kessler, *FEMS Microbiol. Rev.* **2006**, *30*, 825–840.
[168] B. M. Hoffman, D. Lukoyanov, Z.-Y. Yang, D. R. Dean, L. C. Seefeldt, *Chem. Rev.* **2014**, *114*, 4041–4062.
[169] J. Liu, S. Chakraborty, P. Hosseinzadeh, Y. Yu, S. Tian, I. Petrik, A. Bhagi, Y. Lu, *Chem. Rev.* **2014**, *114*, 4366–4469.

[170] H. Beinert, J. Biol. Inorg. Chem. **2000**, *5*, 2–15.
[171] K. Brown, K. Djinovic-Carugo, T. Haltia, I. Cabrito, M. Saraste, J. Moura, I. Moura, M. Tegoni, C. Cambillau, *J. Biol. Chem.* **2000**, *275*, 41133–41136.
[172] R. Hille, *Chem. Rev.* **1996**, *96*, 2757–2816.
[173] J. A. Hernandez, S. J. George, L. M. Rubio, *Biochem.* **2009**, *48*, 9711–9721.
[174] E. I. Stiefel, T. R. Halbert, C. L. Coyle, L. Wei, W.-H. Pan, T. C. Ho, R. R. Chianelli, M. Daage, *Polyhedron* **1989**, *8*, 1625–1629.
[175] E. I. Stiefel, *Pure Appl. Chem.* **1998**, *70*, 889–896.
[176] C. Iobbi-Nivol, S. Leimkühler, *Biochim. Biophys. Acta Bioenerget.* **2013**, *1827*, 1086–1101.
[177] G. Schwarz, R. R. Mendel, *Annu. Rev. Plant Biol.* **2006**, *57*, 623–647.
[178] C. Feng, G. Tollin, J. H. Enemark, *Biochim. Biophys. Acta Proteins Proteom.* **2007**, *1774*, 527–539.
[179] R. Hille, *Biochim. Biophys. Acta Bioenerget.* **1994**, *1184*, 143–169.
[180] K. Heinze, *Coord. Chem. Rev.* **2015**, *300*, 121–141.
[181] E. Hernandez-Marin, T. Ziegler, *Inorg. Chem.* **2009**, *48*, 1323–1333.
[182] Y. Ha, A. L. Tenderholt, R. H. Holm, B. Hedman, K. O. Hodgson, E. I. Solomon, *J. Am. Chem. Soc.* **2014**, *136*, 9094–9105.
[183] A. K. Rappé, W. A. Goddard, *Nature* **1980**, *285*, 311–312.
[184] A. K. Rappe, W. A. Goddard, *J. Am. Chem. Soc.* **1982**, *104*, 3287–3294.
[185] T. Schindler, A. Sauer, T. P. Spaniol, J. Okuda, *Organometallics* **2018**, *37*, 4336–4340.
[186] R. H. Holm, *Coord. Chem. Rev.* **1990**, *100*, 183–221.
[187] K. Johnson-Winters, G. Tollin, J. H. Enemark, *Biochem.* **2010**, *49*, 7242–7254.
[188] R. Hille, S. Dingwall, J. Wilcoxen, *J. Biol. Inorg. Chem.* **2015**, *20*, 243–251.
[189] J.-H. Jeoung, B. M. Martins, H. Dobbek, *Metalloproteins*, Humana Press, New York, **2019**.
[190] G. Mrsdorf, K. Frunzke, D. Gadkari, O. Meyer, *Biodegradation* **1992**, *3*.
[191] J. M. Moxley, K. A. Smith, *Soil Biol. Biochem.* **1998**, *30*, 65–79.
[192] H. Dobbek, L. Gremer, O. Meyer, R. Huber, *Proc. Natl. Acad. Sci. U.S.A.* **1999**, *96*, 8884–8889.
[193] H. Dobbek, L. Gremer, R. Kiefersauer, R. Huber, O. Meyer, *Proc. Natl. Acad. Sci. U.S.A.* **2002**, *99*, 15971–15976.
[194] P. Hänzelmann, H. Dobbek, L. Gremer, R. Huber, O. Meyer, *J. Mol. Biol.* **2000**, *301*, 1221–1235.
[195] B. Zhang, C. F. Hemann, R. Hille, *J. Biol. Chem.* **2010**, *285*, 12571–12578.
[196] P. Kalimuthu, M. Petitgenet, D. Niks, S. Dingwall, J. R. Harmer, R. Hille, P. V. Bernhardt, *Biochim. Biophys. Acta Bioenerget.* **2020**, *1861*, 148118.
[197] P. E. M. Siegbahn, A. F. Shestakov, *J. Comput. Chem.* **2005**, *26*, 888–898.
[198] M. Hofmann, J. K. Kassube, T. Graf, *J. Biol. Inorg. Chem.* **2005**, *10*, 490–495.
[199] Kai Xu, Hajime Hirao, *Phys. Chem. Chem. Phys.* **2018**, *20*, 18938–18948.
[200] A. G. Ritacca, A. Rovaletti, G. Moro, U. Cosentino, U. Ryde, E. Sicilia, C. Greco, *ACS Catal.* **2022**, *12*, 7336–7343.
[201] S. Sarkar, S. Mishra, *Coord. Chem. Rev.* **1984**, *59*, 239–264.
[202] Amit Majumdar, *Dalton Trans.* **2014**, *43*, 12135–12145.
[203] D. Ghosh, S. Sinhababu, B. D. Santarsiero, N. P. Mankad, *J. Am. Chem. Soc.* **2020**, *142*, 12635–12642.
[204] A. Majumdar, *Dalton trans.* **2014**, *43*, 8990–9003.
[205] J.-J. Wang, S. Groysman, S. C. Lee, R. H. Holm, *J. Am. Chem. Soc.* **2007**, *129*, 7512–7513.
[206] R. H. Holm, E. I. Solomon, A. Majumdar, A. Tenderholt, *Coord. Chem. Rev.* **2011**, *255*, 993–1015.
[207] J. H. Enemark, J. J. A. Cooney, J.-J. Wang, R. H. Holm, *Chem. Rev.* **2004**, *104*, 1175–1200.
[208] M. Takuma, Y. Ohki, K. Tatsumi, *Inorg. Chem.* **2005**, *44*, 6034–6043.

[209] S. Groysman, A. Majumdar, S.-L. Zheng, R. H. Holm, *Inorg. Chem.* **2010**, *49*, 1082–1089.
[210] M. Bose, G. Moula, A. Begum, S. Sarkar, *Inorg. Chem.* **2011**, *50*, 3852–3854.
[211] C. Gourlay, D. J. Nielsen, J. M. White, S. Z. Knottenbelt, M. L. Kirk, C. G. Young, *J. Am. Chem. Soc.* **2006**, *128*, 2164–2165.
[212] C. Gourlay, D. J. Nielsen, D. J. Evans, J. M. White, C. G. Young, *Chem. Sci.* **2018**, *9*, 876–888.
[213] U. I. Kaluarachchige Don, S. S. Kurup, T. S. Hollingsworth, C. L. Ward, R. L. Lord, S. Groysman, *Inorg. Chem.* **2021**, *60*, 14655–14666.
[214] U. I. Kaluarachchige Don, Z. Palmer, C. L. Ward, R. L. Lord, S. Groysman, *Inorg. Chem.* **2023**, *62*, 15063–15075.
[215] A. Mouchfiq, T. K. Todorova, S. Dey, M. Fontecave, V. Mougel, *Chem. Sci.* **2020**, *11*, 5503–5510.
[216] J. P. Donahue, C. R. Goldsmith, U. Nadiminti, R. H. Holm, *J. Am. Chem. Soc.* **1998**, *120*, 12869–12881.
[217] O. Back, *2-Iminopyrrolate complexes of alkali and transition metal ions. From luminescent and redox-active complexes to biomimetics*. Dissertation, Johannes Gutenberg-Universität Mainz, **2019**.
[218] K. Hüttinger, C. Förster, T. Bund, D. Hinderberger, K. Heinze, *Inorg. Chem.* **2012**, *51*, 4180–4192.
[219] V. Prelog, G. Helmchen, *Angew. Chem.* **1982**, *94*, 614–631; *Angew. Chem. Int. Ed.* **1982**, *21*, 567–583.
[220] B. P. Block, W. H. Powell, W. C. Fernelius, *Inorganic chemical lnomenclature: principles and practice*, American Chemical Society, Washington, DC, **1990**.
[221] A. von Zelewsky, *Stereochemistry of Coordination Compounds*, John Wiley & Sons Ltd., New York, **1996**.
[222] R. S. Cahn, C. Ingold, V. Prelog, *Angew. Chem.* **1966**, *78*, 413–447; *Angew. Chem. Int. Ed.* **1966**, *5*, 385–415.
[223] According to the Cahn-Ingold-Prelog system for octahedral complexes the following configuration index is applied: OC-6-*a*-*b* with the priority $S > N^{pyrrolato} > N^{imine}$ used. The index *a* refers to the ligand priority of the ligand *trans* to the ligand of the highest priority (of the axial ligands), the index *b* refer to the ligand priority *trans* to the ligand of the equatorial plane which has the highest priority of these four equatorial ligands.[218] In the publication[218], for one complex, two oxido ligands were enumerated for the sake of better comparison with other complexes in the same publication. The same practice was taken up in the dissertation[217] and subsequently in this work. Correctly for complexes **1**-**3** the OC-6-4-4 isomers should be described as OC-6-3-3, since there is no distinguished fourth donor atom present.[218]
[224] I. Buddenberg, O. Buddenberg, P. Hartter, C. Kropf, P. Müller, *Houben-Weyl Methods of Organic Chemistry Vol. IV/1a, Nonmetallic Oxidation Agents,* Thieme, Stuttgart, **2014**.
[225] C. J. Erwin Riedel, *Anorganische Chemie*. *8. Auflage*, Walter de Gruyter, Berlin / New York, **2011**.
[226] A. Friedrich, H. Küppers, P. Müller, H. Müller-Dolezal, G. Rotermund, *Houben-Weyl Methods of Organic Chemistry Vol. IV/1b*, *Metallic and Organic Oxidation Agents, Antioxidants,* Thieme, Stuttgart, **2014**.
[227] J. H. Simpson, *Organic Structure Determination Using 2-D NMR Spectroscopy*, Academic Press, Cambridge, Massachusetts**, 2012**.
[228] L. Braunschweiler, R. Ernst, *J. Magn. Reson.* **1983**, *53*, 521–528.
[229] G. Bodenhausen, D. J. Ruben, *Chem. Phys. Lett.* **1980**, *69*, 185–189.
[230] N. G. Connelly, W. E. Geiger, *Chem. Rev.* **1996**, *96*, 877–910.
[231] I. K. Dhawan, J. H. Enemark, *Inorg. Chem.* **1996**, *35*, 4873–4882.

[232] G. L. Wilson, R. J. Greenwood, J. R. Pilbrow, J. T. Spence, A. G. Wedd, *J. Am. Chem. Soc.* **1991**, *113*, 6803–6812.
[233] R. E. Banks, S. N. Mohialdin-Khaffaf, G. S. Lal, I. Sharif, R. G. Syvret, *J. Chem. Soc., Chem. Commun.* **1992**, 595.
[234] K. Yang, M. Song, A. I. M. Ali, S. M. Mudassir, H. Ge, *Chem. Asian J.* **2020**, *15*, 729–741.
[235] F. Ghorbani, S. A. Harry, J. N. Capilato, C. R. Pitts, J. Joram, G. N. Peters, J. D. Tovar, I. Smajlagic, M. A. Siegler, T. Dudding, T. Lectka, *J. Am. Chem. Soc.* **2020**, *142*, 14710–14724.
[236] Y. Chen, H. Qi, N. Chen, D. Ren, J. Xu, Z. Yang, *J. Org. Chem.* **2019**, *84*, 9044–9050.
[237] S. P. Cramer, R. Hille, *J. Am. Chem. Soc.* **1985**, *107*, 8164–8169.
[238] R. Hille, G. N. George, M. K. Eidsness, S. P. Cramer, *Inorg. Chem.* **1989**, *28*, 4018–4022.
[239] R. Huber, P. Hof, R. O. Duarte, J. J. Moura, I. Moura, M. Y. Liu, J. LeGall, R. Hille, M. Archer, M. J. Romão, *Proc. Natl. Acad. Sci. U.S.A.* **1996**, *93*, 8846–8851.
[240] A. Thapper, J. P. Donahue, K. B. Musgrave, M. W. Willer, E. Nordlander, B. Hedman, K. O. Hodgson, R. H. Holm, *Inorg. Chem.* **1999**, *38*, 4104–4114.
[241] C. J. Doonan, D. J. Nielsen, P. D. Smith, J. M. White, G. N. George, C. G. Young, *J. Am. Chem. Soc.* **2006**, *128*, 305–316.
[242] H. Schmidbaur, A. Schier, *Chem. Soc. Rev.* **2012**, *41*, 370–412.
[243] O. Back, C. Förster, T. Basché, K. Heinze, *Chem. Eur. J.* **2019**, *25*, 6542–6552.
[244] G. R. Fulmer, A. J. M. Miller, N. H. Sherden, H. E. Gottlieb, A. Nudelman, B. M. Stoltz, J. E. Bercaw, K. I. Goldberg, *Organometallics* **2010**, *29*, 2176–2179.
[245] STOE & Cie. X-Area, *STOE & Cie GmbH*, Darmstadt, Germany.
[246] R. H. Blessing, *Acta Crystallogr. A* **1995**, *51 (Pt 1)*, 33–38.
[247] A. L. Spek, *Acta Crystallogr. D* **2009**, *65*, 148–155.
[248] G. M. Sheldrick *Acta Crystallogr. A* **2015**, *71*, 3–8.
[249] G. M. Sheldrick, *Acta Crystallogr. C* **2015**, *71*, 3–8.
[250] G. M. Sheldrick, *Acta Crystallogr. A* **2008**, *64*, 112–122.
[251] C. B. Hübschle, G. M. Sheldrick, B. Dittrich, *J.Appl. Crystallogr.* **2011**, *44*, 1281–1284.
[252] F. Neese, *Wiley Interdiscip. Rev. Comput. Mol. Sci.* **2012**, *2*, 73–78.
[253] A. D. Becke, *J. Chem. Phys.* **1993**, *98*, 5648–5652.
[254] Chengteh Lee, Weitao Yang, Robert G. Parr, *Phys. Rev. B* **1988**, *37*, 785.
[255] B. Miehlich, A. Savin, H. Stoll, H. Preuss, *Chem. Phys. Lett.* **1989**, *157*, 200–206.
[256] F. Neese, F. Wennmohs, A. Hansen, U. Becker, *Chem. Phys.* **2009**, *356*, 98–109.
[257] R. Izsák, F. Neese, *J. Chem. Phys.* **2011**, *135*, 144105.
[258] D. A. Pantazis, X.-Y. Chen, C. R. Landis, F. Neese, *J. Chem. Theory Comput.* **2008**, *4*, 908–919.
[259] V. Barone, M. Cossi, *J. Phys. Chem. A* **1998**, *102*, 1995–2001.
[260] S. Miertuš, E. Scrocco, J. Tomasi, *Chem. Phys.* **1981**, *55*, 117–129.
[261] F. Weigend, R. Ahlrichs, *Phys. Chem*. *Chem. Phys.* **2005**, *7*, 3297–3305.
[262] F. Weigend, *Phys. Chem*. *Chem. Phys.* **2006**, *8*, 1057–1065.
[263] S. Grimme, J. Antony, S. Ehrlich, H. Krieg, *J. Chem. Phys.* **2010**, *132*, 154104.
[264] S. Grimme, S. Ehrlich, L. Goerigk, *J. Comput. Chem.* **2011**, *32*, 1456–1465.

6 Supporting Information

6.1 Supporting Information to chapter "Synthesis of biomimetic molybdenum model complexes for the CODH"

General procedures. All reactions were performed under an inert argon atmosphere. THF was distilled from potassium, acetonitrile was distilled from calcium hydride and petroleum ether 40-60°C distilled from sodium. $K_2MoO_2S_2$, $H^{tBu}L$ and $K^{tBu}L$ were prepared according to literature procedures.[217],[218],[243] $^{i}Pr_3SiCl$ (98 %) and $Ph_2{}^{t}BuSiCl$ (98 %) were dried over molecular sieve (3 Å). All other reagents were used as received from commercial suppliers (Acros, Sigma-Aldrich). NMR spectra were recorded on a Bruker Avance DRX 400 spectrometer at 400.31 MHz (^{1}H), 100.657 MHz (^{13}C). All resonances are reported in ppm versus tetramethylsilane and referenced against the solvent signal as internal standard (C_6D_6: ^{1}H δ (ppm) = 7.16, ^{13}C δ (ppm) = 128.06, CD_3CN: ^{1}H δ (ppm) = 1.94, δ (ppm) = DMSO-d^6: 2.50).[244]

UV/vis-spectra were recorded on a Varian Cary 5000 spectrometer in quartz glass cuvettes with 1 cm path length under argon atmosphere. Electrochemical experiments were carried out with a BioLogic SP-50 voltammetric analyzer using platinum wire as counter and working electrodes and a 0.001 M $Ag/AgNO_3$ electrode as reference electrode.

The cyclic voltammetry measurements were carried out at a scan rate of 100 mV s^{-1} using 0.1 M $[nBu_4N][B(C_6F_5)_4]$ as supporting electrolyte in acetonitrile. Potentials are referenced against the ferrocene/ferrocenium couple ($E_{1/2}$ = 220 ± 5 mV under the experimental conditions).

Intensity data of **5** was collected with a STOE IPDS-2T diffractometer from STOE & CIE GmbH with an Oxford cooling system using Mo K_α radiation (λ = 0.71073 Å). The diffraction frames were integrated using the STOE X-area[245] software package and were corrected for absorption with MULABS[246] of the PLATON software package[247]. The structures were solved with SHELXT[248] and refined by the full-matrix method based on F^2 using SHELXL[249] of the SHELX [250] software package and the ShelXle[251] graphical interface. All non-hydrogen atoms were refined anisotropically, while the positions of all hydrogen atoms were generated with appropriate geometric constraints and allowed to ride on their respective parent atoms with fixed isotropic thermal parameters.[118]

DFT calculations were carried out using the ORCA program package (version 4.1.2).[252] All calculations were performed using the B3LYP functionals[253]–[255] and employed the RIJCOSX approximation.[256],[257] Relativistic effects were calculated at the zeroth order regular approximation (ZORA) level.[258] The ZORA keyword automatically invokes relativistically adjusted basis sets. To account for solvent effects, a conductor-like screening model (CPCM) modelling THF was used in all calculations.[259],[260] Geometry

optimizations were performed using Ahlrichs' split-valence triple-ξ basis set ZORA-def2/J-old-TZVP.[261],[262] Atom-pairwise dispersion correction was performed with the Becke-Johnson damping scheme (D3BJ).[263],[264] The presence of energy minima was checked by numerical frequency calculations.

Synthesis of $Mo^{IV}(^{tBu}L)_2(SSi(^{i}Pr)_3)_2$ 2. $K_2MoO_2S_2$ (100 mg, 0.37 mmol) was added to a solution of $K^{tBu}L$ (195.5 mg, 0.74 mmol) in THF. $^{i}Pr_3SiCl$ (0.47 mL, 2.20 mmol) was added dropwise while stirring. The solution was stirred over night at room temperature. The red solution was then filtered and all volatiles removed in vacuum. The red oily residue was re-dissolved in petroleum ether 40-60°C (10 mL) and the solution filtered for a second time. After removing all volatiles in vacuum to yield **2** (128.53 mg, 74% yield) as a red-brown oil.

^{1}H-NMR (C_6D_6, 400 MHz, 300 K); δ(ppm) = 8.33 (s, 2H, H^7), 7.35 (d, J = 8.5 Hz, 4H, $H^{3,5}$), 7.22 (d, J = 8.5 Hz 4H, $H^{2,6}$), 7.11 (m, 2H, H^{11}), 7.01 (dd, J = 3.5 Hz, 1.4 Hz, 2H, H^9), 6.45 (t, J = 3.1 Hz, 2H, H^{10}), 1.91 (sept, 6H, H^{14}), 1.31 (s, 18H, H^{13}), 1.16 (m, 36H, H^{15}).

13C-{^{1}H}-NMR (C_6D_6, 100 MHz, 300 K); δ(ppm) = 150.3 (C^7), 150.1 (C^4), 147.69 (C^1), 137.1 (C^8), 131.8 (C^{11}), 126.1 ($C^{3,5}$), 122.4 (C^9), 120.4 ($C^{2,6}$), 111.5 (C^{10}), 34.2 (C^{12}), 31.3 (C^{13}), 18.3 (C^{15}), 13.7 (C^{14}).

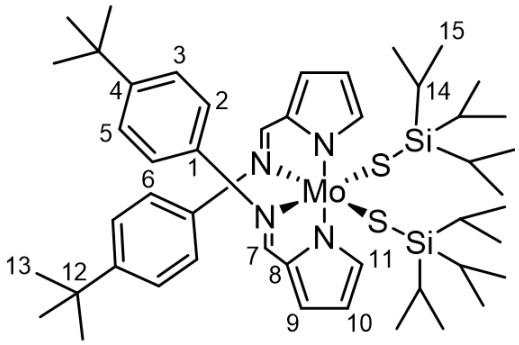

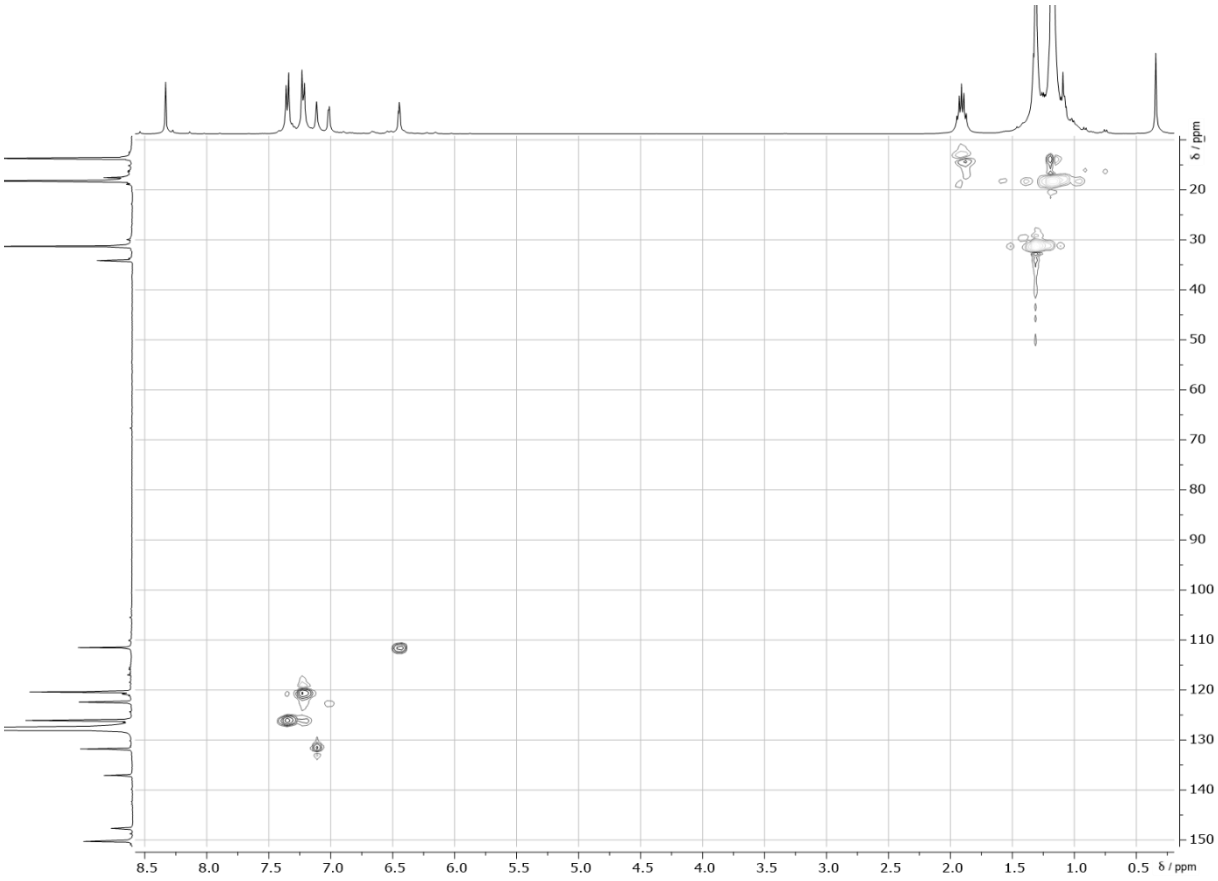

Figure 1: ^{13}C-{^{1}H}-HSQC-NMR spectrum of complex **2** in C_6D_6.

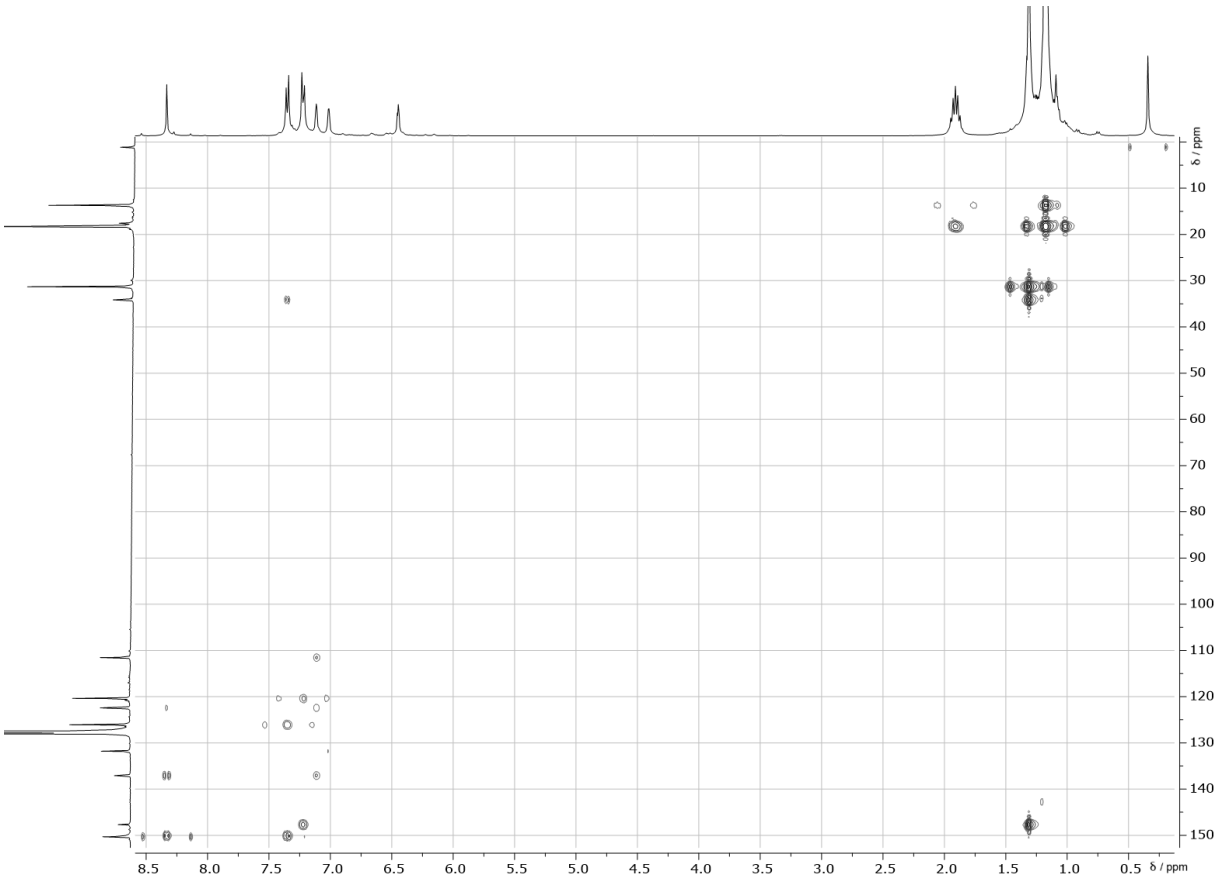

Figure 2: ^{13}C-{^{1}H}-HMBC-NMR spectrum of complex **2** in C_6D_6.

Synthesis of $Mo^{IV}(^{tBu}L)_2(SSi(^tBu)(Ph)_2)_2$ 3. $K_2MoO_2S_2$ (100 mg, 0.37 mmol) was added to a solution of $K^{tBu}L$ (195.5 mg, 0.74 mmol) in THF. $^tBu(Ph)_2SiCl$ (0.577 mL, 2.20 mmol) was added dropwise while stirring. The solution was stirred over night at room temperature. The red solution was then filtered and all volatiles removed in vacuum. The red oily residue was re-dissolved in petroleum ether 40-60°C (10 mL) and the solution filtered for a second time. After removing all volatiles in vacuum, **3** was yielded (351 mg, 87% yield) as a red-brown oil.

^{1}H-NMR (C_6D_6, 400 MHz, 300 K); δ(ppm) = 8.17 (s, 2H, H^7), 7.67 (d, J = 5.9 Hz, 4H, H^a), 7.48 (d, J = 2.3 Hz, 1H, H^9), 7.45 (s, 1H, H^{11}), 7.22-7.12 (m, 8H, $H^{3,5/b/c}$), 6.59 (d, J = 8.5 Hz, 2H, $H^{2,6}$), 6.56 (t, J = 3.2 Hz, 1H, H^{10}), 1.18 (s, 9H, H^{13}), 1.14 (s, 9H, H^e).

13C-{^{1}H}-NMR (C_6D_6, 100 MHz, 300 K); δ(ppm) = 150.0 (C^7), 147.6 (C^4), 137.8 (C^8), 135.1 (C^a), 134.1 (C^1), 131.3 (C^{11}), 129.6 (C^{Ph}), 128.1 (2 C^{Ph}), 125.9 ($C^{3,5}$), 120.5 ($C^{2,6}$), 118.6 (C^9), 112.8 (C^{10}), 34.3 (C^{12}), 31.5 (C^{13}), 28.2 (C^e), 19.9 (C^f).

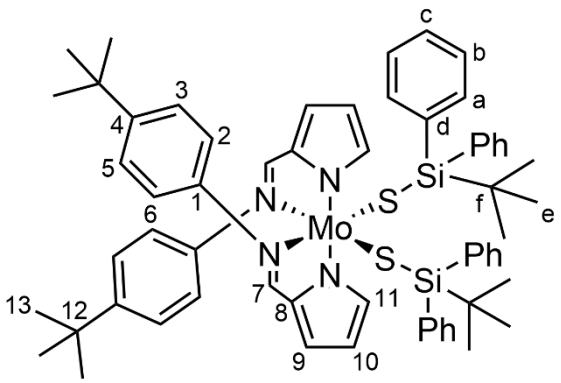

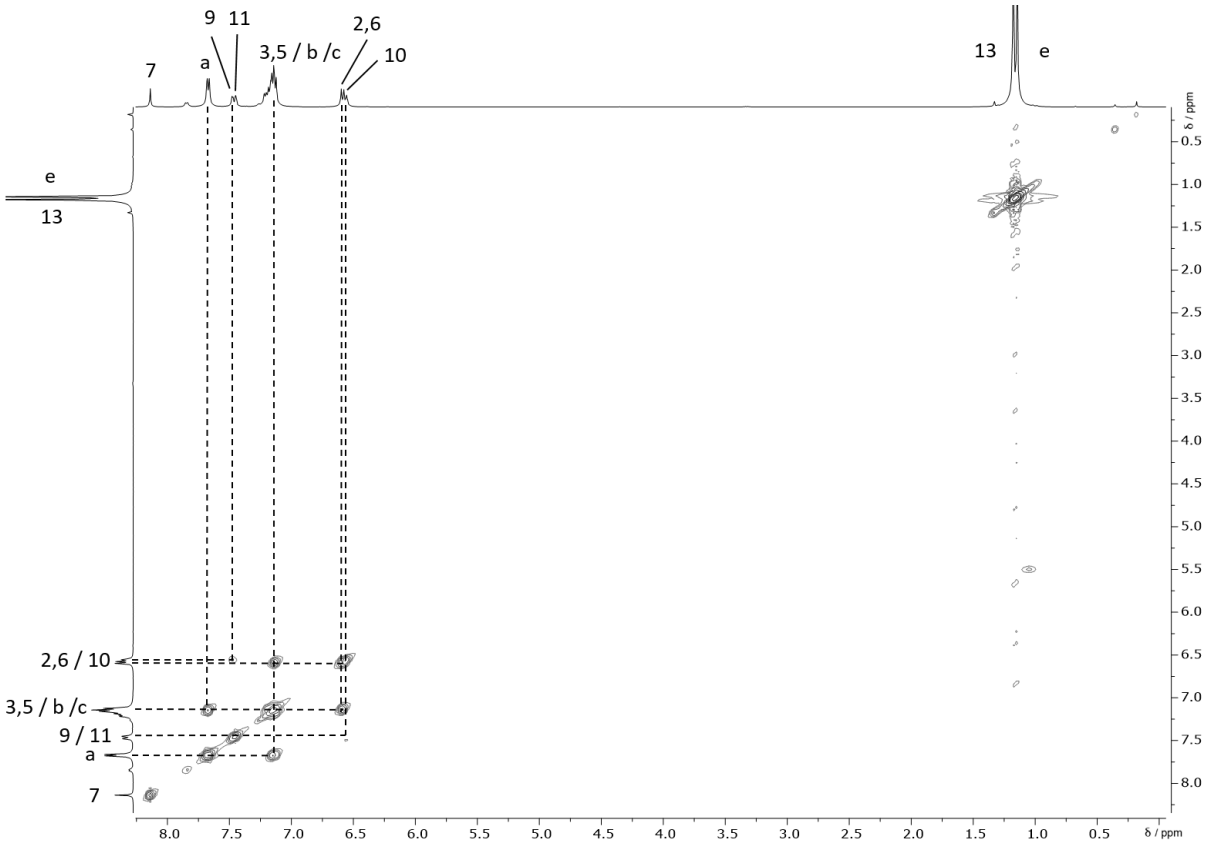

Figure 3: ^{1}H-^{1}H-COSY-NMR spectrum of complex **3** in C_6D_6.

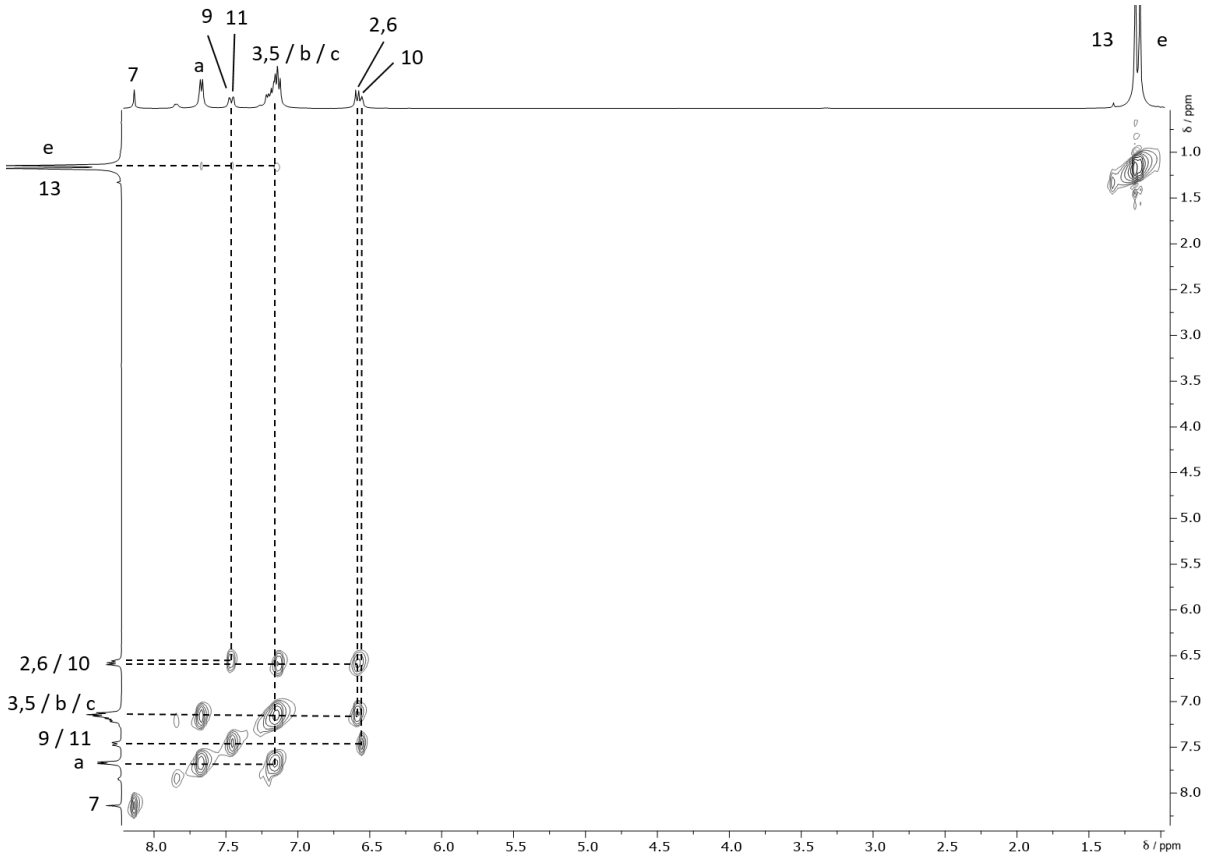

Figure 4: ^{1}H-^{1}H-TOCSY-NMR spectrum of complex **3** in C_6D_6.

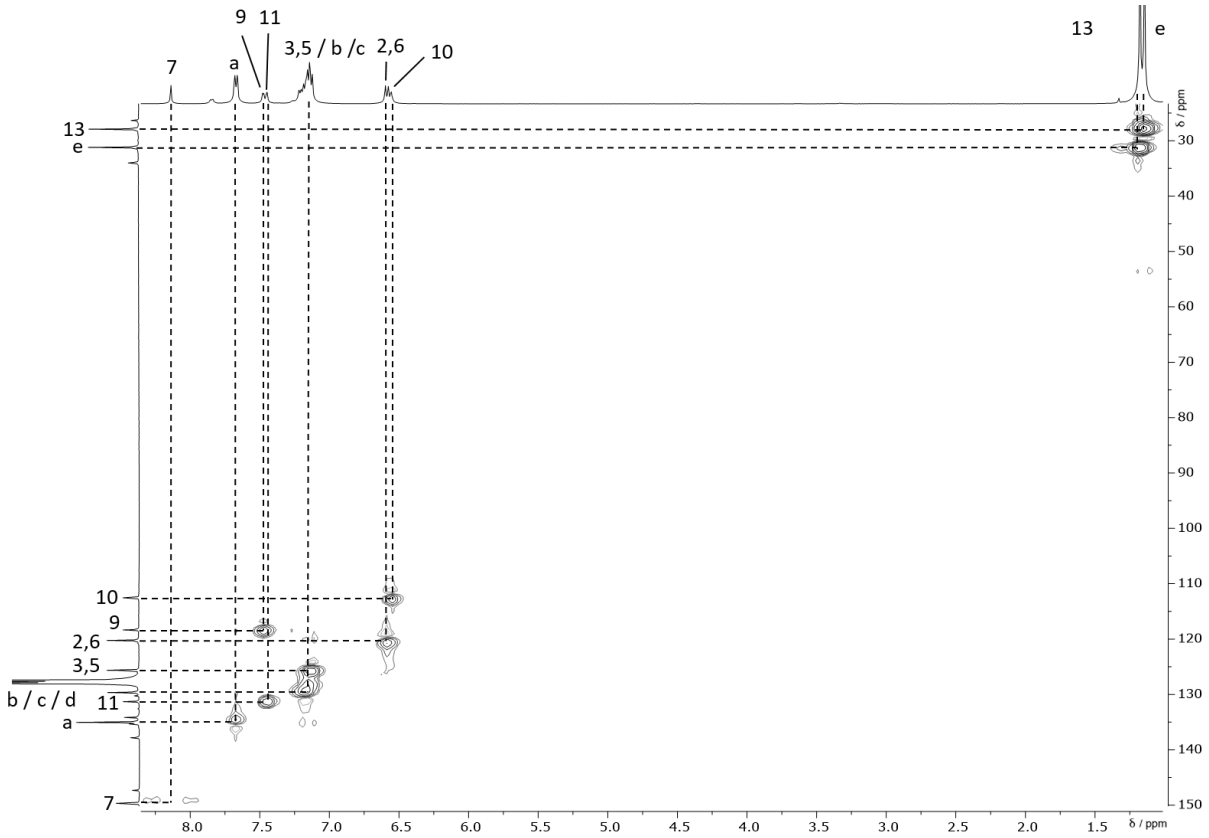

Figure 5: ^{13}C-{^{1}H}-HSQC-NMR spectrum of complex **3** in C_6D_6.

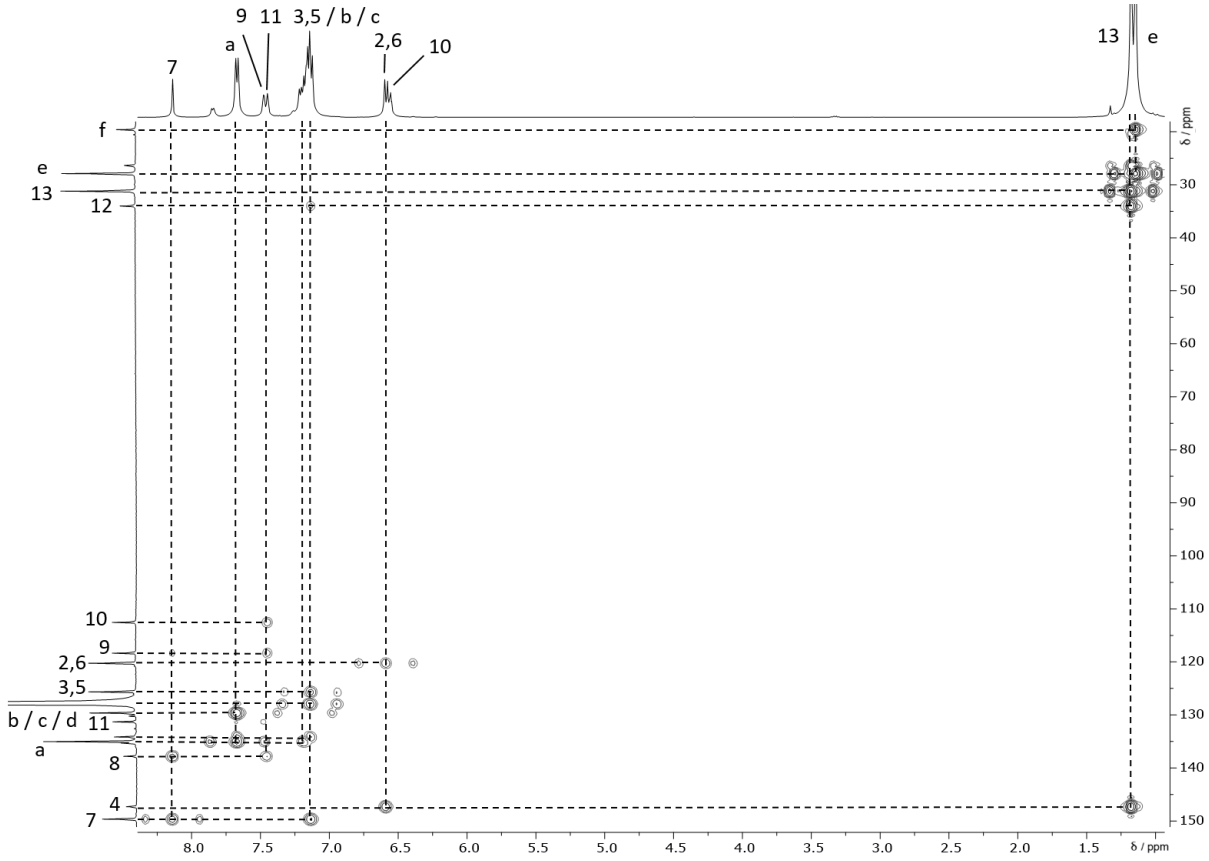

Figure 6: ^{13}C-{^{1}H}-HMBC-NMR spectrum of complex **3** in C_6D_6.

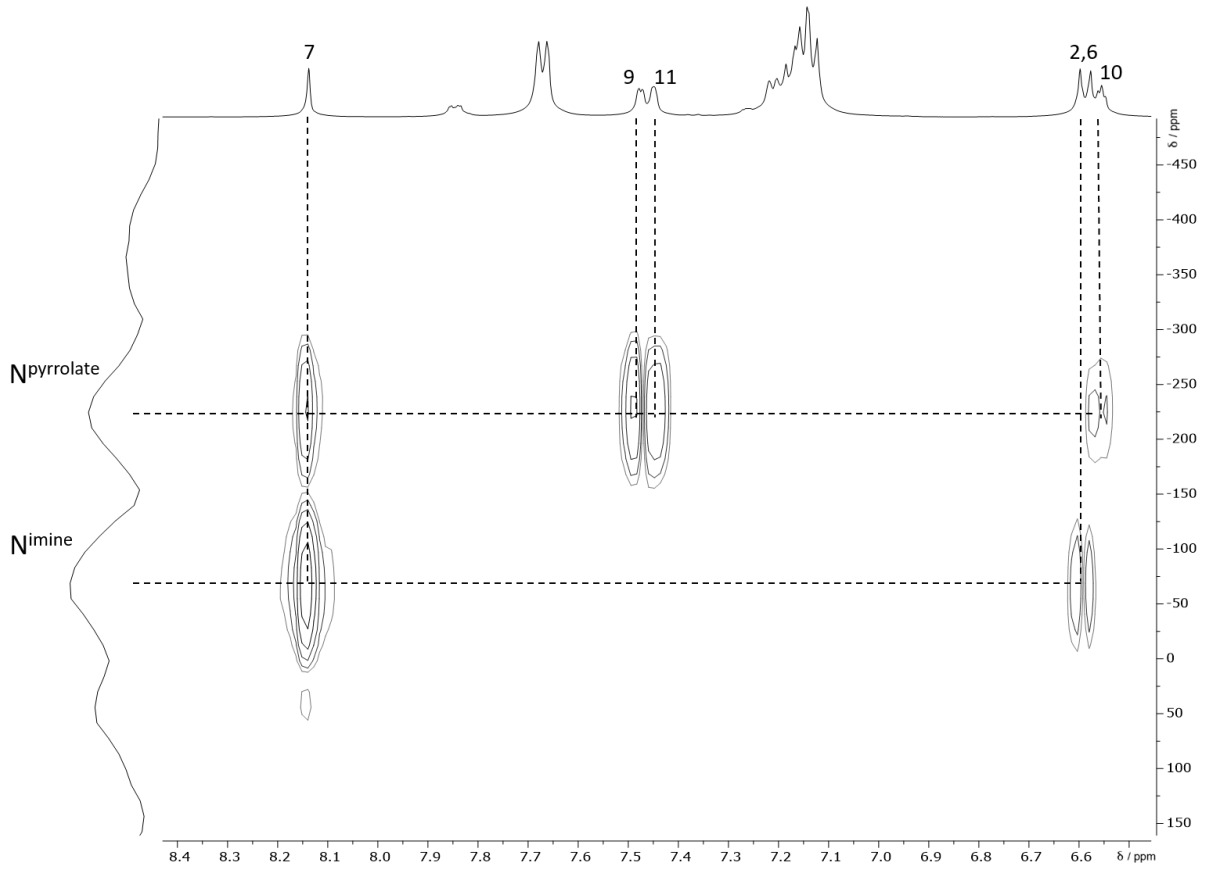

Figure 7: ^{1}H-^{15}N-HMBC-NMR spectrum of complex **2** in C_6D_6.

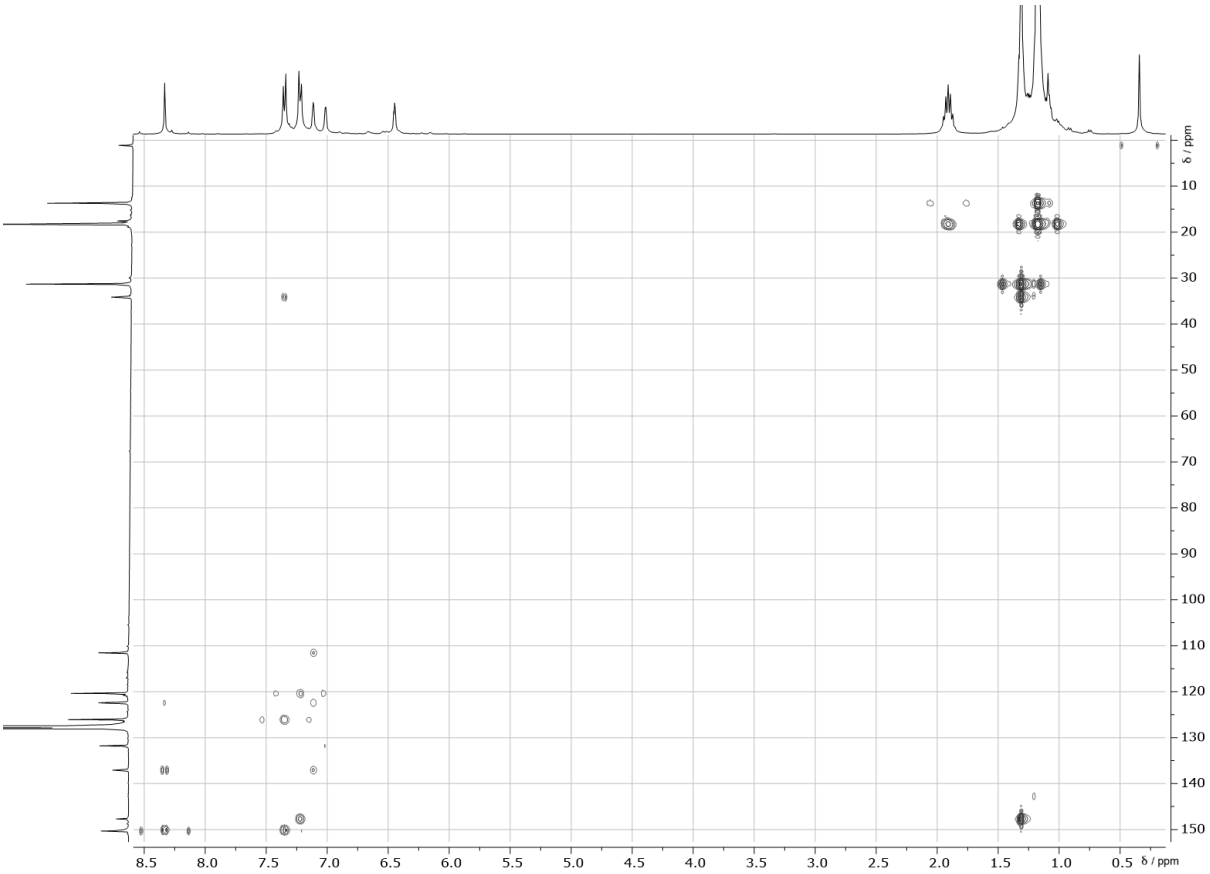

Figure 8: ^{13}C-{^{1}H}-HMBC-NMR spectrum of complex **2** in C_6D_6.

Attempted removal of protection groups of 2 with DMSO. To a solution of **2** (25 mg, 0.033 mmol) in C_6D_6 (0.5 mL) an excess of DMSO (0.5 mL) was added. The solution was heated to 40 °C for 6h and a ^{1}H-NMR spectrum recorded. The same solution was heated to 60 °C for 8h and another ^{1}H-NMR spectrum recorded. A third ^{1}H-NMR spectrum was recorded after heating the solution to 75 °C over night.

Attempted removal of protection groups of 2 with *p*-nitropyridine-*N*-oxide. To a solution of **2** (10 mg, 0.013 mmol) in C_6D_6 (0.3 mL) and CD_3CN (0.7 mL) *p*-nitropyridine-*N*-oxide (1.8 mg, 0.013 mmol) was added. The first ^{1}H-NMR spectrum was measured immediately and a second one after the solution was heated to 40 °C over night. A third ^{1}H-NMR spectrum was recorded after heating the solution to 60 °C for 8h.

Oxidation of 2 with Magic Green. To a solution of **2** (11.2 mg, 0.0121 mmol) in THF (0.5 mL) Magic Green (11.5 mg, 0.0109 mmol) in THF (0.5 mL) was added. The color of the solution changed from dark red to light brown. After six hours EPR measurements at room temperature were performed. Main resonances detected: g = 1.9847, g = 1.9656 and g = 1.9516.

crystallographic data of **5**		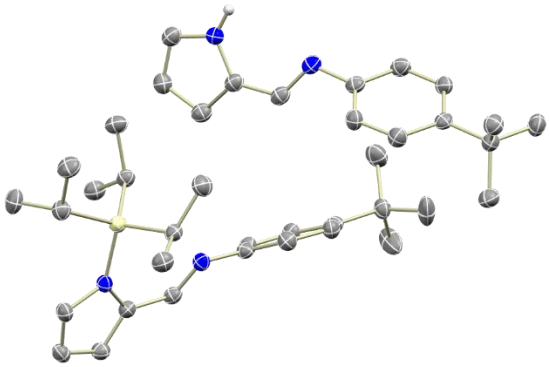
Empirical Formula C39 H56 N4 Si	**Formula Weight** 608.96 g/mol (Z = 4)	
Crystal System monoclinic	**Space group** P 21/n	
Parameter / Reflections 409 / 5241	**Final R_{conv}** R(obs) = 5.69 % R(all) = 10.94 %	

Unit Cell Dimensions			**Crystal System**	**Space group**
a = 4.658(3) Å	α = 90°		monoclinic	P 21/n
b = 9.0932(18) Å	β = 90.48(3)°		**Detector Type**	**Monochromator**
c = 26.980(5) Å	γ = 90°		Image plate	graphite
V = 3596.1(12) Å^3				
Generator Settings 50 kV / 40 mA	**Frame Width** 1°		**Scan Type** Omega scan	**Scan Time** 2 min
Crystal Size 0.770 x 0.307 x 0.050 mm^3	**Crystal Shape** needle		**Crystal Color** colorless	**Temperature** 120(2) K
Wavelength 0.71073 Å	**Theta Limits** 2.636 – 28.056°		**HKL-Limits** -19 ≤ h ≤ 17, -11≤ k ≤ 11, -35 ≤ l ≤ 35	
Reflections Collected 23386	**Unique Reflections** 5241		**Observed Reflections** 8451	**Completeness** 99.3%
Abs.Coefficient 0.097 / mm	**Abs.Correction Type** Semi-empirical from equivalents		**T min/max** 1.21980 / 0.87739	**Decay** ? % / h
R_{int} 8.96%	**R_{sigma}** 5.80%		**Diffraction Density** 1.125 g/cm^3	**Measured Density** 1.125 g/cm^3
Reflections(obs) / Restraints / Parameter 8451 / 0 / 409			**GOF** 1.019	**F(000)** 1328
R_{conv}, R_w(obs) 5.69%, 12.67%	**R_{conv}, R_w(all)** 10.94%, 15.14%		**Obs. Criteria** I > 2s(I)	**Peak / Hole** 0.444 / -0.413
Extinction Method none	**Extinction Coefficent** n/a		**Flack Parameter**	**Hydrogen Solution** geom

Cartesian coordinates of the DFT calculated geometry of OC-6-4-4 of **1**:

42	-0.540149000	-3.097120000	2.369811000
16	-2.722514000	-2.314994000	2.604020000
7	-0.700789000	-4.792896000	1.144790000
6	-0.751506000	-4.621079000	-0.242505000
6	-0.756706000	-6.139072000	1.373688000
6	-0.835104000	-5.862986000	-0.861669000
6	-0.848810000	-6.825142000	0.170767000
1	-0.724135000	-6.523383000	2.379257000
1	-0.887333000	-6.040610000	-1.924539000
1	-0.914787000	-7.895960000	0.058800000
7	0.255506000	-1.243453000	3.041162000
6	1.634787000	-1.027067000	2.912944000
6	-0.262197000	-0.120696000	3.596595000
6	1.956313000	0.241858000	3.403624000
6	0.750745000	0.810512000	3.842630000
1	-1.318366000	-0.033306000	3.780628000
1	2.940084000	0.684330000	3.423105000
1	0.613456000	1.787149000	4.280224000
6	-0.762332000	-3.286535000	-0.700265000
1	-0.859403000	-3.055620000	-1.757290000
6	2.347539000	-2.038145000	2.251253000
1	3.399925000	-1.924473000	2.008584000
7	-0.668169000	-2.341769000	0.190396000
7	1.689212000	-3.112618000	1.902621000
6	2.300557000	-4.032560000	1.014512000
6	2.314453000	-5.392822000	1.298947000
6	2.827831000	-3.590709000	-0.201384000
6	2.844321000	-6.294596000	0.385631000
1	1.893289000	-5.744489000	2.228033000
6	3.355862000	-4.500529000	-1.104578000
1	2.786495000	-2.537104000	-0.448263000
6	3.367279000	-5.874918000	-0.838912000
1	2.825554000	-7.344384000	0.639295000
1	3.739421000	-4.128081000	-2.046044000
6	-0.863352000	-0.996126000	-0.211413000
6	-2.009017000	-0.634248000	-0.917677000
6	0.057232000	-0.005009000	0.128097000
6	-2.221899000	0.691145000	-1.287375000
1	-2.750744000	-1.387322000	-1.152344000
6	-0.163709000	1.308991000	-0.249565000
1	0.946147000	-0.264423000	0.681688000
6	-1.308537000	1.693973000	-0.960346000
1	-3.127777000	0.930679000	-1.825826000
1	0.573750000	2.050839000	0.028709000
6	3.900385000	-6.850981000	-1.891445000
6	3.873442000	-8.305373000	-1.402665000
6	3.021676000	-6.748275000	-3.154860000
6	5.354796000	-6.487706000	-2.248598000
1	4.485436000	-8.441255000	-0.508390000
1	2.857821000	-8.636769000	-1.177261000
1	4.271048000	-8.957581000	-2.182861000
1	3.047175000	-5.742849000	-3.578109000
1	3.374361000	-7.446181000	-3.918552000
1	1.982762000	-6.990095000	-2.919747000
1	5.739882000	-7.177475000	-3.003791000
1	5.430600000	-5.475808000	-2.649106000
1	5.996504000	-6.552443000	-1.366850000
6	-1.519242000	3.165879000	-1.326600000
6	-2.819088000	3.390084000	-2.110647000
6	-1.581817000	4.004652000	-0.034253000
6	-0.340756000	3.652046000	-2.193433000
1	-2.825115000	2.832991000	-3.049980000
1	-3.696131000	3.095098000	-1.530808000
1	-2.919427000	4.450452000	-2.350701000
1	-0.660867000	3.919001000	0.544575000
1	-1.731426000	5.059707000	-0.277080000
1	-2.410454000	3.677158000	0.597712000
1	-0.479047000	4.702858000	-2.459910000
1	0.610089000	3.561412000	-1.666308000
1	-0.274277000	3.070640000	-3.115891000
16	-0.344295000	-4.460349000	4.258850000
14	1.424923000	-4.199491000	5.541243000
14	-3.576176000	-2.468949000	4.632625000
6	3.037734000	-4.718072000	4.717048000
1	2.986671000	-5.751214000	4.370508000
1	3.291118000	-4.081343000	3.872108000
1	3.838409000	-4.646050000	5.459265000
6	1.522511000	-2.425087000	6.163649000
1	2.395299000	-2.326503000	6.816071000
1	1.617419000	-1.711652000	5.347239000
1	0.633875000	-2.170987000	6.743154000
6	1.069747000	-5.356317000	6.991205000
1	1.001744000	-6.393506000	6.655844000
1	1.871887000	-5.285124000	7.731271000
1	0.128837000	-5.091237000	7.478350000
6	-3.969640000	-4.281371000	4.952859000
1	-3.056523000	-4.876487000	4.962241000
1	-4.466575000	-4.384190000	5.921933000
1	-4.635260000	-4.669846000	4.179527000
6	-5.163142000	-1.453356000	4.556131000
1	-5.676493000	-1.491979000	5.521088000
1	-4.944268000	-0.408841000	4.324224000
1	-5.839368000	-1.841788000	3.791658000
6	-2.407525000	-1.768178000	5.928551000
1	-2.331243000	-0.682768000	5.851990000
1	-2.784711000	-2.018293000	6.924072000
1	-1.413269000	-2.195332000	5.815133000

Cartesian coordinates of the DFT calculated geometry of OC-6-3-3 of **1**:

42	0.033146000	-3.026041000	2.486662000
16	-2.274612000	-2.850734000	2.179072000
7	0.176347000	-2.177022000	0.373736000
6	0.358134000	-0.801611000	0.338534000
6	0.107302000	-2.592170000	-0.892625000
6	0.415155000	-0.363971000	-1.005049000
6	0.256570000	-1.502723000	-1.787072000
1	-0.040811000	-3.631143000	-1.137531000
1	0.545035000	0.654937000	-1.336223000
1	0.244576000	-1.561752000	-2.864399000
7	2.266429000	-2.897696000	2.356876000
6	2.825901000	-3.893135000	1.561559000
6	3.276333000	-2.121095000	2.768862000
6	4.224773000	-3.719594000	1.497697000
6	4.508934000	-2.586906000	2.257717000
1	3.100560000	-1.253497000	3.385380000
1	4.919818000	-4.350838000	0.965708000
1	5.476758000	-2.143298000	2.433025000
6	0.381464000	-0.145404000	1.566790000
1	0.503823000	0.930966000	1.628220000
6	1.957189000	-4.864891000	1.064139000
1	2.332727000	-5.695549000	0.475938000
7	0.252796000	-0.853196000	2.673769000
7	0.667942000	-4.784387000	1.336970000
6	-0.220353000	-5.756002000	0.801637000
6	-1.262752000	-6.253545000	1.579901000
6	-0.075927000	-6.230395000	-0.506317000
6	-2.131895000	-7.208280000	1.065944000
1	-1.388239000	-5.896762000	2.591288000
6	-0.950518000	-7.182967000	-1.006494000
1	0.711497000	-5.843749000	-1.140668000
6	-2.002894000	-7.694177000	-0.236890000
1	-2.923237000	-7.569832000	1.706795000
1	-0.812468000	-7.519960000	-2.025876000
6	0.121650000	-0.190514000	3.919920000
6	-0.661476000	0.955609000	4.050581000
6	0.731809000	-0.719794000	5.056846000
6	-0.815919000	1.561556000	5.293360000
1	-1.181161000	1.356717000	3.189870000
6	0.562645000	-0.113077000	6.288476000
1	1.324813000	-1.615573000	4.965977000
6	-0.219599000	1.038775000	6.442044000
1	-1.440847000	2.440826000	5.354869000
1	1.044744000	-0.557059000	7.150109000
6	-2.954216000	-8.732662000	-0.837356000
6	-4.035598000	-9.173982000	0.157951000
6	-3.650559000	-8.129091000	-2.073656000
6	-2.148600000	-9.976833000	-1.261463000
1	-3.601172000	-9.631996000	1.049028000
1	-4.661340000	-8.336171000	0.472511000
1	-4.683259000	-9.914315000	-0.315741000
1	-2.929501000	-7.840920000	-2.840066000
1	-4.335380000	-8.859053000	-2.512361000
1	-4.225445000	-7.242178000	-1.797882000
1	-2.815294000	-10.725683000	-1.696197000
1	-1.389677000	-9.730202000	-2.005528000
1	-1.646815000	-10.423592000	-0.400096000
6	-0.414663000	1.646835000	7.832736000
6	-1.298148000	2.900872000	7.801017000
6	-1.087529000	0.601115000	8.745048000
6	0.956009000	2.033687000	8.422233000
1	-0.862170000	3.685874000	7.179389000
1	-2.299200000	2.680240000	7.424617000
1	-1.402569000	3.295979000	8.813415000
1	-0.473093000	-0.294468000	8.848206000
1	-1.246754000	1.018796000	9.742267000
1	-2.055549000	0.301102000	8.337876000
1	0.827706000	2.463450000	9.418736000
1	1.614276000	1.168336000	8.512083000
1	1.452750000	2.774267000	7.791276000
16	-0.040445000	-4.294187000	4.445201000
14	1.796410000	-4.963389000	5.451812000
14	-3.496070000	-2.747834000	4.005258000
6	2.848037000	-3.531234000	6.075325000
1	3.252251000	-2.945009000	5.250791000
1	2.275733000	-2.876338000	6.734467000
1	3.686350000	-3.938979000	6.648007000
6	1.143708000	-5.952842000	6.919375000
1	1.980379000	-6.343327000	7.505528000
1	0.531182000	-5.325769000	7.570818000
1	0.536063000	-6.795125000	6.582209000
6	2.782001000	-6.074890000	4.297548000
1	3.305082000	-5.488265000	3.543673000
1	3.518956000	-6.632960000	4.882175000
1	2.130288000	-6.788969000	3.790825000
6	-3.835379000	-4.542901000	4.483822000
1	-2.905265000	-5.045637000	4.752349000
1	-4.512977000	-4.579823000	5.341728000
1	-4.296929000	-5.083978000	3.655293000
6	-5.102266000	-1.888761000	3.509957000
1	-5.799038000	-1.877733000	4.352999000
1	-4.912256000	-0.855985000	3.208947000
1	-5.580227000	-2.406710000	2.675603000
6	-2.681905000	-1.827525000	5.428702000
1	-2.502274000	-0.781037000	5.184125000
1	-3.345867000	-1.869571000	6.297366000
1	-1.729351000	-2.281048000	5.697170000

Cartesian coordinates of the DFT calculated geometry of OC-6-1-2 of **1**:

42	0.848669000	-1.805451000	-1.319691000
16	-1.457750000	-2.089951000	-1.912024000
7	1.515467000	-1.317123000	-3.262497000
6	1.595749000	0.051036000	-3.514392000
6	2.017310000	-1.941786000	-4.355224000
6	2.152203000	0.267714000	-4.777417000
6	2.424398000	-1.006916000	-5.309546000
1	2.064607000	-3.015643000	-4.408564000
1	2.337999000	1.225495000	-5.238393000
1	2.855865000	-1.229122000	-6.273081000
7	0.275625000	-2.374235000	0.652161000
6	0.280005000	-3.755799000	0.858255000
6	-0.180664000	-1.823003000	1.803817000
6	-0.187015000	-4.048646000	2.139885000
6	-0.481874000	-2.810512000	2.742419000
1	-0.290131000	-0.756820000	1.901927000
1	-0.296114000	-5.032011000	2.570551000
1	-0.863887000	-2.646953000	3.738004000
6	1.128888000	0.907990000	-2.504075000
1	1.135040000	1.984219000	-2.652463000
6	0.698518000	-4.558738000	-0.220874000
1	0.734216000	-5.641553000	-0.133597000
7	0.666949000	0.385256000	-1.395807000
7	1.029666000	-3.960990000	-1.329075000
6	1.445548000	-4.702157000	-2.465134000
6	0.523293000	-5.048328000	-3.444684000
6	2.793475000	-4.995593000	-2.657922000
6	0.948221000	-5.674099000	-4.613172000
1	-0.519035000	-4.796374000	-3.301239000
6	3.204367000	-5.621064000	-3.826500000
1	3.512073000	-4.706640000	-1.902144000
6	2.295797000	-5.964498000	-4.836227000
1	0.206183000	-5.920115000	-5.358958000
1	4.258869000	-5.828693000	-3.955465000
6	0.191489000	1.256649000	-0.386597000
6	-1.026420000	0.994239000	0.232203000
6	0.927792000	2.372264000	0.018075000
6	-1.497117000	1.830383000	1.239173000
1	-1.599561000	0.133423000	-0.082900000
6	0.450431000	3.194321000	1.026754000
1	1.891892000	2.571243000	-0.432938000
6	-0.769589000	2.943060000	1.666811000
1	-2.447750000	1.592562000	1.694752000
1	1.055522000	4.038952000	1.330673000
6	2.803157000	-6.610200000	-6.129086000
6	1.663209000	-6.935103000	-7.103507000
6	3.774801000	-5.637156000	-6.827174000
6	3.543493000	-7.920110000	-5.795070000
1	0.947156000	-7.635440000	-6.668239000
1	1.123103000	-6.036085000	-7.407484000
1	2.076277000	-7.395631000	-8.003120000
1	4.633754000	-5.406645000	-6.195198000
1	4.146706000	-6.077503000	-7.755706000
1	3.271562000	-4.698488000	-7.070273000
1	3.911840000	-8.387399000	-6.711637000
1	4.398858000	-7.743478000	-5.141432000
1	2.874860000	-8.625259000	-5.296026000
6	-1.242813000	3.863685000	2.795349000
6	-2.596665000	3.428346000	3.371813000
6	-0.203477000	3.844327000	3.934235000
6	-1.384019000	5.301742000	2.258254000
1	-3.382676000	3.444822000	2.613897000
1	-2.549902000	2.423245000	3.796286000
1	-2.887970000	4.114116000	4.169902000
1	0.771707000	4.195055000	3.593349000
1	-0.528717000	4.493262000	4.751264000
1	-0.080902000	2.832542000	4.327202000
1	-1.718364000	5.969926000	3.055865000
1	-0.435597000	5.682503000	1.876330000
1	-2.116490000	5.341284000	1.448796000
16	3.177337000	-1.623955000	-0.766899000
14	3.694859000	-1.332988000	1.334884000
14	-2.205881000	-1.195384000	-3.757066000
6	3.343334000	-2.894248000	2.324613000
1	2.276961000	-3.089117000	2.411381000
6	5.557846000	-1.023657000	1.303428000
1	6.088877000	-1.880004000	0.882264000
6	2.826041000	0.176193000	2.045190000
1	3.120658000	1.075082000	1.502400000
6	-4.038177000	-1.648842000	-3.755528000
1	-4.171058000	-2.732608000	-3.737560000
6	-1.364067000	-1.944184000	-5.262824000
1	-1.427837000	-3.033435000	-5.239106000
6	-2.024632000	0.679101000	-3.724279000
1	-4.517923000	-1.257196000	-4.657126000
1	-4.543908000	-1.225655000	-2.885095000
1	-2.679385000	1.110114000	-4.487213000
1	-1.001632000	0.981044000	-3.941283000
1	-2.309755000	1.085899000	-2.752759000
1	-0.313328000	-1.664691000	-5.314313000
1	-1.866494000	-1.586668000	-6.166705000
1	5.798221000	-0.141694000	0.706121000
1	5.923199000	-0.859487000	2.321405000
1	3.761095000	-2.777679000	3.329255000
1	3.816915000	-3.757687000	1.853544000
1	3.107870000	0.296653000	3.095380000
1	1.744221000	0.087625000	1.983144000

Cartesian coordinates of the DFT calculated geometry of OC-6-4-4 of **2**:

42	0.074804000	-2.529866000	1.056712000
16	-2.044913000	-2.029803000	1.882500000
7	-0.127458000	-4.285524000	-0.063983000
6	-0.194714000	-4.173987000	-1.451458000
6	-0.176468000	-5.618967000	0.222094000
6	-0.273827000	-5.440572000	-2.021558000
6	-0.280518000	-6.357874000	-0.950218000
1	-0.134119000	-5.961556000	1.242159000
1	-0.325303000	-5.660709000	-3.076362000
1	-0.347439000	-7.432547000	-1.016985000
7	0.839741000	-0.662424000	1.797639000
6	2.180374000	-0.368089000	1.514954000
6	0.352124000	0.389405000	2.484273000
6	2.506680000	0.891756000	2.040795000
6	1.344822000	1.367524000	2.656816000
1	-0.664438000	0.396177000	2.832072000
1	3.465342000	1.380965000	1.967132000
1	1.219324000	2.304369000	3.177366000
6	-0.181504000	-2.878057000	-1.989982000
1	-0.172288000	-2.753480000	-3.067616000
6	2.842539000	-1.292949000	0.704407000
1	3.857289000	-1.123853000	0.357768000
7	-0.163361000	-1.846065000	-1.186673000
7	2.195505000	-2.380163000	0.362305000
6	2.772784000	-3.250708000	-0.595276000
6	2.902833000	-4.606910000	-0.323453000
6	3.154331000	-2.767397000	-1.847889000
6	3.389132000	-5.470558000	-1.295488000
1	2.596116000	-4.984004000	0.640205000
6	3.637421000	-3.640443000	-2.811201000
1	3.023658000	-1.716402000	-2.074698000
6	3.754862000	-5.013134000	-2.563575000
1	3.461452000	-6.520460000	-1.052221000
1	3.903371000	-3.240907000	-3.781620000
6	-0.206041000	-0.556956000	-1.782371000
6	-0.884514000	-0.328884000	-2.985108000
6	0.415971000	0.533239000	-1.172658000
6	-0.899639000	0.931496000	-3.570870000
1	-1.429190000	-1.129610000	-3.467004000
6	0.391277000	1.785668000	-1.765004000
1	0.927755000	0.402003000	-0.236799000
6	-0.258359000	2.021118000	-2.981146000
1	-1.444128000	1.052385000	-4.496468000
1	0.893817000	2.597368000	-1.254509000
6	4.232305000	-5.949795000	-3.677144000
6	4.320928000	-7.409342000	-3.211585000
6	3.234861000	-5.876955000	-4.851169000
6	5.627510000	-5.510664000	-4.162336000
1	5.023450000	-7.526906000	-2.383745000
1	3.348553000	-7.790886000	-2.893525000
1	4.669799000	-8.032679000	-4.037367000
1	3.170449000	-4.867056000	-5.259197000
1	3.547785000	-6.547735000	-5.655363000
1	2.235936000	-6.174157000	-4.524158000
1	5.972122000	-6.170093000	-4.962850000
1	5.617071000	-4.490571000	-4.549008000
1	6.351781000	-5.556503000	-3.345816000
6	-0.252567000	3.422254000	-3.596801000
6	-1.018967000	3.475876000	-4.924896000
6	-0.908440000	4.417394000	-2.619241000
6	1.204996000	3.852256000	-3.858272000
1	-0.582560000	2.807341000	-5.670038000
1	-2.069375000	3.206789000	-4.795003000
1	-0.981821000	4.491218000	-5.324587000
1	-0.385367000	4.445383000	-1.662263000
1	-0.892414000	5.424753000	-3.042655000
1	-1.947606000	4.142602000	-2.428603000
1	1.228985000	4.851846000	-4.299436000
1	1.786282000	3.876950000	-2.935307000
1	1.693646000	3.160847000	-4.548614000
16	0.618490000	-3.898486000	2.879762000
14	2.235463000	-3.304605000	4.256536000
6	3.875525000	-3.382294000	3.274815000
1	3.603289000	-2.977574000	2.301731000
6	2.183605000	-4.694256000	5.573606000
1	2.275771000	-5.612620000	4.981758000
6	1.836127000	-1.566104000	4.938525000
1	2.087457000	-0.889572000	4.118478000
6	3.367065000	-4.653642000	6.553785000
6	0.855920000	-4.769639000	6.338998000
6	4.341023000	-4.827502000	3.048048000
6	5.010159000	-2.509193000	3.825063000
6	2.689130000	-1.169655000	6.154288000
6	0.348216000	-1.372679000	5.261797000
1	3.758054000	-1.304347000	5.987656000
1	2.413912000	-1.752211000	7.036035000
1	2.522983000	-0.115206000	6.398765000
1	-0.290885000	-1.650002000	4.425747000
1	0.050028000	-1.970807000	6.125517000
1	0.150364000	-0.323446000	5.502202000
1	5.321659000	-2.821038000	4.824896000
1	4.720371000	-1.458222000	3.876609000
1	5.888354000	-2.577564000	3.174117000
1	3.538419000	-5.458816000	2.661740000
1	4.704373000	-5.284171000	3.971022000
1	5.159693000	-4.855093000	2.322294000
1	3.313615000	-3.781059000	7.206843000
1	3.359391000	-5.541393000	7.194915000
1	4.331091000	-4.625313000	6.044380000
1	0.733452000	-3.909448000	7.000850000
1	0.823296000	-5.668425000	6.963700000
1	-0.003332000	-4.796952000	5.666212000
6	-3.599352000	-3.336918000	-0.967692000
1	-2.721265000	-1.495982000	-1.606634000
1	-3.569935000	-3.778033000	-1.968816000
1	-4.495300000	-3.712168000	-0.469447000
1	-2.732716000	-3.700613000	-0.419384000
6	-3.618355000	-1.805804000	-1.069753000
6	-4.834789000	-1.342222000	-1.887699000
1	-4.890861000	-0.257816000	-1.987568000
1	-4.787999000	-1.765152000	-2.896345000
1	-5.767929000	-1.685514000	-1.436512000
1	-6.551632000	-0.349970000	0.197071000
1	-5.810166000	1.009862000	1.036037000
6	-6.158555000	-0.016295000	1.158614000
1	-6.995178000	0.002238000	1.864377000
14	-3.469687000	-0.909822000	0.607517000
6	-5.055024000	-0.954722000	1.673641000
1	-4.724466000	-0.574761000	2.647100000
6	-5.606163000	-2.370499000	1.888076000
1	-6.423819000	-2.355741000	2.615656000
1	-6.004391000	-2.784072000	0.958912000
1	-4.841745000	-3.056708000	2.257744000
6	-2.767413000	0.859461000	0.478871000
1	-1.693960000	0.711482000	0.342464000
6	-3.272652000	1.657973000	-0.729543000
1	-2.802937000	2.645327000	-0.744745000
1	-3.024248000	1.169256000	-1.670769000
1	-4.354255000	1.809862000	-0.695427000
1	-2.369398000	2.566014000	1.761372000
6	-2.968361000	1.650622000	1.779415000
1	-2.676730000	1.082150000	2.664171000
1	-4.012128000	1.943671000	1.909585000

Cartesian coordinates of the DFT calculated geometry of OC-6-3-3 of **2**:

42	0.621779000	-2.143597000	0.671337000
16	-1.650263000	-1.868082000	1.208324000
7	0.537283000	-0.666864000	-0.915898000
6	0.556697000	0.671411000	-0.550019000
6	0.642884000	-0.716978000	-2.261130000
6	0.657782000	1.465245000	-1.699646000
6	0.708527000	0.577904000	-2.787234000
1	0.653742000	-1.658244000	-2.785629000
1	0.686967000	2.543809000	-1.728747000
1	0.773688000	0.832424000	-3.833754000
7	2.673859000	-2.065069000	-0.162753000
6	2.879373000	-3.033798000	-1.140921000
6	3.792310000	-1.349664000	-0.073583000
6	4.186425000	-2.895108000	-1.668578000
6	4.763279000	-1.826735000	-0.993116000
1	3.877609000	-0.528732000	0.622516000
1	4.631743000	-3.507327000	-2.437708000
1	5.756869000	-1.428050000	-1.127142000
6	0.616980000	0.946202000	0.833795000
1	0.602677000	1.970858000	1.196704000
6	1.822173000	-3.899064000	-1.403580000
1	1.940069000	-4.709378000	-2.116321000
7	0.713190000	-0.051052000	1.666682000
7	0.666510000	-3.764734000	-0.746957000
6	-0.293919000	-4.793238000	-0.967591000
6	-0.788576000	-5.505723000	0.116538000
6	-0.731597000	-5.124914000	-2.250051000
6	-1.667081000	-6.564376000	-0.076923000
1	-0.458636000	-5.238164000	1.108685000
6	-1.628143000	-6.167417000	-2.430550000
1	-0.377845000	-4.558480000	-3.102665000
6	-2.116984000	-6.913955000	-1.351147000
1	-2.019765000	-7.100019000	0.792077000
1	-1.958452000	-6.392121000	-3.436430000
6	0.658699000	0.216288000	3.056606000
6	-0.440180000	0.857235000	3.620476000
6	1.697640000	-0.200907000	3.889460000
6	-0.506890000	1.058833000	4.997780000
1	-1.264231000	1.153688000	2.984673000
6	1.624242000	0.014139000	5.254591000
1	2.551080000	-0.704104000	3.458494000
6	0.514576000	0.634325000	5.846251000
1	-1.388050000	1.537544000	5.400519000
1	2.447528000	-0.320688000	5.872625000
6	-3.114590000	-8.048748000	-1.597621000
6	-3.618331000	-8.669441000	-0.287899000
6	-4.332479000	-7.504426000	-2.370383000
6	-2.432380000	-9.149926000	-2.433051000
1	-2.805244000	-9.113186000	0.290084000
1	-4.120809000	-7.929300000	0.338605000
1	-4.336673000	-9.460012000	-0.513321000
1	-4.046730000	-7.096337000	-3.340575000
1	-5.054447000	-8.306121000	-2.543296000
1	-4.827911000	-6.714001000	-1.804397000
1	-3.133707000	-9.965554000	-2.626634000
1	-2.088621000	-8.764400000	-3.394465000
1	-1.569008000	-9.558417000	-1.902907000
6	0.458729000	0.794387000	7.367995000
6	-0.838558000	1.467667000	7.834548000
6	0.544664000	-0.597804000	8.025525000
6	1.649242000	1.653295000	7.837922000
1	-0.945320000	2.471326000	7.417614000
1	-1.718091000	0.884153000	7.554277000
1	-0.830077000	1.557445000	8.922699000
1	1.473917000	-1.107935000	7.768898000
1	0.501029000	-0.503448000	9.113415000
1	-0.284537000	-1.229476000	7.701764000
1	1.624854000	1.767864000	8.924582000
1	2.603250000	1.197042000	7.569370000
1	1.609945000	2.647762000	7.387503000
16	1.763320000	-3.244493000	2.368447000
14	0.717850000	-4.361005000	3.981511000
6	-1.108265000	-3.868671000	4.113216000
1	-1.423915000	-3.771691000	3.072027000
6	1.722201000	-3.833442000	5.517446000
1	1.628764000	-2.742713000	5.508264000
6	0.872369000	-6.207571000	3.483938000
1	-0.035554000	-6.404091000	2.902212000
6	1.126593000	-4.335305000	6.842163000
6	3.213029000	-4.180267000	5.421134000
6	-1.303797000	-2.494928000	4.758379000
6	-1.994926000	-4.933961000	4.773148000
6	0.835579000	-7.133430000	4.711056000
6	2.072997000	-6.547374000	2.593054000
1	-0.013348000	-6.932279000	5.365676000
1	1.745722000	-7.035008000	5.306003000
1	0.766852000	-8.177524000	4.390318000
1	2.060852000	-5.980152000	1.662172000
1	3.018225000	-6.332552000	3.096979000
1	2.065492000	-7.612837000	2.342158000
1	-1.728006000	-5.097924000	5.819835000
1	-1.939098000	-5.895509000	4.259773000
1	-3.040289000	-4.611433000	4.748648000
1	-0.695207000	-1.733155000	4.278573000
1	-1.051841000	-2.507004000	5.820353000
1	-2.347302000	-2.179513000	4.667206000
1	1.201720000	-5.419598000	6.934999000
1	1.670398000	-3.896005000	7.684398000
1	0.076832000	-4.063145000	6.954815000
1	3.372686000	-5.261279000	5.427571000
1	3.756421000	-3.765443000	6.276164000
1	3.665397000	-3.781960000	4.511742000
6	-3.876723000	-4.610964000	1.621931000
1	-3.417261000	-4.737011000	-0.454274000
1	-4.238474000	-5.641180000	1.705965000
1	-4.443244000	-4.003780000	2.331045000
1	-2.837023000	-4.598450000	1.937203000
6	-4.035568000	-4.104720000	0.186137000
6	-5.494457000	-4.266325000	-0.268398000
1	-5.660424000	-3.927147000	-1.291435000
1	-5.786653000	-5.320406000	-0.218512000
1	-6.175962000	-3.713827000	0.381000000
1	-6.495080000	-1.662203000	-0.379674000
1	-5.554736000	-0.725810000	-1.534988000
6	-5.817005000	-0.814145000	-0.479934000
1	-6.378044000	0.085216000	-0.204191000
14	-3.353555000	-2.341582000	-0.104943000
6	-4.582795000	-0.966939000	0.422098000
1	-3.987106000	-0.051973000	0.324113000
6	-4.999230000	-1.087108000	1.894672000
1	-5.581649000	-0.212837000	2.204567000
1	-5.624000000	-1.968357000	2.059267000
1	-4.131117000	-1.163698000	2.552246000
6	-2.780461000	-2.100832000	-1.911381000
1	-1.776434000	-2.533690000	-1.929030000
6	-3.623485000	-2.853735000	-2.948534000
1	-3.199559000	-2.720117000	-3.949657000
1	-3.654633000	-3.925154000	-2.746493000
1	-4.652285000	-2.486413000	-2.979775000
1	-2.191151000	-0.495864000	-3.252458000
6	-2.653729000	-0.614901000	-2.269244000
1	-2.032437000	-0.078535000	-1.551945000
1	-3.630800000	-0.128395000	-2.304310000

Cartesian coordinates of the DFT calculated geometry of OC-6-1-2 of **2**:

42	5.155978000	0.304914000	-1.086073000
16	2.856232000	-0.356998000	-0.587618000
7	5.305191000	-1.549003000	-2.395365000
6	5.888449000	-2.607339000	-1.706285000
6	5.394326000	-1.832950000	-3.712197000
6	6.283302000	-3.596162000	-2.622366000
6	5.974089000	-3.100021000	-3.896743000
1	5.036151000	-1.142983000	-4.457353000
1	6.738749000	-4.543933000	-2.378499000
1	6.142452000	-3.590603000	-4.842910000
7	4.765264000	1.716473000	0.476023000
6	4.049721000	2.844506000	0.082872000
6	5.174491000	1.935685000	1.758525000
6	3.988920000	3.751307000	1.138594000
6	4.707476000	3.167981000	2.205387000
1	5.740288000	1.201281000	2.300819000
1	3.498510000	4.712221000	1.126285000
1	4.869072000	3.590325000	3.184568000
6	6.008919000	-2.502374000	-0.310466000
1	6.409120000	-3.335202000	0.263257000
6	3.639738000	2.914298000	-1.263985000
1	3.049688000	3.759332000	-1.605934000
7	5.654665000	-1.395044000	0.289987000
7	3.986921000	1.966417000	-2.087397000
6	3.498660000	1.998536000	-3.415920000
6	4.361136000	1.795356000	-4.488475000
6	2.139205000	2.195443000	-3.665674000
6	3.874916000	1.826036000	-5.790871000
1	5.412627000	1.633933000	-4.294090000
6	1.666135000	2.211516000	-4.968314000
1	1.456704000	2.307126000	-2.832889000
6	2.518798000	2.026937000	-6.062875000
1	4.575986000	1.679196000	-6.599723000
1	0.604893000	2.352710000	-5.128042000
6	5.745141000	-1.283362000	1.706674000
6	6.976370000	-1.166530000	2.338185000
6	4.579119000	-1.218581000	2.467947000
6	7.041904000	-0.949067000	3.712648000
1	7.883499000	-1.229539000	1.753099000
6	4.657071000	-1.008729000	3.835247000
1	3.624092000	-1.286238000	1.966495000
6	5.886571000	-0.848508000	4.488759000
1	8.016670000	-0.843918000	4.166452000
1	3.735141000	-0.948135000	4.399157000
6	1.947991000	2.048707000	-7.484188000
6	3.026083000	1.806260000	-8.548808000
6	0.876624000	0.949398000	-7.626817000
6	1.303836000	3.424159000	-7.749948000
1	3.800393000	2.575867000	-8.523723000
1	3.505023000	0.833099000	-8.422936000
1	2.567819000	1.827081000	-9.539477000
1	0.064591000	1.081761000	-6.910660000
1	0.447909000	0.972433000	-8.631607000
1	1.312710000	-0.038237000	-7.464258000
1	0.892295000	3.457766000	-8.761749000
1	0.493023000	3.628673000	-7.049166000
1	2.044277000	4.221653000	-7.654221000
6	5.916553000	-0.554145000	5.990807000
6	7.346742000	-0.403737000	6.526207000
6	5.160298000	0.763208000	6.256079000
6	5.228702000	-1.702825000	6.754635000
1	7.929137000	-1.316819000	6.386275000
1	7.874641000	0.418750000	6.039135000
1	7.312523000	-0.190705000	7.596352000
1	4.118502000	0.699150000	5.939321000
1	5.175693000	0.997468000	7.323287000
1	5.626957000	1.590052000	5.715893000
1	5.244237000	-1.502326000	7.828681000
1	4.187880000	-1.821621000	6.450168000
1	5.744835000	-2.648794000	6.575821000
16	7.128400000	1.096998000	-2.074470000
14	1.624619000	-1.888219000	-1.532099000
6	2.601193000	-3.522521000	-1.616476000
1	3.524299000	-3.252959000	-2.130015000
6	0.985641000	-1.276870000	-3.227230000
1	0.704470000	-0.234286000	-3.048132000
6	0.192843000	-1.972013000	-0.254724000
1	0.705296000	-2.011556000	0.713025000
6	2.982074000	-4.000599000	-0.209707000
6	1.937750000	-4.640373000	-2.431951000
6	2.076775000	-1.281412000	-4.298143000
6	-0.265135000	-2.018994000	-3.723679000
6	-0.691926000	-3.223539000	-0.354782000
6	-0.659277000	-0.694995000	-0.272376000
1	-1.103929000	-1.926892000	-3.033697000
1	-0.584635000	-1.605865000	-4.686460000
1	-0.076057000	-3.083657000	-3.875480000
1	2.480243000	-2.283185000	-4.463136000
1	1.679905000	-0.917605000	-5.249608000
1	2.904370000	-0.632896000	-4.024948000
1	-0.117355000	-4.141866000	-0.230443000
1	-1.209675000	-3.286032000	-1.313343000
1	-1.458238000	-3.207126000	0.427819000
1	-1.395778000	-0.710491000	0.538003000
1	-1.210024000	-0.594281000	-1.210772000
1	-0.044307000	0.198359000	-0.150964000
1	3.678310000	-4.843683000	-0.265241000
1	2.108415000	-4.330745000	0.357692000
1	3.466067000	-3.204226000	0.355773000
1	1.773706000	-4.343735000	-3.468892000
1	0.974292000	-4.943166000	-2.016941000
1	2.582223000	-5.526002000	-2.443220000
1	9.484023000	-0.081747000	-0.169244000
14	8.251731000	2.563479000	-0.830813000
6	8.858496000	2.562992000	2.024078000
1	9.763542000	3.162254000	1.899799000
6	8.591208000	1.660488000	0.814469000
1	7.655454000	1.131883000	1.005720000
1	8.993457000	1.949377000	2.920667000
1	8.026261000	3.242027000	2.214165000
6	9.693284000	0.604941000	0.654190000
1	9.786521000	0.011960000	1.568887000
1	10.666809000	1.061885000	0.467415000
6	9.844776000	2.786288000	-1.857885000
6	10.933570000	3.566873000	-1.102870000
1	10.648204000	4.610196000	-0.958252000
1	11.149270000	3.142508000	-0.121351000
1	11.865930000	3.559959000	-1.675928000
1	10.209488000	1.764229000	-2.007828000
1	8.821614000	2.873239000	-3.793754000
6	9.600602000	3.401883000	-3.241835000
1	10.516506000	3.369675000	-3.840032000
1	9.300494000	4.448660000	-3.161101000
1	6.052592000	3.730690000	-2.486055000
1	7.210393000	5.047960000	-2.629835000
6	6.499977000	4.568305000	-1.953969000
1	5.709310000	5.292992000	-1.738117000
1	8.697679000	5.706389000	-0.726814000
6	7.946363000	5.317562000	-0.036622000
1	7.248350000	6.133215000	0.176212000
1	8.449420000	5.064070000	0.896450000
1	6.406666000	3.835614000	0.054558000
6	7.185567000	4.131113000	-0.651515000

Cartesian coordinates of the DFT calculated geometry of OC-6-4-4 of **4**:

42	0.661792000	-1.791677000	-1.786089000
16	0.131297000	-3.790048000	-2.400024000
7	1.702303000	-1.364653000	-3.550474000
6	1.979041000	-0.041439000	-3.871603000
6	2.198154000	-2.134119000	-4.559302000
6	2.653088000	0.006798000	-5.089154000
6	2.794947000	-1.327668000	-5.520441000
1	2.089548000	-3.205606000	-4.540840000
1	2.988197000	0.898758000	-5.594757000
1	3.265231000	-1.670531000	-6.428231000
7	-0.792531000	-1.397971000	-0.333812000
6	-1.999811000	-0.829037000	-0.719186000
6	-0.845730000	-1.576405000	1.015067000
6	-2.806837000	-0.654104000	0.402176000
6	-2.070411000	-1.136221000	1.502861000
1	-0.010124000	-1.995291000	1.550260000
1	-3.796620000	-0.225381000	0.411819000
1	-2.382137000	-1.155740000	2.534960000
6	1.535052000	0.932468000	-2.954692000
1	1.697175000	1.990006000	-3.144617000
6	-2.153565000	-0.555045000	-2.092411000
1	-3.058138000	-0.084550000	-2.467830000
7	0.942351000	0.524474000	-1.873950000
7	-1.188754000	-0.893857000	-2.892840000
6	-1.225081000	-0.533659000	-4.257751000
6	-1.536157000	0.766160000	-4.651324000
6	-0.883091000	-1.470740000	-5.233676000
6	-1.481981000	1.127446000	-5.994030000
1	-1.789050000	1.507016000	-3.904461000
6	-0.836051000	-1.099333000	-6.565101000
1	-0.645649000	-2.481885000	-4.936890000
6	-1.114232000	0.210442000	-6.978913000
1	-1.709760000	2.150830000	-6.256409000
1	-0.554727000	-1.846744000	-7.295397000
6	0.378291000	1.445532000	-0.964589000
6	-0.418616000	2.500418000	-1.404496000
6	0.566074000	1.268985000	0.407134000
6	-1.033160000	3.347996000	-0.487595000
1	-0.583673000	2.643198000	-2.464234000
6	-0.050551000	2.118270000	1.307555000
1	1.187985000	0.458137000	0.756000000
6	-0.880039000	3.166763000	0.887229000
1	-1.658938000	4.142451000	-0.868364000
1	0.104883000	1.944046000	2.364293000
6	-0.975034000	0.585012000	-8.456847000
6	-1.314272000	2.058418000	-8.718820000
6	0.481970000	0.336285000	-8.898393000
6	-1.920495000	-0.289452000	-9.303596000
1	-2.344755000	2.291095000	-8.441824000
1	-0.650727000	2.729139000	-8.168746000
1	-1.198661000	2.273784000	-9.782989000
1	0.763813000	-0.710529000	-8.777512000
1	0.606299000	0.601626000	-9.951339000
1	1.172707000	0.940023000	-8.305722000
1	-1.815632000	-0.039088000	-10.362210000
1	-1.699445000	-1.351332000	-9.186258000
1	-2.961412000	-0.126055000	-9.015289000
6	-1.595671000	4.032364000	1.927605000
6	-2.462052000	5.121639000	1.281739000
6	-2.507813000	3.130321000	2.783805000
6	-0.555019000	4.715421000	2.836736000
1	-1.864262000	5.806261000	0.676175000
1	-3.241538000	4.694027000	0.647691000
1	-2.951212000	5.706728000	2.063003000
1	-1.934457000	2.368038000	3.313244000
1	-3.040719000	3.730390000	3.525651000
1	-3.244320000	2.621916000	2.157826000
1	-1.058943000	5.330458000	3.586561000
1	0.062361000	3.984764000	3.361497000
1	0.104993000	5.360301000	2.251972000
16	2.264739000	-1.953222000	-0.352401000

Cartesian coordinates of the DFT calculated geometry of OC-6-3-3 of **4**:

42	1.249784000	-1.194884000	-0.142703000
16	-0.684799000	-1.666601000	0.694759000
7	2.891735000	-0.515374000	-1.558243000
6	2.795523000	0.828389000	-1.885931000
6	3.950269000	-1.005094000	-2.199669000
6	3.846450000	1.174130000	-2.769562000
6	4.577318000	0.010510000	-2.968161000
1	4.243273000	-2.038212000	-2.101549000
1	4.028545000	2.151017000	-3.189885000
1	5.455872000	-0.114809000	-3.581698000
7	0.364871000	-1.360854000	-2.216767000
6	0.682459000	-2.551853000	-2.852191000
6	-0.382972000	-0.647669000	-3.056092000
6	0.101002000	-2.564197000	-4.142547000
6	-0.574031000	-1.356628000	-4.270278000
1	-0.763894000	0.324594000	-2.785435000
1	0.174180000	-3.361449000	-4.865943000
1	-1.141846000	-1.010250000	-5.119701000
6	1.759670000	1.534764000	-1.293937000
1	1.624719000	2.594247000	-1.480733000
6	1.445730000	-3.452184000	-2.121686000
1	1.732967000	-4.413331000	-2.533767000
7	0.933324000	0.915062000	-0.460600000
7	1.811886000	-3.142205000	-0.885735000
6	2.630208000	-4.062112000	-0.170904000
6	3.773527000	-4.601984000	-0.750764000
6	2.297484000	-4.422635000	1.135196000
6	4.576648000	-5.483433000	-0.031679000
1	4.052923000	-4.324152000	-1.759110000
6	3.103687000	-5.300979000	1.838763000
1	1.408107000	-4.012434000	1.592986000
6	4.268288000	-5.846142000	1.279294000
1	5.463424000	-5.870052000	-0.512611000
1	2.817980000	-5.559844000	2.850076000
6	-0.127564000	1.677734000	0.106385000
6	-0.922732000	2.493116000	-0.693449000
6	-0.368272000	1.633522000	1.479988000
6	-1.928203000	3.270152000	-0.124956000
1	-0.765552000	2.520536000	-1.764467000
6	-1.370945000	2.412911000	2.032857000
1	0.241088000	1.001008000	2.110453000
6	-2.173592000	3.253370000	1.248184000
1	-2.524971000	3.887959000	-0.780387000
1	-1.523336000	2.366753000	3.103429000
6	5.149493000	-6.778622000	2.114110000
6	6.360968000	-7.292474000	1.324977000
6	5.663368000	-6.009700000	3.348254000
6	4.319364000	-7.992429000	2.576904000
1	6.056651000	-7.863047000	0.444883000
1	7.006549000	-6.474664000	0.998216000
1	6.954930000	-7.951486000	1.961159000
1	6.295031000	-6.659098000	3.959289000
1	6.254979000	-5.143410000	3.043668000
1	4.940903000	-8.665419000	3.172457000
1	3.469903000	-7.689704000	3.190782000
1	3.937236000	-8.548891000	1.718132000
6	-3.260469000	4.104760000	1.909515000
6	-4.017677000	4.972298000	0.895310000
6	-4.274651000	3.181924000	2.613946000
6	-2.608585000	5.035123000	2.952128000
1	-3.350605000	5.665968000	0.378880000
1	-4.528762000	4.364360000	0.145887000
1	-4.773277000	5.562202000	1.417823000
1	-3.795010000	2.568752000	3.378269000
1	-5.050085000	3.779874000	3.099047000
1	-4.755591000	2.514674000	1.895064000
1	-3.372331000	5.650641000	3.433673000
1	-2.093638000	4.469093000	3.729574000
1	-1.882529000	5.699159000	2.477546000
16	2.667378000	-1.113040000	1.486323000
1	4.840361000	-5.656283000	3.971197000

6.2 Supporting Information to chapter "Redox Activation of Acyclic (Aryl)(Amino)Carbene Gold(I) Complexes"

Supporting Information

Redox Activation of Acyclic (Aryl)(Amino)Carbene Gold(I) Complexes

Maurice P. Schrick,[†⊥] G. Kabelo Ramollo,[‡⊥] Cristina-Maria Susanne Hirschbiegel,[†] Manuel Fernandes,[‡] Andreas Lemmerer,[‡] Christoph Förster,[†] Daniela I. Bezuidenhout,[§*] Katja Heinze[†*]

[⊥] Authors contributed equally

[†] Department of Chemistry, Johannes Gutenberg University, Duesbergweg 10-14, 55128 Mainz, Germany

[‡] Molecular Sciences Institute, School of Chemistry, University of the Witwatersrand, Johannesburg 2050, South Africa

[§] Laboratory of Inorganic Chemistry, Environmental and Chemical Engineering, University of Oulu, P. O. Box 3000, 90014 Oulu, Finland

Synthesis and characterisation of P2 and P3

AuCl[C(OEt)(4-DMA)] **P2**. A dried mixture of AuCl(tht) (0.0.163 g, 0.51 mmol) and $W(CO)_5$[C(OEt)(4-DMA)] (0.255 g, 0.51 mmol) was dissolved in CH_2Cl_2 (10 mL) and stirred for 16 hours at –78 °C. The resulting dark brown solution was warmed up to room temperature, at which point the CH_2Cl_2 solvent was completely removed under reduced pressure. The resulting brown paste was washed with *n*-hexane (2 x 10 mL). The product was extracted with CH_2Cl_2 (10 mL) *via* cannula filtration methods and dried under reduced pressure to give a yellow powder. Yield = 0.199 g, 97 %. Mp (dec) 143 – 145 °C. ^{1}H NMR (500 MHz, CD_2Cl_2): δ = 8.20 (s, br, 2H, DMA-$H_{\alpha,\alpha'}$), 6.68 (d, ^3J(HH) = 9.5 Hz, 2H, DMA-$H_{\beta,\beta'}$), 5.06 (q, ^3J(HH) = 7.1 Hz, 2H, OCH_2CH_3), 3.18 (s, 6H, DMA-N(CH_3)$_2$), 1.58 (t, ^3J(HH) = 7.2 Hz, 3H, OCH_2CH_3). ^{13}C{^{1}H} NMR (126 MHz, CD_2Cl_2): δ = 246.2 ($C_{carbene}$), 157.3 (DMA-C_q), 131.0 (DMA-C_{ipso}), n.o. (DMA-$C_{\alpha,\alpha'}$), 111.9 (DMA-$C_{\beta,\beta'}$), 78.9 (OCH_2CH_3), 40.9 (DMA-N(CH_3)$_2$), 15.2 (OCH_2CH_3). Anal. Calcd for $C_{11}H_{15}NOClAu$: C 32.25, H 3.69, N 3.42. Found: C 32.80, H 3.63, N 3.42. ESI-HRMS (15 V, positive mode, *m*/*z*): calcd for $[C_{11}H_{15}NOAu]^+$ 374.0819, found 374.0792.

The analogue AuCl[C(OEt)(2-furyl)] **P3** was similarly prepared as an orange powder.

AuCl[C(OEt)(2-furyl)] **P3**. Yield = 0.308 g, 96 %. Mp (dec): 131 – 132 °C. ^{1}H NMR (500 MHz, CD_2Cl_2): δ = 8.23 (s, br, 1H, Fu-H_γ), 8.06 (s, br, 1H, Fu-H_α), 6.82 (s, br, 1H, Fu-H_β), 5.21 (q, ^3J(HH) = 6.7 Hz, 2H, OCH_2CH_3), 1.65 (t, ^3J(HH) = 7.2 Hz, 3H, OCH_2CH_3). ^{13}C{^{1}H} NMR (126 MHz, CD_2Cl_2): δ = 235.7 ($C_{carbene}$), 159.2 (Fu-C_{ipso}), 154.5 (Fu-C_γ), 142.1 (Fu-C_α), 116.6 (Fu-C_β), 82.7 (OCH_2CH_3), 15.2 (OCH_2CH_3). Anal. Calcd for $C_7H_8O_2ClAu$: C 23.58, H 2.26. Found: C 23.49, H 2.25. ESI-HRMS (15 V, positive mode, *m*/*z*): calcd for $[C_7H_8O_2Au]^+$ 321.0190, found 320.9951.

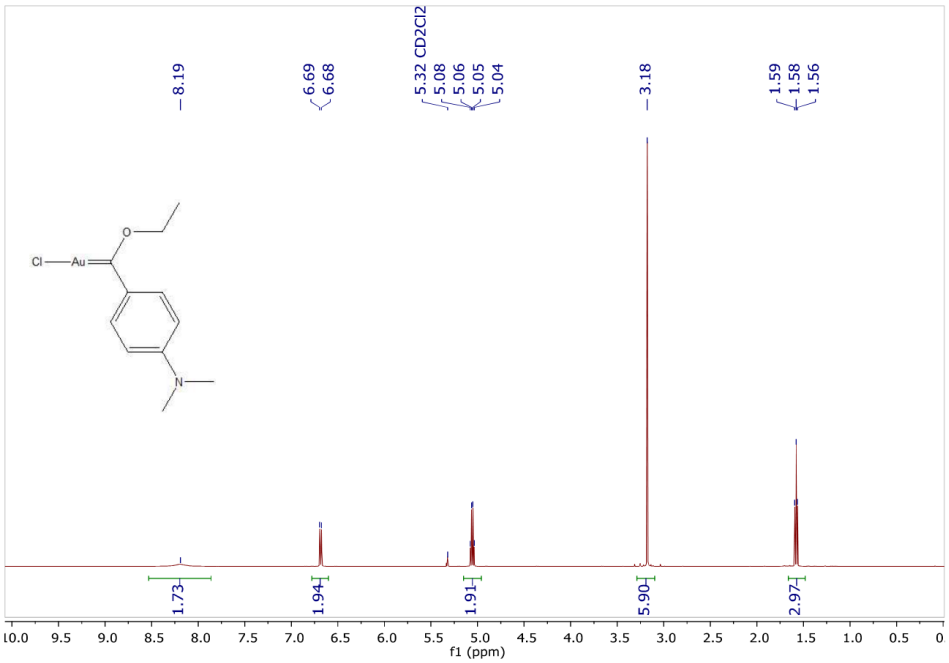

Figure S1. ^{1}H NMR spectrum of **P2** in CD_2Cl_2.

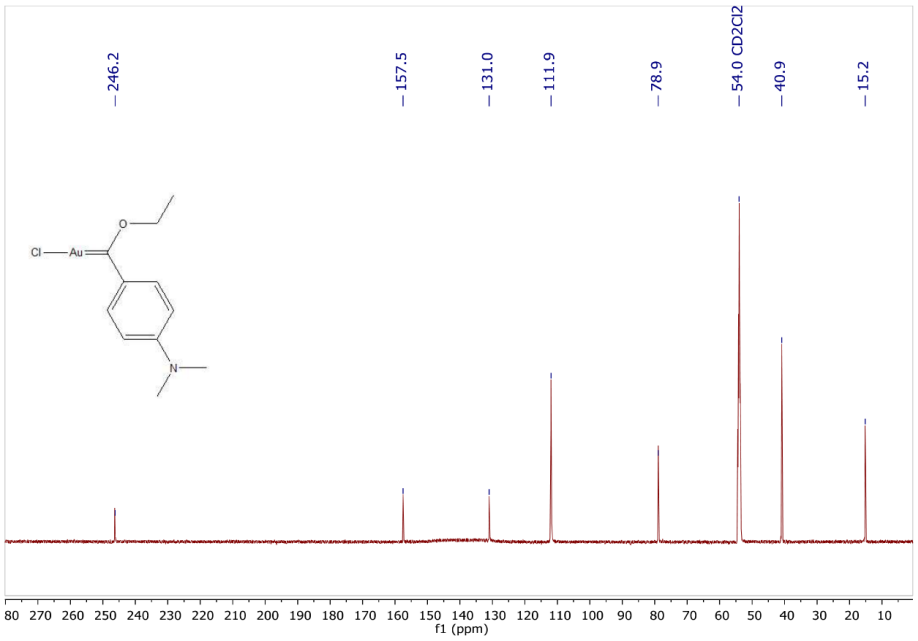

Figure S2. $^{13}C\{^{1}H\}$ NMR spectrum of **P2** in CD_2Cl_2.

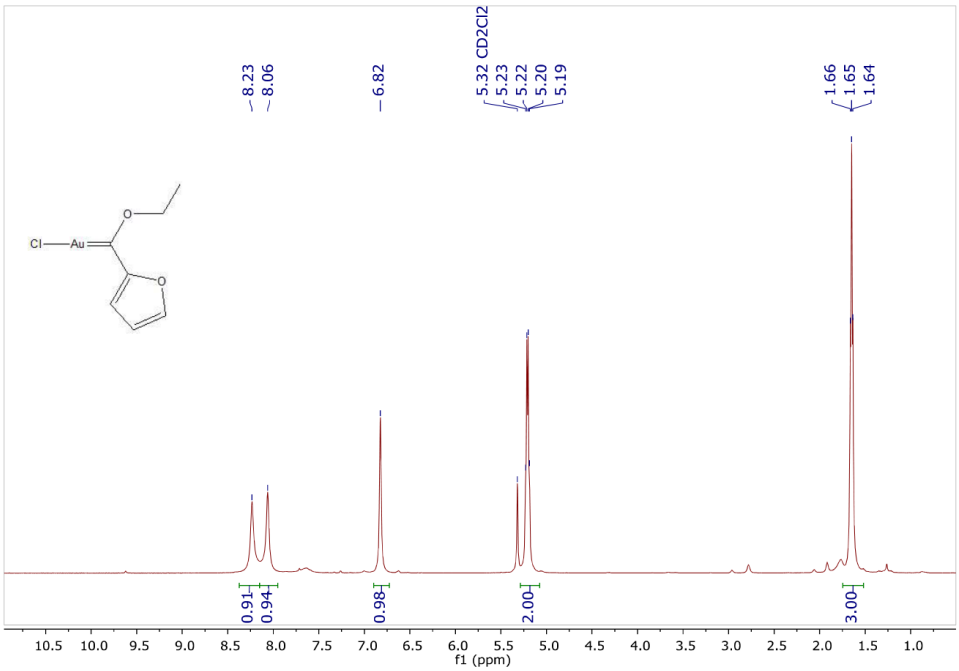

Figure S3. ^{1}H NMR spectrum of **P3** in CD_2Cl_2.

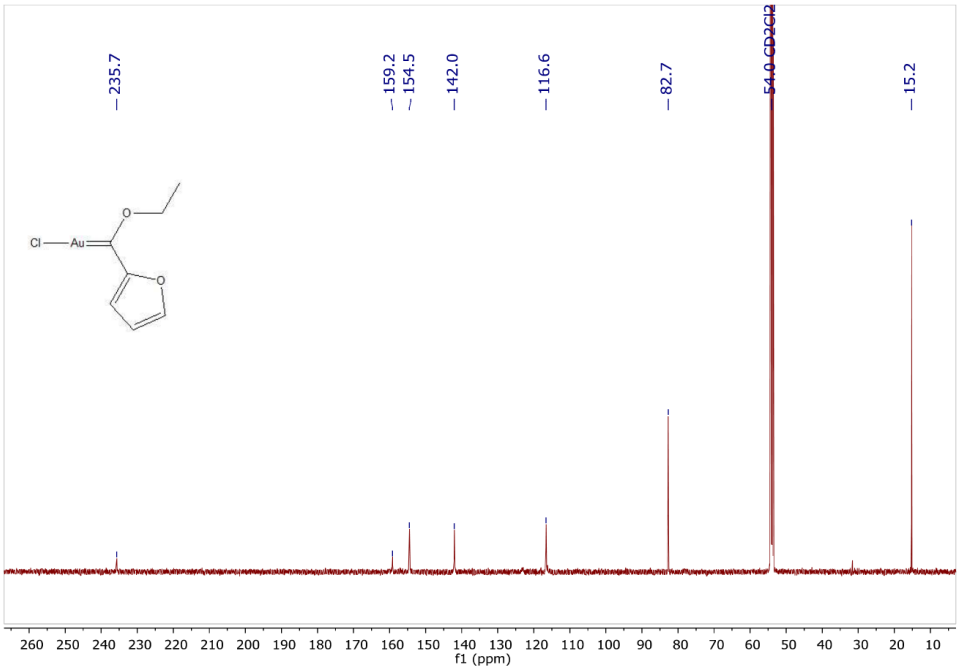

Figure S4. $^{13}C\{^{1}H\}$ NMR spectrum of **P3** in CD_2Cl_2.

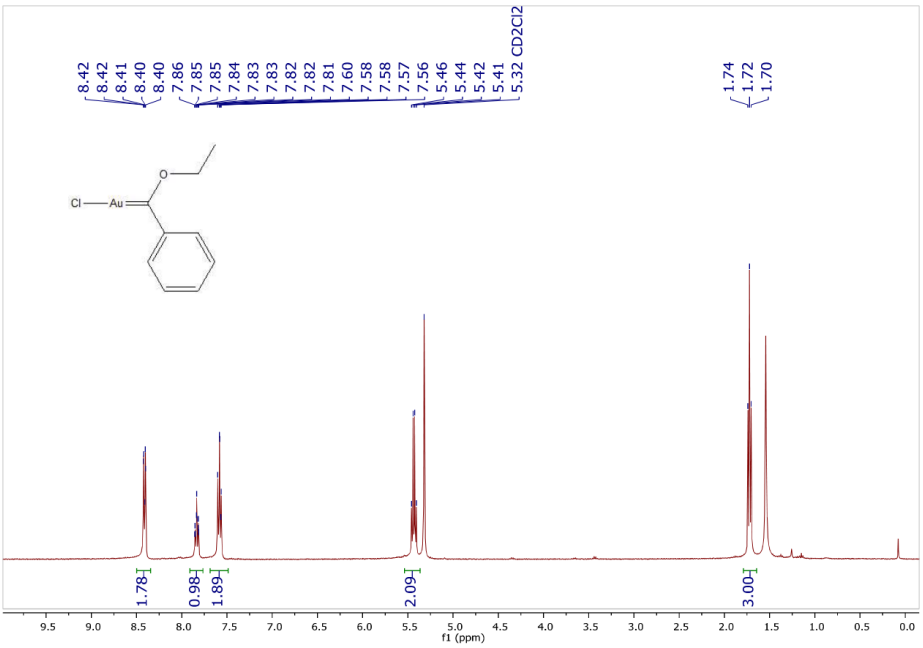

Figure S5. ^{1}H NMR spectrum of **1** in CD_2Cl_2.

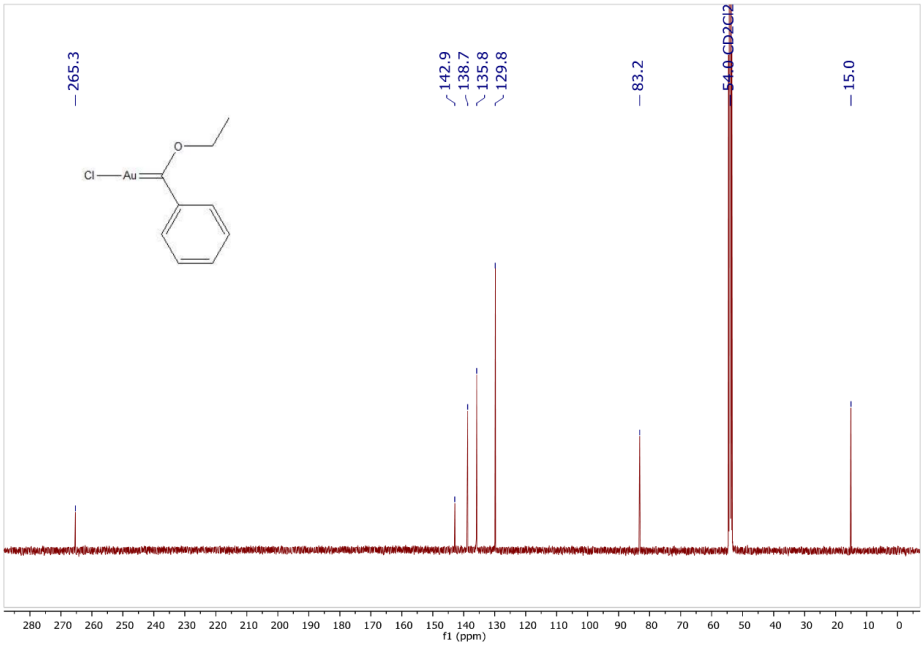

Figure S6. $^{13}C\{^{1}H\}$ NMR spectrum of **1** in CD_2Cl_2.

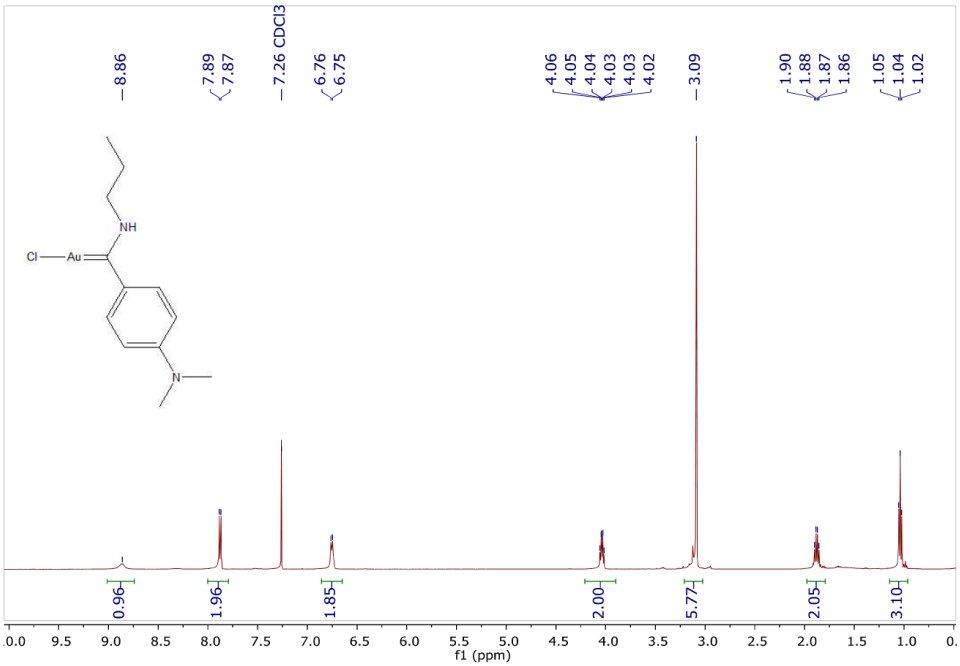

Figure S7. ^{1}H NMR spectrum of **2a** in $CDCl_3$.

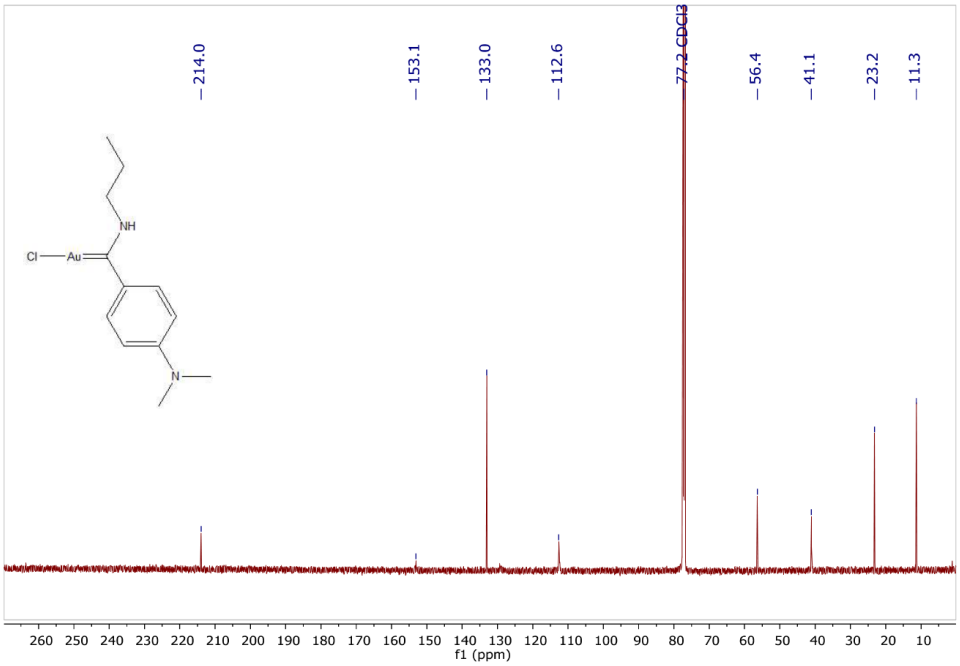

Figure S8. $^{13}C\{^{1}H\}$ NMR spectrum of **2a** in $CDCl_3$.

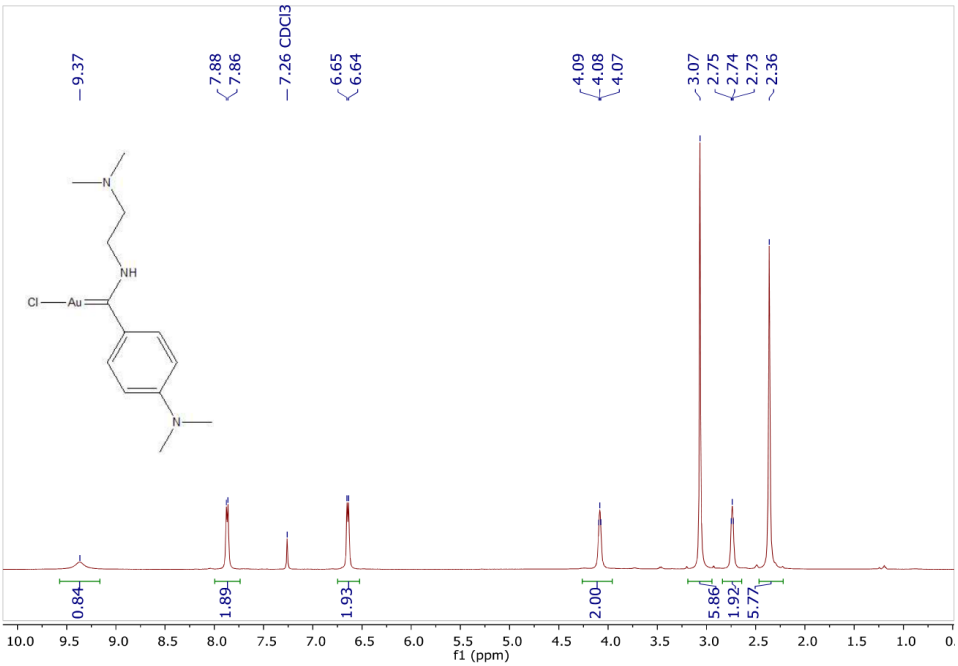

Figure S9. ^{1}H NMR spectrum of **2b** in $CDCl_3$.

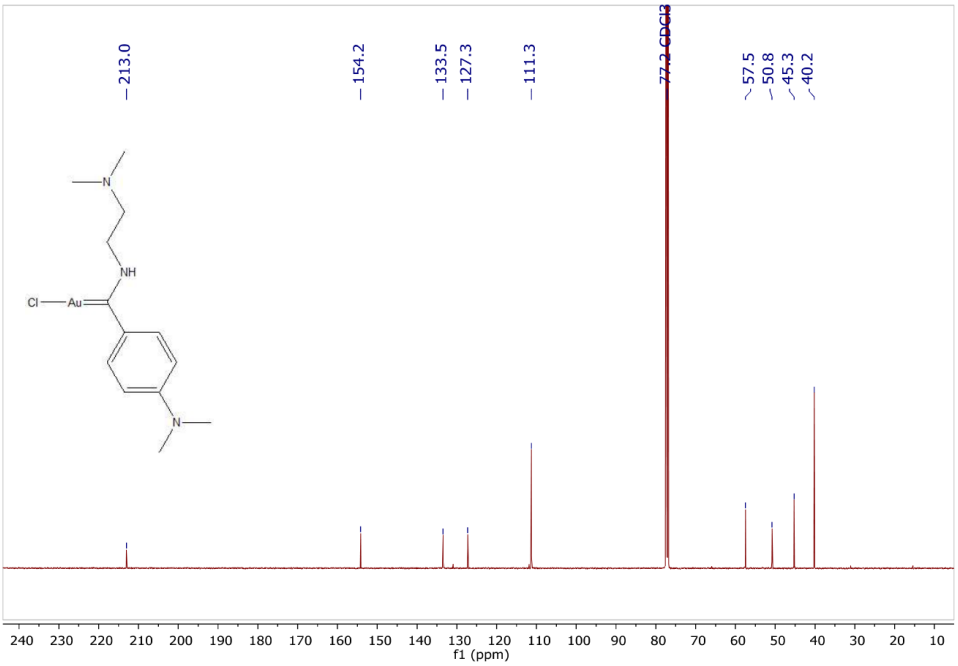

Figure S10. $^{13}C\{^{1}H\}$ NMR spectrum of **2b** in $CDCl_3$.

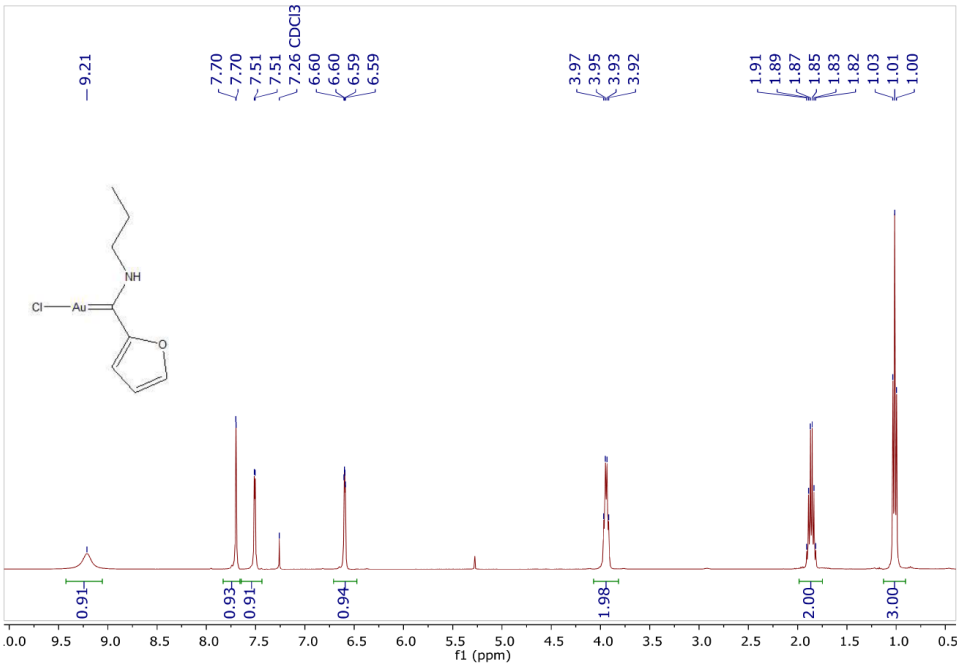

Figure S11. ^{1}H NMR spectrum of **3a** in $CDCl_3$.

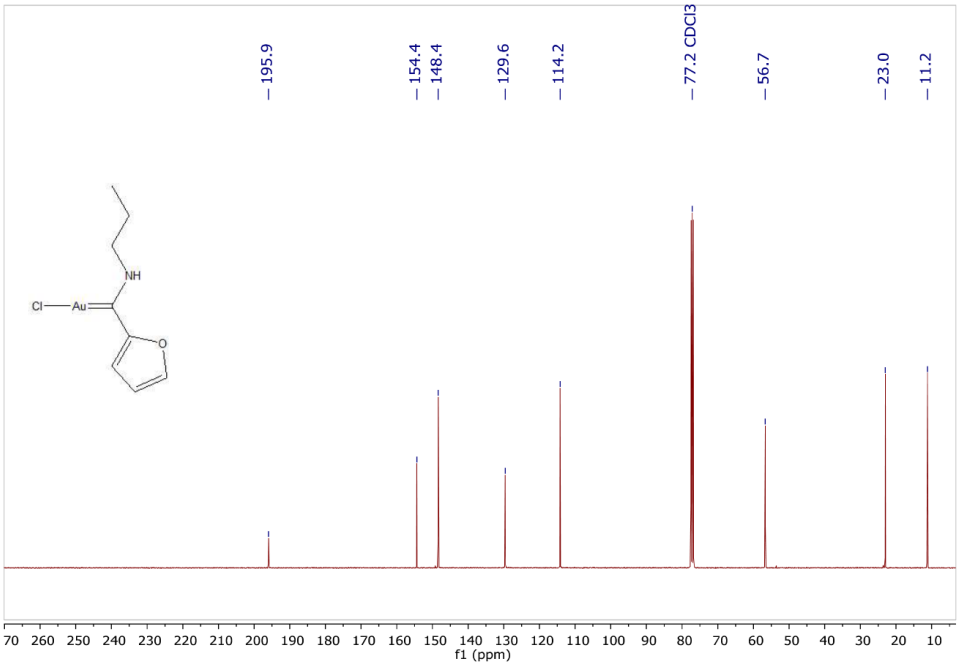

Figure S12. $^{13}C\{^{1}H\}$ NMR spectrum of **3a** in $CDCl_3$.

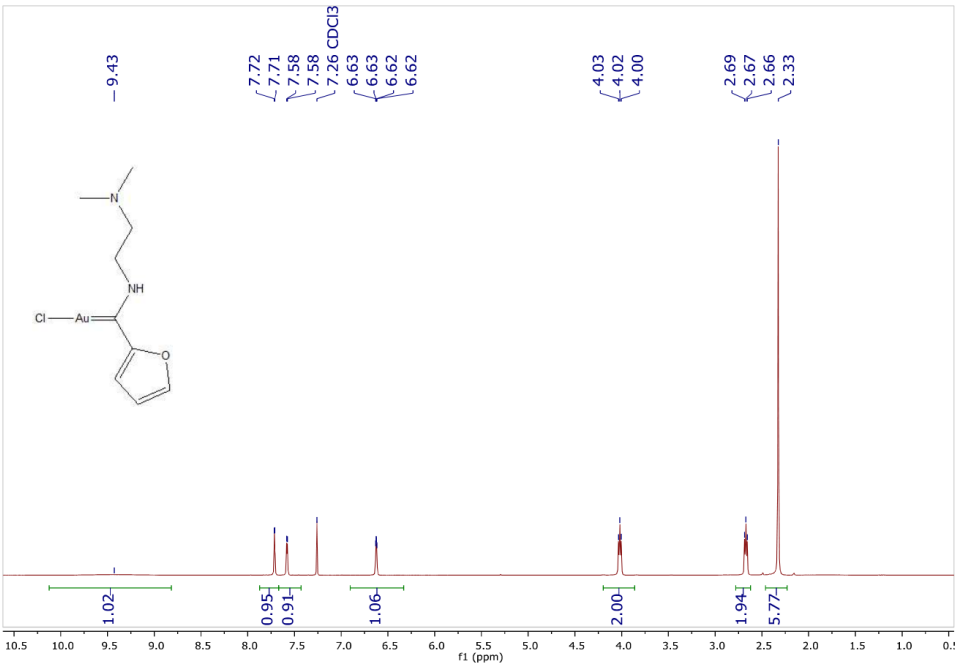

Figure S13. ^{1}H NMR spectrum of **3b** in $CDCl_3$.

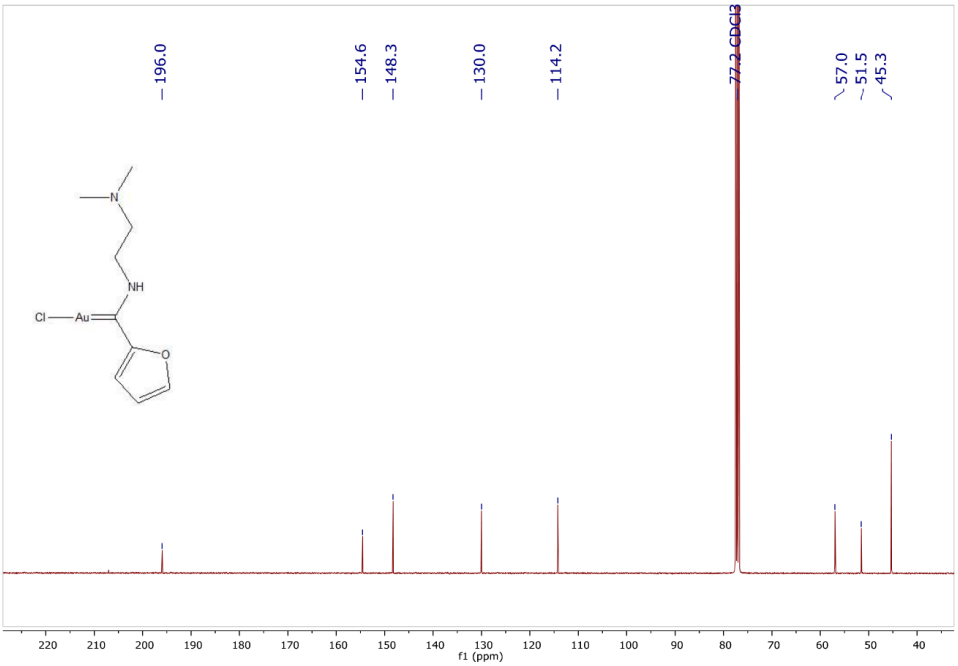

Figure S14. $^{13}C\{^{1}H\}$ NMR spectrum of **3b** in $CDCl_3$.

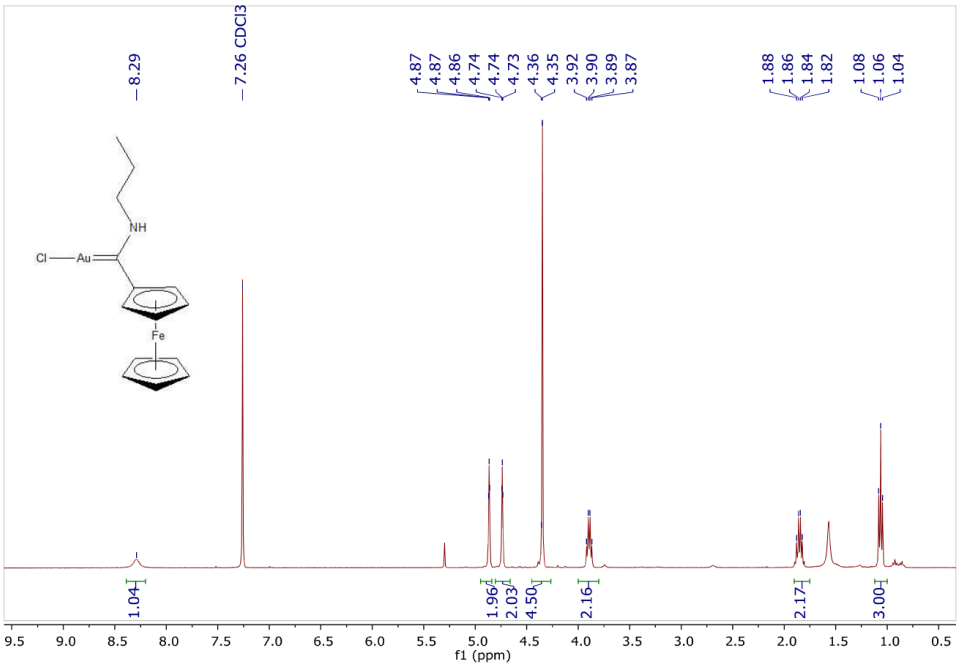

Figure S15. ^{1}H NMR spectrum of **4a** in $CDCl_3$.

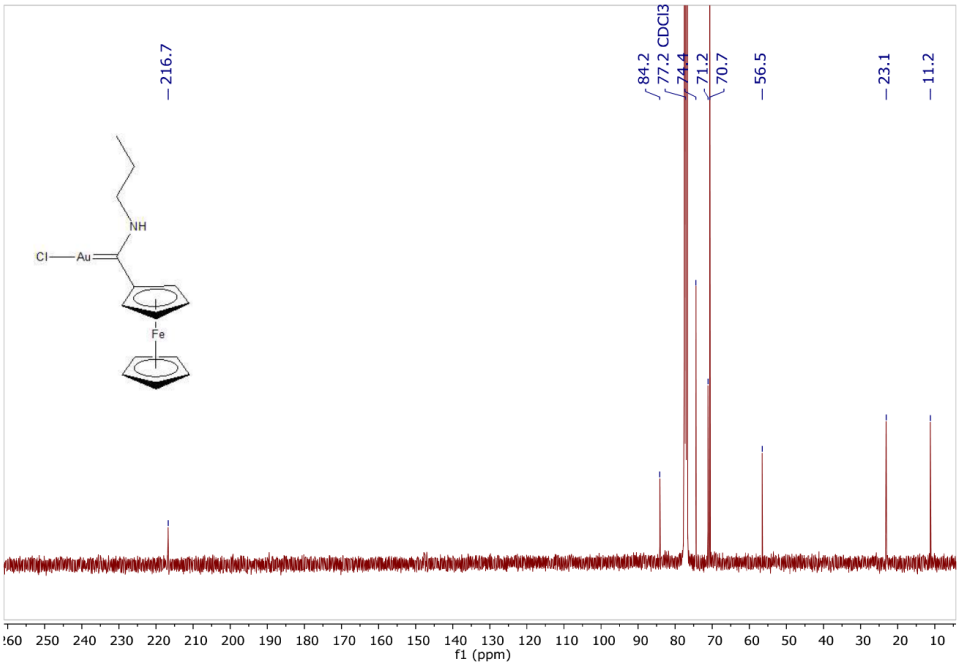

Figure S16. $^{13}C\{^{1}H\}$ NMR spectrum of **4a** in $CDCl_3$.

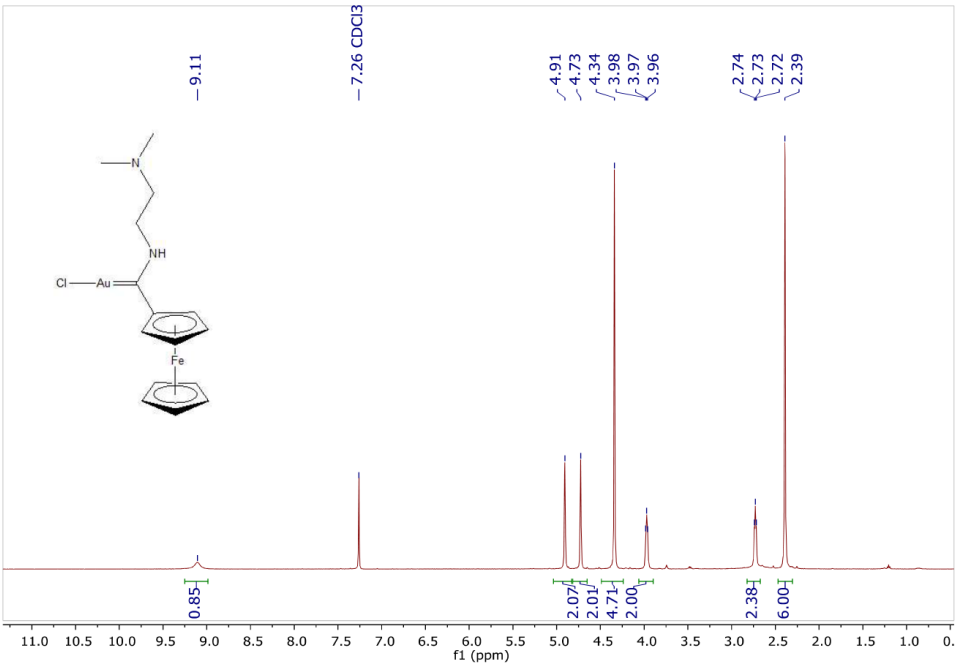

Figure S17. ^{1}H NMR spectrum of **4b** in $CDCl_3$.

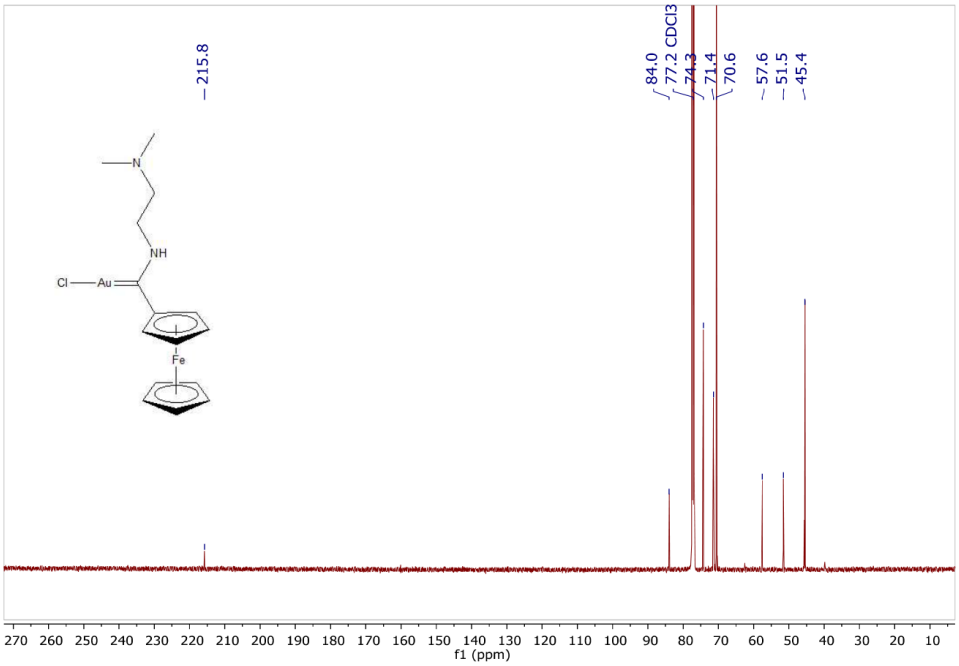

Figure S18. $^{13}C\{^{1}H\}$ NMR spectrum of **4b** in $CDCl_3$.

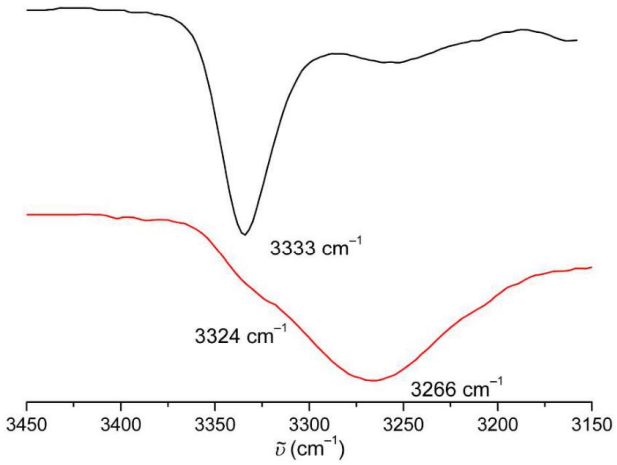

Figure S19. IR spectra of aminocarbene complexes **2a** (black) and **2b** (red) in CH_2Cl_2 in the $\tilde{\nu}_{NH}$ region.

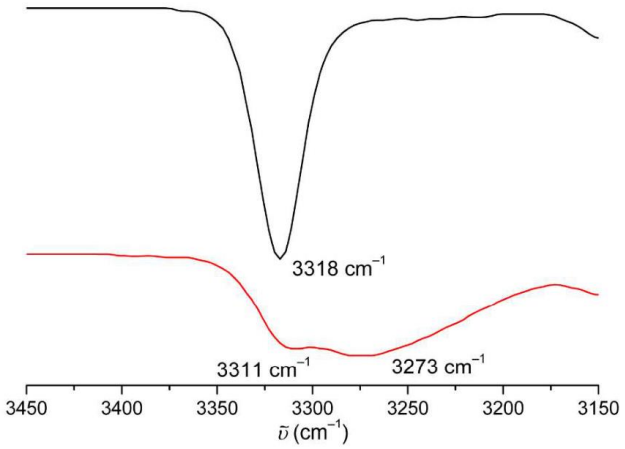

Figure S20. IR spectra of aminocarbene complexes **3a** (black) and **3b** (red) in CH_2Cl_2 in the $\tilde{\nu}_{NH}$ region.

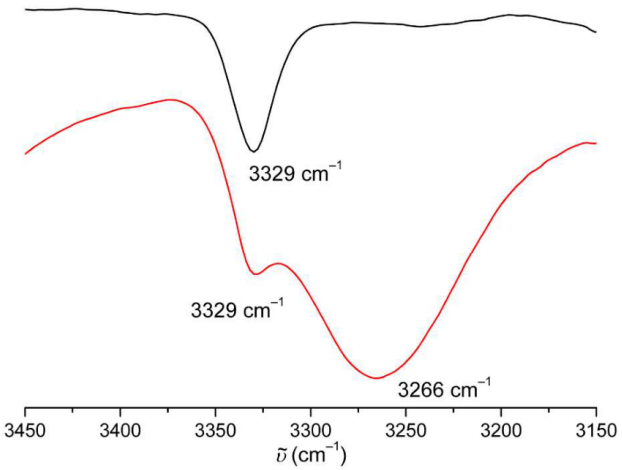

Figure S21. IR spectra of aminocarbene complexes **4a** (black) and **4b** (red) in CH_2Cl_2 in the $\tilde{\nu}_{NH}$ region.

Table S1. Crystal data and summary of data collection and refinement for complexes **P2 – P4**.

	P2	**P3**	**P4**
Chemical formula	$C_{11}H_{15}AuClNO$	$0.5(C_{28}H_{32}Au_4Cl_4O_8)$, $0.5(C_2H_4Cl_2)$	$C_{13}H_{14}AuClFeO$
M_r	409.66	798.03	474.51
Crystal system	Orthorhombic	Orthorhombic	Orthorhombic
Space group	*P*na2$_1$	*P*nma	*P*ca2$_1$
Temperature (K)	173	173	173
a (Å)	7.3391(8)	10.1229(6)	16.9502(4)
b(Å)	15.5386(17)	6.4542(4)	7.3598(2)
c (Å)	10.7564(11)	32.0692(19)	10.4161(2)
α (°)	90	90	90
β (°)	90	90	90
γ (°)	90	90	90
V (Å^3)	1226.7(2)	2095.2(2)	1299.41(5)
Z	4	4	4
μ (mm^{-1})	12.185	14.514	12.578
Crystal size (mm)	0.174 × 0.153 × 0.14	0.401× 0.3 × 0.19	0.219 × 0.214 × 0.042
T_{min}, T_{max}	0.057, 0.190	0.053, 0.164	0.146, 0.901
measured	11184	23083	18202
independent	2962	2818	3202
observed [*I*> 2σ(*I*)]	2151	2724	2883
R_{int}	0.0978	0.0244	0.0343
$(\sin\theta/\lambda)_{max}$ (Å^{-1})	0.6604	0.6672	0.6668
$R[F^2> 2\sigma(F^2)]$	0.0387	0.0274	0.0175
$wR(F^2)$	0.0877	0.0636	0.0304
S	0.937	1.343	0.836
No. of reflections	2962	2818	3202
No. of parameters	139	151	154
No. of restraints	1	0	1
H-atom treatment	Constrained	Constrained	Constrained
$\Delta\rho_{max}$, $\Delta\rho_{min}$ (e Å^{-3})	2.33, -0.94	0.89, -2.35	0.64, -0.51

Table S2. Crystal data and summary of data collection and refinement for complexes **2a**, **2b**, **3a**, **4a** and **4b-[H-4b]Cl**.

	2a	**2b**	**3a**	**4a**	**4b-[H-4b]Cl**
Chemical formula	$C_{12}H_{18}AuClN_2$	$C_{13}H_{21}AuClN_3$	$C_8H_{11}AuClNO$	$C_{14}H_{17}AuClFeN$	$C_{15}H_{21}AuClFeN_2$, $C_{15}H_{20}AuClFeN_2$, $CHCl_3$, Cl
M_r	422.70	451.74	369.59	487.55	1189.02
Crystal system	Monoclinic	Monoclinic	Monoclinic	Orthorhombic	Monoclinic
Space group	$P2_1/c$	$P2_1/c$	$P2_1/c$	$P2_12_12_1$	$P2_1/n$
Temperature (K)	173	173	173	173	173
a (Å)	14.4677(9)	15.7593(16)	8.5012(3)	7.2466(4)	10.7145(3)
b(Å)	8.4912(5)	10.7545(11)	17.1550(8)	13.9354(9)	18.4675(5)
c (Å)	22.2849(14)	9.2841(9)	7.7212(3)	14.1747(9)	19.2118(5)
α (°)	90	90	90	90	90
β (°)	92.979(3)	101.503(4)	116.4296(16)	90	93.5689(14)
γ (°)	90	90	90	90	90
V (Å^3)	2734.0(3)	1541.9(3)	1008.35(7)	1431.42(15)	3794.07(18)
Z	8	4	4	4	1
μ (mm^{-1})	10.934	9.702	14.808	11.418	8.910
Crystal size (mm)	0.23 × 0.205 × 0.038	0.563 × 0.112 × 0.06	0.321 × 0.214 × 0.105	0.343 × 0.085 × 0.066	0.513 × 0.219 × 0.036
T_{min}, T_{max}	0.225, 0.760	0.378, 0.746	0.087, 0.305	0.063, 0.644	0.059, 0.775
measured	44099	48955	10720	14445	61787
independent	6816	4383	2509	3561	9431
observed [I> 2σ(I)]	5484	3814	2107	3458	7645
R_{int}	0.0501	0 (merged in TwinAbs in point group 2/m)	0.0484	0.0282	0.0426
(sin θ/λ)$_{max}$ (Å^{-1})	0.6679	0.6604	0.6670	0.6676	0.6681
$R[F^2> 2\sigma(F^2)]$	0.0280	0.0362	0.0266	0.0157	0.0245
$wR(F^2)$	0.0550	0.0976	0.0640	0.0367	0.0490
S	1.035	1.165	1.035	1.029	1.020
No. of reflections	6816	4383	2509	3561	9431
No. of parameters	295	168	110	164	410
No. of restraints	0	0	0	0	0
H-atom treatment	Constrained	Constrained	Constrained	Constrained	Constrained
Δρ$_{max}$, Δρ$_{min}$ (e Å^{-3})	3.00, -0.75	1.58, -1.52	1.23, -1.76	0.64, -0.68	1.54, -0.90

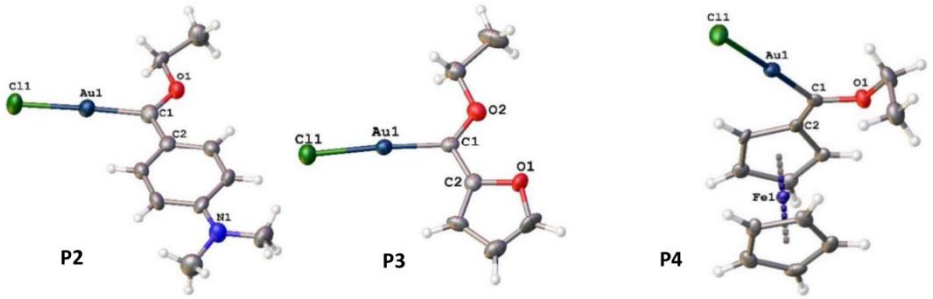

Figure S22. Ellipsoid plots of precursor ethoxycarbene complexes **P2** – **P4** (50% probability level). A second molecule was removed from **P3**. Solvent molecules were also removed from **P3** for clarity. Selected bond lengths (Å), bond angles (°) and torsion angles (°): **P2** Au–$C_{carbene}$ 2.001(15), $C_{carbene}$–O 1.314(17), $C_{carbene}$–C_{ipso} 1.410(2), Au–Cl 2.301(4), $C_{carbene}$–Au–Cl 177.4(4), O–$C_{carbene}$–C_{ipso} 114.6(13), C_{α}–C_{ipso}–$C_{carbene}$–N 0.0(2); **P3** Au–$C_{carbene}$ 1.956(7), $C_{carbene}$–O 1.299(8), $C_{carbene}$–C_{ipso} 1.411(10), Au–Cl 2.279(19), $C_{carbene}$–Au–Cl 176.4(2), O–$C_{carbene}$–C_{ipso} 113.2(7), C_{α}–C_{ipso}–$C_{carbene}$–O 0.0(2); **P4** Au–$C_{carbene}$ 1.972(5), $C_{carbene}$–O 1.309(6), $C_{carbene}$–C_{ipso} 1.424(7), Au–Cl 2.285(13), $C_{carbene}$–Au–Cl 177.4(15), O–$C_{carbene}$–C_{ipso} 112.2(4), C_{α}–C_{ipso}–$C_{carbene}$–O 10.6(6).

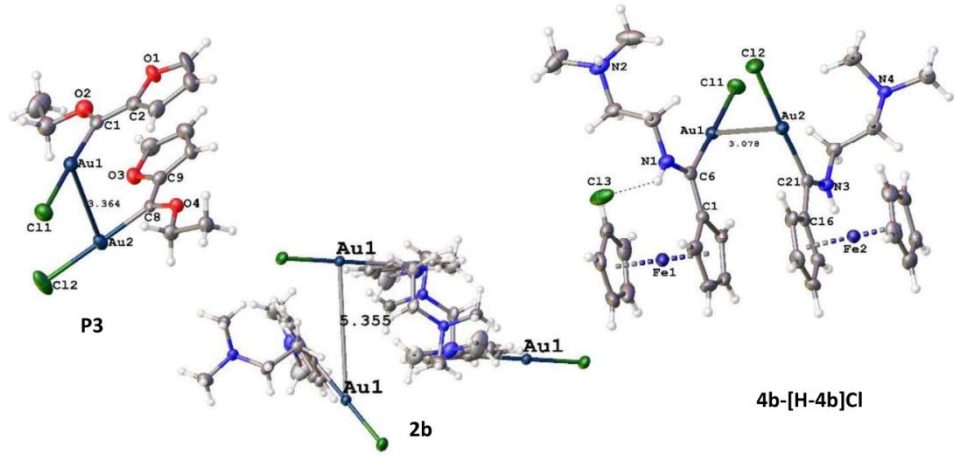

Figure S23. Partially labeled crystal structures of complexes **P3** and **4b** depicting aurophilic interactions (Au1–Au2 distances of 3.3641(3) Å and 3.0783(2) Å, respectively). Structure **2b** is shown here as an example of the absence of these interactions from the rest of the complexes. Complex **4b** shows a gold-gold interaction with its *N*-protonated counterpart **[H-4b]Cl**.

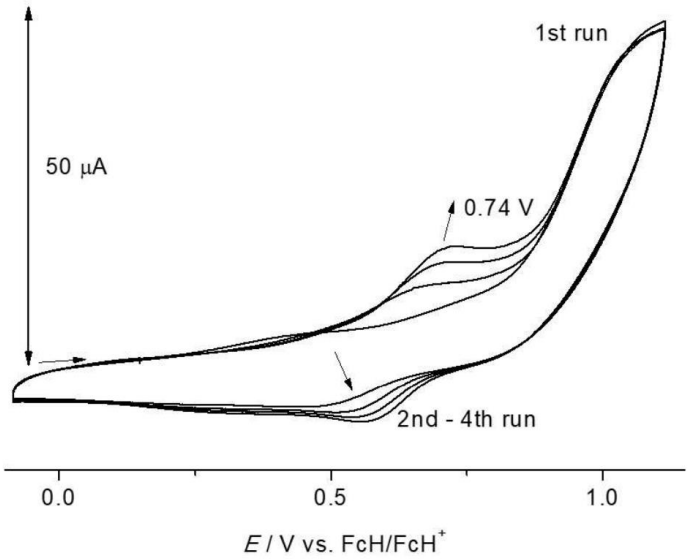

Figure S24. Cyclic voltammograms of **1** in CH_3CN with [^{n}Bu$_4$N][PF_6] as supporting electrolyte.

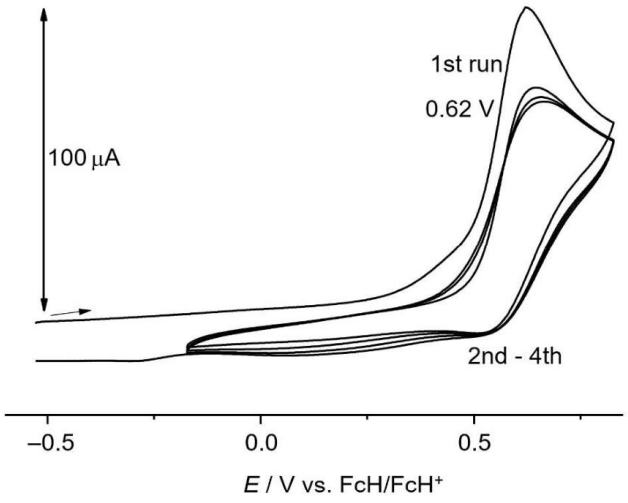

Figure S25. Cyclic voltammograms of **2a** in CH_3CN with [^{n}Bu$_4$N][PF_6] as supporting electrolyte.

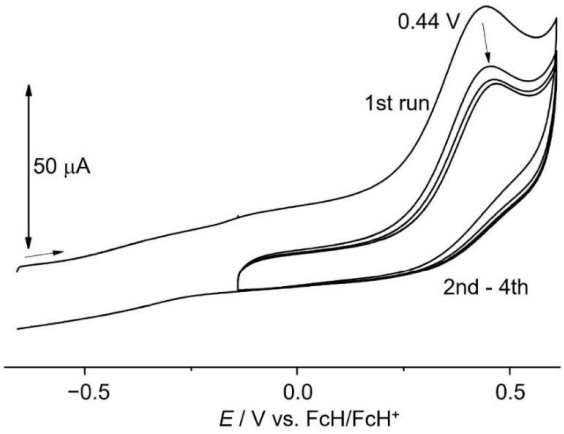

Figure S26. Cyclic voltammograms of **2b** in CH_3CN with $[^nBu_4N][PF_6]$ as supporting electrolyte.

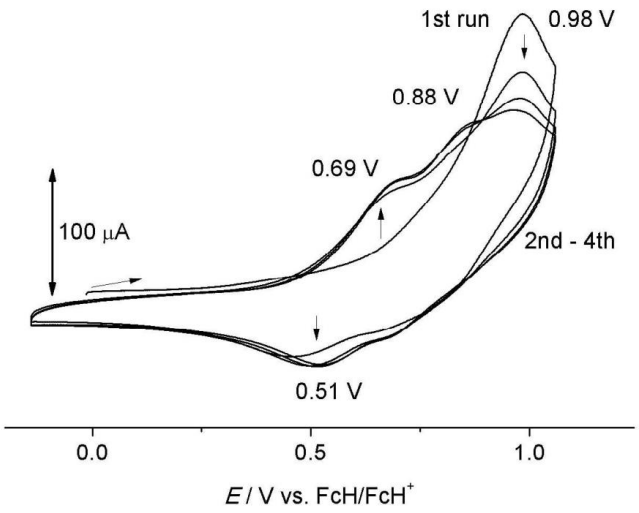

Figure S27. Cyclic voltammograms of **3a** in CH_3CN with $[^nBu_4N][PF_6]$ as supporting electrolyte.

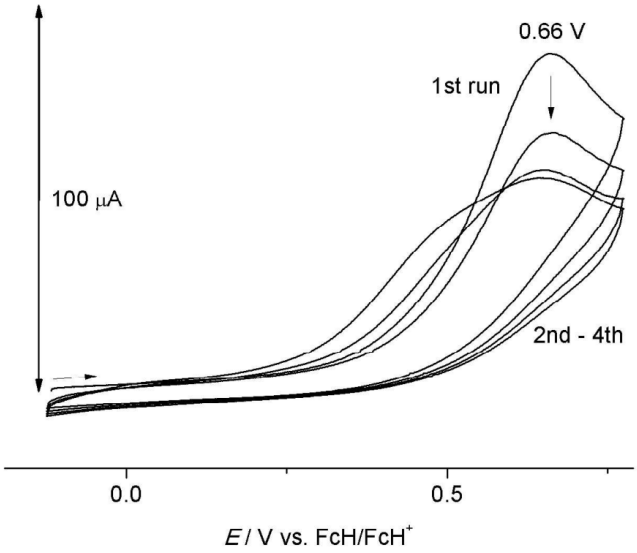

Figure S28. Cyclic voltammograms of **3b** in CH_3CN with [^{n}Bu$_4$N][PF_6] as supporting electrolyte.

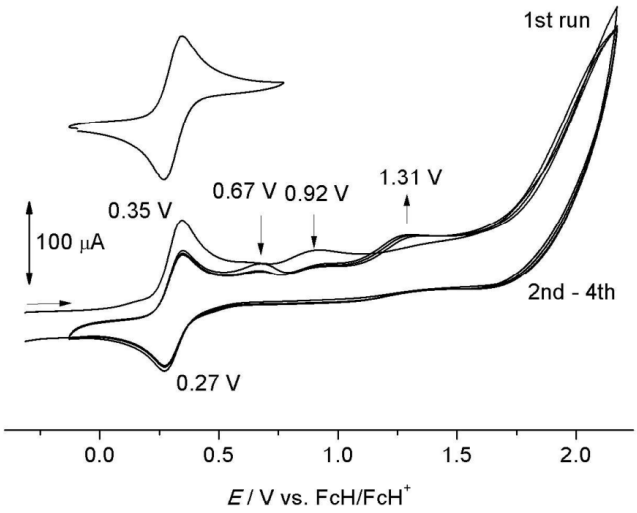

Figure S29. Cyclic voltammograms of **4a** in CH_3CN with [^{n}Bu$_4$N][PF_6] as supporting electrolyte.

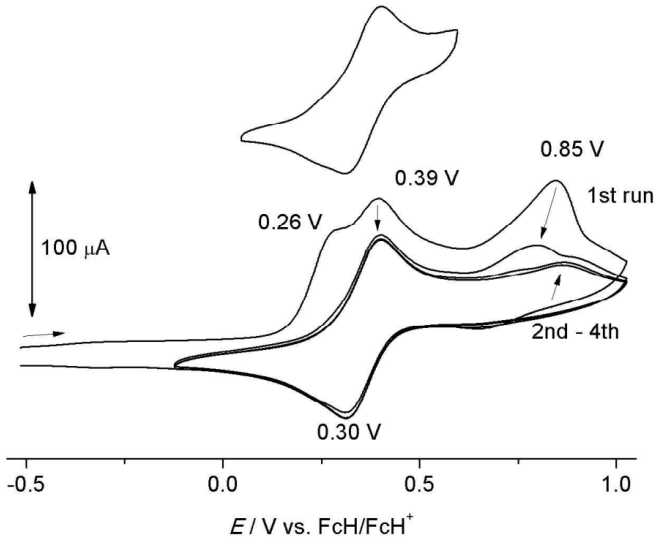

Figure S30. Cyclic voltammograms of **4b** in CH_3CN with $[^nBu_4N][PF_6]$ as supporting electrolyte.

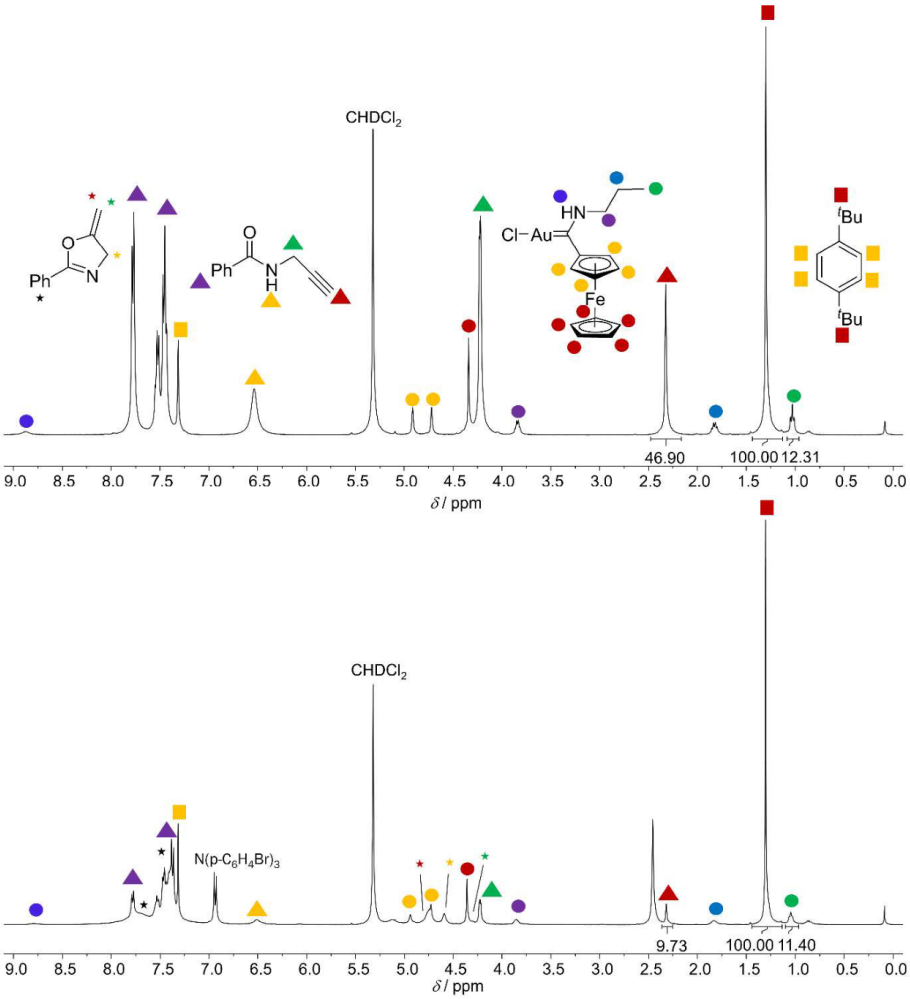

Figure S31. ^{1}H NMR spectra of **4a** (0.01 mM; 10 mol-%; circles) and Magic Blue (1.0 eq) in CD_2Cl_2 at the beginning of the catalytic reaction (top) and after ca. 79 % conversion of *N*(2-propyn-1-yl)benzamide (triangles) to 2-phenyl-5-vinylidene-2-oxazoline (stars) (bottom) stopped by addition of $FeCp^*_2$ (1.05 eq with respect to **4a**) indicating a 92±5 % recovery. 1,4-Di-*tert*-butylbenzene (squares) was used as internal standard.

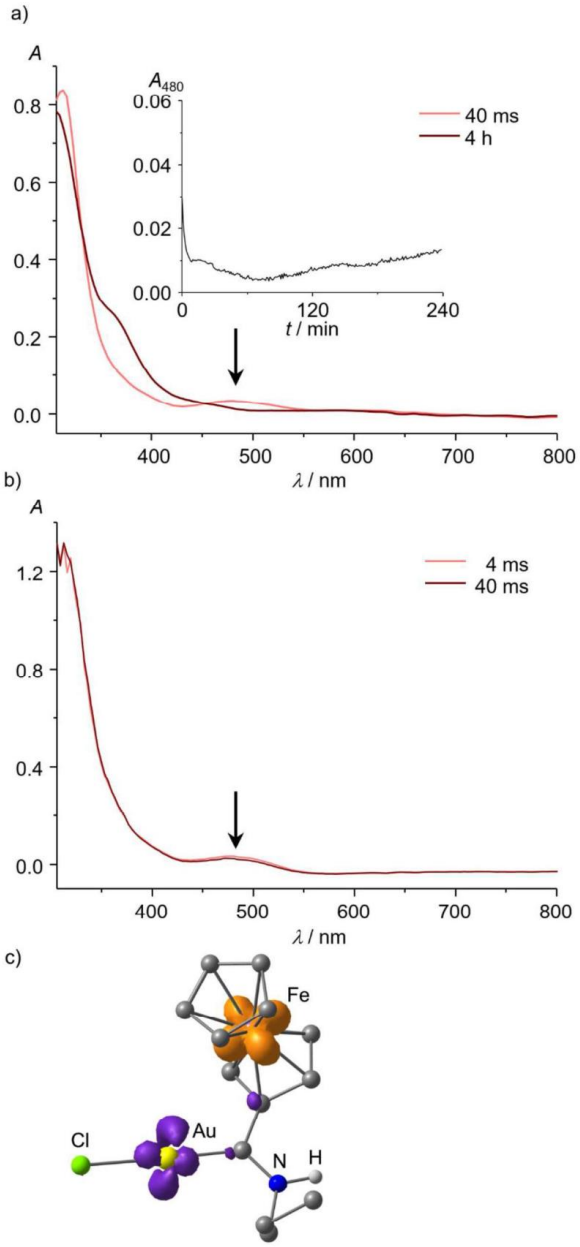

Figure S32. a) UV/Vis spectra of **4a** in CH_2Cl_2 recorded a) 40 ms (light red) and 4 h (red) after mixing with Magic Blue at 22 °C including a time trace observed at λ = 480 nm (marked with an arrow and inset) and b) 4 ms (light red) and 40 ms (red) after mixing with Magic Blue at –90 °C. c) Difference electron density of the TD-DFT calculated transition (553 nm assigned to the experimental 480 nm band (purple = electron loss; orange = electron gain; displayed at an isosurface value of 0.01 a.u.).

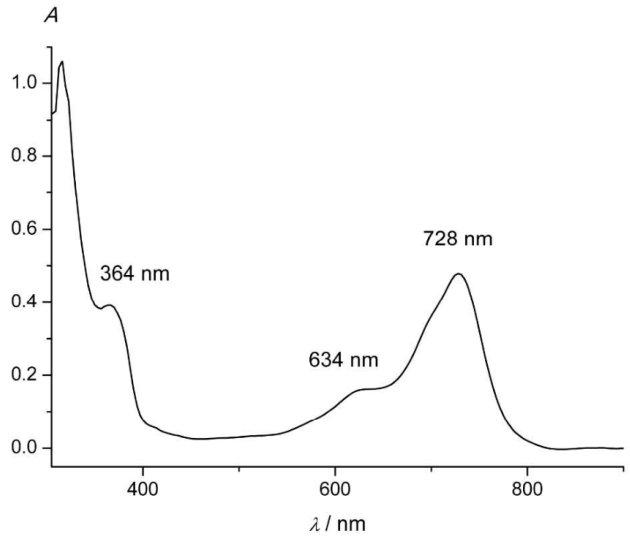

Figure S33. UV/Vis/NIR spectrum of Magic Blue in CH_2Cl_2.

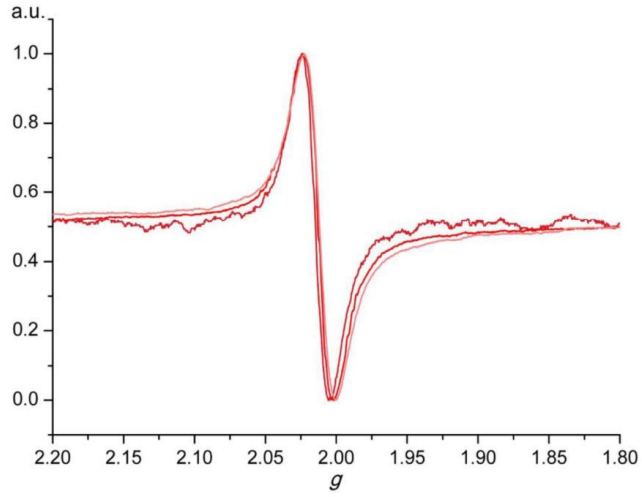

Figure S34. Normalized X-band EPR spectra of **4a** with oxidants $[N(4\text{-}C_6H_4Br)_3][SbCl_6]$ (red), $[C_{12}H_8S_2][SbCl_6]$ (light red) after 3 h in THF at 35 °C and $[NH_4]_2[Ce(NO_3)_6]$ (dark red) after 3 h in THF at 22 °C.

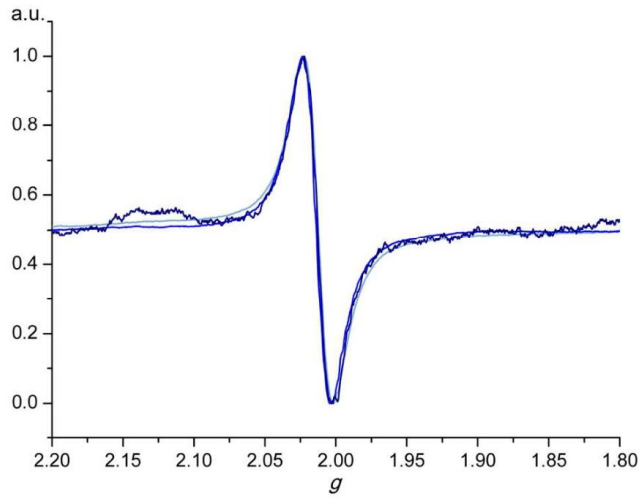

Figure S35. Normalized X-band EPR spectra of **4b** with oxidants $[N(4\text{-}C_6H_4Br)_3][SbCl_6]$ (blue), $[C_{12}H_8S_2][SbCl_6]$ (light blue) after 3 h in THF at 35 °C and $[NH_4]_2[Ce(NO_3)_6]$ (dark blue) after 3 h in THF at 22 °C.

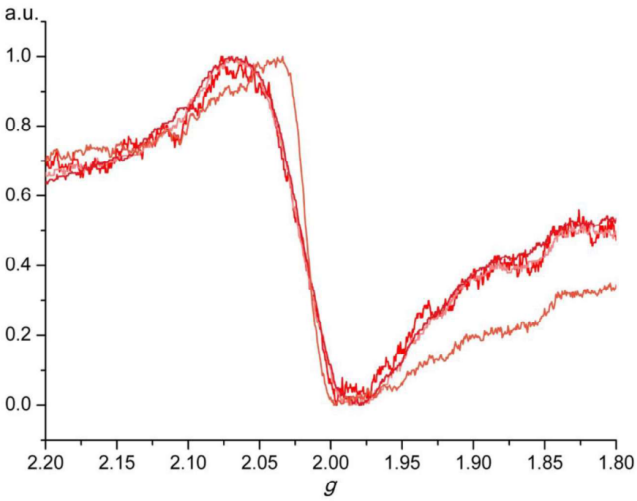

Figure S36. Normalized X-band EPR spectra of **4a** with oxidants $[N(4\text{-}C_6H_4Br)_3][SbCl_6]$ (red), $[C_{12}H_8S_2][PF_6]$ (light red), $[C_{12}H_8S_2][SbCl_6]$ (dark red) and $[C_{12}H_8S_2][PF_6]$ in the presence of 1 eq $[^nBu_4N]Cl$ (orange) after 3 h in CH_2Cl_2 at 35 °C.

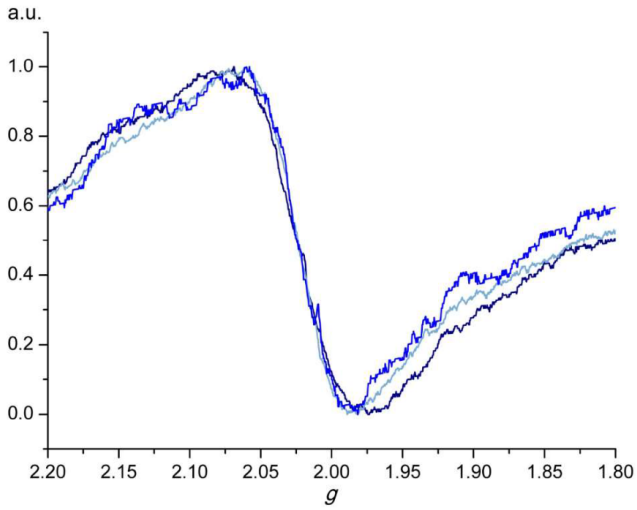

Figure S37. Normalized X-band EPR spectra of **4b** with oxidants $[N(4\text{-}C_6H_4Br)_3][SbCl_6]$ (blue), $[C_{12}H_8S_2][PF_6]$ (light blue) and $[C_{12}H_8S_2][SbCl_6]$ (dark blue), after 3 h in CH_2Cl_2 at 35 °C.

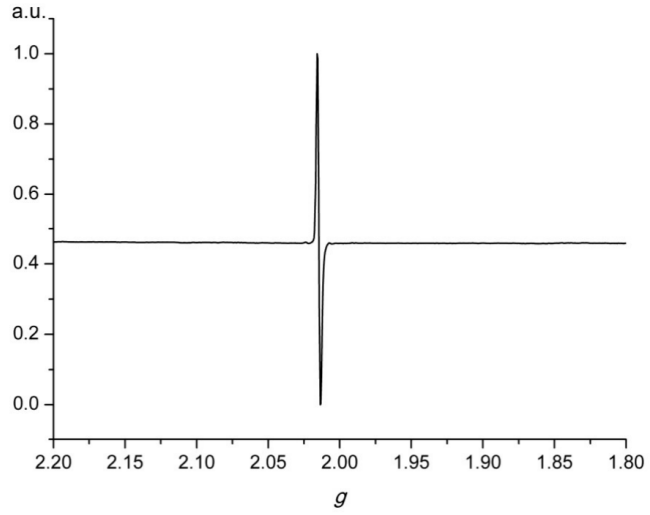

Figure S38. X-band EPR spectrum $[C_{12}H_8S_2][PF_6]$ (black) in CH_2Cl_2 at 22 °C.

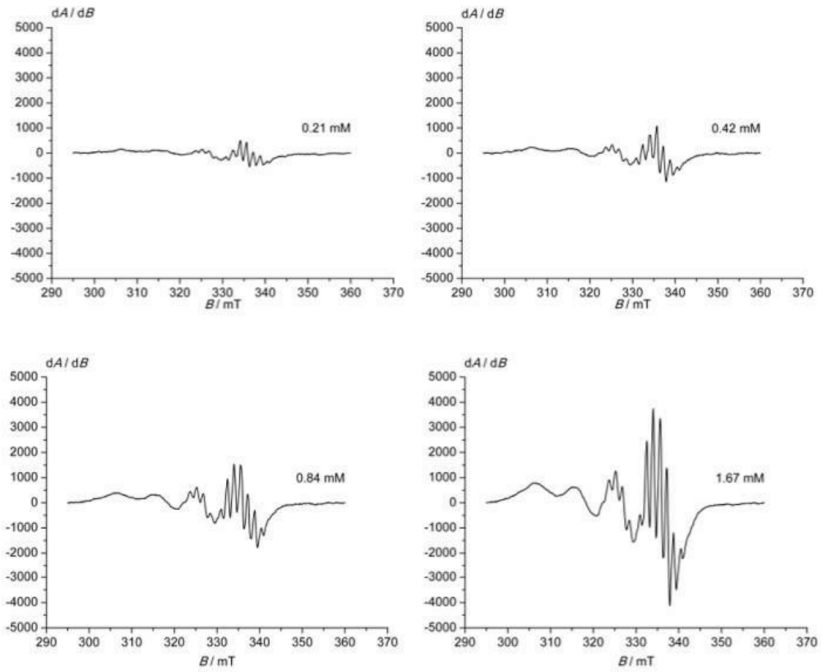

Figure S39. X-band EPR spectra of Cu(TPP) at different concentrations in THF used for calibration of the EPR resonance intensity.

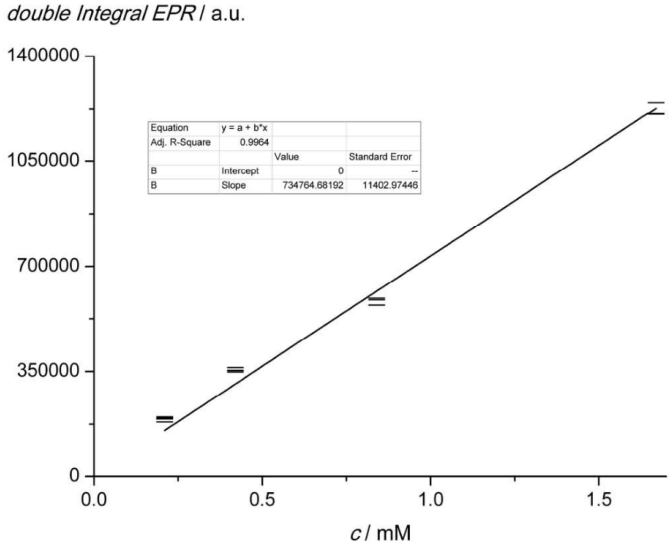

Figure S40. Calibration curve obtained from the double integration of the Cu(TPP) EPR resonances.

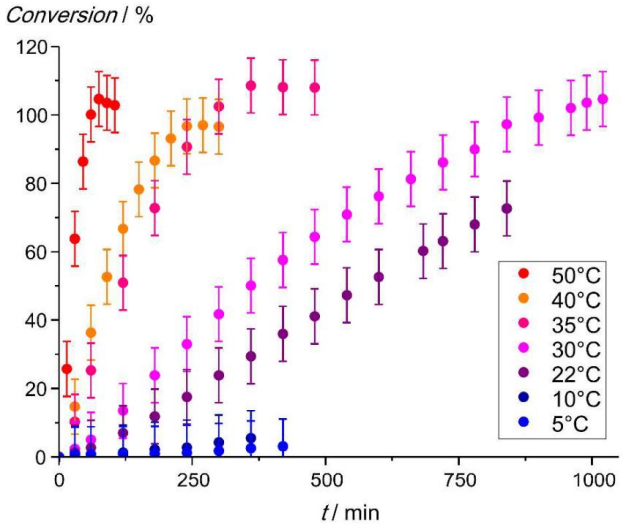

Figure S41. Conversion vs. time plot obtained from the double integration of the EPR resonances arising from **4a** and Magic Blue in THF at various temperatures.

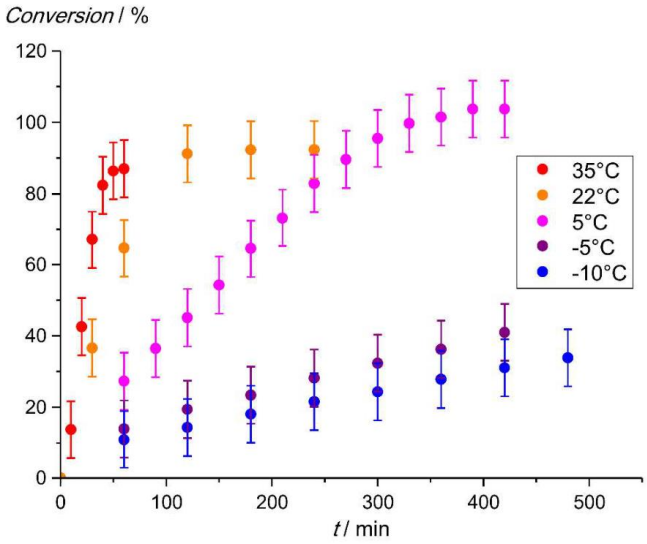

Figure S42. Conversion vs. time plot obtained from the double integration of the EPR resonances arising from **4b** and Magic Blue in THF at various temperatures. Please note the different scale of the x-axis as compared to Figure S41.

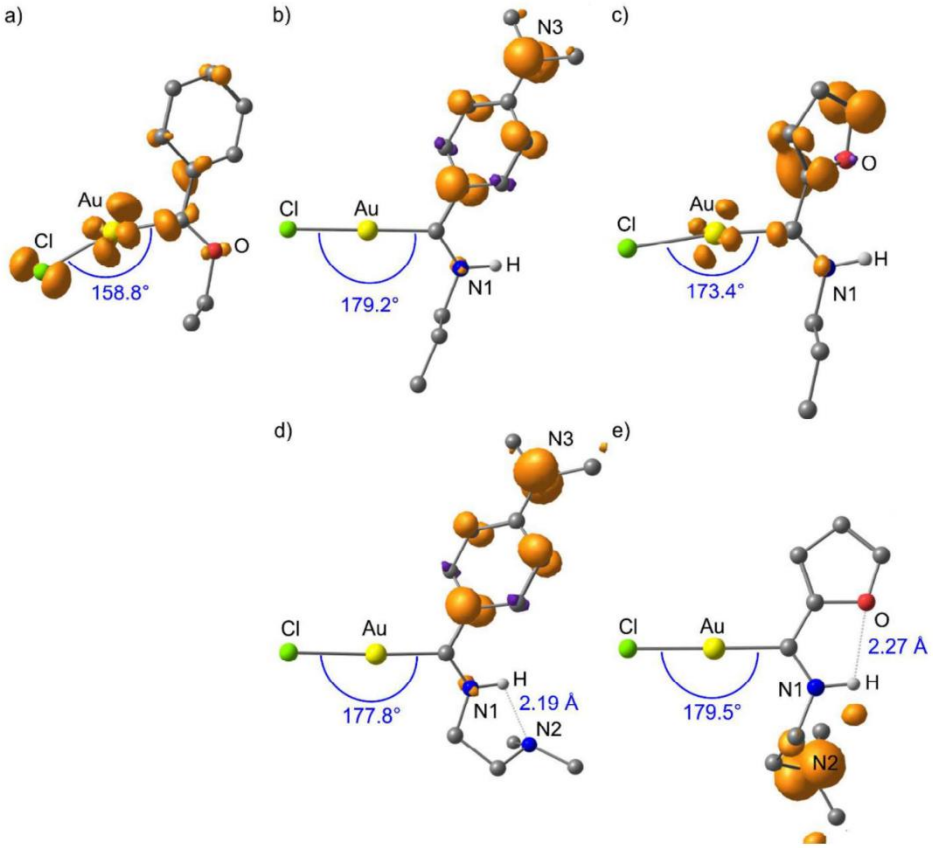

Figure S43. DFT calculated geometries and spin-densities of a) **[1]**$^{\bullet+}$, b) **[2a]**$^{\bullet+}$, c) **[3a]**$^{\bullet+}$, d) **[2b''']**$^{\bullet+}$ with hydrogen bond and e) **[3b]**$^{\bullet+}$. Spin densities are displayed in orange at a contour value of 0.01 a.u.; CH hydrogen atoms omitted.

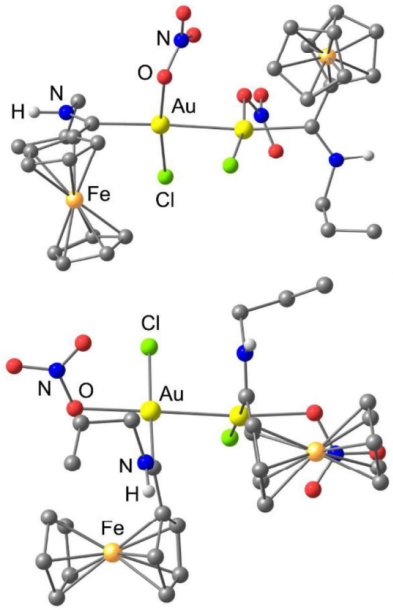

Figure S44. DFT calculated geometry of a the less stable dimers **SP-4-4-(4a–ONO_2)$_2$** (top, 119 kJ mol^{-1}) and **SP-4-3-(4a–ONO_2)$_2$** (bottom, 11 kJ mol^{-1}) with a gold(II)-gold(II) σ bond (singlet multiplicity). Energies relative to the dimer of Figure 9. CH hydrogen atoms omitted.

6.3 Supporting Information to chapter "Di-substituted Fischer gold(I) carbene complexes"

DFT calculations were carried out using the ORCA program package (version 4.1.2).[252] All calculations were performed using the B3LYP functionals[253]–[255] and employed the RIJCOSX approximation.[256],[257] Relativistic effects were calculated at the zeroth order regular approximation (ZORA) level.[258] The ZORA keyword automatically invokes relativistically adjusted basis sets. To account for solvent effects, a conductor-like screening model (CPCM) modelling CH_2Cl_2 was used in all calculations.[259],[260] Geometry optimizations were performed using Ahlrichs' split-valence triple- ξ basis set ZORA-def2-TZVP.[261],[262] Atom-pairwise dispersion correction was performed with the Becke-Johnson damping scheme (D3BJ).[263],[264] The presence of energy minima was checked by numerical frequency calculations.

Cartesian coordinates of the DFT calculated geometry of **7**:

6	2.379600000	4.020904000	9.988883000
79	-0.362390000	6.356506000	9.796539000
79	2.581686000	5.687458000	8.929398000
26	0.097331000	2.212374000	9.075746000
17	0.321414000	7.923011000	11.380660000
6	1.403022000	1.259407000	7.752019000
1	1.107749000	0.827290000	6.810090000
17	2.878774000	7.580733000	7.606170000
8	-1.143576000	5.158583000	7.232915000
8	2.518376000	3.924956000	11.274886000
6	1.783889000	2.598132000	7.960880000
1	1.857414000	3.372927000	7.215786000
6	2.045872000	2.769723000	9.369302000
6	-1.692427000	2.527305000	8.108823000
1	-1.806787000	2.541966000	7.038443000
6	-1.005412000	4.984915000	8.511434000
6	-1.345887000	3.656155000	8.933843000
6	-1.821073000	1.403092000	8.953178000
1	-2.039298000	0.397385000	8.632886000
6	1.789629000	1.506999000	10.011999000
1	1.860924000	1.313450000	11.068556000
6	-1.248713000	3.181704000	10.293577000
1	-0.978581000	3.784614000	11.144584000
6	-1.551574000	1.807388000	10.295167000
1	-1.529123000	1.158073000	11.154799000
6	1.403442000	0.588477000	9.012018000
1	1.113052000	-0.436071000	9.178014000
6	2.830714000	5.106307000	12.059344000
1	3.673859000	5.624391000	11.608405000
1	3.079514000	4.736835000	13.048934000
1	1.956601000	5.753343000	12.088341000
6	-0.810684000	6.442140000	6.641171000
1	-1.387924000	7.221984000	7.132547000
1	-1.082852000	6.353636000	5.594370000
1	0.255961000	6.622946000	6.755853000

Cartesian coordinates of the DFT calculated geometry of **[7]**$^+$:

6	2.318540000	3.987575000	10.054803000
79	-0.170264000	6.318623000	9.687844000
79	2.391745000	5.713791000	9.028332000
26	0.116056000	2.253384000	9.079395000
17	0.496634000	7.896339000	11.237430000
6	1.394969000	1.338912000	7.689230000
1	1.088976000	0.951953000	6.731437000
17	2.730384000	7.587757000	7.722403000
8	-1.159271000	5.137502000	7.184851000
8	2.515980000	3.878991000	11.320107000
6	1.780441000	2.663960000	7.951423000
1	1.853490000	3.463188000	7.232106000
6	2.063760000	2.767804000	9.367806000
6	-1.710913000	2.509683000	8.162250000
1	-1.855804000	2.483835000	7.095762000
6	-0.952142000	4.947714000	8.439680000
6	-1.338063000	3.670029000	8.934753000
6	-1.805413000	1.420971000	9.052301000
1	-2.025629000	0.402879000	8.776078000
6	1.810463000	1.474649000	9.954710000
1	1.890577000	1.232308000	11.000548000
6	-1.192575000	3.244291000	10.311393000
1	-0.906591000	3.872251000	11.139176000
6	-1.496087000	1.874230000	10.369902000
1	-1.446992000	1.257420000	11.251842000
6	1.405459000	0.611203000	8.917490000
1	1.107296000	-0.417071000	9.039612000
6	2.756416000	5.052932000	12.151222000
1	3.477943000	5.700780000	11.659866000
1	3.148489000	4.663717000	13.083915000
1	1.811665000	5.567500000	12.304884000
6	-0.798127000	6.399711000	6.548717000
1	-1.277787000	7.215570000	7.083996000
1	-1.174975000	6.321234000	5.535300000
1	0.283878000	6.503428000	6.559004000

Cartesian coordinates of the DFT calculated geometry of **[7]**$^{2+}$:

6	2.361038000	4.019527000	10.092840000
79	-0.181917000	6.310352000	9.684423000
79	2.389716000	5.726495000	9.042679000
26	0.108998000	2.177151000	9.060557000
17	0.533664000	7.826775000	11.248129000
6	1.513641000	1.273976000	7.762969000
1	1.255687000	0.851576000	6.805570000
17	2.618929000	7.586776000	7.723917000
8	-1.192482000	5.179128000	7.169798000
8	2.583599000	3.901287000	11.337756000
6	1.836826000	2.626663000	8.012497000
1	1.896250000	3.415178000	7.279582000
6	2.067437000	2.764294000	9.425411000
6	-1.760262000	2.536973000	8.069504000
1	-1.869072000	2.530646000	6.996952000
6	-0.969537000	4.981049000	8.405004000
6	-1.333090000	3.652441000	8.862892000
6	-1.919460000	1.435688000	8.930635000
1	-2.173727000	0.433309000	8.624411000
6	1.896177000	1.474088000	10.024905000
1	1.950803000	1.256810000	11.079365000
6	-1.249269000	3.211588000	10.229769000
1	-0.963053000	3.817264000	11.074472000
6	-1.605686000	1.844601000	10.259753000
1	-1.610563000	1.211579000	11.132109000
6	1.551886000	0.570468000	9.003256000
1	1.299080000	-0.468124000	9.146102000
6	2.886852000	5.063144000	12.181068000
1	3.521459000	5.748446000	11.626604000
1	3.393945000	4.653563000	13.046408000
1	1.941311000	5.524329000	12.452886000
6	-0.868264000	6.461585000	6.533245000
1	-1.205677000	7.268096000	7.178148000
1	-1.404419000	6.446903000	5.592026000
1	0.207194000	6.492624000	6.38127600

7 Acknowledgements

8 Curriculum vitae